Topological effects on the quantum properties of magnetic nanographene molecules



Federico Lombardi

A thesis submitted for the degree of
Doctor of Philosophy

St Cross College, University of Oxford
Trinity Term 2021

Abstract

Graphenoids are nanometer-sized flakes that share the same honeycomb framework of graphene. Novel chemistry has allowed the bottom-up synthesis of molecular graphenoids with atomic-like control of their structure. The electronic properties of these finite-sized graphene nanoislands actively depend on the topology of their edges and their π-electron network. Rational design of the topology in terms of size, conjugation, and presence of defects, has highlighted exotic magnetic properties that were predicted for quantum confined graphene structures. The presence of free spins, and the similarity to the graphene lattice would render them promising materials for all carbon-based spintronic and quantum devices. While a large number of structures are being synthetised by chemists everywhere, the quantum properties of these molecules remain widely unexplored.

In this work, we study the quantum properties of three categories of graphenoids: units with pentagonal defects, segments with zigzag edges, and ring-shaped molecules. Defects have been observed in graphene and are expected to play a key role in its optical, electronic, and magnetic properties. However, because most of the studies focused on the structural characterization, the implications of topological defects on the physicochemical properties of graphene remain poorly understood. Zigzag segments of carbon edges are a fundamental ingredient for most proposals of graphene nanostructures: they allow nontrivial topologies, where spin states can be used for quantum information processing and new communication pathways. Ring structures are intriguing for their aromatic and antiaromatic properties, and because they could show compelling quantum interference patterns.

In this thesis, we use Electron Paramagnetic Resonance (EPR) to study the quantum properties of ensemble of isolated molecules. We measure coherence times at different temperatures and in different hosting matrices in order to evaluate structural and environmental effects on the properties. The molecular graphenoids obtain large coherence times up to room temperature that we compare to metal-based molecular systems and inorganic systems. We use advanced decoupling sequences to increment the coherence of the systems. Finally, we suggest synthetic strategies to remove the main channels of decoherence. These results shine new light on the fundamental quantum properties of topological defects and edge states in nanographene structures.

Acknowledgements

Much of this work would have not been possible without the guidance of my supervisor Prof Lapo Bogani. I am most grateful for building in the group a friendly environment, a culture of trust and support, and for sharing your curiosity towards all fields of science. I would also like to thank you for your mentorship in these four years, and for letting me grow as an independent researcher capable of bringing forward his own ideas.

I would also like to thank my co-supervisor Prof Kyriakos Porfyrakis for welcoming me in his group and supporting me throughout my PhD journey.

This project could have not been completed without the constant help of Dr Will Myers, who taught me everything I know about EPR instrumentations and helped me throughout all the technical problems I encountered.

I would like to acknowledge all the collaborators who provided the splendid compounds I could study in this thesis: Ji Ma, Junzhi Liu, and Prof Xinliang Feng from Technische Universität Dresedn; Fan Wei, Yong Ni, and Prof Jishan Wu from the National University of Singapore. I would also like to thank Prof Boris Naydenov for hosting me in his laboratory at the Helmotz Zentrum in Berlin to carry out measurements when our laboratories were closed.

I acknowledge financial support from the EPSRC (Grant No. EP/N509711/1).

I am forever indebted to the members of the group for their support. A special mention for Dimitris who put up with my ignorance of chemistry and helped me in any practical way from sample preparation to finding the right solvent for my measurement. All the postdocs in the group were instrumental for their guidance, and for sharing their expertise: Alex, Iago, Jennifer, Michael, Tian, Wenjing, and Xuelin. Moreover, I was privileged to encounter on my path like-minded individuals who shared the same PhD journey as me. From long hours in the lab, to sharing a room at a conference, I would like to thank Alessandro, Fanmiao, Ming-Yee, and Simen for forming bonds that go beyond scientific collaborations and for never making a day in the office boring.

I am grateful to my friends Adam, Andrew, Brooke, Danielle, Helena, Marianne, Moritz, Pernille, and Sam for enduring my complaints (for several years), and for laughing at my jokes even when they were not that funny.

Thanks to my parents for their constant support and love.

Finally, thanks to Lonie for always being there for me.

Contents

Abstract ii

Acknowledgements v

Introduction 1

1 Background 4

1.1 Quantum Description of Magnetic States 4

1.1.1 Electron Spin 4

1.1.2 Spin Hamiltonian 5

1.1.3 Density Matrix 8

1.2 Quantum Information Processing 9

1.3 Decoherence 12

1.3.1 Modelling 13

1.3.2 Protecting Against Decoherence 16

1.4 Molecular Spin Qubits 17

1.4.1 Improving Coherence 19

1.4.2 Coupling Qubits 20

1.5 Graphene 23

1.5.1 Structure and Properties 23

1.5.2 Edge states 25

1.5.3 Topological Defects 31

1.6 Open-shell Aromatic Hydrocarbons 32

2 Methods **37**

2.1 Electron Paramagnetic Resonance . . . 37

2.1.1 Continuous Wave EPR . . . 37

2.1.2 Pulse EPR . . . 41

2.2 Hyperfine spectroscopy . . . 46

2.2.1 ESEEM techniques . . . 48

2.2.2 ENDOR techniques . . . 50

2.2.3 Comparison . . . 51

2.3 Density Functional Theory . . . 52

2.3.1 Calculation of EPR parameters . . . 54

2.4 Remarks on the Methods . . . 57

3 Pentagonal Units in Graphenoids **59**

3.1 Introduction . . . 59

3.2 Magnetic Properties . . . 61

3.3 Quantum properties . . . 66

3.4 Synthetic Tuning of Quantum Properties . . . 72

3.4.1 Magnetic Properties . . . 73

3.4.2 Spin-lattice Relaxation . . . 78

3.4.3 Coherence Time . . . 82

3.5 Outlook . . . 85

3.6 Project Overview . . . 88

4 Zigzag Segments **89**

4.1 Introduction . . . 89

4.2 Magnetic Properties . . . 91

4.3 Spin-lattice relaxation . . . 97

4.4 Spin coherence . . . 99

4.5 ^{13}C Isotropic hyperfine coupling . . . 104

4.6 Outlook . . . 106

4.7 Project Overview . . . 107

5 Ring Shaped Graphenoids **108**

5.1 Introduction . . . 108

5.2 Magnetic Properties . . . 110

5.3 Quantum Properties . . . 114

5.4 Hyperfine Spectroscopy . . . 118

5.5 Outlook . . . 120

5.6 Project Overview . . . 121

6 Improving Coherence **122**

6.1 Introduction . . . 122

6.2 Theoretical Modelling . . . 125

6.3 Methods Discussion . . . 127

6.4 Results . . . 131

6.4.1 Instantaneous Diffusion . . . 131

6.4.2 Decoupling . . . 132

6.5 Discussion . . . 133

6.5.1 Spectral decomposition . . . 137

6.6 Outlook . . . 138

6.7 Project Overview . . . 138

7 Conclusions and Perspectives **139**

A EPR on Charge Transfer Tryads **143**

A.1 Introduction . . . 143

A.2 Experimental Methods . . . 145

A.3 Results . . . 147

A.3.1 UV-Vis Spectroscopy . . . 147

A.3.2 EPR . . . 147

A.4 Outlook . . . 148

A.5 Project Overview . . . 150

B Additional Data **152**

B.1 Pentagonal units in graphenoids . . . 152

B.2 Zigzag graphenoids 157
B.3 Ring shaped graphenoids 158

Acronyms **162**

List of Figures **177**

List of Tables **178**

Bibliography **213**

Introduction

In this work, we study the properties of topologically-modified graphenoids. By topology, we intend the ability to precisely manipulate the graphene lattice, without altering its elemental composition. Research on the manipulation of graphene has faltered due to the inadequacy of top-down fabrication to shape the graphene lattice with atomic precision. The necessary level of control of the graphene lattice has become possible only recently using bottom-up synthetic techniques [1]. A very large set of small molecules and long polymers with different sizes, conjugations, and features has been achieved [2–4]. Although the related chemistry is seeing an explosion for optoelectronic, biological, and energy applications, the quantum properties of these molecules remain unexplored and untapped.

Current hopes of developing radically new technologies in computation, communication, security, and sensing rely on the manipulation of quantum states. Quantum computers might expedite the solutions of problems that are particularly challenging on classical devices [5]. Quantum cryptography may produce unbreakable codes that are not protected by a 48-character key, but by the law of quantum physics [6]. Quantum sensing aims at lowering the limit of current metrology for electric and magnetic fields detection, nanoscale imaging, and atomic clocks [7]. Quantum engineering overall hinges on controlling physical states whose fragility has, until now, curbed their enormous potential.

Prototype quantum computers based on superconducting circuits are already available and under research in the industry [8]. These systems are hosted in dilution refrigerators and cooled down to $\sim$100 mK. However, due to limitations in circuit design and cooling power of the refrigerator, the maximum number of qubits is $\sim$50. Therefore, while these prototypes offer ample testbeds to understand what it is possible to do with quantum computers, active research is trying to increase the operating temperature of quantum systems so that more qubits can be connected.

There is a long list of candidates for implementation of quantum information processing, the majority of which is based on manipulation of spin states [9] or photons [10] in different hardware.

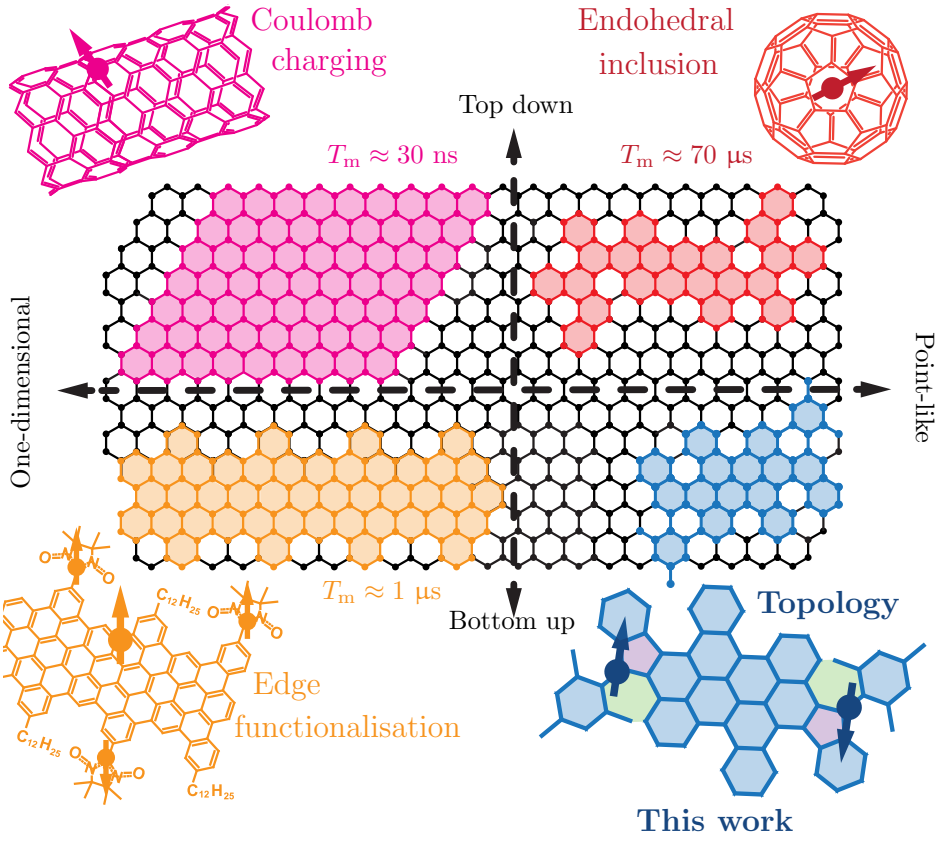


Figure 1: Carbon-based nanostructures are generally diamagnetic, but different strategies have been devised to include and manipulate spins. It is possible to electrically confine single electron spins in carbon nanotubes but their performance is limited at mK temperature and hindered by spin-orbit coupling [13]. Single or multiple magnetic elements can be included inside the cage of fullerenes, but their synthesis is extremely inefficient, and it is hard to link different fullerenes with each other [14]. An intriguing strategy is to functionalise Graphene Nanoribbons (GNRs) with spin active components in order to inject spin density into their edge and make use of their magnetic properties [15]. The different structures are showed together with their characteristic coherence time T_m, which we will assess for our molecules in the experimental part of this thesis.

Single spins electrically constrained in Si or GaAs quantum dots offer interesting perspective [11], especially because they can build future developments on the solid expertise of the semiconducting industry. Photon systems have the advantage that they could be readily used with the current optical fibre infrastructure [10]. For quantum sensing, nitrogen vacancies in diamonds are very promising because they can work up until room temperature [12].

Building up on previous results on Single Molecule Magnets (SMMs) [16], control of spins in molecular materials is opening up as viable alternative with respect to materials discussed above. While their performances are not yet up to their counterparts, molecular materials main advantage is their incredible flexibility [17]. They can be tailored with specific groups for sensing of a particular

environment [18], they can be individually grafted into surfaces [19] or into junctions [20], and they can be deposited in multilayer devices [21]. Overall, they allow multifunctional interface of electrical, magnetic, optical, and biological properties. The majority of the molecules considered for quantum applications have been, so far, metal-based systems. Nonetheless, conjugated sp^2-carbon nanomaterials would, in principle, be extremely appealing for spintronics and quantum applications because they can be integrated into engineered devices and possess intriguing mechanical and transport properties [22].

The thesis is organised as following: the first two chapters introduce the background and the concepts necessary to understand the results; the middle four chapters describe the experimental results we obtained on three different topologies of molecules; the last chapter concludes on the results and discusses possible future research paths. In chapter 1, we begin by covering the basis of electron spin and its quantum mechanics representation. We expand the concept of quantum engineering and provide a literature review of the main results for molecular qubits, and bottom-up synthesised graphene structures. In chapter 2, we describe the experimental and theoretical methods used in this thesis. As the main technique adopted in this work was Electron Paramagnetic Resonance (EPR), a detailed theoretical and technical explanation is provided. In chapter 3, we discuss the experimental results on saddle-shaped molecules with pairs of pentagonal defects included at specific positions. We use *ad hoc* tailored molecules to observe how properties change when the size and conjugation increase. In chapter 4, we analyse measurements on zigzag edged molecules that are representative of Graphene Nanoribbon (GNR). We put emphasis on comparing the experiments to the large body of theoretical predictions and we argue that the theory should be reviewed to take into consideration results that surpass previous expectations. In chapter 5, we study ring-shaped molecules with pentagonal defects at precise positions. In chapter 6, we discuss dynamical decoupling as a possible route to improve the quantum performance of the three categories of molecules analysed. We tie up together all the previous results and interpret them with a unified framework. In appendix A, we present the preliminary results and some comments on a charge transfer tryad project that has not been finished yet. In appendix B we provide additional data and simulations on the molecules described in chapter 3, 4, and 5.

Background

1.1 Quantum Description of Magnetic States

1.1.1 Electron Spin

The spin of an electron is an intrinsic angular momentum that has no classical correspondent. Such quantity is described by the quantum operator $\hat{\mathbf{S}}$, which for a free electron is $S = \frac{1}{2}$. The spin can assume $2S + 1$ values on the three axes with operators $\hat{S}_x$, $\hat{S}_y$, $\hat{S}_z$, and quantised momentum $m_s\hbar$, where $\hbar$ is the Planck constant, and, for a free electron, $m_s = \pm\frac{1}{2}$. The two states are generally referred as spin-up for $m_s = \frac{1}{2}$, and spin-down for $m_s = -\frac{1}{2}$.

For an individual free electron, the Hilbert space has dimension 2, and we describe it with the standard Dirac notation using the following basis set:

$$|\uparrow\rangle = \begin{pmatrix} 1 \\ 0 \end{pmatrix}; \quad |\downarrow\rangle = \begin{pmatrix} 0 \\ 1 \end{pmatrix} \tag{1.1}$$

therefore, any arbitrary spin state can be defined by the wavefunction:

$$|\psi\rangle = \alpha\,|\uparrow\rangle + \beta\,|\downarrow\rangle \tag{1.2}$$

where α and β are complex numbers respecting the normalisation condition $|\alpha|^2 + |\beta|^2 = 1$.

1.1.2 Spin Hamiltonian

The Hamiltonian of a system contains all the information necessary to describe the dynamics of the system itself. The time trajectories are ruled by the time-dependent Schrödinger equation:

$$i\hbar\frac{\partial\left|\psi\right\rangle}{\partial t}=\hat{\mathcal{H}}\left|\psi\right\rangle. \tag{1.3}$$

In general, given any system with any number of electrons, the Hamiltonian is divided in three parts: the Born-Oppenheimer Hamiltonian (see 2.14), the relativistic correction, the interactions with external fields [23]. This is a many-body problem that has no analytical solution. Therefore, to simplify the problem, a lower–dimension Hamiltonian is used to interpret magnetic resonance experiments: the spin Hamiltonian (SH). For the typical magnetic fields involved in such experiments, the energy scale of the interaction with the magnetic field $\mathbf{B}$ is a small perturbation with respect to the orbital terms, hence we can disregard orbital coordinates and just focus on the spin coordinates.

We can write the spin Hamiltonian for a spin S interacting with N nuclei as a sum of different terms:

$$\begin{aligned}\hat{\mathcal{H}} &= \hat{H}_{eZ}+\hat{H}_{ZFS}+\hat{H}_{Ex}+\hat{H}_{nZ}+\hat{H}_{HF}+\hat{H}_{n\text{-}n}= \\ &= \mu_{\mathrm{B}}\mathbf{B}\mathbf{g}\hat{\mathbf{S}}+\hat{\mathbf{S}}_1\mathbf{D}\hat{\mathbf{S}}_2+J\hat{\mathbf{S}}_1\hat{\mathbf{S}}_2+\mu_{\mathrm{n}}\sum_i^N g_{\mathrm{n}}^{(i)}\mathbf{B}\hat{\mathbf{I}}_i+\sum_i^N\hat{\mathbf{S}}\mathbf{A}_i\hat{\mathbf{I}}_i+\sum_{i,j}^N\hat{\mathbf{I}}_i\mathbf{P}_{i,j}\hat{\mathbf{I}}_j\end{aligned} \tag{1.4}$$

where $\mathbf{B}$ is the external static magnetic field, $\hat{\mathbf{S}}$ and $\hat{\mathbf{I}}$ are electron and nuclear spin operators, μ_{B} and μ_{n} the electron and nuclear Bohr magneton, $\mathbf{g}$ is the Landé factor, which for a free electron is $g_S = 2.002319$, $g_{\mathrm{n}}^{(i)}$ the nuclear g-factor that depends on the isotope, $\mathbf{D}$ the electron dipolar tensor, J the scalar exchange coupling, $\mathbf{A}$ the electron-nuclear hyperfine coupling, and $\mathbf{P}$ a tensor that generically includes any nuclear interactions, for example nuclear quadrupole interactions and nuclear-nuclear dipolar interactions. In the following we will describe the individual terms appearing in eq. (1.4) and their parameters.

The electron Zeeman (eZ) term depicts the interaction between the electron spin and an external magnetic field. The degenerate energy levels relating to different m_s numbers will be split by an energy proportionate to the magnetic field, the spin number, and the g-factor. The latter is a tensor,

which we can write in its reference frame with its principal axis values as:

$$\mathbf{g} = \begin{pmatrix} g_x & & \\ & g_y & \\ & & g_z \end{pmatrix}. \tag{1.5}$$

If $g_x \neq g_y \neq g_z$ the tensor is called rhombic, if $g_x = g_y = g_\perp,\ g_z = g_\parallel$ it is called axial, and if $g_x = g_y = g_z = g_{\text{iso}}$ it is called isotropic.

For spin systems $S \geq 1$ spin-spin coupling is included in the Zero Field Splitting (ZFS) Hamiltonian. This scenario applies both for two spins located in distant centres, or multiple spins on the same centre, for instance on a transition metal or a lanthanide. This interaction can be modelled as a classical magnetic dipole-dipole coupling:

$$\hat{H}_{ZFS} = \frac{\mu_0}{4\pi} g_1 g_2 \mu_{\text{B}} \left[\frac{\hat{\mathbf{S}}_1 \cdot \hat{\mathbf{S}}_2}{r^3} - \frac{3(\hat{\mathbf{S}}_1 \cdot \mathbf{r})(\hat{\mathbf{S}}_2 \cdot \mathbf{r})}{r^5} \right], \tag{1.6}$$

where μ_0 is the vacuum magnetic permeability, and $\mathbf{r}$ is the distance vector between the two spins. Here, for simplicity it was considered that the g-factors of the two electron spins were isotropic. The previous equation can be expanded and expressed in terms of the total spin $\hat{\mathbf{S}} = \hat{\mathbf{S}}_1 + \hat{\mathbf{S}}_2$, to yield the more common $\hat{H}_{ZFS} = \hat{\mathbf{S}}\mathbf{D}\hat{\mathbf{S}}$. The $\mathbf{D}$ tensor is traceless and its expression in the principal axes of its frame is:

$$\hat{\mathbf{S}}\mathbf{D}\hat{\mathbf{S}} = D_x \hat{S}_x^2 + D_y \hat{S}_y^2 + D_z \hat{S}_z^2 = D\left[\hat{S}_z^2 - \frac{1}{3}S(S+1)\right] + E(\hat{S}_x^2 - \hat{S}_y^2) \tag{1.7}$$

where $D = \frac{2D_z - (D_x + D_y)}{2}$ and $E = \frac{D_x - D_y}{2}$ [24], although sometimes different conventions are adopted in different textbooks and $D = \frac{3}{2}D_z$ with $D = 3E$ [25, 26]. When the frames of the $\mathbf{D}$ and $\mathbf{g}$ tensor differ, rotation matrices will be used to express the tensors in one or the other frame. For systems with large spin and large crystal field contribution, the $\mathbf{D}$ tensor alone is often not enough to represent the spin levels and higher order terms are necessary [27].

If two or multiple spins are on separate centres, it is necessary to consider their exchange coupling. The exchange coupling is a Coulomb interaction between two electrons that does not take into consideration the coupling of their magnetic moments (which is incorporated into $\mathbf{D}$). Hence, the exchange coupling is referred as through bond interaction, whereas the dipolar coupling is a through

space interaction. In the most general case, the exchange parameter is a tensor $\mathbf{J}$, but we often consider a Heisenberg exchange coupling, which is isotropic: $J = \mathrm{tr}\{\mathbf{J}\}$. In first approximation, J can be related to the overlap of the two electron wavefunctions [25]:

$$J = -2\langle\phi_a(1)\phi_b(2)|\frac{e^2}{4\pi\epsilon_0 r}|\phi_a(2)\phi_b(1)\rangle, \tag{1.8}$$

where ψ_a and ϕ_b are normalised molecular orbitals, and the term $\frac{e^2}{4\pi\epsilon_0 r}$ is the Coulomb exchange.

The hyperfine (HF) coupling describes the electron-nuclear interaction. In the most general case the tensor $\mathbf{A}$ is a sum of three different terms: the isotropic Fermi contact interaction, the dipolar interaction, and the pseudo-hyperfine interaction. The isotropic interaction accounts for the spin density that resides on the nucleus:

$$a_{\mathrm{iso}} = \frac{2\mu_0}{3} g\mu_{\mathrm{B}} g_{\mathrm{n}} \mu_{\mathrm{N}} |\psi_0(0)|^2 \tag{1.9}$$

where $|\psi_0|^2$ is the spin density at the nucleus. The dipolar interaction represents the classical coupling between two dipoles and can be written as a traceless tensor $\mathbf{T}$:

$$\hat{\mathbf{S}}\mathbf{T}\hat{\mathbf{I}} = \frac{\mu_0}{4} g\mu_{\mathrm{B}} g_{\mathrm{n}} \mu_{\mathrm{N}} \left[\frac{3(\hat{\mathbf{S}}\cdot\mathbf{R})(\hat{\mathbf{I}}\cdot\mathbf{R})}{R^5} - \frac{\hat{\mathbf{S}}\hat{\mathbf{I}}}{R^3}\right] \tag{1.10}$$

where $\mathbf{R}$ is the distance vector between the nucleus and the electron in a point-dipole approximation. Lastly, the pseudo-hyperfine coupling accounts for the interaction between the nuclear spins and the electron orbital momentum. This term can be neglected for the organic radical under study since their spin-orbit coupling is modest. Analogously to the g-factor, the hyperfine coupling can be isotropic, axial or rhombic, depending on how many parameters are necessary to describe its principal values. For example, in the axial case:

$$\mathbf{A} = a_{\mathrm{iso}}\mathbf{I} + \mathbf{T} = \begin{pmatrix} a_{\mathrm{iso}} & & \\ & a_{\mathrm{iso}} & \\ & & a_{\mathrm{iso}} \end{pmatrix} + \begin{pmatrix} T & & \\ & T & \\ & & -2T \end{pmatrix} = \begin{pmatrix} A_\perp & & \\ & A_\perp & \\ & & A_\parallel \end{pmatrix} \tag{1.11}$$

In addition to electron spin and electron-nuclear couplings, fully nuclear terms can become important in the SH, although they are more often observed in Nuclear Magnetic Resonance (NMR).

The nuclear Zeeman (nZ) term is analogous to the eZ term, but referred to nuclear spins instead. Degenerate nuclear spin levels are also split by the external magnetic field. In this case the g-factor is generally isotropic, it is a fingerprint of a specific isotope, and it can also be negative. Quadrupolar interactions can arise for nuclei with $I \geq 1$, they are isotope-specific, and describe the anisotropic distribution of electric charge in the nucleus. Nuclear-nuclear exchange and dipolar coupling can also be present for multiple, interacting nuclei. A deeper discussion about nuclear-nuclear dipolar interactions will be provided below when explaining the problem of coherence.

1.1.3 Density Matrix

In a quantum mechanics experiment, we will generally work with a statistical ensemble. This can be a temporal ensemble if we prepare a single spin system in the same state and repeat the measurement several times, or a spatial ensemble if we have a collection of identical quantum systems that are measured at the same time so that the behaviour is an average over them all. In standard magnetic resonance experiments we will fall in the latter case. When working with ensembles, instead of the wavefunction formalism we will use the density matrix formalism. For any state $|\psi\rangle = \alpha |\uparrow\rangle + \beta |\downarrow\rangle$, the density matrix is defined as:

$$\hat{\rho} = |\psi\rangle \langle\psi| . \tag{1.12}$$

One advantage of the density matrix formalism is in the treatment of pure and mixed states. In a two-dimensional Hilbert space, a pure state is expressed as a general superposition of states of the basis set. For example $|a\rangle$ and $|b\rangle$ are two separate pure states:

$$|a\rangle = \alpha |\uparrow\rangle + \beta |\downarrow\rangle \tag{1.13}$$

$$|b\rangle = \gamma |\uparrow\rangle + \delta |\downarrow\rangle . \tag{1.14}$$

However, a statistical ensemble with n members could be formed of a mix: n_a elements in state $|a\rangle$ and n_b elements in state $|b\rangle$. Therefore, the probability of finding an element in $|a\rangle$ is $p_a = n_a/n$ and in $|b\rangle$ is $p_b = n_b/n$. This can be readily incorporated in the density matrix as:

$$\hat{\rho} = \sum_{i=1}^{m} p_i \hat{\rho}_i = \sum_{i=1}^{m} p_i |\psi_i\rangle \langle\psi_i| . \tag{1.15}$$

In this way it is possible to easily take into consideration quantum statistical mechanics for ensembles.

The density matrix formalism also facilitates calculations when treating quantum decoherence. The density matrix has some important properties: all the diagonal elements are populations and they are related to the probability of finding the system in that particular state, the difference between diagonal elements indicates the polarisation of the transition between the two states; the off-diagonal elements are called coherences and they represent superposition between two states.

It can be demonstrated from the Schrödinger equation that the time evolution of a quantum system is governed by the Liouville-von Neumann equation:

$$i\hbar\frac{\partial\hat{\rho}}{\partial t} = [\hat{\mathcal{H}}, \hat{\rho}]. \tag{1.16}$$

We can write the density matrix at any t, using the propagator $\hat{U}$ for which it applies $\hat{U}^{-1} = U^{\dagger}$. If the Hamiltonian is time-dependent, the propagator is expressed in terms of a Dyson time-ordering operator:

$$\hat{U}(t) = T\exp\left\{-i\int_0^t \hat{\mathcal{H}}(t')\mathrm{d}t'\right\}. \tag{1.17}$$

For a time-independent Hamiltonian the propagator can be simplified, and it can be written as:

$$\hat{U}(t) = e^{-i\hat{\mathcal{H}}t} \tag{1.18}$$

with the time dynamics of the density matrix described by

$$\hat{\rho}(t) = e^{-i\hat{\mathcal{H}}t}\hat{\rho}(0)e^{i\hat{\mathcal{H}}t} = \hat{U}(t)\hat{\rho}(0)\hat{U}^{-1}(t). \tag{1.19}$$

If n operations are carried out in a sequence then we can write

$$\hat{\rho}(t) = \hat{U}_n(t)\hat{U}_{n-1}(t)...\hat{U}_1(t)\hat{\rho}(0)\hat{U}_1^{-1}(t)...\hat{U}_{n-1}^{-1}(t)\hat{U}_n^{-1}(t). \tag{1.20}$$

1.2 Quantum Information Processing

A quantum bit (qubit) is the logical representation of a quantum two level system whose wavefunction can be written as

$$|\psi\rangle = \alpha|0\rangle + \beta|1\rangle e^{i\phi}, \tag{1.21}$$

with the normalisation condition $|\alpha|^2 + |\beta|^2 = 1$, and ϕ a phase difference. Similarly to classical bits, qubits are eventually found in a 0 or in a 1 state, but they also have all the properties of a quantum system, most notably entanglement [28]. By entanglement we intend that the state of one qubit is connected to one or to a group of other qubits and that they can only be described as one entity and not individually. As an example, we can consider the following entangled state:

$$|\psi\rangle = \frac{|00\rangle + |11\rangle}{\sqrt{2}}, \tag{1.22}$$

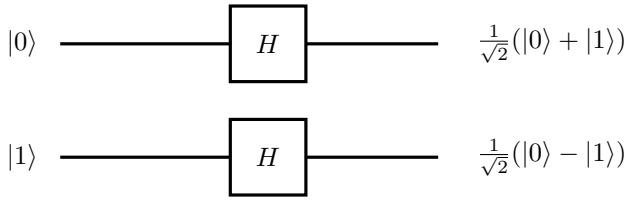
if we carry out a measurement on particle one and we get $|0\rangle$, we will immediately know that the second particle will also be in $|0\rangle$, similarly if we get $|1\rangle$ for the first particle the second will also be in $|1\rangle$. This indicates that by measuring any part, we can get information about the whole system, because the system behaves as a single entity even if the particles are spatially separated or non-interacting [29].

In parallel to classical computation, operations on qubits are carried out by quantum gates. Quantum gates are mathematically described by unitary transformations and can be represented as circuits with an input and an output as seen in fig. 1.1. Gates can operate on one qubit, as the Hadamard gate of the top panel of fig. 1.1, or on multiple qubits, such as the two-qubit Controlled NOT (CNOT) gate of the middle panel of fig. 1.1.

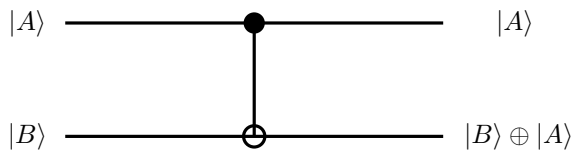
It can be demonstrated that a universal set of quantum gates can be obtained by combining single-qubit gates and one two-qubit gate [30, 31]. This set can then be used to exactly approximate any other multiple-qubit operation. In the literature there are many examples of universal sets of quantum gates, here for instance we show how a set of single-qubit gates and the CNOT gate can be used to produced entangled Bell states as seen in the bottom panel of fig. 1.1 [5].

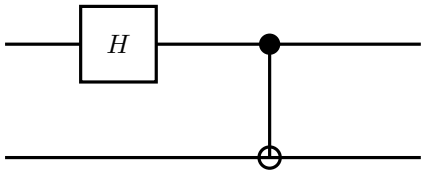
The thrive towards quantum computation was initially motivated by some pioneer works of Deutsch [32], Shor [33], and Grover [34]. They showed that certain algorithms would perform better on a quantum computer than on any classical supercomputer, a concept that would be later defined "quantum supremacy" [35, 36]. Some of the fundamental theory of quantum computing was formulated at the time of this initial work, generating the question of how to physically realise a quantum computer [37]. For instance, it can be noted that the wavefunction written for a qubit in eq. (1.21) is analogous to the one written for an electron spin in eq. (1.2) and that the gate operations are similar to the unitary propagators described above. Indeed, spin systems were chosen

$$H = \frac{1}{\sqrt{2}}\begin{pmatrix} 1 & 1 \\ 1 & -1 \end{pmatrix}$$



$$U_{CN} = \begin{pmatrix} 1 & 0 & 0 & 0 \\ 0 & 1 & 0 & 0 \\ 0 & 0 & 0 & 1 \\ 0 & 0 & 1 & 0 \end{pmatrix}$$





Input	Output	
$\|00\rangle$	$\frac{1}{\sqrt{2}}(\|00\rangle + \|11\rangle)$	$\|\Phi^{\pm}\rangle$
$\|10\rangle$	$\frac{1}{\sqrt{2}}(\|00\rangle - \|11\rangle)$	
$\|01\rangle$	$\frac{1}{\sqrt{2}}(\|01\rangle + \|10\rangle)$	$\|\Psi^{\pm}\rangle$
$\|11\rangle$	$\frac{1}{\sqrt{2}}(\|01\rangle - \|10\rangle)$	

Figure 1.1: (Top) Matrix representation of the Hadamard gate, a single qubit gate that generates a superposition of states where the states $|0\rangle$ and $|1\rangle$ have equal probability. It is easy to demonstrate $H^\dagger H = I$. (Middle) Matrix representation of the CNOT gate and its schematic: $|A\rangle$ is the control qubit and $|B\rangle$ is the target one which is flipped only if $|A\rangle = |1\rangle$. (Bottom) reparation of Bell states with a Hadamard gate and a CNOT gate, they represent the most simple entanglement between multiple qubits.

for implementation of qubits as they naturally represent a two-level system and can be manipulated through electromagnetic pulses as in standard magnetic resonance experiments. Here, we will elaborate on the study of spin systems, but other architectures could be equally valid, most notably photons [38] and superconducting circuits [39].

The Di Vincenzo criteria provide five requirements that need to be fulfilled for a system to be a candidate for quantum computing [40]. The principles were formulated more than 20 years ago, they are, without doubt, outdated and other authors have revised them in more recent years [41, 42], but their simplicity allows to immediately glance the obstacles on the route to quantum computing. In synthesis, the Di Vincenzo principles are: (i) a scalable and well characterised quantum system; (ii) the possibility of initialising the quantum system in any arbitrary state; (iii) the coherence of quantum system several order of magnitude longer than the gate operation time; (iv) the ability of implementing a set of universal quantum gates; (v) the capacity of reading out the state of the system at any point. For instance, if we consider a (electron or nuclear) spin qubit, quantum gates

could be implemented with radio frequency or microwave pulses, while initialisation and read-out could be achieved by electrical or optical means. On the basis of this idea several authors proposed schemes for implementation of quantum computation in bulk NMR [43], quantum dots [44, 45], dopants in silicon [46], nitrogen vacancies [47], and molecular magnets [48]. However, since the very beginning of the field, it was recognised that the third criterion, the problem of decoherence, would pose a very difficult challenge [49]. Decoherence, together with other sources of quantum noise, destroys entanglement and therefore makes quantum computation no longer viable. A way to obviate this problem is to implement quantum error correction schemes, which exploit ancilla qubits to detect and correct errors during computation (for a more thorough explanation of quantum error correction please see [5]). In fact, quantum error correction can only work if the error rate is below a certain threshold indicated by the specific code. Therefore, even with this more complicated schemes decoherence needs to be limited. In the next section, we will analyse the main factors that contribute to decoherence and how to mitigate them.

1.3 Decoherence

The problem of decoherence is not only related to quantum computing, it is a much larger issue that encompasses quantum mechanics and other technological applications. First, from a quantum mechanics fundamental point of view, Zurek's theories [50] argue that decoherence can explain the quantum-to-classic-transition when considering the system and measurement apparatus as open quantum systems that become entangled during the measurement process. This approach provided a more natural solution to postulates such as the collapse of the wavefunction introduced by the Copenhagen interpretation [51]. Second, it is now established that quantum systems can be used in quantum sensing to probe external stimuli such as electric fields, magnetic fields, pressure, and temperature. In particular, increasing the coherence of the system improves its sensitivity, which could go beyond classical sensors [7]. Hence, this pinpoints the importance of coherence and understanding the factors that affect it.

In order to quantify the quantum properties of a spin quantum system, we will use two classical parameters that were introduced by the magnetic resonance literature much before the advent of quantum information: the spin-lattice relaxation time and the spin-spin relaxation time [26]. The spin-lattice relaxation time, referred to as T_1, describes the time constant for a spin flip, and it is

related to the diagonal elements of the density matrix. As the spin levels are split by the magnetic field, the spin flip requires an exchange of energy that needs to be provided or absorbed by the lattice, which broadly encompasses the phonon spectrum. The spin-spin relaxation time, T_2, is the actual coherence time, that describes the survival of a coherent superposition of states. In the literature there tends to be multiple definitions of the coherence time. Here, we intend T_2 as the coherence time of an individual quantum system. However, measuring T_2 requires external stimuli, e.g. microwaves in the case of electron spins, that introduce some inhomogeneity, in that case what is measured is T_2^*. In this work, the methods we used were chosen to refocus inhomogeneities (see Hahn echo experiment in section 2.1.2), hence we can disregard T_2^*, but our measurements are in ensembles for which T_2 is not rigorously defined. Therefore, we will adopt a more conservative approach and define T_m as the coherence time [26]. While inhomogeneities are removed, the definition of T_m will include instantaneous diffusion and partial dilution in a randomly oriented ensemble. In general $T_2^* \leq T_\mathrm{m} \leq T_2$. Ultimately, the spin-lattice relaxation time indicates the time constant for any out-of-equilibrium state that will revert to thermal equilibrium, therefore the theory shows that T_1 is the limit of the coherence time and $T_2 \leq 2T_1$ [26].

1.3.1 Modelling

We use the central spin model to describe decoherence: we consider a single spin system that is immersed in a bath of N nuclei. If we assume $T_1 \gg T_2$, the main decoherence mechanism is provided by spin diffusion (SD). SD is related to spin-spin dipolar interactions and applies both to electron and nuclear spins. Here we consider that the central spins are far enough so that electron spin-spin interactions are negligible, because all the measurements were carried out in diluted samples at sufficiently low spin concentrations. Therefore, we can refer specifically to nuclear spin diffusion (NSD). The simplest model to describe decoherence treats the central spin as a quantum variable and the nuclear bath as a stochastic classical noise. Nearby nuclei interact through dipolar coupling, and at any point a nucleus spin can flip. For the principle of conservation of energy, another nucleus must absorb or give the energy necessary for the first flip, so that the spin of the second nucleus will be raised while the one of the first nucleus will be lowered, or viceversa. Such interaction is often referred as flip-flop and it causes fluctuations of the local magnetic field perceived by the central

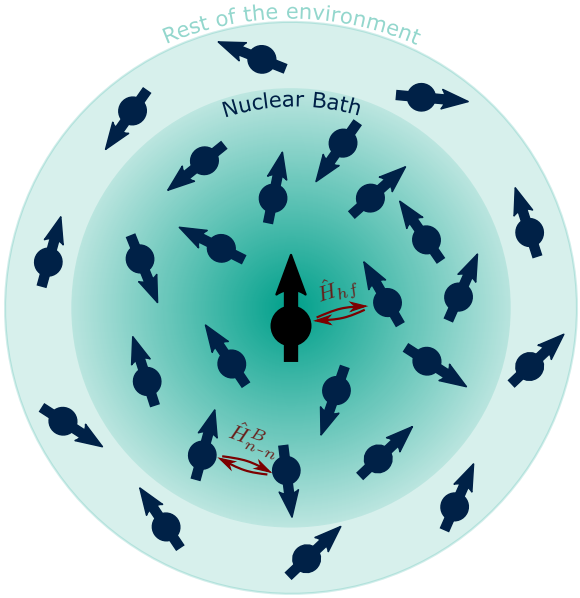


Figure 1.2: Visual representation of the central spin model. An electron spin is coupled to a nuclear bath, only the nuclei within a certain radius contribute to the decoherence, while the ones too far can be discarded. Here, the spin-bath interaction ($\hat{H}_{hf}$), and the intrabath dipolar interaction ($\hat{H}^{\mathrm{B}}_{n--n}$) are highlighted.

spin. In terms of Hamiltonian, we can write the phenomenon as:

$$\hat{H} = \mu_B \mathbf{B} \mathbf{g} \hat{\mathbf{S}} + \tilde{\mathbf{b}}(t)\hat{\mathbf{S}} \tag{1.23}$$

where $\tilde{\mathbf{b}}(\mathbf{t})$ incorporates the magnetic field fluctuations that drive decoherence. The first phenomenological interpretation of decoherence considered the flip-flops events as stochastic and $\tilde{\mathbf{b}}(\mathbf{t})$ as a random variable [52, 53]. While this model might even be successful in reproducing the order of magnitude of the decoherence process, it presents some flaws: it does not provide a microscopic explanation of the flip-flop event, and it often requires *ad hoc* assumptions such a Markovian dynamics [54, 55].

A model that treats both the central spin and the nuclear bath as quantum entities can obviate to the problems of the stochastic model:

$$\hat{H} = \hat{H}_S + \hat{H}_B + \hat{H}_{SB} \tag{1.24}$$

where $\hat{H}_S$ is the Hamiltonian of the central spin system, $\hat{H}_B$ of the bath, and $\hat{H}_{SB}$ the spin-bath interaction. With the formalism of section 1.1.2 we can write for a single spin $S = 1/2$ coupled to N

nuclei:

$$\hat{H} = \mu_B \mathbf{B} \mathbf{g} \hat{\mathbf{S}} + \sum_i^N \mu_N g_{n,i} \mathbf{B} \hat{\mathbf{I}}_i + \sum_{i,j}^N \hat{\mathbf{I}}_\mathbf{i} \mathbf{P}_{\mathbf{i},\mathbf{j}} \hat{\mathbf{I}}_\mathbf{j} + \sum_i^N \hat{\mathbf{S}} \mathbf{A}_\mathbf{i} \hat{\mathbf{I}}_\mathbf{i}, \tag{1.25}$$

with the third term embodying all nuclear-nuclear interactions. However, for the purpose of NSD we can restrict ourselves to magnetic dipolar interactions, simplifying the term as:

$$\hat{H}^B_{n\text{-}n} = \frac{\mu_0}{4\pi} \sum_{i \neq j}^N \gamma_i \gamma_j \hbar^2 \left[\frac{\hat{\mathbf{I}}_\mathbf{i} \cdot \hat{\mathbf{I}}_\mathbf{j}}{R^3_{ij}} - \frac{3(\hat{\mathbf{I}}_\mathbf{i} \cdot \mathbf{R}_\mathbf{ij})(\hat{\mathbf{I}}_\mathbf{j} \cdot \mathbf{R}_\mathbf{ij})}{R^5_{ij}} \right], \tag{1.26}$$

and if we only consider the secular term, we obtain:

$$\hat{H}^B_{n\text{-}n} = \sum_{i \neq j} \frac{\mu_0 \gamma_i \gamma_j \hbar^2}{4\pi R^3_{ij}} (1 - 3\cos^2\theta)[\hat{I}^+_i \hat{I}^-_j + \hat{I}^-_i \hat{I}^+_j - 2\hat{I}^z_i \hat{I}^z_j], \tag{1.27}$$

where γ is the gyromagnetic ratio of the nucleus, R_{ij} the distance between the two nuclei, and θ the angle between the distance vector and the static magnetic field $\mathbf{B}$. With the Hamiltonian defined in eq. (1.25), we can describe the decoherence in an experiment where the spin starts in a superposition of states, it is flipped by a π pulse after a time τ, and it gets refocused at 2τ (see Hahn echo sequence in section 2.1.2). The initial state of the electron can be written as $|\psi_0\rangle = \frac{1}{\sqrt{2}}(|\uparrow\rangle + |\downarrow\rangle)$ and with the density matrix formalism as $\rho_0 = |\psi_0\rangle \langle\psi_0|$. The nuclear initial state can be approximated as $\rho_n \approx \frac{1}{2^N} I$ for any temperature $T \gg$ nK. We can consider the total initial state of the system and bath to be separated as: $\rho(0) = \rho_0 \otimes \rho_n$. At the time 2τ the signal intensity will be given by:

$$v_E(2\tau) = 2 \operatorname{Tr}\Big\{ (\hat{S}_x + i\hat{S}_y) \rho(2\tau) \Big\}. \tag{1.28}$$

Following eq. (1.20), we can write the density matrix at the time 2τ, knowing the initial density matrix and the propagators: free evolution with Hamiltonian $\hat{H}$ for τ, ideal π pulse applied on the x axis, and free evolution with Hamiltonian $\hat{H}$ for τ:

$$\rho(2\tau) = e^{-i\hat{H}\tau} \sigma_x e^{-i\hat{H}\tau} \rho(0) e^{i\hat{H}\tau} \sigma_x^\dagger e^{i\hat{H}\tau}, \tag{1.29}$$

then coherence at any time will be given by the ratio of off-diagonal elements at time 2τ and the off-diagonal elements at time 0:

$$W(2\tau) = \frac{|\langle \rho_{\downarrow\uparrow}(2\tau) \rangle|}{|\langle \rho_{\downarrow\uparrow}(0) \rangle|}. \tag{1.30}$$

It is not possible to compute this equation for more than 10 nuclei because the Hilbert space increase exponentially with N. Nevertheless, Witzel *et al.* [56, 57] and Yao *et al.* [58, 59] independently developed a mathematical approach to approximate the central spin dynamics and calculate decoherence. This idea would later produce a more general theory known as the Cluster Correlation Expansion (CCE) [60, 61]. This model approximates the interactions in subsets down to nuclear-nuclear pairwise interactions which are the main drive of NSD.

1.3.2 Protecting Against Decoherence

In the previous model, the main cause of decoherence in coupled spin systems was found to be nuclear-nuclear pairwise interactions. In principle, removing all the nuclei would eliminate the problem, and indeed, many of the longest cohering spins are hosted in nuclear-free environments [62, 63]. However, isotopic substitution is not always possible, practical, or cheap. Different paths need to be devised.

A very interesting option to protect against decoherence is to individuate specific regions in the Hamiltonian that are insensitive to external noise, which we define as Optimal Working Points (OWPs). For example, using a tuned Hamiltonian it was possible to reduce the charge noise in superconducting flux qubits [64]. A similar situation in spin systems is produced by atomic clock transitions. A way to observe atomic clock transitions is to have the hyperfine coupling of the same strength of the Zeeman energy.[1] At these specific field positions, which usually correspond to avoided level crossings, $\hat{\mathbf{S}}$ and $\hat{\mathbf{I}}$ are not good quantum numbers since the nuclear and electron states are strongly mixed, and a correct description of the quantum state is given by $\hat{\mathbf{F}} = \hat{\mathbf{S}} + \hat{\mathbf{I}}$. At the OWP, the resonant frequency becomes independent of magnetic field fluctuation at first order ($df/dB = 0$). This means, for instance, extremely accurate measurements of the clock frequency can be taken which can be used as a reference for a precise clock (hence the name clock transitions) [65]. In terms of decoherence, we discussed how local variations of resonant frequency are detrimental to quantum coherence. Therefore, the additional stability of f obtained at the OWP has been found to increase the coherence time by up to two orders of magnitude in multiple systems [66–69].

Another way to preserve the coherence of an open quantum system is to use an external control to cancel out the effect of the spin-bath Hamiltonian. Taking the Hamiltonian in eq. (1.24), we

[1] A completely different way to achieve clock transitions would be with the zero field splitting of the same strength of the Zeeman energy

can write a new time-dependent expression that takes into account an external decoupling with microwaves [70]:

$$\hat{H}'(t) = \hat{H} + \hat{H}_{\mathrm{MW}}(\omega, t). \tag{1.31}$$

The role of the external Hamiltonian is to provide a contribution that goes against the spin-bath evolution, so that the average effect becomes zero. In practice, this translates into very quick flipping of the central spin.

1.4 Molecular Spin Qubits

As stated above, a definitive candidate for quantum applications (sensing and computing) has not emerged yet. In this thesis we focus on molecular systems, intended as any possible paramagnetic complex that is produced through chemical synthesis, both organic or inorganic. The possibility of using SMMs as spin qubits was first foreseen by Leuenberger and Loss in their 2001 proposal [48]. On the one hand, there are several advantages in using molecules. First of all, the almost endless possibilities given by chemistry: molecules can be tailored for specific purposes, they can be functionalised to introduce optical properties and even interact with biological systems. Second, molecules can be produced with higher yield and reproducibility than, for instance, quantum dots. Third, they can self-assemble, they can be grafted on a surface, or inserted in a single molecule transistor in specific and rational positions [19]. On the other hand, there are compelling drawbacks: research on semiconducting qubits [71], NV centres [12], and SiC [72] has demonstrated significantly higher coherence time than molecules. Nevertheless, magnetochemistry research has succeeded in the last ten years in synthesising molecular systems with longer coherence. The incredibly large activity in the field is also corroborated by the plethora of recent reviews [73–76]. Here, we divide the ongoing research on molecular qubits in two phases: improving coherence, and coupling qubits.

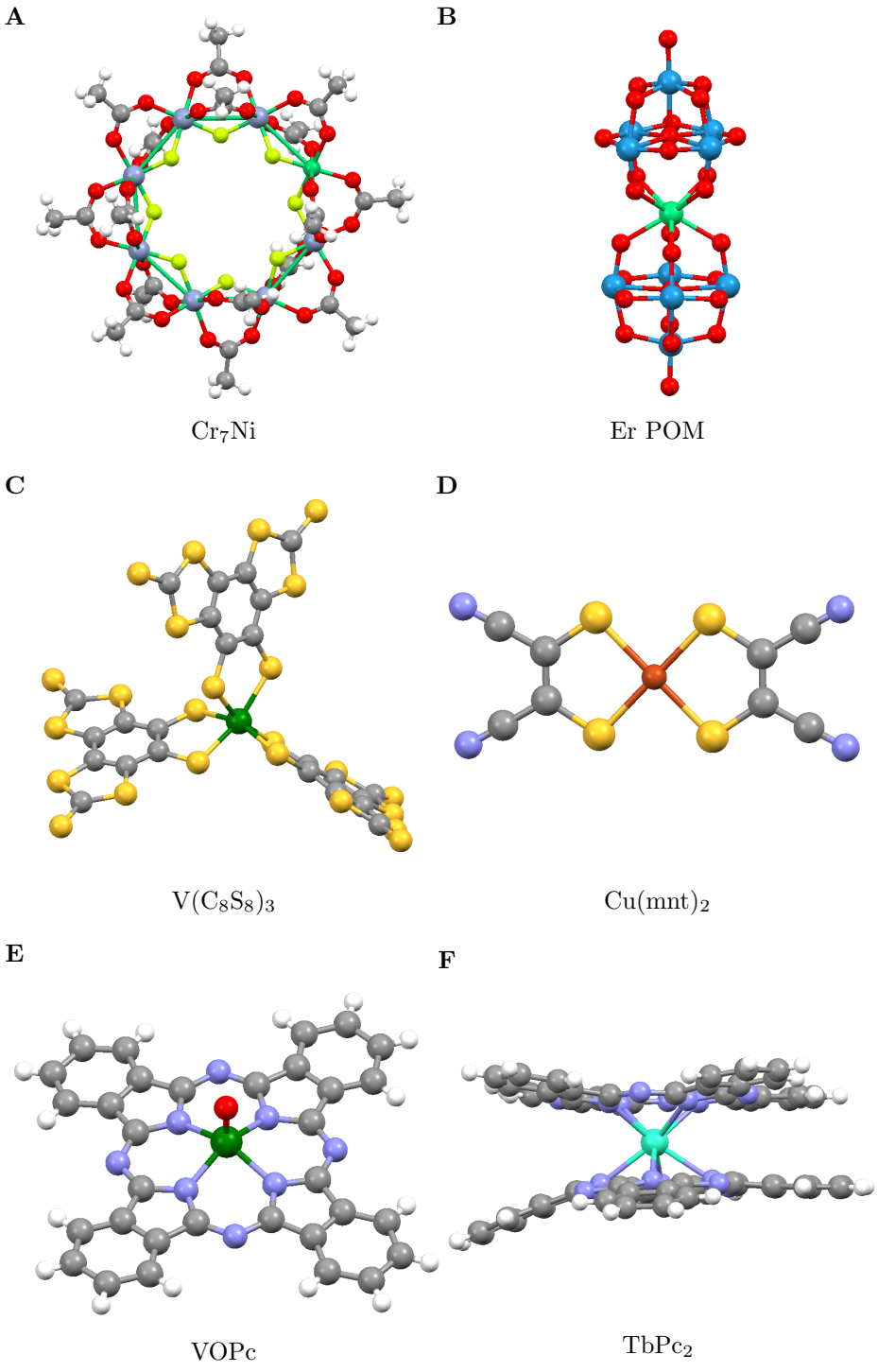


Figure 1.3: (A) Cr_7Ni, counterion omitted (C = gray, H = white, F = light green, O = red, Cr = blue, Ni = green) [77]. (B) Er polyoxometalate, part of the molecule omitted for clarity (O = red, W = blue, Er = green) [78]. (C) $V(C_8S_8)_3$ counterion omitted (C = gray, S = yellow, V = green) [79]. (D) $Cu(mnt)_2$ counterion omitted (C = gray, S = yellow, N = blue, Cu = amber) [80]. (E) VO phthalocyanine (C = gray, H = white, O = red, N = blue, V = green) [81]. (F) Tb bis-phthalocyanine (C = gray, H = white, O = red, N = blue, Tb = cyan) [82].

1.4.1 Improving Coherence

In the first phase of research in molecular qubits, the objective was to find a set of compounds with robust coherence. Up until that point, magnetochemistry research was dominated by the study of SMMs [16], hence it seemed natural that strongly coupled poly-metallic compounds would be the first to be investigated, and some lessons learned from SMMs could apply. The first generation of molecular qubits included Cr_7Ni rings [77, 83], and the two SMMs Fe_4 [84] and Fe_8 [85, 86]. These first compounds had a very small window of functioning, below 10 K, and only achieved coherences in the order of 1 µs. They highlighted immediately some issues: remnant intermolecular dipolar interactions destroy coherence and are eliminated by dilution in a frozen solvent or an isostructural diamagnetic matrix; nuclear spin diffusion in the environment hampers coherence and can be mitigated by deuteration of the matrix or removal of nuclear spins.

The second generation of molecular qubits shifted towards mono-metallic compounds. One of the first compounds of this family was copper phthalocyanine (CuPc), that was deposited as a film in a diamagnetic matrix of H_2Pc and displayed 1 µs coherence up to 200 K [21]. Not only the performance was extended, but the thin film deposition would also allow straightforward implementation in multilayered devices. A further improvement in coherence was granted by the new idea of using nuclear free ligands. $Cu(mnt)_2$ had 4 sulphurs coordinating the central Cu, with S isotopes nuclear free at 99.2%. Its deuterated counterpart in a diamagnetic $Ni(mnt)_2$ matrix achieved 68 µs coherence at 7 K that stands as the longest coherence time for molecular systems in a diluted crystal [80]. Similarly, in $[V(C_8S_8)_3]$ all ligands are largely nuclear free (C is nuclear free at 98.7%), when put in a CS_2 frozen solution, also nuclear free, this compound yielded 675 µs coherence at 10 K, which is the highest reported value for any molecular system [79, 87]. While these are the most relevant examples, a long list of compounds that followed analogous synthetic guidelines was produced: Gd polyoxometalate [88]; $VO(C_8S_8)_2$ [81, 89]; vanadyl phthalocyanine [90]; nickel [91], copper [92], and chromium [93] based compounds.

Such interesting results followed extremely fine tuning of synthetic parameters. The choice of the central metal determines the spin-orbit coupling (SOC). It was possible to experiment in series of transition metal complexes [94, 95], showing that the vanadyl moiety is generally the highest performing. Additionally, lanthanides can be used to design complexes that exhibit avoided crossing and clock transitions. As discussed in section 1.3, clock transitions are particularly insensitive to

perturbations. Experiments in molecular systems showed that significant increases in coherence can be obtained when exploiting clock transitions even at very high spin concentration [68, 69]. Nuclear spin diffusion was obviated when possible introducing nuclear free ligands. The theory delineated in section 1.3 argues that the strength of internuclear interaction is proportional to the gyromagnetic ratio of the nuclei involved. Therefore, substitution of the high-gyromagnetic-ratio hydrogen with deuterium or halogenation is preferable and demonstrated to provide an increase in coherence [96]. Similarly, nuclear flip-flops are locked if the hyperfine coupling to the spin centre is larger than the nuclear Zeeman, but still smaller than the electron Zeeman. Therefore, it is possible to determine a nuclear diffusion barrier: a geometrical sphere that includes the nuclei that are strongly coupled to the central spin. In a series of compound in which nuclei are farther apart from the spin centre, it can be shown that the strongly coupled nuclei contribute less to the decoherence [89, 97, 98]. Finally, a more recent idea to diminish the effect of nuclear spin diffusion is nuclear patterning. Nuclei with different gyromagnetic ratio cannot flip-flop because of the mismatch in nuclear Zeeman energy. Therefore, if we pattern the ligands so that adjacent nuclei are of different types, they will not flip-flop and pairwise interaction between same nuclei will be decreased [99, 100]. Systems implementing the previous design strategies would have actively reduced nuclear spin diffusion.

However, a common trend is observed in the compounds cited above: while coherence can reach even large value at low temperatures, it decreases when increasing the temperature and usually disappears above 100 K because it becomes limited by T_1. Thus, the most recent research is directed towards understanding synthetic ways of prolonging spin-lattice relaxation by producing series of compounds with different central metal or ligands [101, 102]. Magnetic experiments are also being complemented by more sophisticated techniques such as THz infrared spectroscopy and inelastic neutron scattering [103]. Experiments are then interpreted using advanced multi-reference theoretical methods that link the data to microscopic spin-phonon couplings [104]. Such efforts in rationalising vibronic behaviour of single metal molecular qubits are proving successful and might help prolonging coherent behaviour to higher temperatures.

1.4.2 Coupling Qubits

The second phase of the research on molecular spin qubits involves coupling the building blocks in order to implement two-qubit operations. Early theoretical proposals focused on coupling two Cr_7Ni rings and explore their properties [105]. Supramolecular chemistry offered a pathway to implement

these ideas: it was possible to introduce different linkers to engineer the through-bond exchange coupling J and modulate the distance between the building blocks and their through-space dipolar coupling D [106–110]. Ardavan *et al.* [111] showed that the coherence of the obtained dimers suffers from the coupling, but the decrease is much smaller than expected and not a limiting factor on the computation. Through dipolar EPR techniques they also measured the coupling between the two dimers to be weak enough so that the inversion time of a CNOT operation would be smaller than the decoherence.

Seminal success in linking Cr_7Ni was reproduced in coupling different building blocks such as monomeric lanthanide complexes [112, 113], and organic radicals [114]. Nonetheless, the presence of a supramolecular link between two monomers implies that the coupling between the two is always on. This might be a problem because it will not allow distinguishing between single qubit and two-qubit operations. Some authors [110, 114, 115] suggest that the problem can be overcome if the two units have different g-factors, so that they display distinguishable resonant fields. Selective microwave pulses with narrow bandwidth or advanced composite pulses can then address single monomer without exciting the other in order to produce single qubit operations. A different scheme was theoretical proposed by Lehman and coworkers [78], who considered a polyoxometalate bridging two VO units grafted on a surface. By means of a conductive Scanning Tunnelling Microscopy (STM) tip, the interaction between the two units can be turned on and off changing the charge of the linker. The idea of a switchable coupling has been picked up by two recent work, that included as a link a redox-reactive compound whose charge can be altered [115, 116]. Both cases produced experimental realisation of complexes single qubit and two-qubit operations by means of local and non-local control.

Recently, a different approach from supramolecular chemistry has been investigated. Building blocks of molecular qubits have been embedded in 2D [117] and 3D [118, 119] extended networks. In particular, metal-organic frameworks (MOFs) have been very successful because the network can be tailored in order to achieve a certain average distance between the qubits, the components can be chosen to be nuclear free, and even at reasonably high concentration the coherence is not affected so negatively [119]. Therefore, this appears as a promising topic that will be explored in the future.

The entirety of the experimental characterisation mentioned above was carried out in ensembles. Working with ensembles provides a strong proof-of-principle of the properties of the complexes, but an operating device will suffer of scalability issues if based on an ensemble. For example, it was

demonstrated that two-qubit operations can be carried out linking two monomers, but to scale this to higher number of qubits, larger and more complicated molecules would be necessary. Following the example laid out by superconducting quantum computers, it would be best to have a circuit linking identical building blocks that can be coupled via electrical or optical means. Such hypothetical devices would require a sensitivity down to the single molecule. Several proposals address this challenge by means of single molecules on surfaces [19], single-molecule transistors [20], and single molecules coupled to superconducting resonators [120]. Among the previous three ideas, the first two have been already implemented, while the third one still appears to be very challenging. In a series of influential papers Heinrich's group showed that it is possible to conduct EPR characterisation of single atoms on conductive surfaces using an STM tip at low temperatures, that not only yield Hamiltonian parameters but also information on the quantum coherence [121–124]. Such experiments are also being extended to magnetic phthalocyanine molecules.[2] A similar single-molecule control was obtained in a single-molecule junction of a $TbPc_2$ between gold leads [125]. They demonstrated measurement of the quantum properties and coherent control of the central Tb spin with Rabi oscillations [82]. Additionally, they achieved control of the nuclear spin of Tb using radiofrequency excitation in similar fashion to an EPR ENDOR (see chapter 2) experiment. Exploiting the multi-level nature of the nuclear spin, they demonstrated a simple implementation of the Grover's algorithm [126].

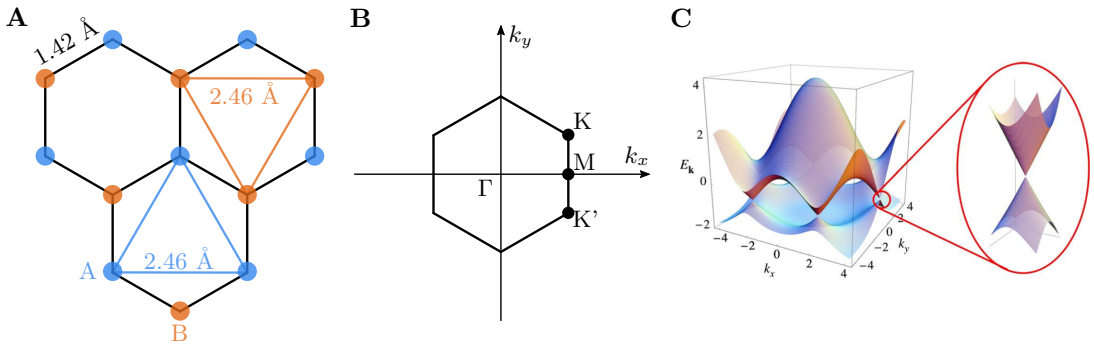


Figure 1.4: (A) Geometry of the hexagonal lattice of graphene. (B) First Brillouin zone of the honeycomb lattice. (C) Graphene band dispersion calculated with the Hubbard model with nearest neighbour hopping energy 2.7 eV, and next-nearest neighbour hopping energy -0.54 eV. The inset shows the Dirac cones at a K point. Adapted from [127].

[2] Unpublished data showed by Prof Heinrich during a talk at University of Oxford, February 2021.

1.5 Graphene

1.5.1 Structure and Properties

Graphene is a one-layer, two-dimensional hexagonal lattice made of sp^2-hybridized carbon atoms. The lattice constant is 2.46 Å, and the carbon-carbon average distance 1.42 Å [128]. The hexagonal network has two atoms per unit cell, and it can be broken down into two triangular sub-lattices, which are referred to as A and B (fig. 1.4A). Each atom belonging to A is coordinated by three atoms belonging to B, and viceversa. This structure is common to other carbon-based materials, and graphene can be thought as the building block for them all: insertion of pentagons and wrapping up produce fullerenes, rolling up from one side makes carbon nanotubes (see fig. 1), and stacking sheets results in graphite.

The hexagonal carbon-carbon network grants graphene extraordinary mechanical [129], optical [130], and electrical properties [127]. The electronic structure of graphene can be studied with a tight-binding model:

$$\hat{H} = -t \sum_{\langle i,j\rangle,\sigma} (\hat{a}^{\dagger}_{\sigma i}\hat{b}_{\sigma j} + H.c.) - t' \sum_{\langle\langle i,j\rangle\rangle,\sigma} (\hat{a}^{\dagger}_{\sigma i}\hat{a}_{\sigma j} + \hat{b}^{\dagger}_{\sigma i}\hat{b}_{\sigma j} + H.c), \tag{1.32}$$

where t and t' are nearest-neighbour and next-nearest-neighbour hopping integrals, $\hat{a}_{\sigma i}$ ($\hat{a}^{\dagger}_{\sigma i}$) and $\hat{b}_{\sigma i}$ ($\hat{b}_{\sigma i}$ are creation (annihilation) operators for atoms on site A and B, respectively [127]. Derivation of the dispersion energy for this model results in:

$$E_{\pm}(\mathbf{k}) = \pm t\sqrt{3 + f(\mathbf{k})} - t' f(\mathbf{k}) \tag{1.33}$$

with $f(\mathbf{k})$ defined as:

$$f(\mathbf{k}) = 2\cos\sqrt{3}k_y a + 4\cos\frac{\sqrt{3}}{2}k_y a \cos\frac{3}{2}k_x a, \tag{1.34}$$

where $a = 1.42$ Å, the minus sign is for the valence band (π orbital), and the plus sign for the conduction band ($\pi*$ orbital). Equation (1.33) shows that for $t' = 0$ the energy dispersion is symmetric with respect to zero energy. As can be seen from fig. 1.4C, the zero energy condition is satisfied at the K and K' points of the Brillouin zone, which are called Dirac points. A first consequence of eq. (1.33) is that the density of state at the zero energy is exactly zero, which means that the bands are half filled [127]. Hence, pristine graphene is referred to as a zero-bandgap

semiconductor, or as a zero-overlap semimetal [128].

A second consequence is that, in proximity of the Fermi level, the energy dispersion becomes linear with $\mathbf{k}$, and the electrons are described by the Dirac equation with Hamiltonian:

$$\hat{H} = v_{\mathrm{F}}\boldsymbol{\sigma}\mathbf{k} = v_{\mathrm{F}}\begin{pmatrix} 0 & k_x - ik_y \\ k_x + ik_y & 0 \end{pmatrix} \tag{1.35}$$

where v_{F} is the Fermi velocity equal to 10^6 m/s, σ is a Pauli matrix describing the pseudospin (which is not related to the electron spin), and charge carriers behave as massless fermions. The Dirac equation describes relativistic particles in the framework of quantum electrodynamics. The possibility of testing the theory on high quality samples partially motivated the very large interest towards graphene. From this model it is also possible to derive other properties that are well matched by experimental results [127].

Magnetism in Graphene

While electrical, mechanical, and optical properties have been widely studied, magnetism in graphene is an often neglected feature. A review from 2012 describing possible fields of application of graphene did not mention magnetism or spin-related phenomena even once [131]. This is not unexpected since theory and experiments indicate that pure graphene sheets are diamagnetic [132]. Nevertheless, several magnetic measurements of graphene resulted in low temperature paramagnetism [133] or even weak ferromagnetism [134, 135]. The origin of such phenomena was not fully understood, and generally related to the presence of random edge states, vacancies, adatoms or defects, which introduced modification in the otherwise perfect graphene lattice. Lieb's theorem [136] can be used to understand why defects introduce a magnetic moment in graphene. The theorem demonstrates that the total magnetic moment depends on the difference between the number of atoms in the two sublattices: $S = |N_A - N_B|$. Additional simulations based on the tight-binding model also supported the concept that magnetism is related to lattice imbalance [137, 138]. While this fully explains paramagnetism, the presence of long range ferromagnetism is controversial and often attributed to presence of impurities or experimental errors [139].

There has been a stimulating progress in graphene for spintronic applications in the past ten years, but its full potential is still unexploited (see [22], the spintronics section in [140], and reference

therein). The unpredictability of edges and defects means that their properties can not be fully understood and exploited. Here, we review the novel approaches used to overcome the fabrication limits and the opportunities that arise from precise control of graphene edges and defects.

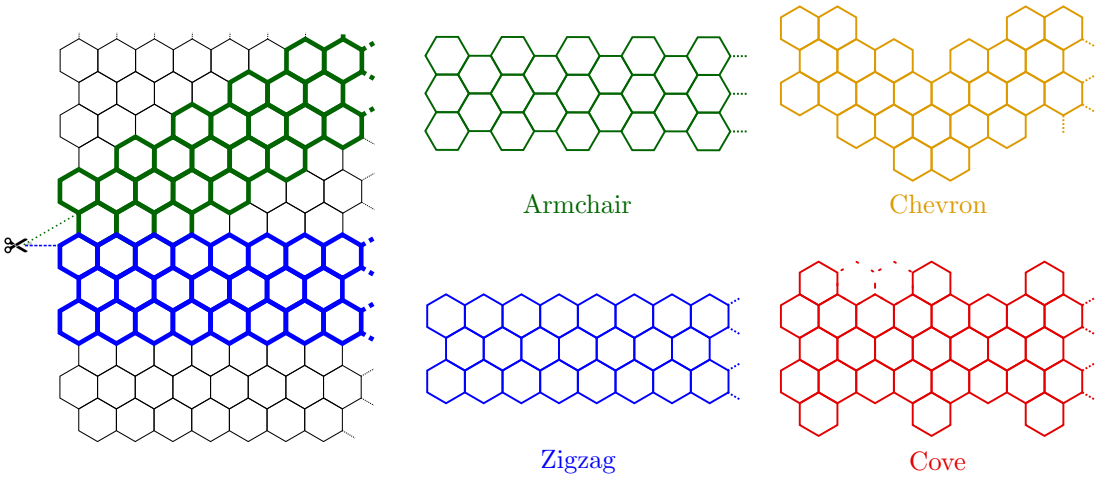


Figure 1.5: Different geometries of graphene nanoribbons. Armchair and zigzag nanoribbons can be thought of as stripes cut from a graphene sheet with the cutting directions differing of a 30° angle. Armchair are usually referred to by their width counting the carbon atoms on the shorter edge, while zigzag by counting the number of horizontal carbon lines. For example, in the figure they would be 7-AGNR and 4-ZGNR. Cove GNRs are zigzag ribbons in which there is a carbon vacancy that produces the fjord. Chevron GNRs can be seen as two armchair ribbons fused at an angle.

1.5.2 Edge states

GNRs are 1D stripes of a graphene sheet with a width of few carbon atoms and an ideally infinite length. Two main geometries have been investigated: armchair GNR (AGNR) and zigzag GNR (ZGNR), yet others are also possible: fig. 1.5 illustrates some examples. Pioneer theoretical work on the subject suggested that the quantum confinement of the narrow width contributes to exotic properties that are not present in 2D graphene. Tight-binding model calculations on the band structures of GNRs showed that a band gap appears in armchair structures as a function of the width of the ribbons, with the band structure eventually replicating the one of graphene when the width is larger than 30 carbon atoms [141, 142]. Further density functional theory [143], first-principle [144], and Dirac-equation [145] simulations agreed that nanoribbons have a band gap that decreases increasing the width. More interestingly, though, all the calculations showed that for zigzag nanoribbons the bands become flat in proximity of the Fermi level and so called edge states appear [142, 144]. Here, the striking difference between zigzag and armchair is only produced by the different

topology of the π electron network, in other words by the shape of the ribbon edge. The presence of the edge states is of paramount importance because it makes available unpaired spins. The topology of the ribbon mandates that all the carbons on one edge belong to, for example, sublattice A, while the carbons on the opposite edge belong to sublattice B. Therefore, it can be demonstrated that a ferromagnetic ordering is achieved between adjacent edges and an antiferromagnetic one between opposite edges [142, 144, 146]. This still means that the ground state has spin $S = 0$. Nevertheless, Son, Cohen and, Louie [147] theoretically showed that upon application of an external field, a spin-dependant band shift could make one edge state energetically favourable with respect to the other. Hence, it would be possible to use zigzag GNRs to produce spin polarised currents.

The scientific community developed a great interest towards GNRs because they obviated to two problems of graphene: the absence of a band gap and lack of free spins. However, the excellent theoretical results had to face the challenge of fabricating GNRs which could show the predicted properties. State-of-the-art lithographic patterning and cutting of graphene sheet could only produce structures with width down to 20 nm. The GNRs produced in this way would typically have very little control over the roughness of the edge and their properties would be dominated by defect scattering [148, 149]. Unzipping of carbon nanotubes [150–152] and sonochemical exfoliation of graphene flakes [153] brought the lower limit to the sub-10 nm region with larger control on the edge smoothness. Nonetheless, state-of-the-art top-down methods cannot achieve the required width and edge quality for GNRs [154].

The high level of precision required for experiments can only be obtained with bottom-up synthesis [155]. Cai and coworkers [156] demonstrated the bottom-up synthesis of chevron graphene nanoribbons on a gold surface starting from precise precursors. STM characterisation of these nanoribbons showed nm width, flat structure, and an atomic control of the edge smoothness. Hence, with bottom-up synthesis the main challenge shifted to designing a good precursor and setting the right reaction conditions, so that the precursors can polymerise and then form carbon bonds on a surface (for a review of surface chemistry see [157]).

In very few years, surface–assisted synthesis succeeded in producing numerous atomically–precise structures of arbitrary width for meaningful experiments. Since most of the structures were synthesised on surface, the main techniques for studying their properties were Atomic Force Microscopy (AFM), Scanning Tunnelling Microscopy (STM), Scanning Tunnelling Spectroscopy (STS), and Angle Resolved PhotoEmission Spectroscopy (ARPES). Early results focused in particular on armchair

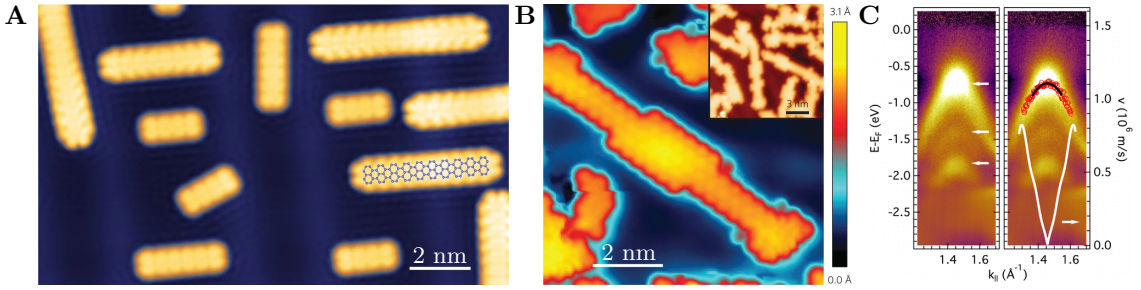


Figure 1.6: (A) High-resolution STM image of 5-AGNR on a gold surface. Adapted from [158]. (B) High-resolution STM image of a heterojunction between 7- and 13-AGNR. Adapted from [159]. (C) ARPES image of the occupied bands of a 7-AGNR on a gold surface. White arrows indicate the top of each band, and the highest band is the valence band. The red circle on the right are peak positions of the valence band that are fit with a parabolic dispersion to yield the effective mass of the charge carrier $m \approx 0.21 m_0$ (m_0 is the rest mass of an electron). The white curve refers to the average carrier velocity on the right axis. Adapted from [160].

GNRs, because they are more stable and easier to synthesise than zigzag ribbons. Additionally, they are particularly interesting because they behave as semiconductors, so that their band structure can be imaged, and the band gap can be measured with the techniques cited above. In a series of papers, 5- [158], 7- [160], 9- [161], and 13-AGNR [162] were synthesised and imaged on top of Au(111) surfaces. For example, fig. 1.6A shows a high-resolution STM image of 5-AGNR. The figure displays the structure of these molecules down to the single atom and proves the complete control of the edge morphology, although it appears harder to select the length. Figure 1.6C shows the ARPES of the occupied bands of a 7-AGNR at the projection of the K point onto $k_{||}$. By fitting the top of the valence band with a parabolic dispersion, it is possible to obtain the effective mass of charge carriers: $0.2m_0$, where m_0 is the rest mass of the electron. This demonstrates the different physics in GNRs with respect to graphene, where, in proximity of the Fermi level, charge carriers resulted as massless fermions. Differently from ARPES, STM also allows to probe the empty bands, such as the conduction band, and to measure the bandgap: 2.3 eV for 7- [160], 1.4 eV for 9-, and 1.4 eV for 13-AGNR. These measurements are in accordance with an inversion law between the width of the ribbon and the bandgap, although in some samples, the length of the ribbon might also influence the gap (some length effects in the conductance were also studied in a two terminal device in [163]).

It is also possible to achieve composite systems combining different precursors. Figure 1.6B shows that AGNRs of different widths can be laterally fused to produce heterostructures [159]. Other geometries included fusing of functionalised precursors at an angle to form chevron-type GNRs [164–166]. They allow additional engineering of the bandgap and the possibility of mimicking type I and type II junctions that are common between p- and n-type semiconductors.

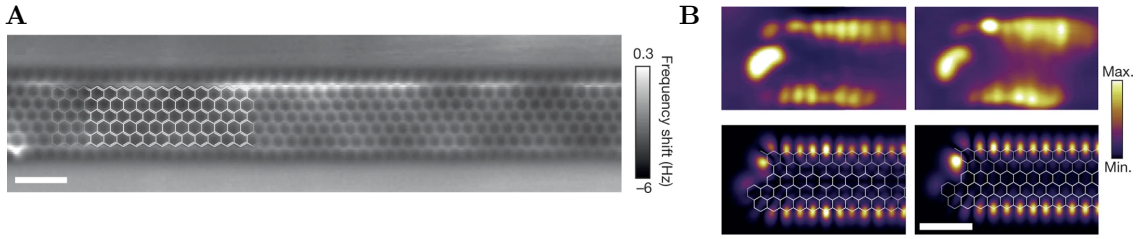


Figure 1.7: (A) Non-contact AFM image of 6-ZGNR on gold surface. (B) Differential conductance map of filled (left) and empty states (right) on the edge of the graphene nanoribbons. The top panels are experimental data, and the bottom panels are simulations with a DFT local density of states approach. Scale bars are 1 nm. Adapted from [167].

Zigzag nanoribbons have been more elusive than armchair. Wide top-down produced ZGNRs were first studied: STS was used to probe the local density of state at the zigzag edge of GNRs, showing the existence of states that exponentially decrease moving towards the centre of the molecule, providing an indirect proof of the existence of edge states in zigzag nanoribbons [152]. Later on, Ruffieux and coworkers [167] succeeded in the surface–assisted bottom-up synthesis, in a similar fashion to armchair ribbons. Their imaging technique showed precise control of the edge and strongly localised density of state at the edge. At the same time, chemists developed liquid-phase syntheses that could provide equally precise nanoribbons with the possibility of larger scale production than on-surface synthesis [154, 168, 169]. The challenge of producing solution-processable GNRs can be further understood considering that graphene and numerous graphene-related nanostructure are extremely poorly soluble in any solvent. This problem could only be overcome by careful design of long chain group that have the double function of protecting the edge and improve solubility (for a detailed review of synthetic routes see [170]). With solution-processed ribbons, a plethora of other characterisation techniques became available. A final direct proof of the existence of magnetic edge states was eventually obtained using EPR on functionalised cove GNRs with nitroxyl radicals [15]. The radicals injected a spin density in the nanoribbon and a clear magnetic fingerprint of the edge state was observed as separate from the radical. Additionally, it was demonstrated that the edge state has superior coherence even at room temperature in a non-diluted system, which makes GNRs very promising for spintronics applications. Ongoing effort is directed towards studying single zigzag graphene nanoribbons in molecular gaps, this would demonstrate the possibility of tuning the magnetic properties with electrical control.

Topological States

In the last 20 years a new class of materials have been highly investigated in solid state physics: topological insulators. Topological insulators have a bulk insulating behaviour but they display conducting states on their surface or edges [171]. Exotic effects have been theoretically predicted to arise at the interface between topological insulators and other materials. For example, it was suggested that, at the interface between a topological insulator and a superconductor, Majorana fermions could arise and their properties could be used for efficient topological quantum computing [172]. Hence, the theoretical and experimental study of topological insulators has been a high priority in condensed matter physics.

The search of topological states focused in particular on 3D insulators or semiconductor based on heavy metals, whihc would allow a large spin–orbit coupling, for example bismuth complexes have attracted strong interest [173]. Cao, Zhao and Louie [174] argued that similar topological considerations should be extended to graphene nanoribbons, that their edge states could be topologically protected by time-reversal symmetry or inversion symmetry, and their properties should be exploited for device applications.

Before discussing the results in GNRs we introduce the formalism to describe topology in a 1D periodic system. The topology of the nth band of a crystal is characterised by its Zak phase [175]:

$$\gamma_n = i\left(\frac{2\pi}{d}\right)\int_{-\pi/d}^{\pi/d} \mathrm{d}k \left\langle u_{nk}\middle|\frac{\partial u_{nk}}{\partial k}\right\rangle, \tag{1.36}$$

where k is the wave vector, d the unit cell size, u_{nk} is the periodic part of the wavefunction in the nth band, and $\left\langle u_{nk}\middle|\frac{\partial u_{nk}}{\partial k}\right\rangle$ is the Berry connection [176]. In general, the Zak phase can take any value, but for system with inversion or mirror symmetry it is quantised to 0 or π.

Another classification can be used to describe topological states: the Z_2 invariant. The Z_2 invariant is related to the Zak phase according to the following equation:

$$(-1)^{Z_2} = e^{i\sum_n \gamma_n}, \tag{1.37}$$

where n are the occupied bands. If γ_n is quantised, Z_2 is also quantised and can assume the values 0 or 1: $Z_2 = 0$ corresponds to a trivial insulator, while $Z_2 = 1$ corresponds to nontrivial.

Cao, Zhao and Louie [174] showed that for GNRs, the Z_2 invariant depends only from the choice

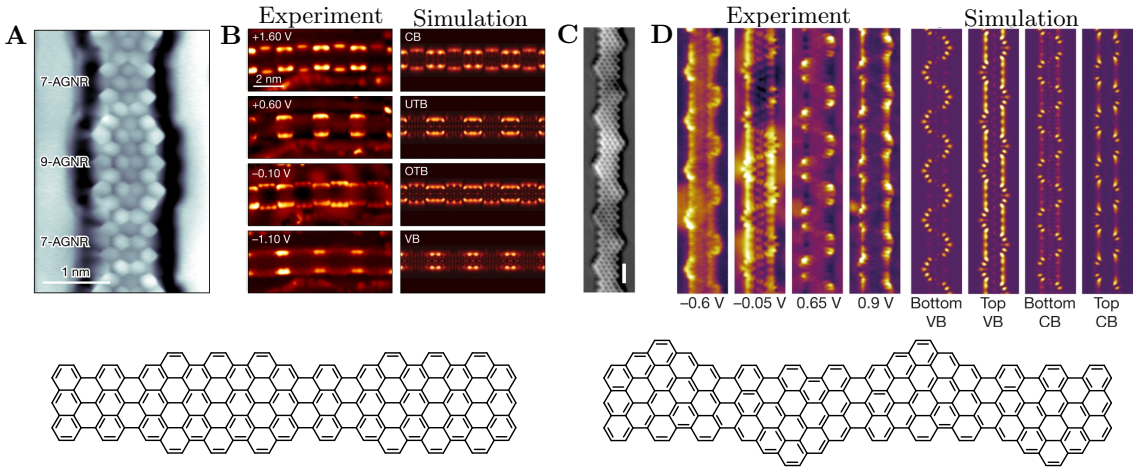


Figure 1.8: (A) Bond-resolved STM image of an heterojunction between 7-AGNR and 9-AGNR. (B) Experiment and simulation of constant current $\mathrm{d}I/\mathrm{d}V$ maps at different voltages for the 7/9-AGNR heterojunction. The local density of states is obtained via a density functional theory calculations. The different states are attributed to different bands of the global heterostructure: conduction band (CB), unoccupied topologically-induced band (UTB), occupied topologically-induced band (OTB), and valence band (VB). Experimental STM images in A-B were taken at 4 K. Adapted from [177]. (C) Non contact AFM image of a 7-AGNR-S (S for staggered). Scale bar is 1 nm. (D) Experiment and simulation of constant current $\mathrm{d}I/\mathrm{d}V$ maps at different voltages for the 7-AGNR-S. C-D adapter from [178]

of the unit cell and termination of the ribbon, and they calculated it for some common cases of armchair GNRs. In subsequent papers, the Zak phase and its correspondent Z_2 invariant were calculated for cove, chevron, and zigzag ribbons, using numerous theoretical methods such as local density approximation density functional theory (LDA-DFT), tight-binding model, Wannier function methods, and chiral phases [179–182].

The most interesting part of the discussion on topological states in GNRs is to understand what drives the change from a trivial insulator to a nontrivial one, and how the two can be combined. While the approach to topological states has been mostly theoretical, a few, well designed experiments managed to exactly focus on the latter point. Li *et al.* [181] studied the topological transition in chiral graphene nanoribbons. They theoretically predicted that increasing the width of the ribbon above a certain threshold it would transition from a trivial insulator ($Z_2 = 0$) to a topological insulator ($Z_2 = 1$). They successfully synthesised a family of chiral GNRs on gold surface, and they observed that STM results, in terms of band gap and band interaction patterns, matched their theoretical predictions and confirmed the phase transition.

In two independent papers [177, 178] researchers studied *ad hoc* designed structures (fig. 1.8) with periodic junctions between nanoribbons with different topological phases and band behaviour. Rizzo and coworkers [177] synthesised on surface periodic junctions of 7-AGNR ($Z_2 = 0$) and 9-AGNR

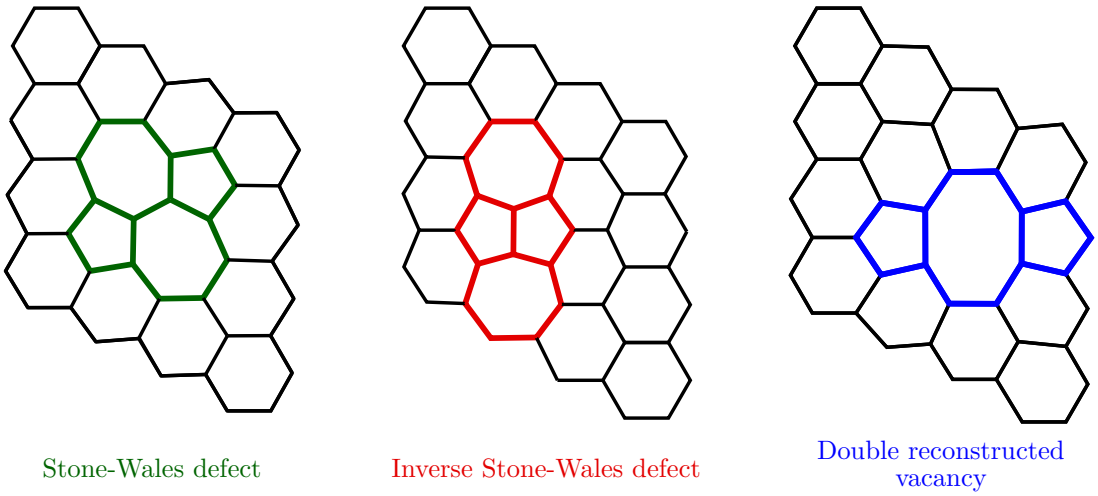


Figure 1.9: Examples of topological defects: Stone-Wales defect (55-77), inverse Stone-Wales defect (7557), and a reconstructed double vacancy that yields a pentagon pair and an octagon (5-8-5).

($Z_2 = 1$). They observe with STM that at the junction the topological phase transitions from trivial to nontrivial, producing topological states localised in the proximity of the Fermi level (OTB and UTB bands fig. 1.8B). They concluded that rational combinations of different topology of GNRs would allow additional degrees of freedom in band engineering of the final material. Gröning *et al.*[178] focused on staggered armchair ribbons of different periodicity and symmetries. They too observed interesting states at the junctions between segments of different width (fig. 1.8D). In both previous paper special attention was given to terminal states of the GNRs. Indeed, vacuum can be seen as a trivial insulator ($Z_2 = 0$), which means that at the interface between a non trivial GNR and the vacuum we expect to observe topologically protected end states, which were reported at the STM in both previous papers for the different structures.

1.5.3 Topological Defects

Defects in graphene are classified as: vacancies, adatoms, doping, topological defects and combinations of the above [183]. For topological defects, we intend modifications of the graphene honeycomb lattice that do not change the chemical structure or chemical coordination of sp^2 carbon but only the geometry of the π network. Topological defects can be obtained, for instance, by a 90° rotation of a carbon bond (Stone-Wales defect) or by reconstructing a double vacancy as seen for example in fig. 1.9.

Microscopy studies of graphene showed that these defects can be produced upon irradiation with

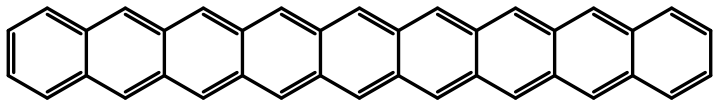
an electron beam, they can propagate in the graphene lattice, and they are stable at room temperature [184]. The generation of defects is stochastic which makes it cumbersome to obtain defined structures for experiments. While *in situ* observations with Transmission Electron Microscope (TEM) or STM have been reported, the study of defects in graphene has been mostly theoretical. Calculations showed that topological defects are associated with curvature in the graphene sheet [185–187]. As pentagonal and heptagonal defects have opposite curvature signs, it is often suggested that the total Gaussian curvature is zero. Theoretical models show that such ripples in the graphene lattice are associated with high local density of states and peculiar electronic properties [188]. Additionally, the imbalance introduced in the bipartite system by topological defects can be interpreted with the Lieb's theorem. Several propositions showed a net magnetic moment arising from the presence of defects [189, 190], which is also corroborated by experiments in graphitic systems.

Due to the difficulty in fabricating definite structures, the magnetism and quantum properties of topological defects remain widely unexplored. In the next section we will outline how to prepare the precise structures needed to investigate magnetic properties in defective nanographene molecules.

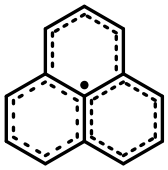
As a concluding remark, we highlight that a similar formalism of edge and defect properties can be applied to other 2D materials such as transition metal dichalcogenides [191]. There are hints that such structures could present similar properties to the one observed in graphene, yet the field is still developing. For example, defect engineering, magnetic resonance, and spin control have been recently reported on 2D sheets of hexagonal boron nitride (hBN) [192].

1.6 Open-shell Aromatic Hydrocarbons

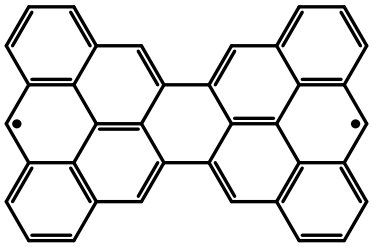
Polycyclic aromatic hydrocarbons (PAHs), also referred to as nanographene molecules or graphenoids, are molecules based on the fundamental unit benzene, they resemble the lattice of graphene and are often indicated as model systems for studying its properties. PAHs are essentially zero-dimensional graphene flakes that benefit of the same quantum confinement discussed above, and have properties that depend on their topology. The chemistry of these molecules has seen an explosion in the past 10 years as corroborated by the large number of papers and review in the field [2, 3, 193–195]. This was motivated by the possibility of synthetically tailoring properties for electrical [196], photovoltaic [197], nonlinear optic [198], energy storage [199], and spintronic applications [200]. In particular we focus on their magnetism. Lieb's theorem can again be used to predict the spin state of the



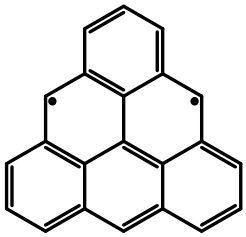
11 - Nonacene



12 - Phenalenyl



13 - Clar's goblet



14 - [3]Triangulene

Figure 1.10: Examples of zig zag edge nanographene molecules: nonacene **11** in its closed shell form, phenalenyl **12**, Clar's goblet **13**, and [3]triangulene **14** in their open-shell structure.

molecules, but in the chemistry community the origin of the magnetism in PAHs is often explained with Clar's rule [201]. Clar's rule states that whenever multiple resonant structures of a molecule are present, the resonant structure with the largest number of aromatic π-sextets gains additional energy stabilisation and contributes the most to the ground state. For the majority of systems, Clar's rule and Lieb's theorem are equivalent and correctly predict the same ground state.

Following Clar's rule, PAHs can have a strong contribution from open-shell structures. This intrinsic radical character makes PAHs very reactive, and their synthesis requires careful design and several steps, making the yield often low. However, recent advances made it possible to synthesise many complexes that were originally only predicted, both with ultra-high vacuum surface-assisted methods [202], and liquid processable phases (for reviews of synthetic methods see [193, 195, 203]). A current challenge at the moment is to synthesise larger and larger nanographenes, whose structure can approximate better the one of graphene [3]. These molecules can be controlled at the atomic level and can incorporate the element discussed above: zigzag edges and topological defects. Therefore, they act as splendid model systems to study structure-property relationships in graphene.

Polyacenes are the narrowest zigzag graphene nanoribbons (e.g. nonacene in fig. 1.10). A very wide theoretical literature is dedicated to the study of their ground state. Several computational methods agree in describing polyacenes until pentacene or hexacene as closed-shell molecules and longer acenes as open-shell molecules with a singlet diradical character, and polyradical behaviour for acenes longer than ten units [204–206]. There is also consensus that the singlet-triplet gap would decrease when increasing the length of the chain. Due to their extreme reactivity, for very long, it was

possible to synthetise acenes only up to pentacene (for an overview of the chemical problem see [207, 208] and reference therein). This problem could be circumvented using surface-assisted techniques in ultra high vacuum. Hence, hexacene [209], heptacene [210], octacene, and up to undecacene [211, 212], and dodecacene [213] were synthesised using different chemical routes on gold surfaces. STS characterisation showed a high density of states at the center of nonacene that would be compatible with an open-shell structure. Such density of states was not observed for other acenes up to hexacene [212]. Furthermore, STS allowed to measure the band gap, showing that it decreases when increasing the number of rings up until dodecacene. The latest result in dodecacene showed that the band gap is larger than undecacene, going against the theoretical predictions and sparking new interest in the subject [213]. Polyacenes and related structures have also recently attracted topological interest similar to GNRs. Cirera et al. synthesised on surface a series of laterally bridged polyacenes polymers which displayed remarkable topological phase transitions. In particular, they theoretically rationalised that polymers composed of laterally bridged [n]-acenes with $n < 5$ would be topologically trivial, while starting from pentacene ($n = 5$) they would observe a transition to a nontrivial phase. This idea was also matched by the observation with STM of localised topological states at the Fermi level in laterally bridged pentacene, which were absent in laterally-bridged anthracene ($n = 3$).

There are also other classes of zigzag edged molecules that are inspired from polyacenes that we do not dicuss or show here. For instance, it is worth citing zethrenes [215–218] and uthrenes [219]. Some armchair edged structures have been also reported as singlet diradical i.e. rylenes [220].

Triangular nanoflakes, such as [3]triangulene in fig. 1.10, have also attracted the attentions of chemists and physicists for long [221–223]. Any triangular shaped nanoflake presents an intrinsic imbalance in the number of elements belonging to the two sublattices that increases with the size of the flake. Hence, they represent a perfect model for validating Lieb's theorem and studying high-spin ground state molecules. The smallest triangular flake is phenalenyl (**12**) that has a spin $S = 1/2$ with a vast literature studying the magnetic properties of its derivatives [199, 224]. Here we focus on larger structures that due to their high reactivity have been synthesised only recently with new chemical methods. While derivatives of [3]triangulene have been known for some time [225, 226], recently it was possible to synthesise and characterise on surface unsubstituted [4] and [5]triangulene that are expected to have ground spin state of $S = 3/2$ and $S = 2$ respectively [227, 228]. In both cases, STM images showed a very high local density of states at the edge contrasted by no activity in the bulk of the molecule, agreeing with the numerous theoretical predictions. Similar results were

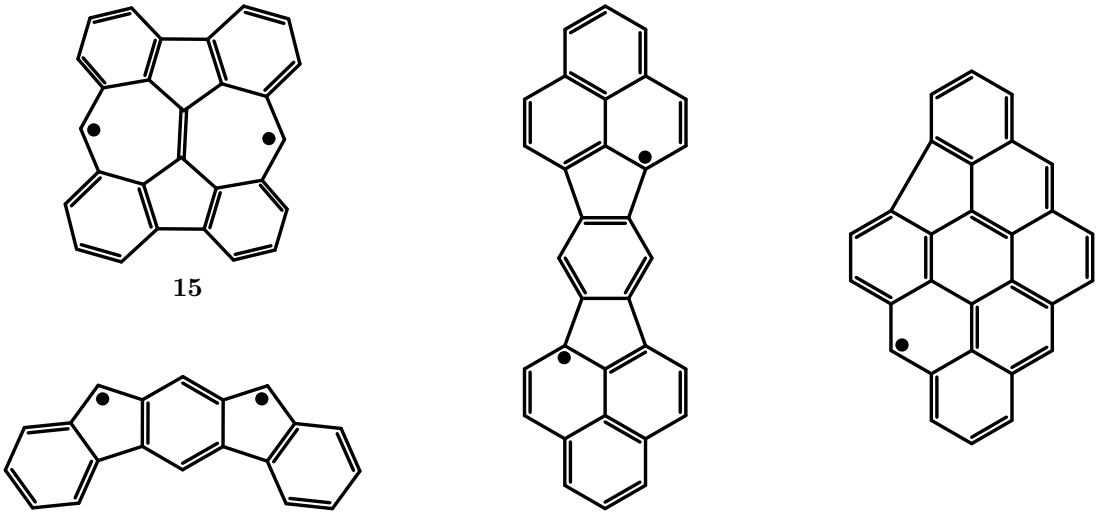


Figure 1.11: Examples of nanographene molecules bearing topological defects: difluoreno[1,9,8- *alkj*:1',9',8'-*gfed*] heptalene **15**, *para*-quinodimethane embedded indenofluorene **16**, *para*-quinodimethane bridged biphenalenyl **17**, 9,10-bis(4-bromo-2,6- dimethylphenyl)anthracene **18**.

also obtained for larger hexagonal systems with zigzag edge [229].

Another zigzag-edge molecule that was for long only a theoretical construct is Clar's goblet (**13**). Clar's goblet is a bow tie shaped structure that, differently from the triangular flakes, has no imbalance in the two graphene sublattices. Nevertheless, Wang and coworkers [230] predicted the open-shell ground state with a strong antiferromagnetic coupling between the two unpaired spins. They suggested that such coupling provides a natural platform for a quantum CNOT gate, because flipping of one spin would automatically produce flipping of the coupled spin due to the antiferromagnetic exchange. Mishra *et al.* [231] synthesised on gold surface unsubstituted Clar's goblet and imaged its density of state obtaining an antiferromagnetic exchange of 23 meV that would be enough for near room temperature logical applications.

There are fewer examples in the literature of molecules with topological defects. Biphenalenyl molecules like **17** have been studied extensively [232–235]. They present two pentagonal defects, but they owe their magnetism more to the two phenalenyl subunits than to the defects themselves. A similar reasoning can be done for **15** [236] where the biradical character is more likely due to the zigzag edges rather than to the presence of a Stone-Wales defect. On the contrary, the presence of two topological defects becomes critical for indenofluorene **16** and its topology strongly influences the excellent magnetic, optical, and electrical properties properties [237–240]. A very recent example of the importance of topological defects for magnetic properties is also provided by **18** [241] and its

derivatives [242]. STS images clearly show the effect on the spin density before and after introducing a topological defect.

The majority of compounds including defects have exploited pentagonal sites because they were easier to synthesise. However, novel chemistry has been adopted to include 5-7 pairs [243], heptagonal defects [244], and also octagonal ones [245]. While these are a small minority of compounds, future developments will surely rise from these new opportunities.

Methods

2.1 Electron Paramagnetic Resonance

Electron Paramagnetic Resonance (EPR), often referred to as Electron Spin Resonance (ESR), is a magnetic resonance spectroscopy used to probe electron spin levels. The basic principle of EPR relies on the concepts illustrated in chapter 1: when a static magnetic field is applied to a paramagnetic species, the degenerate spin levels are split according to their quantum number m_S. Upon irradiation with microwaves, spin transitions can occur if the microwave frequency is resonant with the energy difference and if the spin selection rule $\Delta m_S = \pm 1$ is satisfied. The identification of spin transitions is the spectroscopic signature that allows characterisation of the spin levels of the system and its electric and magnetic properties.

The general set up of an EPR experiment requires a series of standard components: a magnet, a source of microwaves in the GHz range, a detection system, the electronics to amplify the signal, a resonator, and a cryostat with controller to adjust the temperature. For technical reasons, commercial spectrometers come with standard frequency ranges, the most common are X-band (9-10 GHz), Q-band (34 GHz), and W-band (94 GHz). Nevertheless, high frequency experiments from 100 GHz up to even 1 THz are becoming more common. Here, we present the two possible ways of exciting the sample: Continuous Wave (CW) and pulsed microwaves.

2.1.1 Continuous Wave EPR

In a Continuous Wave (CW) EPR experiment, the magnetic field is swept while a continuous microwave excitation at fixed frequency irradiates the sample, resulting in a spectrum with lines at field values where the resonant condition is satisfied. Typical CW-EPR results can be seen in fig. 2.2. The interpretation of a CW spectrum relies on the spin Hamiltonian introduced in section 1.1.2.

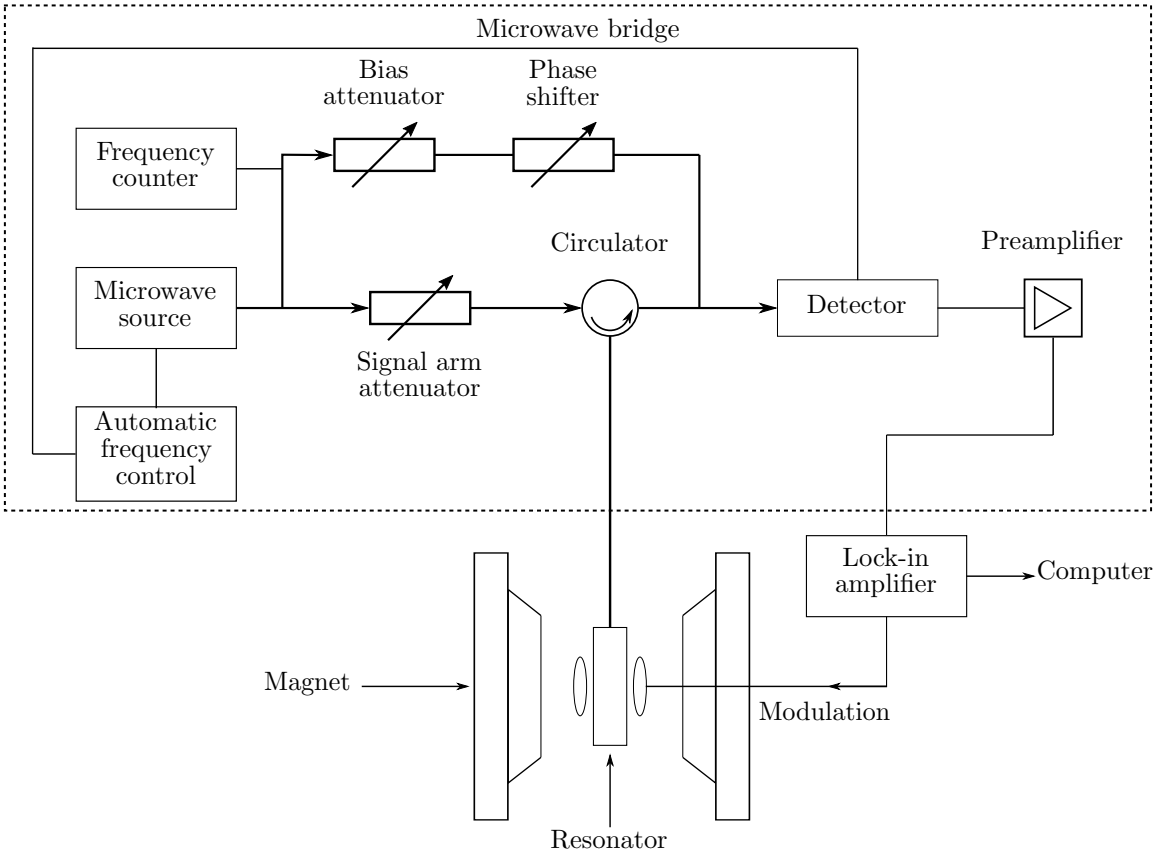


Figure 2.1: Schematics of a CW microwave bridge, and setup of an experiment. The microwave bridge includes the solid state microwave (MW) source, and the electronics necessary to amplify and phase it. A set of waveguides directs the MW excitation towards the resonator. The circulator allows the MW to go only in one direction, for example counterclockwise, and is necessary to measure the reflection of the signal. The resonator is equipped with side coils that generate the modulation fields and are connected to the lock-in amplifier. Adapted from [246].

Interpretation of spectra can be complicated due to the large number of contributions that need to be deconvoluted. Figure 2.2 presents three typical cases in EPR interpretation where the main features in the Hamiltonian are, in order, g anisotropy, hyperfine coupling, and dipolar coupling. It is good practice to carry out experiments at multiple frequencies to highlight the terms of the Hamiltonian. For example, organic radicals have very small g anisotropies that might overlap at X-band while they are distinguishable at high frequency. Similarly, for some metal ions, the zero field splitting is so large that X-band frequency is not enough to excite the transitions and high frequency EPR would also be required. Crystals and randomly oriented samples will yield different spectra both in terms of lines shown and linewidth.

It can be noted that the graphs in fig. 2.2 appear as a prime derivative of an absorption spectrum. This is due to the lock-in detection used in EPR to overcome the weak population difference between

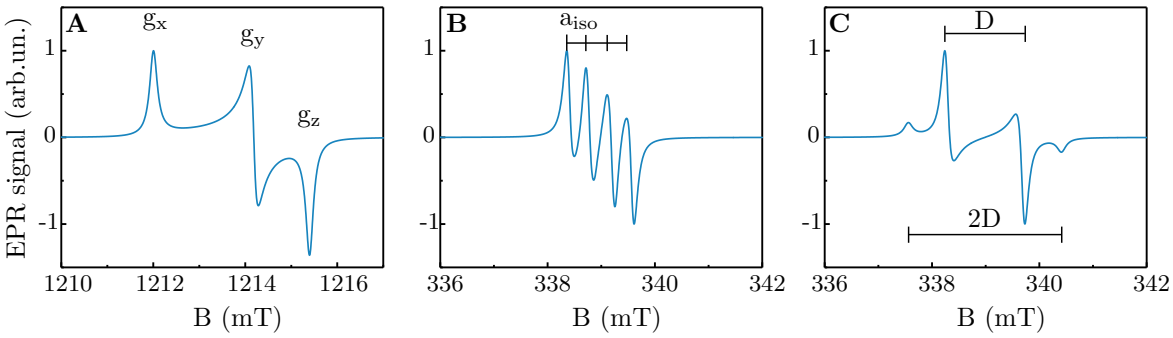


Figure 2.2: (A) Q-band spectrum of a spin $S = 1/2$ with g anisotropy, $g = (1.9987\ 2.0007\ 2.0043)$ in a powder. (B) X-band spectrum of a copper $S = 1/2$ sample in a slow-tumbling solution. The electron spin is coupled to the copper nucleus, both ^{63}Cu and ^{65}Cu have spin $I = 3/2$ which explains the $2I + 1 = 4$ lines of the spectrum. The distance between the lines gives indication of the isotropic hyperfine coupling, while the y-axis values depend on the tumbling time, here 5 ns. (C) X-band spectrum of an $S = 1$ powder sample with zero-field splitting $D = 40$ MHz, the spectrum is the derivative of the famous Pake pattern. All simulations were produced with the Matlab package Easyspin [247]. The EPR linewidth was 0.2 mT of Lorentzian shape for all three graphs.

spin levels. An intrinsic obstacle in CW experiments is that the energy difference between the spin levels is small compared to the thermal energy. At a typical magnetic field for X-band experiments $B = 0.34$ T, the energy difference in a spin $S = 1/2$, $g = 2$, is given by the electron Zeeman term (see chapter 1) $H_{eZ} \approx 40$ μeV, while the thermal energy at 300 K is $k_B T \approx 25$ meV, and at 4 K ≈ 345 μeV. According to Boltzmann law, the population difference between the two levels is $\Delta N = 1 - e^{-H_{eZ}/k_B T}$, which corresponds to 0.0016 at 300 K and 0.11 at 4 K. Since the absorbance is proportional to the population difference, a high quality-factor resonator and a modulation magnetic field with lock-in detection are applied in order to improve the sensitivity. Here, the Q-factor describes how good the resonator is at storing energy:

$$Q = \frac{2\pi \times energy\ stored}{energy\ dissipated\ per\ cycle} = \frac{\nu_{res}}{\Delta\nu}, \tag{2.1}$$

where ν_{res} is the resonator frequency, and $\Delta\nu$ the resonator bandwidth.

While this approach grants a sensitivity down to 10^9 spins in commercial instruments, it also comes with drawbacks. First, using a resonator with high Q-factor will narrow the bandwidth of the experiment. Second, the magnetic field modulation limits the time response to 10 μs. Third, the modulation amplitude, frequency, and phase need to be adjusted to avoid artefacts and distortion to the spectrum.[1] This anticipates that a large set of experimental parameters needs to be mindfully

[1]Some of the problems with the modulation field can be overcome, for slowly relaxing samples, using rapid-scan EPR, which requires a modified hardware. There has been a large body of research in rapid-scan EPR in the last 10 years, and commercial spectrometers have been available for about 3 years. In this thesis we will not discuss rapid-scan EPR, for a review see [248].

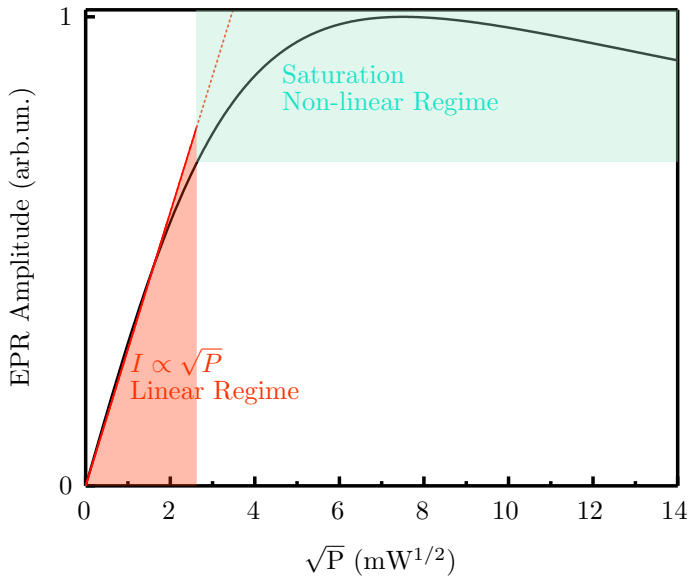


Figure 2.3: EPR line amplitude as a function of the square root of the microwave power as in eq. (2.2). The two regimes are highlighted. In the calculation we used $P_{1/2} = 24.8$ mW, $b = 1.44$, adapted from [250].

adjusted to record an EPR spectrum. An in-depth explanation of such parameters can be found in standard EPR textbooks (see for instance [249, 250]), here, as an example, we illustrate the problem of saturation, that will also be useful for the experimental discussion in the following chapters.

The amplitude of an EPR line depends on the steady-state population difference between the two levels: absorption of microwave decreases the population difference, while spin-lattice relaxation brings it back to equilibrium. Hence, an important balance is established between the two: if the power is too strong and the relaxation time not fast enough, too many spins are inverted and the transition becomes saturated. We can write an expression for the amplitude I:

$$I \propto \frac{\sqrt{P}}{(1 + P/P_{1/2})^{b/2}} \tag{2.2}$$

where P is the microwave power, $P_{1/2}$ the saturation power, and b a parameter that depends on the linewidth and can range between 1 and 3 [250]. The saturation power depends on the relaxation regimes of the sample and it is defined as the power for which:

$$\frac{1}{(1 + (g\mu_B/\hbar)^2 B_1^2 T_1 T_2)} = \frac{1}{2}. \tag{2.3}$$

As can be see from fig. 2.3, above a certain power threshold, the signal decreases non-linearly even if

the microwave power increases. Additional complications are included considering that, in general, T_1 and T_2 are temperature dependent, the population difference is temperature dependent, and the converted power B_1 depends on the resonator Q-factor and filling factor.

There are several tools in the literature that allow fitting and simulation of EPR spectra, for instance the Matlab packages Easyspin [247] or Spinach [251]. Successful interpretation and simulation of a spectrum provides a set of parameters of the SH, which represent the electronic structure of the compound. A full understanding of the electronic structure needs additional modelling of the sample, possibly with *ab initio* calculations. Due to the vast diffusion of Density Functional Theory (DFT) tools in the last years, this has also become a prime tool for relating EPR spectra to the electronic structure of compounds (*vide infra*).

2.1.2 Pulse EPR

There are several limitations in CW EPR, for example couplings that are too small cannot be detected, and often too complicated spectra cannot be deconvoluted. Pulse EPR can solve some of these problems and also probe spin relaxation. With the advent of Fourier Transform (FT) EPR [26], any CW spectrum could be obtained with pulse excitation. However, while in NMR pulses have completely substituted CW, in EPR it has not happened yet, because pulse instrumentation is much more expensive, complex, and less compact than a CW spectrometer.

A few modifications in hardware are indeed necessary to perform a pulse experiment. In pulse EPR the low power continuous excitation is substituted by high power microwave pulses as short as 10 ns. The simplest pulses that can be generated are rectangular pulses, but for instruments equipped with an Arbitrary Wave Generator (AWG), pulses with arbitrary shapes can be produced for advanced applications. The shape and length of the pulse determine its excitation bandwidth: if the EPR spectrum of the sample is larger than the excitation bandwidth, not all spins will be excited and the result will be affected by orientation selection [26]. For a rectangular pulse, in first approximation, the bandwidth is $\approx 1/t_p$, where t_p is the pulse length. Additional bandwidth limitations are introduced by the resonator. For maximum bandwidth, the Q-factor of the resonator needs to be reduced compromising the sensitivity of the measurement. Similarly, lowering the dead time of the instrument also requires a low Q-factor. We can calculate the dead time for a typical X-band experiment with $Q \approx 200$, $\Delta\nu_R \approx 50$ MHz $t_\mathrm{d} = \dfrac{16}{\pi\Delta\nu_R} \approx 100$ ns.[2] Lastly, the detection

[2]Equation for dead time taken from Bruker training slides.

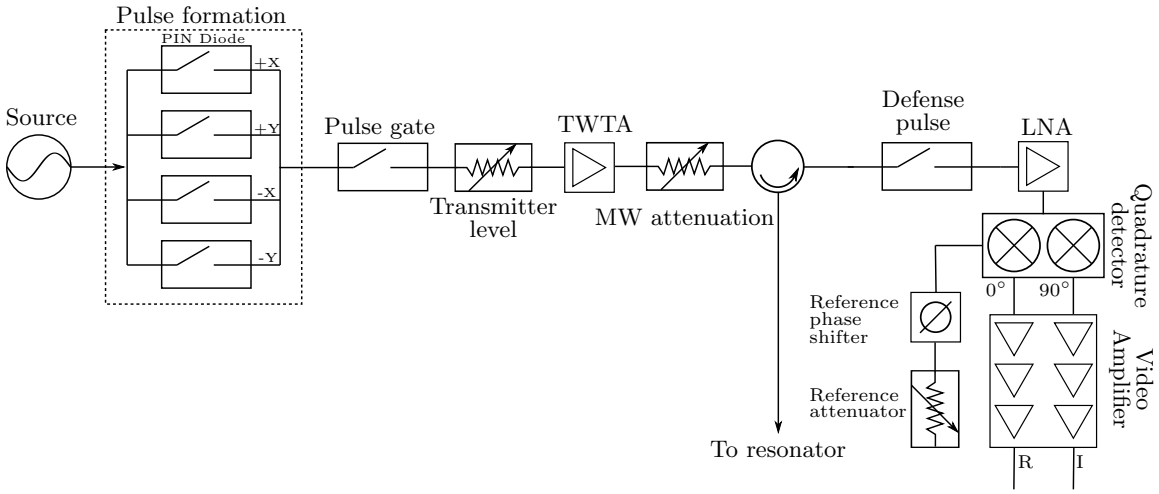


Figure 2.4: Simplified schematics of a pulse EPR setup. Pulses are generated through PIN (P-type Intrinsic N-type) diode switches. In the drawing, 4 channels (+X, +Y, -X, -Y) are shown with fixed amplitudes, whereas the majority of the instruments have 4 additional channels that can be adjusted. The pulses produced are low power and they need to be amplified by a Travelling Wave Tube Amplifier (TWTA). The amplified pulses are so high power that the pulses reflected from the resonator could easily destroy the detection system, therefore a defence pulse protects the detector. A Low Noise Amplifier (LNA) is used to amplify the signal before the quadrature detection. The output is visualised as real and imaginary and allows full reconstruction of the phase and amplitude of the signal. Adapted from R. T. Weber, E580 Pulse EPR Course, Bruker Biospin Manual, 2007.

system does not measure the absorption of the spins, but their emission through Free Induction Decay (FID) or echos, that are acquired by a quadrature detector as in-phase and out-of-phase signals with respect to a reference frequency [252].

A simple description of a pulse experiment can be pictured using the Bloch sphere. The Bloch sphere visualises the ensemble magnetisation vector $\mathbf{M} = (M_\mathrm{x}, M_\mathrm{y}, M_\mathrm{z})$ in a 3D space. Since the dynamics of a spin $S = 1/2$ is encoded in the three operators $\hat{S}_\mathrm{x}, \hat{S}_\mathrm{y}, \hat{S}_\mathrm{z}$, a correspondence among them and the magnetisation components can be made, and the Bloch sphere represents an exact solution of the problem. For any situation also involving nuclear spins or more than one electron spins, only the density matrix description can provide an exact solution, but the Bloch sphere is commonly used.

The classical dynamics of the magnetisation vector under the effect of an external magnetic field $\mathbf{B}$ is given by the torque equation:

$$\frac{d}{dt}\mathbf{M} = \frac{g\mu_\mathrm{B}}{\hbar}\mathbf{B} \times \mathbf{M}, \tag{2.4}$$

at equilibrium the magnetisation is parallel to the external field $\mathbf{B}$ (for convention on the z axis) and $d\mathbf{M}/dt = 0$. A magnetic field $\mathbf{B_1}(t)$ applied in the xy-plane will rotate the magnetisation vector which will precess around z at the electron Larmor frequency $\omega_s = \frac{g\mu_\mathrm{B}B}{\hbar}$. It is easier to study this

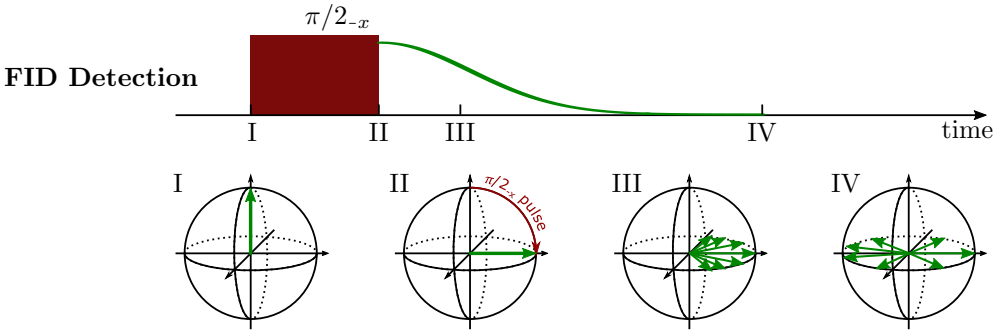


Figure 2.5: Single pulse FID generation and Bloch sphere representation. (I) At the thermal equilibrium the magnetisation is parallel to the z-axis, (II) the magnetisation is flipped by a $\pi/2$ pulse to the y-axis. (III) Only a certain number of spin packets are resonant with the excitation while the others have a frequency difference $\Delta\omega$ with respect to the rotating frame that determines their precession around z. (IV) After a certain time the spin packets are incoherent and the FID is extinguished.

dynamics in a frame that rotates around z at the same frequency of the microwave (the maths for transition from a static to a rotating frame is shown in any EPR textbook, see [26, 252]). The effect of a resonant pulse is to rotate the magnetisation vector of a flip angle θ with respect to the axis where the pulse was applied:

$$\theta = \omega_1 t_p, \tag{2.5}$$

where $\omega_1 = g\mu_B B_1/\hbar$ is related to the pulse power, and t_p is the pulse length. The most used pulses in EPR experiments, indicated by their flip angle, are $\pi/2$ and π. The former brings the magnetisation in the xy-plane, while the latter flips the spins.

Free Induction Decay

The simplest pulse experiment involves a single pulse and results in a FID signal. Inhomogeneous broadening yields spin packets that have different resonance frequencies. Using a rotating frame for the xy-planes, the frame will rotate at ω_{MW}, and each spin packet will have a certain precession frequency ω_i, so that $\Delta\omega = \omega_{MW} - \omega_i$. Only the resonant spin packet has $\Delta\omega = 0$, while the non-resonant spin packets will precess clockwise if they have negative $\Delta\omega$, and counterclockwise if positive. Therefore, at a certain time t they will have gained a phase difference $t\Delta\omega$ [252]. The dephasing due to inhomogeneous contributions makes the FID signal decay. The decay is usually related to T_2^*, but it also depends on the length of the pulse. In fact, longer pulses will have a narrower bandwidth that excites less spin, reducing the inhomogeneous effects. In many cases, the FID is so short that the signal is completely lost in the dead time of the instrument. However, for long–enough pulses it is possible to detect the FID. By sweeping the magnetic field and detecting

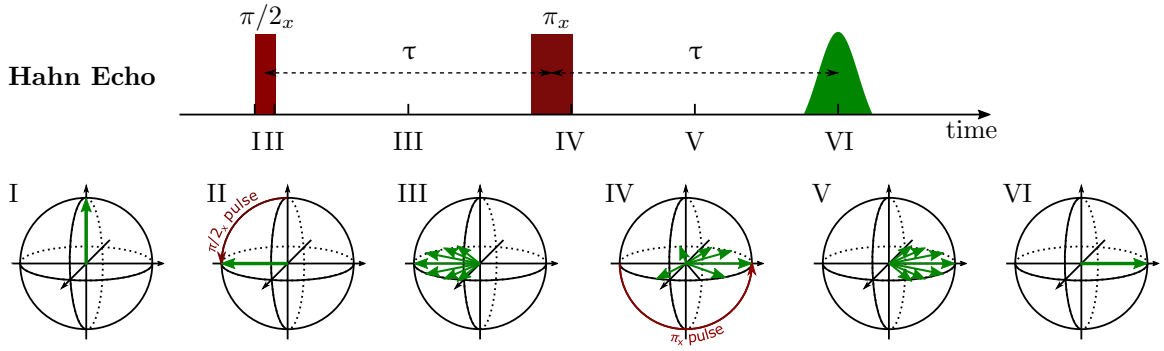


Figure 2.6: Pulse sequence and Bloch sphere representation for the Hahn echo. (I) At equilibrium the magnetisation vector is parallel to the external field on z, (II) the $\pi/2$ pulse rotates the magnetisation in the xy-plane. (III) Spin packets with $\Delta\omega \neq 0$ gain a phase difference, (IV) then their precession frequency is flipped by the π pulse, (V) and in the free precession the phase difference is refocused (VI) until the spin packets come together and emit an echo signal that is detected at a time 2τ from the initial pulse.

the FID it is possible to record an absorption spectrum that compares to a CW one (FID-detected field sweep).

Hahn Echo

While FIDs are important in NMR, inhomogeneous broadening makes them so short that it is often quite hard to detect them in EPR. The way signals are recorded in EPR is through an experiment called Hahn echo [253]. As shown by fig. 2.6, the sequence consists of 2 pulses: an initial $\pi/2$ pulse that generates the superposition of states, and a subsequent π pulse that flips the spins. The spin dynamics can be followed on the Bloch sphere, and the initial evolution is analogous to the FID case. The spin packets that are slightly off-resonance branch out gaining a phase difference, the π pulse reverses the phase difference, and the spin packets are refocused in an echo. The echo is generated at a time 2τ from the initial pulse, hence for τ large enough the signal will be cleared of the dead time of the instrument and easily detectable. By sweeping the magnetic field, keeping τ constant and detecting the echo, it is possible to obtaining an absorption spectrum similar to a CW spectrum (echo-detected field sweep).

The most important application of the Hahn echo is to measure the coherence time of a spin system. In fact, the refocused spins will emit an echo as long as their phases are coherent. At a fixed magnetic field, increasing τ the echo will have an exponential decay $\propto T_{\mathrm{m}}$ as defined in 1.3. The shape of the decay is crucial to understand the decoherence mechanism. There is no general theory to predict the shape of the echo decay, but the most common phenomenological model suggests

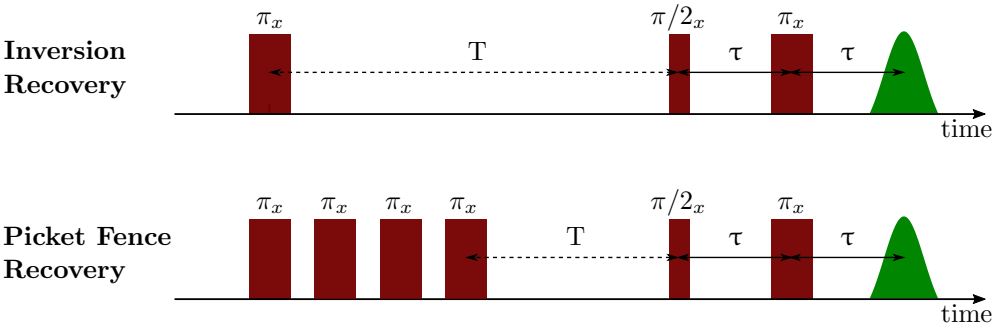


Figure 2.7: In the inversion recovery sequence, the first π pulse reverses the population of the spin level. The magnetisation will the precess towards equilibrium during the time T and its state will be detected with an Hahn echo. In picket fence recovery, a train of π pulses demagnetises the sample, and similarly the recovery of the magnetisation is followed varying T.

fitting the echo decay with a stretched exponential decay:

$$y = y_0 \exp\left\{\left(-\frac{2\tau}{T_\mathrm{m}}\right)^{\beta}\right\}, \tag{2.6}$$

where β is referred to as the stretching parameter [254]. Nevertheless, there are several examples in the literature where different phenomenological models are adopted when appropriate: a biexponential decay [91, 94] or a stretched biexponential decay [255].

$\mathbf{T}_1$ Measurements

There are numerous ways to measure the spin-lattice relaxation time [254], here we consider two sequences: inversion recovery and picket fence recovery, as seen in fig. 2.7. In inversion recovery a π pulse flips the magnetisation, the spin will then precess from an out-of-equilibrium situation to equilibrium due to spin-lattice relaxation. The recovery of the magnetisation is detected through an Hahn echo sequence while varying the time T. The same principle applies to picket fence recovery, a train of pulses is applied (the turning angle of the pulses is not crucial as long as the sum of the turning angle is $\gg \pi$) that results in complete demagnetisation of the sample, the recovery is then followed varying T.

There are several spin processes that can affect the detection of spin-lattice relaxation time in either of the two sequences. In inversion recovery the first pulse has a limited bandwidth which means that for large spectra only a portion of the spins is excited. The non-excited spin can transfer equilibrium magnetisation to the excited spin that will be detected as a faster magnetisation. This

process is referred as spectral diffusion in the literature [26]. With a train of π pulses, the picket fence sequence is less affected by spectral diffusion when the spacing between the pulses is chosen correctly [256].

Interpretation of spin-lattice relaxation data can be thus complicated by the phenomena described. In general, recovery data is fitted with a double exponential:

$$y = A_1 e^{T/T_{\mathrm{fd}}} + A_2 e^{T/T_1} + y_0, \tag{2.7}$$

where T_{fd} includes all the fast decays and T_1 is the spin-lattice relaxation time. It is possible to distinguish T_1 from T_{fd} because the contribution from fast decays it is usually very small so that $A_1 \ll A_2$. However, in situations where $A_1 \approx A_2$ it will be ambiguous to attribute spin-lattice relaxation to one of the time constants.

2.2 Hyperfine spectroscopy

Hyperfine couplings represent the interaction between electron spins and nuclear spins. As seen in section 1.3 the nuclear bath has a unique effect on the coherence of a spin system. Understanding electron-nuclear and nuclear-nuclear coupling is therefore important to design better performing quantum devices. CW-EPR is sensitive to large hyperfine couplings that show as seen in fig. 2.2**B**. However, it is often the weakly coupled nuclei that are responsible for the decoherence. Using pulse EPR even small hyperfine couplings or even intrabath nuclear interactions are accessible.

In the simplest case we can consider a spin $S = 1/2$ coupled to a nucleus $I = 1/2$, the full system Hamiltonian, as defined in section 1.1.2, is:

$$\hat{H} = \hat{H}_{eZ} + \hat{H}_{HF} + \hat{H}_{nZ} = \mu_{\mathrm{B}} \mathbf{B} \mathbf{g} \hat{\mathbf{S}} + \hat{\mathbf{S}} \mathbf{A} \hat{\mathbf{I}} - \mu_{\mathrm{n}} g_{\mathrm{n}} \mathbf{B} \hat{\mathbf{I}}. \tag{2.8}$$

In an EPR experiment, the eZ term will always dominate the nZ terms, and possibly the HF term, hence the electron spin can be considered quantised on the z-axis and we can disregard $\hat{S}_x$ and $\hat{S}_y$. However, the respective magnitude of the HF and nZ terms depends on the external field and on the system, and it is not necessarily known *a priori*. Two notable cases can be distinguished: weakly

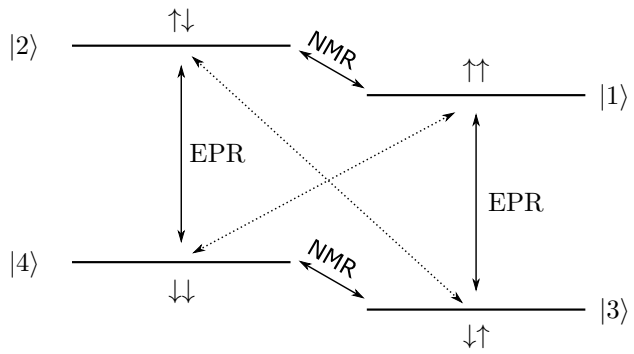


Figure 2.8: Level schematics of a spin $S = 1/2$ coupled to one nucleus $I = 1/2$, assuming $A > 0,\ g_n > 0$ and weakly coupled system. The arrows indicate the spin number for electron spin and nuclear spin respectively.

coupled $H_{HF} < H_{nZ}$, and strongly coupled $H_{HF} > H_{nZ}$. In the most general case:

$$\hat{H} = \mu_{\mathrm{B}} g B \hat{S}_z - \mu_{\mathrm{n}} g_{\mathrm{n}} B \hat{I}_z + \hat{S}_z A_{zz} \hat{I}_z + \hat{S}_z A_{zx} \hat{I}_x + \hat{S}_z A_{zy} \hat{I}_y \tag{2.9}$$

where the matrix elements A_{ij} are obtained performing a projection of the $\mathbf{A}$ tensor on the principal axes of the molecular frame [257]. If we restrict ourselves to the simplest case of a weakly coupled nucleus, writing the Hamiltonian in angular frequency units:

$$\hat{H} = \omega_S \hat{S}_z - \omega_I \hat{I}_z + \hat{S}_z A \hat{I}_z + \hat{S}_z B \hat{I}_x \tag{2.10}$$

where $\omega_S = \mu_{\mathrm{B}} g B/\hbar$, $\omega_I = \mu_{\mathrm{n}} g_{\mathrm{n}} B/\hbar$, $A = A_{zz}$, and $B = \sqrt{A_{zx}^2 + A_{zy}^2}$, respectively the secular and pseudosecular hyperfine terms.

This situation can be better pictured as a four-level system as in fig. 2.8, where EPR transitions satisfy the condition $\Delta m_S = \pm 1,\ \Delta m_I = 0$, NMR transitions satisfy the condition $\Delta m_S = 0,\ \Delta m_I = \pm 1$, and forbidden transition represented by dashed arrows satisfy the condition $\Delta m_S = \pm 1,\ \Delta m_I = \pm 1$. This is the simplest schematics of the hyperfine coupling that can be extended to more complicated cases with more nuclei or higher spin levels. In general there are three families of hyperfine spectroscopy: Electron Spin Echo Envelope Modulation (ESEEM), Electron Nuclear DOuble Resonance (ENDOR), and ELDOR-detected NMR (EDNMR). Here, we will describe the first two, while no discussion of EDNMR will be provided as we will not make use of such techniques.

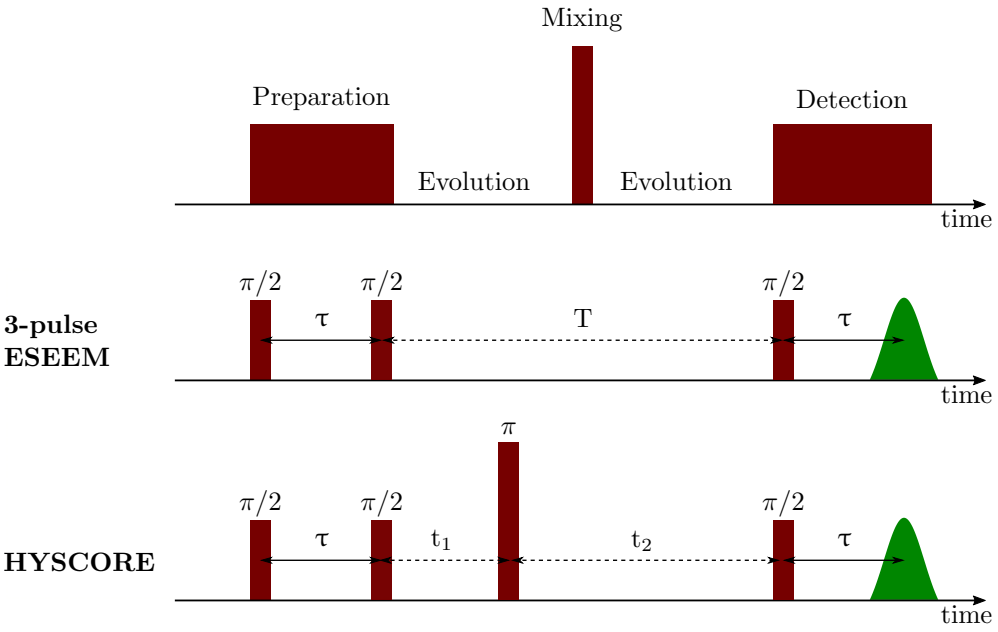


Figure 2.9: (Top) General schematics of ESEEM techniques, involving preparation of coherent superposition, evolution and mixing of nuclear and electron coherence, and detection of electron coherence [258]. (Middle) Schematics of a 3-pulse ESEEM sequence. In a typical experiment τ is fixed and T is varied. (Bottom) Schematics of a HYSCORE sequence. In a typical experiment the π pulse has same length of the $\pi/2$ pulses but double power.

2.2.1 ESEEM techniques

The principle behind ESEEM techniques is to transfer coherence from the electron spin manifold to the nuclear one, let the coherences mix, and revert nuclear coherence back to the electron one for detection. The simplest ESEEM experiment is the Hahn echo (fig. 2.6), also referred as 2-pulse ESEEM. Indeed, the echo does not only decay with T_m, but it can present a modulation that is a fingerprint of the hyperfine coupling.

We illustrate the modulation of 2-pulse ESEEM on the Bloch sphere of fig. 2.6, we use ideal pulses resonant with the (1,3) transition (fig. 2.8), and we consider a rotating frame. The first $\pi/2$ pulse rotates the magnetisation vector in the xy plane, after which it gains a phase $(\omega_{13} - \omega_\mathrm{MW})\tau$ during free evolution. At this point, the π pulse flips the magnetisation vector, but it also flips – with lower probability – the nuclear spin, transferring the initial coherence in the (1,3) transition to all others. In the following free precession, the (1,3) vector gains a phase equal and opposite to the one in the first evolution and it is refocused in an echo. However, the coherence in the other transitions will have precessed with a different rotation frequency: for example, the coherence in transition (2,4) will have precessed at frequency $\omega_{24} - \omega_\mathrm{MW}$, gaining a phase with respect to (1,3)

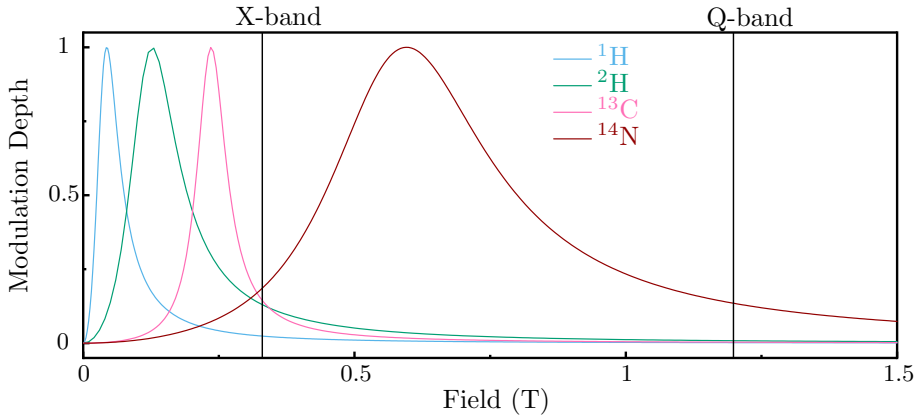


Figure 2.10: Trend of the modulation depth with respect to the external magnetic field for a 2-pulse ESEEM experiment on a system of spin $S = 1/2$ coupled to one hydrogen ($A = 3$ MHz, $B = 2.1$ MHz), one deuterium ($A = 1.5$ MHz, $B = 0.7$ MHz), one ^{13}N ($A = 5$ MHz, $B = 0.7$ MHz), and one ^{14}N ($A = 3.5$, $B = 1.1$). The computation follows the expression for modulation depth from [258]. The vertical lines mark the typical magnetic field for experiments at X-band and Q-band.

$|\omega_{13} - \omega_{24}|\tau$. Hence, the maximum echo intensity will be reached only when the coherences from the different transitions are in phase, and a modulation will be superimposed to the signal that can be related back to the transition frequencies of fig. 2.8. The modulation will decay with the T_m of the complex, which is a limitation to the compounds that can be probed and produces broadening of the lines. Additionally, the modulation will not only be sensitive to the fundamental frequencies but also to higher harmonics and combination frequencies, making the entire spectrum very difficult to interpret. In general, for systems with multiple coupled nuclei, 2-pulse ESEEM can provide qualitative information but it will not be possible to deconvolute different contributions. Finally, the modulation depth is proportional to the number of coupled nuclei, their Larmor frequency (see fig. 2.10), and their anisotropic hyperfine coupling (B). In particular, in the absence of anisotropic hyperfine coupling there will be no modulation, thus ESEEM cannot be applied to compounds in the fast tumbling regime. These considerations will also apply, albeit in different fashion, to all the following ESEEM experiments.

Some of the problems with 2-pulse ESEEM are solved by 3-pulse ESEEM (see fig. 2.9), which is also referred to as the stimulated echo. The first two $\pi/2$ pulses generate nuclear coherence, which means that the reference time in the free evolution is no longer T_m but $T_\mathrm{m,n}$, the nuclear coherence time, which is usually $\approx T_1$, therefore much longer than T_m. Additionally, fundamental frequencies will be preferably observed, with fewer combination frequencies [258]. However, the modulation depth will be strongly influenced by the value τ showing τ-dependent blindspots. Thus,

the experiment should be repeated at multiple τ values.

Both 2 and 3-pulse ESEEM can provide quantitative information on very simple systems, but they are elementary sequences that have been, nowadays, supplemented by more sophisticated techniques. As seen also in NMR, recording 2D spectra enormously improves the quality of the information that can be drawn. At the price of a more complicated sequence, with more parameters to set and longer acquisition times, the spectra obtained allow deconvolution of multiple contributions after a Fourier transform.

An advanced 2D sequence is HYperfine Sublevel CORrElation (HYSCORE) which is showed in fig. 2.9. HYSCORE is based on the same initial canvas of 3-pulse ESEEM with the first two pulses generating nuclear coherence, which is then allowed to freely evolve for a time t_1. The mixing pulse π flips the electron spin and transfer nuclear coherence from one spin manifold to the other. The flipping of the electron spins means that the local magnetic field perceived by the nuclei will be different before and after the π pulse, which implies that the nuclei will precess with different frequencies during t_1 and t_2. Analogously to the previous two experiments, the intensity of the modulation will depend on the Larmor frequency of the nuclei, and there will be τ-dependent blindspots, therefore the experiments should be repeated at multiple τ values for a complete understanding.

HYSCORE yields a set of time-dependent results on two axes, that are then subjected to 2D Fourier transformation. The frequency domain presents signal in all four quadrants of the axes, but usually only the top two quadrants with $\nu_2 > 0$ is showed since the signal should be symmetric. The position of the signal in either of the two top quadrants is a fingerprint of the hyperfine interaction. For weakly coupled nuclei, the $\nu_1 < 0$ quadrant has no features, while the signal will appear as cross peaks in the $\nu_1 > 0$ quadrant in a position symmetric with respect to the diagonal and centred at Larmor Frequency of the nucleus. For strongly coupled nuclei, the $\nu_1 < 0$ quadrant presents all the signal, which again appears as symmetric with respect to the diagonal and centred at $(-\omega_L, +\omega_L)$. In general, for disordered systems the peaks are broadened and appear as ridges instead of sharp dots.

2.2.2 ENDOR techniques

The principle behind ENDOR techniques is to transfer polarisation from the electron spin manifold to the nuclear one, using a mix of resonant MW and radio frequency (RF) excitation. It is possible to execute ENDOR both in CW and pulse mode. We will refer to the simple four-level description

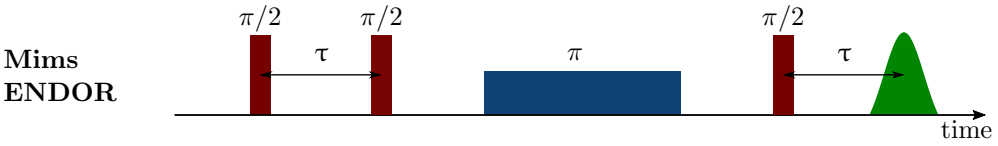


Figure 2.11: Sequence for Mims ENDOR, MW pulses are in red while RF pulses are in blue.

in fig. 2.8 to describe the techniques.

In CW ENDOR the magnetic field is fixed at the resonant condition for a specific EPR transition. Strong, continuous MW excitation is used to partially saturate the EPR line while the frequency of continuous RF is swept across a certain range. When the RF frequency matches the frequency of an NMR transition, the level is depopulated and the saturation lifted producing a peak in MW absorption. CW ENDOR is particularly useful for deconvoluting spectra with many equivalent nuclei, since they will only show as one peak.

In pulse ENDOR continuous excitation is substituted by MW and RF pulses. The two most used sequences are Davies and Mims ENDOR [26, 259]. As can be seen in fig. 2.11, Mims ENDOR is based on the 3-pulse ESEEM of fig. 2.9, with the addition of an RF pulse. In a typical experiment all time intervals are kept constant while the frequency of the RF pulse is swept.

2.2.3 Comparison

While ENDOR and ESEEM techniques should in principle produce the same results, considerations such as signal-to-noise-ratio and resolution make one technique better than the other. For example, since the modulation depth of single nuclei decreases with the Larmor frequency, ESEEM techniques are best suited to study nuclei with low Larmor frequencies. Conversely, ENDOR efficiency increases with increasing Larmor frequency, therefore ENDOR proves extraordinary useful when characterising systems with overlapping nuclear frequencies at low field that can be better resolved in high-field EPR. Furthermore, no signal can be obtained with ESEEM techniques when the hyperfine dipolar coupling is averaged out, while ENDOR is efficient at picking up also isotropic couplings. In terms of relaxation times, ENDOR requires sequences to incorporate RF pulses that can be several μs long, while ESEEM sequences can be much shorter allowing to probe samples with much faster relaxation. Finally, none of the two techniques is immune to artefacts. In ESEEM, sampling errors might arise if the Nyquist-Shannon theorem is not respected or the sampling frequency is not large enough. Both techniques suffer from deadtime artefacts that can be removed with more complicated deadtime-free

sequences [258, 259], and blind spots might require repeating the experiments at different times. In this case, measurement time and signal-to-noise-ratio can become limiting factors that allow choice of one or the other technique.

2.3 Density Functional Theory

While this work is almost completely of experimental nature, calculation results as obtained by DFT will be presented in the following chapters in order to aid understanding of experiments. For clarity, here we present a very brief description of the theory behind DFT [260–262], concentrating in particular on its advantages and limitations when calculating quantities relevant for EPR experiments [263].

In the absence of external fields and with a non-relativistic approximation, all properties of a certain system can be related to the many-body Schrödinger equation:

$$\Big[-\sum_i \frac{\hbar^2}{2m_e}\nabla_i^2 - \sum_I \frac{\hbar^2}{2M_I}\nabla_I^2 + \\ -\sum_{i,I}\frac{e^2}{4\pi\epsilon_0}\frac{Z_I}{|\mathbf{r}_i+\mathbf{R}_I|} + \frac{1}{2}\sum_{i\neq j}\frac{e^2}{4\pi\epsilon_0}\frac{1}{|\mathbf{r}_i-\mathbf{r}_j|} + \frac{1}{2}\sum_{I\neq J}\frac{e^2}{4\pi\epsilon_0}\frac{Z_I Z_J}{|\mathbf{R}_I-\mathbf{R}_J|}\Big]\psi = E_{TOT}\psi \tag{2.11}$$

where m_e and M_I are the mass of the electron and of the I-th nucleus, Z_I is the atomic number of the I-th nucleus, $\mathbf{r}_i$ and $\mathbf{R}_I$ are the coordinates of the i-th electron and I-th nucleus in the chosen reference system, $\psi(\mathbf{r}_1, \mathbf{r}_2, ..., \mathbf{r}_N, \mathbf{R}_1, \mathbf{R}_2, ..., \mathbf{R}_M)$ is the wavefunction that depends on electron and nuclear coordinates, E_{TOT} indicates the energy of the ground state of the system. The first two terms in the equation represents electron and nuclear kinetic energy respectively, while the other three are, in order, electron-nuclear Coulomb attraction, electron-electron Coulomb repulsion, and nuclear-nuclear Coulomb repulsion. Exact solution of this equation guarantees complete knowledge of the ground state of the system under study. However, there does not exist an analytical solution to this equation, and *ab initio* methods rely on approximations of the many-body equation.

A traditional simplification of the many-body equation is the Born-Oppenheimer approximation that considers the nuclei frozen. Therefore, the nuclear kinetic energy is ≈0 and the nuclear-repulsion

is a constant that we can include in the energy E:

$$\Big[-\sum_i \frac{\hbar^2}{2m_e}\nabla_i^2 - \sum_{i,I}\frac{e^2}{4\pi\epsilon_0}\frac{Z_I}{|\mathbf{r}_i-\mathbf{R}_I|} + \frac{1}{2}\sum_{i\neq j}\frac{e^2}{4\pi\epsilon_0}\frac{1}{|\mathbf{r}_i-\mathbf{r}_j|}\Big]\psi = E\psi. \tag{2.12}$$

The approximation stands because the nuclear mass is much larger than the one of an electron, therefore the nuclei can be represented as static with respect to the timescale of electrons. Furthermore, by assuming each electron to be independent the total electron wavefunction can be written as a product of individual electron wavefunctions $\psi = \prod_i \phi_i(\mathbf{r}_i)$. This transforms a $3N$-dimensional equation into N 3-dimensional equations which are much easier to solve.

Nevertheless, the main obstacle for any *ab initio* method is how to express the electron-electron Coulomb repulsion. Different methods include a certain number of terms to try to approximate this interaction. For the case of DFT, the initial many-body equation is approximate by the Kohn-Sham (KS) equation:

$$-\frac{\hbar^2}{2m_e}\nabla_i^2\phi_i + (V_\mathrm{N} + V_\mathrm{H} + V_x + V_c)\phi_i = \mathcal{E}_i\phi_i, \tag{2.13}$$

where the first two terms are the electron kinetic energy and the nuclear Coulomb potential as defined in eq. (2.11), while the three terms V_H, V_x, and V_c model electron-electron interactions. V_H is the Hartree potential that represents the potential of a certain charge distribution in classical electromagnetism according to the Poisson equation $\nabla^2 V_\mathrm{H}(\mathbf{r}) = -4\pi n(\mathbf{r})$. V_x is the local Fock exchange potential that arises from the Pauli exclusion principle. V_c is the correlation potential that arises from electron-electron repulsion.

How to solve the KS equation is the core concept of DFT which is incorporated in the Hoenberg-Kohn [264] and Kohn-Sham [265] theorems. Given the wavefunction ψ we can define the electron density $n(\mathbf{r})$ as the probability of finding a certain electron at position $\mathbf{r}$:

$$n(\mathbf{r}) = N\int |\psi(\mathbf{r},\mathbf{r}_2,...,\mathbf{r}_N,\mathbf{R}_1,\mathbf{R}_2,...,\mathbf{R}_M)|^2 d\mathbf{r}_1 d\mathbf{r}_2...d\mathbf{r}_N d\mathbf{R}_1 d\mathbf{R}_2...d\mathbf{R}_M. \tag{2.14}$$

The first theorem states that the energy of the ground state is a functional of the electron density: $E = E[n]$. The second theorem allows rewriting of the Kohn-Sham equation in terms of the electron density and inclusion of the Fock potential and correlation potential in one term:

$$E[n(\mathbf{r})] = \int n(\mathbf{r})V_\mathrm{N}(z\mathbf{r})d\mathbf{r} + \sum_i \langle\phi_i| -\frac{1}{2}\nabla_i^2 |\phi_i\rangle + \frac{1}{2}\int d\mathbf{r}\int \frac{n(\mathbf{r})n(\mathbf{r}')}{|\mathbf{r}-\mathbf{r}'|}d\mathbf{r}' + E_{xc}[n(\mathbf{r})] \tag{2.15}$$

where E_{xc} is the exchange and correlation potential, which is a functional of the electron density, and it is unknown. The initial problem of how to approximate the Coulomb interaction, now translates in how to approximate the exchange and correlation functional. An enormous body of literature is dedicated to producing and testing new functional that can work in specific cases. When a certain functional has been chosen, solution of the KS equation requires a self-consistent calculation which starts with an initial guess of the electron density. The initial density is used to calculate V_{H} and V_{xc} which are then used to calculate a new density by solving the equation. The process is then iterated until the differences between the initial and final densities are below a predefined threshold.

Spin degree of freedom has never appeared in the previous discussion. Indeed, the KS equation considers electrons of opposite spin as restricted to the same spatial orbital. Such treatment is referred as spin-restricted (or spin-unpolarised) and it is applicable to closed-shell systems that do not have unpaired electrons. A way to include spin polarisation into DFT calculation is by considering up and down spins spatially separate. In spin-unrestricted DFT, two sets of separated α and β orbitals host spin up and spin down electrons, respectively. Each set of electron spins ($\uparrow$ or $\downarrow$) is assigned an electron density and the total electron density can be written as:

$$n(\mathbf{r}) = n^{\uparrow}(\mathbf{r}) + n^{\downarrow}(\mathbf{r}), \tag{2.16}$$

the unrestricted KS equation will then show terms that are functional independently of $n^{\uparrow}(\mathbf{r})$ and $n^{\downarrow}(\mathbf{r})$, while others will still be functional of the total electron density. In the unrestricted framework another important quantity is defined, the spin density written as:

$$n^{\mathrm{spin}}(\mathbf{r}) = n^{\uparrow}(\mathbf{r}) - n^{\downarrow}(\mathbf{r}). \tag{2.17}$$

2.3.1 Calculation of EPR parameters

Our main interest is to calculate the parameters of the SH, here we evaluate what are the possibilities and limitations of DFT when performing such calculations [263]. The quality of any DFT result will depend on the chosen functional. It is not possible to choose a certain functional *a priori*, but in general it is possible to benchmark them in model systems for which high-level computational techniques are not too expensive and high quality experimental results are available. While there are several categories of functionals, the literature of organic radicals has been dominated by few. These

are hybrid functionals that are obtained through general gradient approximation (GGA) methods, they admit a certain degree of Hartree-Fock exchange, and include some parameters that come from fitting with experiments. The single most used functional in this category is B3LYP [266], other relevant hybrid functionals are PBE0 [267, 268] and TPSSh [269]. The CAM-B3LYP [270] is the range separated version of B3LYP that includes an additional parameter.

The quality of the results is also affected by the choice of the basis set. In DFT the wavefunctions ψ are molecular orbitals that are unknown, but need to be expressed using known functions: the basis set. There are two types of basis sets: Slater-Type Orbitals (STOs), and Gaussian-Type Orbitals (GTOs). STOs are in general more accurate, but GTOs are much easier to handle computationally. The large majority of DFT software are based on GTO basis sets. Basis sets are also classified according to the number of functions included, in principle the higher the number the higher the accuracy, but the computational cost also scales with the number of functions. A Single Zeta basis set only includes functions for the occupied orbitals of the atom. A Double Zeta basis set has double the amount of functions, and so on for Triple Zeta, Quadruple Zeta etc. For example, in a Double Zeta basis set two orbitals are used to describe hydrogen: 1s and 1s'. Another important factor is polarisation, which means that even though only certain orbitals are occupied in an atom, the effect of unoccupied orbitals with higher angular momentum is important to describe the properties of the systems and therefore they must be included. For example, in Double Zeta with single polarisation an hydrogen atom is described by three orbitals: 1s, 1s', and 2p. Similarly to the functionals, the literature offer a very large number of basis sets, here we mention some of the most used. The Pople basis sets include: 6-31G (double zeta) and 6-311G (triple zeta) and their respective single and double polarisation [271]. For instance in the 6-31G(d,p) (equivalent to writing 6-31G**) H is described by 2s1p orbitals and C by 3s2p1d, while in 6-311G(2df,2pd) H is 3s2p1d and C 4s3p2d1f. The Karlsruhe-Type basis set are SVP (double zeta) and TZV (triple zeta) with polarisation [272, 273]. In SVP H is 2s1p and C 3s2p1d, while in TZV H is 3s2p1d and C 5s3p2d1f. These are two sets of general basis set, but specific for EPR parameters we can find also Barone EPR-II (H 3s1p C 5s2p1d) and EPR-III (H 6s2p C 7s4p2d) basis sets.

Critical analyses on calculations of **g**-tensors show that its result is weakly dependent on the choice of functional and basis [261, 274–276]. The quality of **g**-tensor results depend on the method used to calculate single electron and two-electron spin orbit coupling operators. Very sophisticated methods have been developed to take into account relativistic corrections, that make calculation of

g-tensors reliable.

A much larger interest is devoted towards calculating the hyperfine coupling constants. We have discussed in section 1.1.2 that the hyperfine coupling is made of an isotropic part and a dipolar part. While the dipolar part is straightforward to calculate, it is more difficult to represent the isotropic one. As seen from eq. (1.9) the most important part of the calculation is the spin density at the nucleus, therefore the quality of the result will depend strictly on how well DFT represents the spin density. The literature show that very good results can be obtained using hybrid functionals and the basis set EPR-II or EPR-III at least for organic radicals, which is our interest [261, 275, 277–279].

On the other hand, it is very complicated to model the zero field splitting with DFT [261]. For metal compounds, DFT calculations have been in general far from the experimental results and in same cases predicting even the wrong sign of the interaction. A much better performance is observed for small organic biradicals [280]. Some calculations have been extended to larger and more delocalised hydrocarbons, but there are no comparisons with experimental results or more accurate methods [281].

The final parameter we might be interested in simulating is the exchange coupling J. There are ways to extrapolate this parameter using a broken symmetry method that allows calculation of the energy of the high spin state and the low spin state. The exchange coupling as defined by Yamaguchi [282] is:

$$J = \frac{E_{\mathrm{HS}} - E_{\mathrm{LS}}}{\langle \hat{S}^2 \rangle_{\mathrm{HS}} - \langle \hat{S}^2 \rangle_{\mathrm{LS}}}, \tag{2.18}$$

where HS and LS refer to the high spin and low spin state, respectively. Here we will not get into the details of the broken symmetry method. However, such method is largely applied in the chemistry literature. Neese [261] reviews the idea that the method might not correctly represent the physics of the problem, but in several cases, using the B3LYP functional, the result are surprisingly close to what achieved with more sophisticated *ab initio* techniques. Nonetheless, it appears that such occurrence is fortuitous, and calculation of exchange coupling should rely more on multi reference methods that can picture the phenomenon in a more physical way.

Overall, there is a significant amount of literature that examines the reliability of DFT when calculating EPR parameters. Very good performances are obtained when calculating **g**-tensors and hyperfine coupling constants, while calculation of zero field splitting and exchange coupling appears less reliable. More sophisticated methods might be able to allow a more precise results but they

also require a much larger insight into the theory and they are enormously expensive so that they might not be applicable for the molecules under study with 100+ atoms. We believe that the single most important source of error in our calculation comes from the geometry used. As discussed by Improta and Barone [275], hyperfine couplings can be susceptible to small variations of geometry. All the calculations assume the molecule to be in an isolated gas phase, while in EPR experiments the molecule will be dissolved in a certain solvent. It is unknown what would be the effect of the solvent in changing the geometry of the molecule, low polarity solvent (as the ones used in this thesis) might have a low effect, or at least localised to substituents whose hyperfine couplings might prove negligible with respect to the bulk of the molecule. There are models that allow calculating the effect of the solvents (this is possible with ORCA), notwithstanding the possibilities of molecular dynamics, but these are computationally expensive and beyond the scope of this thesis.

2.4 Remarks on the Methods

We carried out all the experiments with a commercial setup. All the CW EPR measurements were carried out on a Bruker EMXmicro equipped with a Bruker ER4102ST rectangular resonator. The majority of X-band pulse measurements were carried out on a Bruker Elexsys E680, fewer measurements were done on a Bruker E580. There should be very little difference as in both cases we used a 1kW TWTA, the split ring resonator Bruker EN 4118X-MS3, an Oxford Instruments CF935 cryostat, and an ITC503 temperature controller. All Q-band measurements were carried out on a Bruker E580 with an ER5106 QT-2W resonator.

All DFT calculations were completed on the software ORCA 4.2 [23, 283]. The pairing functional/basis set will be specified every time. For all calculations strict convergence threshold were used, applying the keywords *TightOPT* (when geometrical optimisation was required) and *TightSCF*. The RIJCOSX approximation with auxiliary basis set def2/J [284] was used in all cases to speed up the calculations. For all calculations we implied large grids using at least *Grid5* and *GridX5* for the RIJCOSX approximation. Two definitions of the B3LYP functional are available in ORCA, we always used the keyword *B3LYP/G* that remarks the B3LYP functional as defined on the software Gaussian.

All EPR simulations were done using the Matlab package Easyspin [247]. Solid state simulations were done using the function *pepper*, simulations in solution were computed with the function *chili*

although we found that using the function *garlic* with fictitious spin 1/2 would yield analogous results in much less time, simulations of pulse EPR were computed with the function *salt* and *saffron*. Whenever more than 5 nuclei with a full hyperfine diagonal tensor were included, we computed the simulations using the method *perturb* that is known to yield almost exact results but in much less time.

All the fitting of experimental data was carried out with the software Mathematica using a Levenberg-Marquardt algorithm.

Pentagonal Units in Graphenoids

3.1 Introduction

The manipulation of the honeycomb lattice introducing topological defects has seen a large theoretical investigation [183]. Predictions suggest that defects might not only modify the electrical property but also optical, mechanical, and magnetic features as a whole, though only in recent years it has been possible to rationally include defects [285]. Greatly improved results were then obtained using a bottom-up approach that allowed to synthetically produce structures that embed defects at precise locations. Such defects are confined in molecules whose extension is sensibly inferior to a graphene sheet, but provide a substantial model to study the effect of topology.

In this chapter, we study graphenoid molecules that include pairs of pentagonal defects. As exemplified by the schematic synthesis in fig. 3.1, the inclusion of pentagonal sites starts from a precise precursor. The defects are introduced at specific positions and the topology of the molecule can be controlled throughout the process. The inclusion of such defects produces a deviation from the planarity of the graphene lattice that yields a saddle shape as showed from simulated geometries in fig. 3.6 and fig. 3.13. The synthetic details and chemical characterisation of the molecules will not be discussed here and we refer to the published work: see [286] for **1**, [287] for **2-3**, and [288] for **4**.

According to the simple rules illustrated in chapter 1, we expect the molecules to show magnetic activity. As depicted in fig. 3.3, both Lieb's theorem and Clar's rule equally predict the presence of a paramagnetic state. According to Lieb's theorem, the lattice imbalance due to the pentagonal defects would produce a state with $S = 1$. Similarly, a resonant structure that admits two radicals at the pentagonal sites would have 8 aromatic groups instead of 6 in the non magnetic structure. According to Clar's rule, the additional aromatic groups provide energy to stabilise the triplet state.

In this chapter, we study four molecules hosting different numbers of pentagonal defects, and

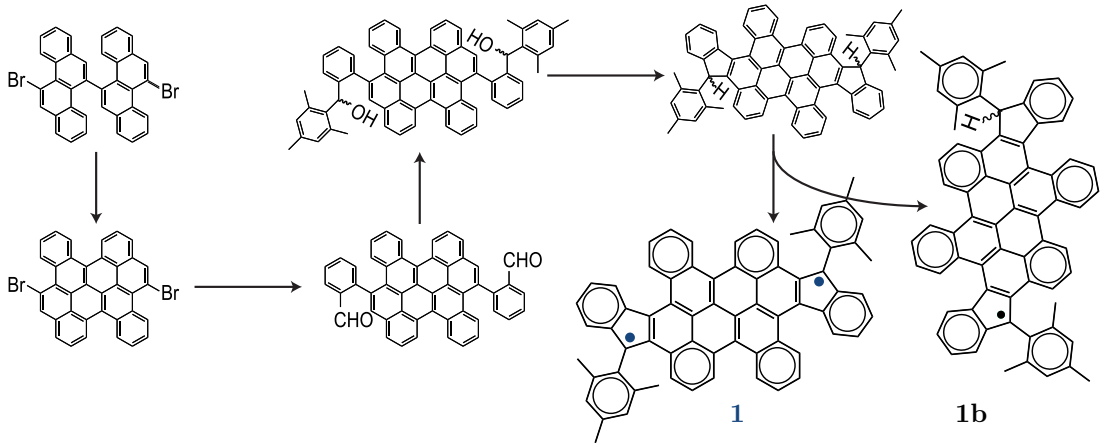


Figure 3.1: Schematics of the synthesis of **1**, for reaction conditions we refer to publications. In the last step of the synthesis, partial de-hydrogenation can result in production of **1b** at impurity levels.

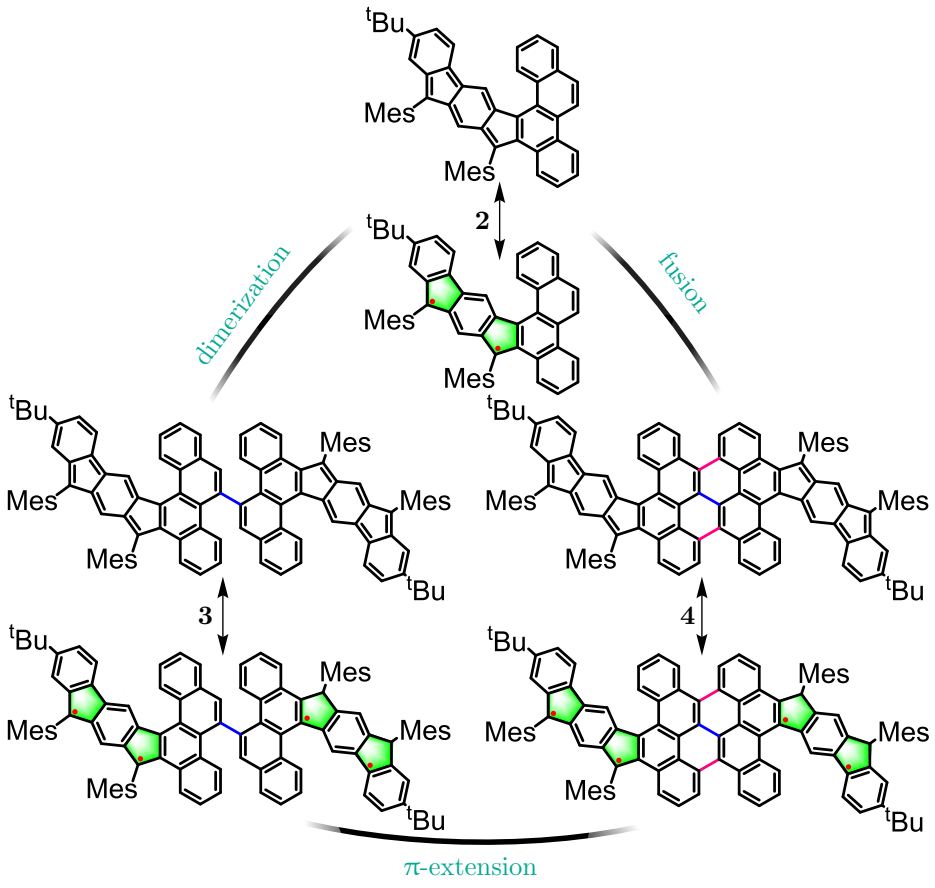


Figure 3.2: Molecular structures and relationship between monomer **2** and the two dimers **3** and **4**. For each molecule both the non-magnetic and the magnetic resonant structures are shown.

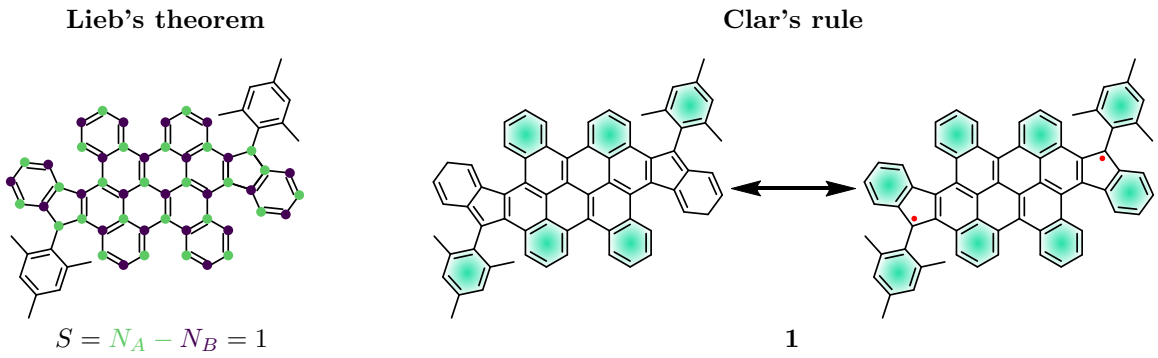


Figure 3.3: Equivalency of the Lieb's theorem and Clar's rule for the explanation of the magnetism of **1**.

with different topologies. In the first part of the chapter we discuss extensively the results for **1** only. Indeed, **1** was the first prototype of graphenoids, and it fuelled most of the studies in this thesis. In the second part of the chapter we compare the results for **2**-**4**. Molecules **2**, **3**, and **4** are related to **1** and mostly to each others in terms of shape and size. In ways that we are going to describe they are lower performing than **1**, but they give us the opportunity to probe their quantum properties, and establish structure-property relationship upon extension of their backbone.

3.2 Magnetic Properties

Figure 3.4A shows the EPR spectrum of **1** in powders at different temperatures. We observe a single peak of width 0.8 mT which proves the magnetic activity of **1**. Indeed, the linewidth (<1 mT) is incompatible with possible metal impurities, and the spectrum is analogous to the one reported for other graphenoids [193, 218, 220, 289]. Figure 3.4A also displays that the signal intensity changes when varying the temperature T. In Figure 3.4B we show the trend of the EPR integrated signal from fig. 3.4A. In absence of saturation (which we checked for) the integrated EPR signal is proportional to the magnetic susceptibility of the sample and instrumental parameters:

$$\text{EPR Signal} = \chi'' \eta Q \sqrt{P Z_0}, \tag{3.1}$$

where η is the resonator filling factor, Q is the Q-factor, P is the MW power, and Z_0 is the characteristic impedance of the transmission line [249]. Here χ'' is the imaginary part of the magnetic susceptibility that at 10 GHz frequency we consider $\simeq \chi$. In eq. (3.1) P and Z_0 are temperature independent, but we can expect both η and Q to have some indirect dependency on T. In this case,

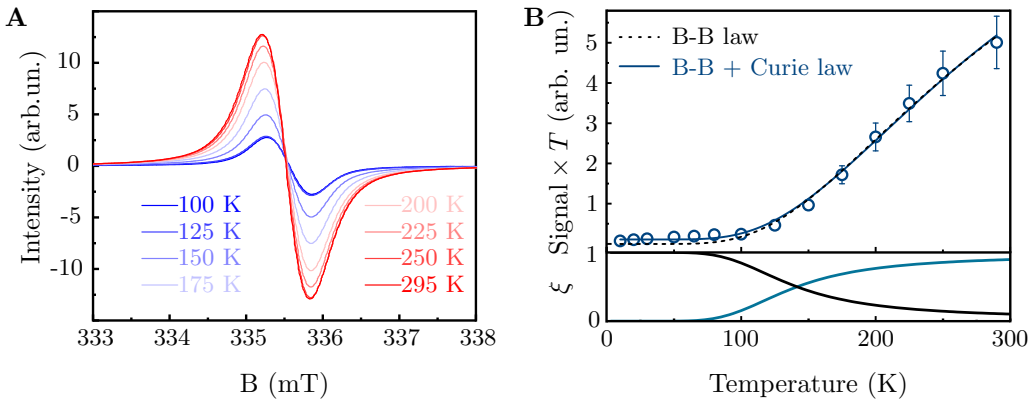


Figure 3.4: (A) Room-temperature CW spectra of **1** in powders and solution. (B) Temperature dependence of the integrated signal multiplied by the temperature and fit with the Bleaney-Bower's equation, and a combination of the Curie law and the Bleaney-Bowers' equation as discussed in the text. The inset shows the variation of the contribution of the EPR signal by **1** and **1b**.

using a powder is helpful, because the sample does not undergo phase transitions that might change its MW absorption, thus η should also be roughly constant. However, the resonator will expand due to thermal effects when increasing T which can produce oscillations of Q. The spectrometer software offers a tool to estimate Q based on the shape of the resonance dip, hence we estimated possible variations of Q on the order of 10%.

From fig. 3.4B we observe that the signal decreases when decreasing the temperature. We can exclude that the phenomenon is an artefact of possible oscillations of Q due to the magnitude of the effect (more than fivefold). This is compatible with a radicaloid with a singlet ground state and a triplet excited state that can be thermally populated. We can fit the data using Bleaney-Bowers' equation [290]:

$$\chi T = \frac{k}{3 + \exp(-J/k_{\mathrm{B}}T)}, \tag{3.2}$$

where k is a general constant that includes the EPR factors from eq. (3.1) and the constants from Bleaney-Bowers' equation, k_{B} is the Boltzmann constant, and J the exchange coupling. The best fit line yields $J/k_{\mathrm{B}} = -560$ K in thermal units. However, the signal does not completely disappear at low temperature, and even at $T < 10$ K it is still possible to observe a peak, while we according to Bleaney-Bowers' equation, at 10 K, **1** should be completely diamagnetic.

We attribute the signal at low temperature to a different paramagnetic species. In fact, the synthesis of such radicaloids has one often-overlooked feature: incomplete de-hydrogenation in the final step can lead to open-shell monoradical species (**1b**), at low concentrations, which are hard to identify by traditional structural characterisation methods. Presence of monoradical species has been

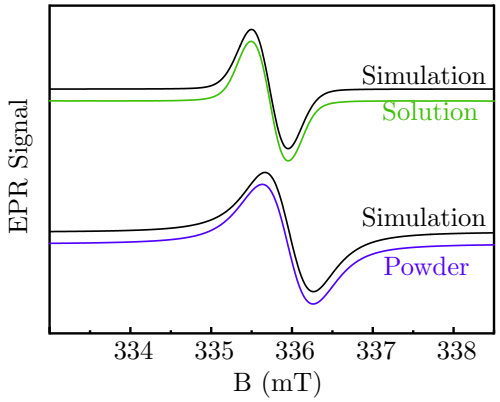


Figure 3.5: Room–temperature EPR spectra of **1** in powder and toluene solution. Black lines are simulations with the Hamiltonian in text.

reported in a few papers on similar compounds [232, 291]. Taking into consideration **1b**, we can improve the previous model including the effect of a spin $S = 1/2$ in the total magnetic susceptibility. We fit a weighted sum of the Curie law and Bleaney-Bowers' equation to the data in fig. 3.4 with the expression:

$$\chi T = k\left[\frac{\alpha}{8} + (1-\alpha)\frac{1}{3+\exp(-J/k_{\mathrm{B}}T)}\right] \tag{3.3}$$

where k is a general constant, and α is the fraction of **1b**. Keeping k, α, and J as free-fitting parameters we obtain $\alpha = 0.017$ and $J = -580$ K. As can be seen from fig. 3.4 the function that includes **1b** is a better fit than the pure Bleaney-Bowers' equation. Nonetheless, the value of 1.7% appears to be high. Such large quantity would have a sensible trace in high resolution mass spectroscopy and produce line broadening in structural NMR. Therefore, we will consider the value of α as an upper bound for the occurrence of **1b**.

Having established that **1** is a singlet radicaloid we can model the EPR signal with the following Hamiltonian:

$$\hat{H} = J\hat{\mathbf{S}}_{\mathbf{1}}\hat{\mathbf{S}}_{\mathbf{2}} + \mu_{\mathrm{B}} g B \hat{S}_z + \hat{\mathbf{S}}_{\mathbf{1}}\mathbf{D}\hat{\mathbf{S}}_{\mathbf{2}} + \sum_{i=1}^{N} \hat{\mathbf{S}}\mathbf{A}_i\hat{\mathbf{I}}_i \tag{3.4}$$

where, all the terms have been defined in chapter 1. Practically, some of the terms in the Hamiltonian have no effect on the appearance of the spectrum. The compound is in the high exchange limit $J \gg \omega_S$, so that the exchange coupling can be excluded from the simulation since no singlet-triplet transition is driven by the microwaves. We only observe one peak in the powder spectrum and we do not see any half-field transition even at the maximum power of the spectrometer. Therefore, the value of D must be limited, and also this term can be excluded from the simulations. We find as

upper limit $D < 1$ MHz. The absence of any structure in the signal also suggests that the hydrogen nuclei are weakly coupled and only contribute to increasing the signal linewidth.

We use DFT to simulate the geometry of **1** and its EPR parameters at the B3LYP/6-31G** level of theory. The simulated geometry and the spin density are showed in fig. 3.6, while the calculated parameters are displayed in table 3.1. The EPR spectrum shows no structure, therefore it is not really possible to verify if the simulated hyperfine parameters are truly representative of the molecule, but at least it is possible to say that they are coherent with the picture of weakly coupled nuclei.

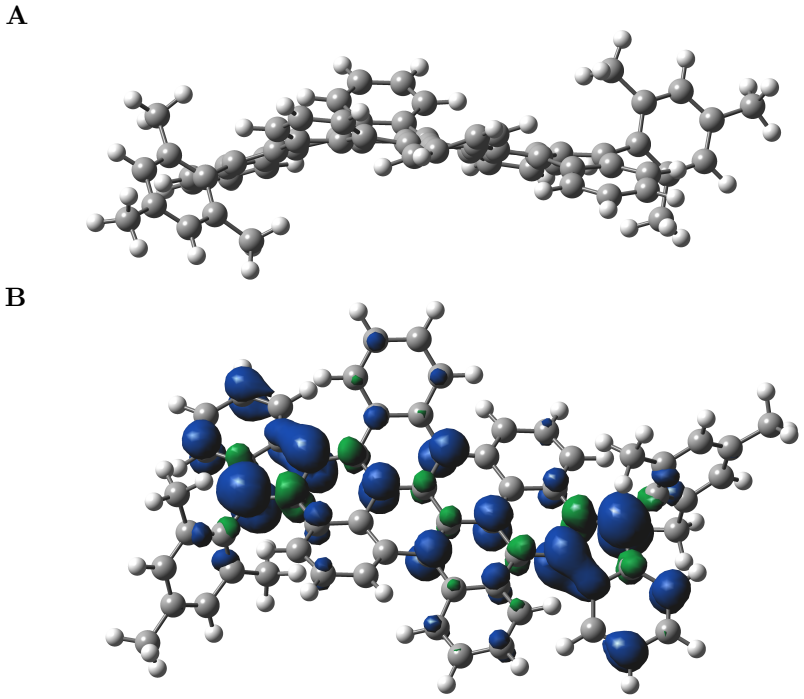


Figure 3.6: (A) Simulated geometry of **1** at the B3LYP/6-31G** level of theory. (B) Calculated spin density for a triplet state, iso value 0.002.

	Powder			Solution
	xx	yy	zz	Isotropic
S		1		1
g	2.0025	2.0027	2.0030	2.0027
$\mathbf{A}_1$ (MHz)	1.19	3.89	5.59	3.56
$\mathbf{A}_2$ (MHz)	1.90	4.55	5.14	3.86
$\mathbf{A}_3$ (MHz)	1.12	3.78	5.40	3.43
$\mathbf{A}_4$ (MHz)	1.88	4.57	5.03	3.83
$\mathbf{A}_5$ (MHz)	1.04	1.20	1.78	1.34
$\mathrm{lw}_{\mathrm{Lor}}$ (mT)		0.8		0.175
$\mathrm{lw}_{\mathrm{Gaus}}$ (mT)		0		0.315

Table 3.1: EPR parameters used for simulations of powder and solution spectra. All the hyperfine couplings and the g-factor are obtained by DFT calculations.

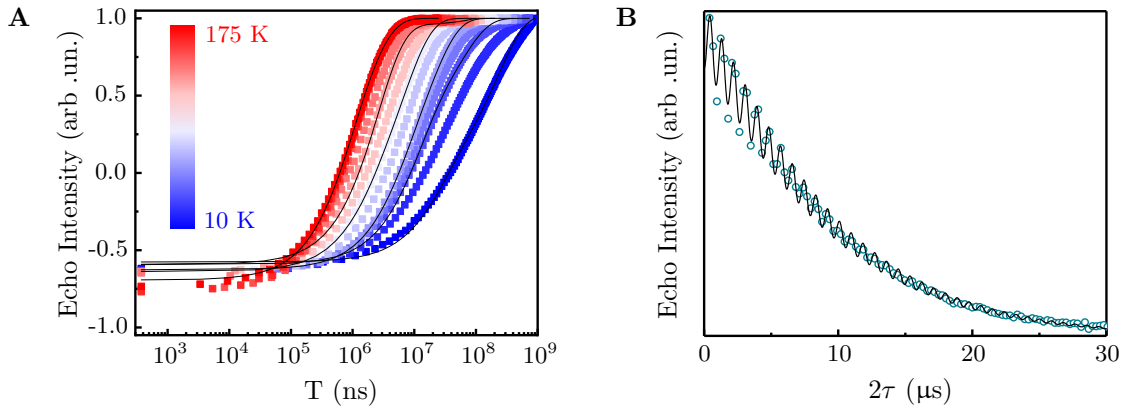


Figure 3.7: (A) Inversion recovery traces in toluene at different temperatures. Black lines are fit to the data with a bi-exponential recovery. (B) Hahn echo decay at 100 K in d_8-toluene. Black line is a fit with the model in text.

3.3 Quantum properties

In order to distinguish and quantify environmental effects on the quantum properties, we performed a complete examination in different conditions: powders, toluene solution (Tol), deuterated toluene (d_8Tol), and carbon disulfide (CS_2). All solution samples had a concentration of 2 mM. The different solvents offer multiple platforms to understand the decoherence mechanisms in the molecules. For example, toluene, d_8Tol and CS_2 present decreasing hyperfine contribution from the solvent nuclei.

We measured the quantum properties, T_1 and T_m, with inversion recovery and Hahn echo techniques respectively. In fig. 3.7 we show some traces obtained with the two techniques and their respective fits. In fig. 3.8 we present the summary of the relaxation times of **1**. We fit the inversion recovery trace with a bi-exponential decay that takes into consideration instantaneous diffusion as a faster decay. The spin-lattice relaxation rate T_1^{-1} increases monotonically when increasing the temperature. In solid state, molecules are closely stacked and the main limiting factors are intermolecular interactions and cooperative behaviours. In a diamagnetic matrix, intermolecular effects are strongly reduced and for low enough concentrations the molecules can be considered isolated. A three order of magnitude difference is observed between powders and diluted samples. We fit the d_8Tol data with direct and Raman processes in the temperature range 5-125 K [254]:

$$T_1^{-1} = A_{\text{dir}} T + A_{\text{Ram}} \left(\frac{T}{\theta_D}\right)^9 \int_0^{\theta_D/T} \frac{x^8 e^x}{(e^x - 1)^2} \mathrm{d}x \tag{3.5}$$

where A_{dir} and A_{Ram} are weights, θ_D is the Debye temperature, and x is an integrating variable of the transport integral.

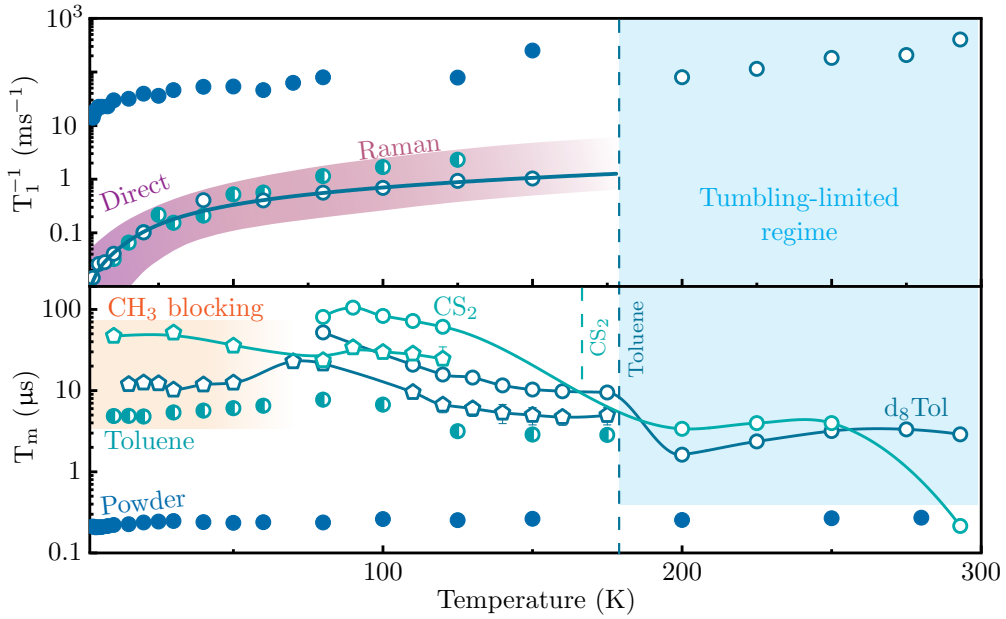


Figure 3.8: Summary of the relaxation times for **1** and **1b**. (Top) Trend of the spin-lattice relaxation rate with temperature. Solid symbols are powders, half-empty symbols toluene, and empty symbols are d_8Tol. The solid line is a fit to eq. (3.5). The dashed line marks the melting spot of toluene/d_8Tol. (Bottom) Trend of coherence time with temperature. Pentagons refer to the coherence time of **1b** while empty circles are for **1** in d_8Tol and CS_2. Lines are guide for the eye.

For the treatment of the coherence time, we adopt two separate fit routines in different conditions: for powders and toluene we fit with a mono-exponential in all temperature ranges; for d_8Tol and CS_2 we fit the T_m traces with a mono-exponetial in the range 5-70 K where the signal is dominated by **1b**, and in the range 150-293 K where the signal is dominated by **1**, but we use a bi-exponential where they coexist. In particular for the middle range we fit the function:

$$Y(2\tau) = A[\xi e^{-2\tau/T_{\mathrm{m1b}}} + (1-\xi)e^{-2\tau/T_{\mathrm{m1}}}] \tag{3.6}$$

where A is a fit constant, T_{m1b} is the coherence for **1b**, T_{m1} is the coherence of **1**, and ξ is the signal fraction as shown in fig. 3.4B:

$$\xi = \frac{\alpha}{\alpha + (1-\alpha)e^{J/k_{\mathrm{B}}T}} \tag{3.7}$$

with ξ fixed at every temperature, A, T_{m1b}, and T_{m1} free fit parameters. The parameter ξ is obtained purely according to the Boltzmann distribution. We acknowledge that an alternative formulation

could take into account the ratio of the magnetic susceptibility according to the Curie law for the monoradical, and the Bleaney-Bowers' equation for the diradical. The latter equation and eq. (3.7) only produce slightly different results.

The choice of fitting function respects the different EPR contributions of **1** and **1b** at different temperatures. However, the uncertainty on the value of J is carried over in ξ and increases the error on the evaluation of T_m, which is higher than a simple error from the fitting procedure. We argue that in toluene and powders the coherence time is limited which makes us unable to appreciate the difference between the two contributions. On the other hand, since we experience a much larger T_m in $d_8$tol and CS_2, we are able to distinguish the two species. In hindsight, also looking at the results in chapter 4, it might be possible that the bi-exponential behaviour would be better attributed to aggregation. Indeed, in the literature, bi-exponential decays in deuterated matrices and CS_2 were often explained by partial aggregation, and even with switching behaviours between mono-exponential and bi-exponential at different temperatures [255].

We highlight that we took into consideration the distinction between **1** and **1b** only when fitting the coherence time. The spin lattice relaxation time below 100 K is only related to the monoradical, and, accordingly, eq. (3.5) was formulated for an half-integer species (an integer species would have had an exponent equal to 7 in the Raman contribution [254]). In turn, the spin-lattice relaxation time observed between 100-150 K can be considered as an average between the parameters of the two species. We did not make the distinction in this temperature regime, because this would have required fitting an exponential recovery with four terms (including the fast decay), which would have easily resulted in overfitting.

As discussed in chapter 2, the Hahn echo decay is superimposed to an ESEEM signal that comes from the hyperfine coupling with the nuclei. This signal is always present in frozen solution, but it is averaged out in liquid solution due to molecular tumbling. We can fit the modulation as in fig. 3.7B multiplying the exponential decay by a term $1 + k_1 \cos(\omega\tau + \phi)$, where k_1 is the modulation depth, ω is the Larmor frequency of the nucleus, and ϕ a phase factor. If multiple nuclei are present, additional modulations can be taken into consideration by including other cosine terms at different frequencies.

In powders, the coherence time is roughly constant for the entire temperature range and the main limiting factor is provided by the close stacking of the molecules. In toluene and $d_8$tol, T_m slowly increases between 5-80 K with a peak at 80 K, it then decreases between 80 K and the melting point

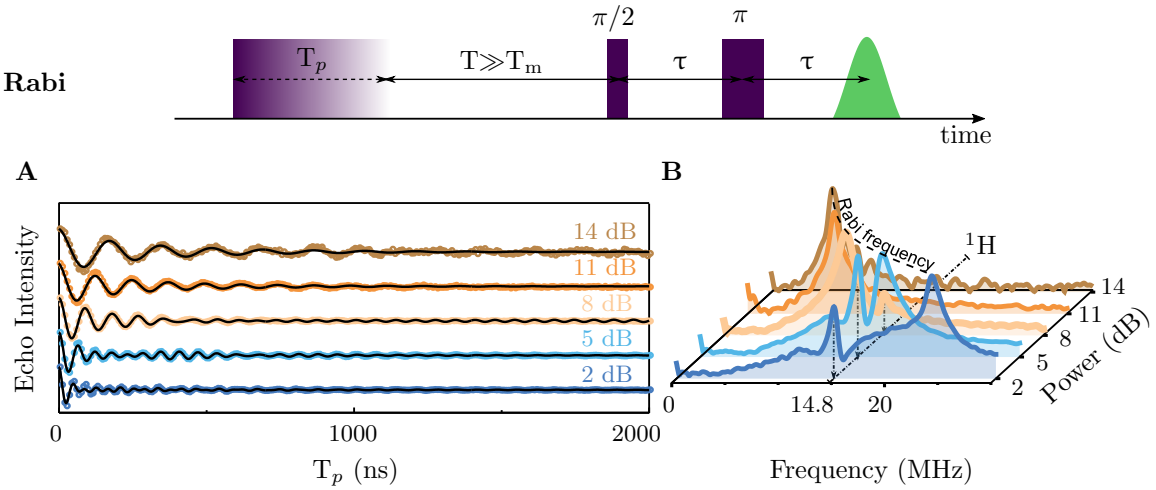


Figure 3.9: (Top) Sequence for detection of Rabi oscillations. (A) Examples of Rabi oscillations at 80 K in $d_8$tol. Different traces refer to different power attenuation used. Lines are fit to the data. (B) Fourier transform of the time traces in (A). The dashed line is a fit of the Rabi frequency with respect to the power used. The peak at 14.8 MHz refers to the Larmor frequency of hydrogen nuclei at the field of the experiment.

of the solvent, above which the system enters the tumbling limited regime. In CS_2, the coherence time remains roughly constant between 5-100 K, and then it possibly decays, although we do not have enough data points to follow its trend.

We attribute the 10-60 K temperature trend in tol and $d_8$tol to the hindered rotation of methyl groups. Methyl groups can tunnel through their rotational barrier with a temperature-dependent frequency. As the methyl group rotation can invert the nuclear spin state, it produces a resonant enhancement of the spin diffusion decoherence channel, as previously observed in methyl malonic acid and nitroxyl radicals at $T = 6 - 60$ K [292, 293]. The spin state of **1** is not only affected by the many methyl groups in the molecule but also, and possibly even in majority, by the ones in the solvent. Therefore, the effects of single methyl groups overlap, and do not produce distinguishable peaks in CW studies or ENDOR. The resonant enhancement is averaged out above 60 K, giving rise to the peak at 80 K. Since CS_2 has no methyl groups, it appears that the effect is absent.

Rabi Oscillations

In fig. 3.9 we show Rabi oscillations in $d_8$tol at 80 K, and analogous results were also obtained at 150 K. The Rabi frequency (also called nutation frequency) could be used as a fingerprint of the

multiplicity of the spin system. Indeed for a specific transition we can write:

$$\Omega(m_s, m_s+1) = \frac{g\mu_B B_1}{\hbar}[S(S+1) - m_s(m_s+1)]^{1/2}, \tag{3.8}$$

where B_1 is the strength of the MW field. For example, the ratio between the Rabi frequency of a triplet and a doublet would be $\sqrt{2}$. However, if the MW field strength is not selective all transitions can be excited and the nutation frequency becomes independent of S [26]:

$$\Omega = \frac{g\mu_B B_1}{\hbar}. \tag{3.9}$$

In other words, if B_1 is too strong with respect to the D so that both $|-1\rangle \rightarrow |0\rangle$ and $|0\rangle \rightarrow |1\rangle$ transitions are excited, it will be impossible to distinguish it from a doublet with $|-1/2\rangle \rightarrow |1/2\rangle$ [294]. We believe this is the situation in **1**, therefore we are unable to use nutation spectroscopy to confirm the multiplicity of the spin state.

Rabi oscillations also represent a proof that the electron spin can be initialised to any arbitrary state by the first pulse. We repeated the experiment at different powers to prove that the Rabi signal effectively comes from the spin, since it could also be an artefact of the cavity. Varying the field, the only parameter changing in eq. (3.9) is B_1 that we know is $\propto \sqrt{P}$, where P is the applied MW power. In fig. 3.9 we clearly see that the nutation frequency scales as $\sqrt{P}$, therefore we establish that the effect we see is not an artefact. It is also interesting to observe that an additional peak at frequency 14.8 MHz appears. We relate this peak to the Larmor frequency of the ^{1}H nuclei on the edge of the molecule. It appears that when the Rabi frequency is close enough to the Larmor frequency, nuclear transitions can be driven as well, this phenomenon is often referred as the Hartmann-Hahn condition [295]. This confirms once again the importance of nuclear spins and their detrimental effect to the coherence of our systems.

In fig. 3.9A, we also show a fit of the Rabi time trace. The fitting model that we used can be summarised with the following equation:

$$Y(T_p) = \sum \cos \Omega_i T_p e^{-T_p/\tau_i}, \tag{3.10}$$

where Ω_i refers to the peak frequencies observed in the Fourier domain, both the nutation frequency and ^{1}H Larmor frequency, and τ_i are decay time constants. It is known that Rabi oscillation decays

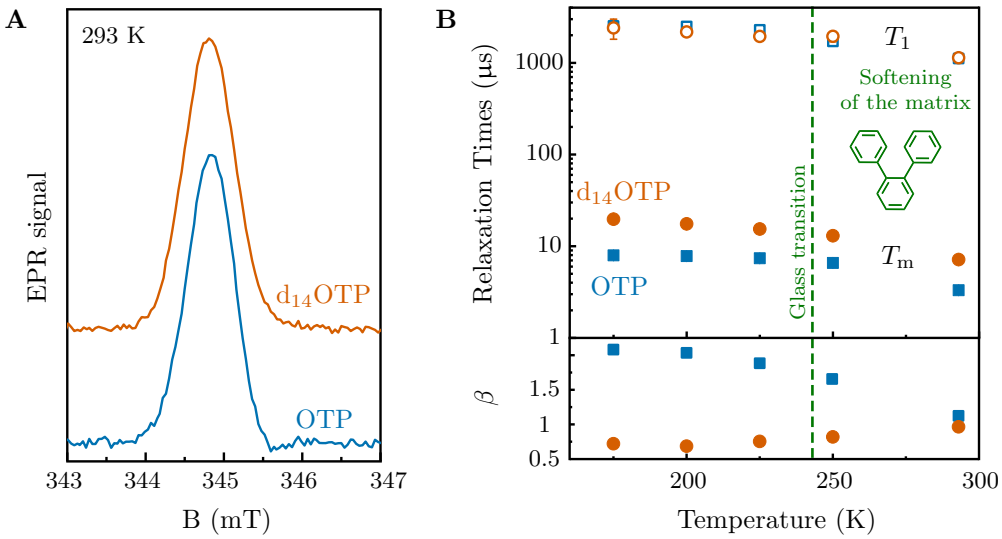


Figure 3.10: (A) Echo detected field sweep of **1** in OTP and d_{14}OTP at 293K. (B) Relaxation constants T_1 (empty symbols) and T_m (full symbols) in OTP (squares) and d_{14}OTP (circles) at different temperatures.

with time constants $\propto T_2^* \ll T_m$ and longer at lower applied power. Therefore, since the nuclear spins decay much slower than electron spins, different time decays should be assigned to their contribution. As a comment on the use of sinusoidal functions in the fit in eq. (3.10), the literature suggest that Bessel functions might be more appropriate, although the result would be very similar [296].

Ortho-terphenyl High Temperature Measurements

In addition to the previous measurements we also conducted more studies in the high temperature regime using samples in *ortho*-terphenyl (OTP) and deuterated OTP (d_{14}OTP). OTP has a melting point of 329 K, and therefore allows studying coherence up to room temperature in the solid state. We prepared two solution of 1 mM concentration and we degassed the samples with 5 cycles of freeze-pump-thaw before flame sealing the tubes.[1]

In fig. 3.10 we show the spectrum of **1** in the new matrices and the measured relaxation times. As we are in the high temperature regime we disregarded **1b** and fit T_m traces with a stretched exponential decay:

$$Y(2\tau) = A \exp\left\{ -\left(\frac{2\tau}{T_m}\right)^{\beta} \right\}. \tag{3.11}$$

As can be seen from fig. 3.10B, T_1 monotonically decreases with increasing temperature and there is negligible difference between the results in the protonated and deuterated matrix since nuclear effects

[1]The previous samples were not degassed which produces a difference in T_1 as also discussed later in this chapter.

have little impact on spin-phonon interactions. The trend of T_1 is also weakly temperature dependant which is common for a relaxation affected by a Raman process above the Debye temperature. Which means we can extend the treatment done in fig. 3.8.

T_m decreases with increasing temperature, with the difference between the two matrices owning to the lower gyromagnetic ratio of deuterium that produces an inferior nuclear-nuclear dipolar coupling, and therefore longer T_{m}. However, the most striking difference between OTP and d_{14}OTP is in the stretching parameter β which can be related to the main decoherence channel. In OTP, the stretch parameter $\beta \sim 2$ highlights that the main decoherence channel is NSD. While in d_{14}OTP $\beta < 1$ suggests that the main decoherence channel is provided by molecular motions. Above the glass transition temperature of the matrix, self rotation becomes relevant while transitioning into a viscous regime [297, 298] and the decoherence becomes dominated by matrix effects. As can be seen OTP and d_{14}OTP stretch parameters converge toward the same value because the two matrices are similar, except for the fact that d_{14}OTP has a larger inertia because deuterium is heavier than hydrogen.

3.4 Synthetic Tuning of Quantum Properties

Molecule **1** was the first example of coherence in molecular graphenoids. However, in order to engineer their quantum coherence behaviour, it is necessary to understand the relationship between the molecular structures and quantum properties. Here we show the structure-property relations of three related open-shell radicaloids **2**, **3** and **4**, developed from a common unit (fig. 3.2). The three molecular systems are tailored so as to investigate the effect of a different number of pentagonal defects, different degrees of conjugation, and different extension of the π orbitals. Compound **2** is the monomer, **3** and **4** are related to it because they contain two units of **2** linked by dimerization and fusion, respectively. In **3** two units of **2** are connected by single C-C bond, which results into highly twisting non-planar structure with a bichrysene subunit. In contrast to **3**, compound **4** is the π-extended derivative with larger degree of conjugation in which the two chrysene units are fused, possessing a stable singlet tetraradical character.

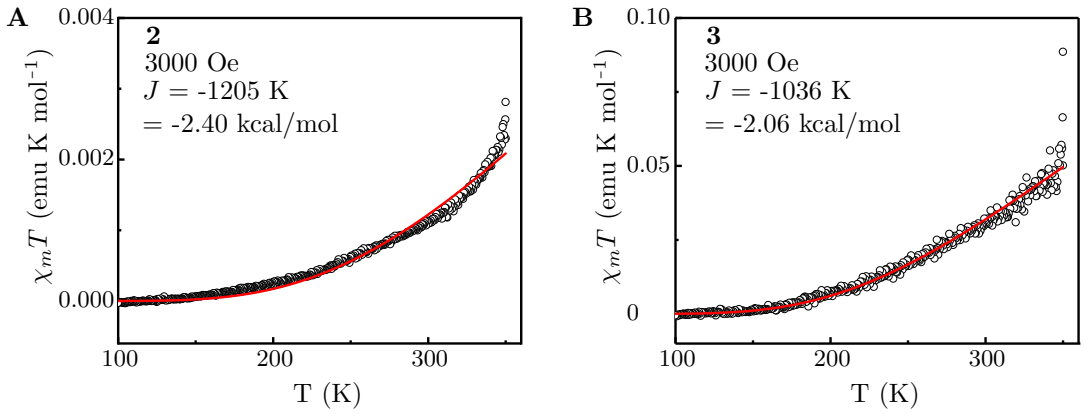


Figure 3.11: SQUID magnetometry $\chi_m T$ vs T for **2** and **3** at 3000 Oe. The red line is a fit to the equation in text. The data is cut at 100 K because low temperature measurements present an oxygen artefact.

3.4.1 Magnetic Properties

Variable-temperature direct current (dc) magnetic susceptibility data were collected by Dr Dimitris Alexandropolous on a Quantum Design MPMS-XL Superconducting QUantum Interference Device (SQUID) magnetometer equipped with a 7 T magnet. Continuous measurements were performed in 350-10 K temperature range, with a 3 K/min rate, under a dc field of 0.3 T. We measured 25.3 mg of sample **2** and 5.4 mg of sample **3** in powders. The diamagnetic contribution of the sample holder was subtracted from the raw data. Pascal's constants were used to estimate the diamagnetic corrections, which were subtracted from the experimental susceptibilities to give the molar paramagnetic susceptibilities (χ_m). The resulting $\chi_m T$ was corrected to remove the diamagnetic contribution of the sample and possible paramagnetic contributions of partially hydrogenated species: we performed a linear regression for which the angular coefficient would yield the diamagnetic constant and the y-axis intercept would yield the Curie constant or mono-hydrogenated paramagnetic species weighted for their relative abundance. Such contribution was removed from the signal to obtain the data in fig. 3.11.

For both **2** and **3**, $\chi_m T$ increased when increasing the temperature confirming the presence of a singlet ground state with a thermally excited paramagnetic state. We fit the signal with the the mass-corrected Bleaney-Bowers equation:

$$\chi_m T = \frac{N_A \mu_B^2 g^2 n}{k_B} \frac{1}{3 + \exp(-J/k_B T)} \tag{3.12}$$

where N_A is the Avogadro constant, and n is a mass correction parameter. The fit admitted the

two free parameters n and J. The correction n is related to the radical character of the molecules and needs to be included because of the diamagnetic correction. In fact, the mass measured for the sample from which we obtain the value χ_m is the sum of both the diamagnetic part of the sample and the singlet radical one. For **2** and **3** we obtain $n \simeq 0.05$ and $n \simeq 0.2$ confirming the modest radical character of the molecules. The fit also yielded the exchange coupling J that is equal to the singlet-to-triplet gap, for **2** we obtain J=-1205 K, and for **3** J=-1036 K analogous to previous reports for **4** of J=-1046 K [288].

As for **1**, EPR measurement in fig. 3.15 and 3.18 show signal down to 10 K where no signal is expected. We try to estimate the amount of partially hydrogenated species from the correction to $\chi_m T$. As mentioned, the linear regression gives us the value of C, the Curie constant for the half-integer species. From Curie's law:

$$C = \frac{nN_A\mu_B^2 g^2 S(S+1)}{3k_B}. \tag{3.13}$$

We obtained for **2** and **3** $C = 0.00078$ and $C = 0.0053$ emu K mol^{-1}, which solving for n gives 2×10^{-4} and 1.4×10^{-3} respectively. If we compare these values with the n obtained from the Bleaney-Bower's equation fitting, we can get the ratio of mono-hydrogenated species with respect to **2** and **3**, which yields 0.4-0.7% presence of impurities, which is also in line with the result obtained for **1**. Hence, if we consider a 0.5% probability of the dehydrogenation reaction failing, we identify two possible mono-radical species for **2** bearing one hydrogen in each pentagonal site. We identify two mono-radical species for **3** and **4** due to molecular symmetry. Bi-hydrogenated species of **3** and **4** might not be magnetic and tri-hydrogenated species come at very low probability ($< 10^{-6}$) and can be neglected. Mono-hydrogenated species dominate the signal between 10-160 K, they coexist with **2**-**4** in the range 160-250 K and they become negligible above 250 K when the contribution from the thermally populated states of **2**-**4** increases exponentially with T.

We can compare the J results obtained by variable temperature EPR and SQUID in fig. 3.4 and fig. 3.11. The measurement of χ with EPR as seen from eq. (3.1) is indirect, the instrumental parameters involved are very hard to estimate and would require an extremely careful calibration of the instrument. Additionally, the quantity measured is χ'' that can be considered equal to χ only in first approximation. Therefore, while the trend of the EPR signal is characteristic of the singlet ground state, extraction of J from the EPR usually tends to be an underestimate of the

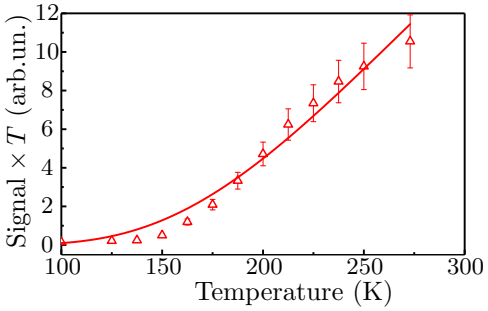


Figure 3.12: Measurements of integrated EPR signal times temperature at different temperature for sample **4** in powders. The solid line is a fit with the Bleaney-Bower equation from eq. (3.2).

true exchange coupling. SQUID measures directly χ and is in general more reliable. Nonetheless, EPR measurements are sensitive only to paramagnetic species, while SQUID is sensitive to both paramagnetic and diamagnetic ones. As it can be seen from the very low value of n the diamagnetic contribution has a massive effect on these samples. Therefore, the magnitude of the diamagnetic contribution introduces an error on J that can be difficult to estimate. In addition to this, SQUID requires a sizeable amount of sample in the mg, while for EPR fractions of mg are sufficient to have a good signal. Considering that the yield of the reactions is not large and sometimes it is very difficult to purify the sample, often is not practicable to use SQUID. On the other hand, EPR has also its own limitation. For example, eq. (3.1) is valid only in the regime where the EPR signal is not saturated, which is related to relaxation times as showed in eq. (2.3). We found that even in powders **2** and **3** have very long relaxation times and therefore the signal saturates even at the minimum instrumental power. Therefore, the variable temperature CW-EPR obtained for **1** could not be repeated for **2** and **3**, but variable temperature EPR measurements of **4** are showed in fig. 3.12, which did not show any EPR line saturation. Fitting with eq. (3.2) yields $J = -779$ K, which is roughly 20% off from the value measured with SQUID in [288], showing good agreement between the two techniques.

Previous attempts in tuning the exchange coupling by means of π extension have been reported in rylenes [220]. Recently Dressler and co-workers have tried to rationalise trends in exchange coupling by means of bond order and making large use of simulations [299]. Molecules **1**-**4** are not the most suitable systems to replicate those studies, as this was also not our intention. Indeed, π extension is accompanied by the introduction of additional defects and admixtures of tetraradical states that complicate a clear analysis of the exchange coupling behaviour. Overall, we establish a trend for the four molecules: $J_1 < J_2 \approx J_3 < J_4$. Intuitively, the value of J depends on the overlap of the wavefunctions of the two different spins. Thus, we can refer its value to the distance between the

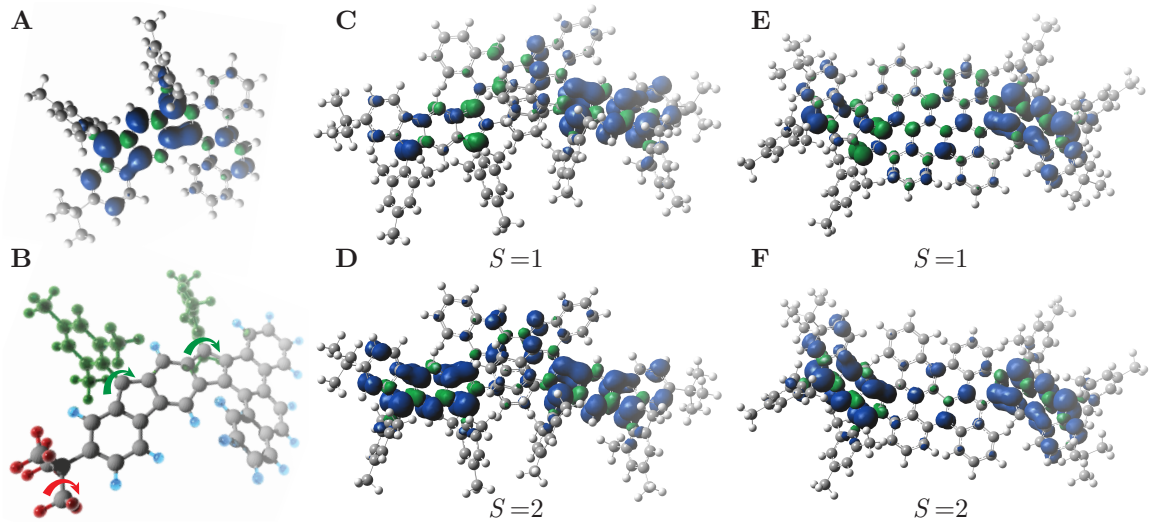


Figure 3.13: (A) Calculated spin density of **3** in the triplet state, iso value 0.002. (B) Simulated geometry of **3**, highlighted in red are the hydrogens that contribute to methyl rotation, in green the hydrogen that contribute to mesithyl rotation, and in blue the hydrogens that do not participate to molecular motions. (C) Calculated spin density of **3** in the triplet state, iso value 0.002. (D) Calculated spin density of **3** in the quintet state, iso value 0.002. (E) Calculated spin density of **4** in the triplet state, iso value 0.002. (F) Calculated spin density of **4** in the quintet state, iso value 0.002.

pentagonal sites (as can be seen from fig. 3.6 and 3.13 the large majority of the spin density in the four molecules is concentrated around the pentagonal defects). In **2** the two pentagons are the closest, therefore J_2 has the largest value. In **3** and **4** different exchange couplings could be defined since there are multiple pentagons. However, as seen from fig. 3.13, in the triplet state the spin density is mostly concentrated in one lobe of the molecule, which, in turn, dominates the measured J. In the lobe, the distance between the pentagons is the same as in **2**, but the extended backbone facilitates delocalisation of the wavefunction in the other lobe, reducing overlap. Hence, $J_3 \approx J_4 < J_2$. Finally, in **1** the two active pentagons are the farthest apart, and J_1 has the lowest value.

We model the spin properties of **2**-**4** with the Hamiltonian in eq. (3.4). In fig. 3.13 we show the spin densities calculated at the B3LYP/6-31G** level of theory for the three molecules in their possible spin states. Figure 3.14A shows the continuous wave (CW) X-band EPR spectra of compounds **2**, **3** and **4**, as acquired at room temperature in solution and powders, and fig. 3.14B highlights the differences among their solution spectra. The choice of solvent does not modify the CW EPR spectrum, and thus only toluene is shown, for simplicity. For all three compounds we obtain $g = 2.0027$, which is comparable to **1** and other open shell PHs in the literature and with the prediction of weak spin-orbit coupling in carbon nanostructures.

The hyperfine contribution is largely unresolved in the powders except for two shoulders in **2**. This

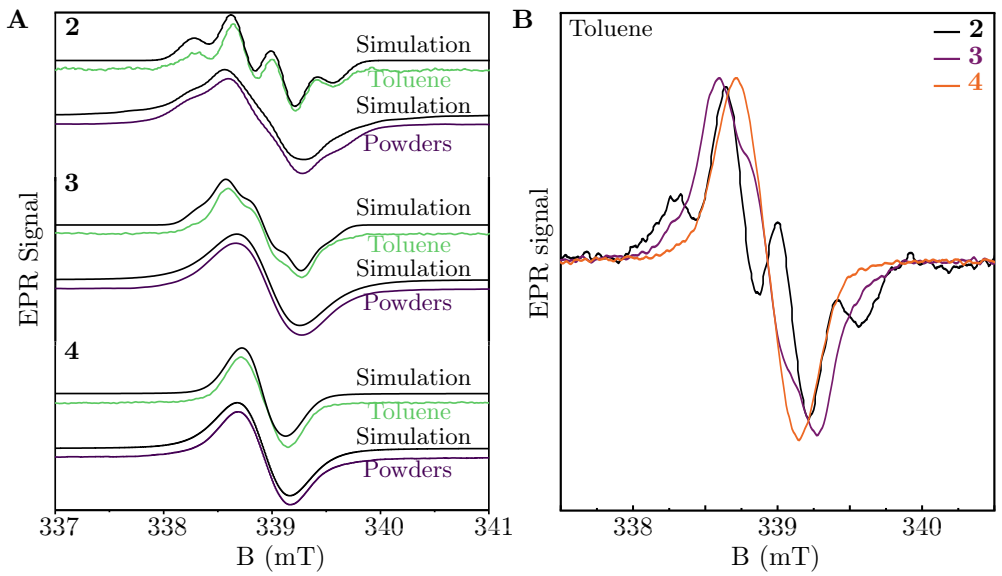


Figure 3.14: (A) CW spectra of **2**-**4** in powders and toluene solution with respective simulations. (B) Direct comparison of the solution spectra of **2**-**4**. The different width of the spectra is a consequence of different hyperfine couplings in the three molecules. **2** has the largest hyperfine coupling constants and the widest spectrum, while **4** has the smallest couplings and the narrowest spectrum.

		DFT	Experiment
2	A_1 (MHz)	10.5	10.5
	A_2 (MHz)	5.1	8
	A_3 (MHz)	4.1	8
	A_4 (MHz)	3.8	4
3	A_1 (MHz)	10.3	6.2
	A_2 (MHz)	4.8	6.2
	A_3 (MHz)	4.5	6
	A_4 (MHz)	3.8	6

Table 3.2: Isotropic hyperfine parameters for **2** and **3** from DFT and used in the simulation of the experiment.

is linked to the presence of several hydrogen nuclei on the compound edges that are weakly coupled to the electron spin and cannot be distinguished, and thus merely increase the signal linewidth. In liquid solutions the averaging produced by molecular tumbling hides trends in the anisotropy and dipolar coupling. However, dilution reduces the individual linewidth and we are able to distinguish an isotropic hyperfine contribution for both **2** and **3**. In section 3.4.1 we display the hyperfine parameters obtained by DFT and the ones used in the simulation. We dismiss the parameters for **4** as it does not present any structure. We observe a discrepancy between the calculated parameters and the ones that produce the best fit with the experimental data. It appears that such difference cannot be solved by scaling all the parameters by a constant factor. In solution, the width of the CW

spectra is only determined by the strength of the isotropic hyperfine coupling, which can be used as a fingerprint of the delocalization of the electron spin over the whole molecule. The delocalization of the spin is strongly correlated to the size of the molecule, so that the smallest molecule, **2**, would also show the smallest degree of delocalization. However, **3** and **4** have comparable size but differ in conjugation degree. The hyperfine coupling in **3** is much larger than in **4** showing that in the former the electron spin is mostly delocalized on one lobe, while in the latter it is delocalized over the entire molecule due to the extended conjugation.

3.4.2 Spin-lattice Relaxation

In fig. 3.15 we show the dependence of T_1^{-1} on T for **2-4**. The T dependence of the relaxation times was measured from room temperature down to 10 K for **2**, **3** and **4** in all solvents. Measurements on powders are not shown, because in the absence of sufficient dilution the systems were dominated by instantaneous diffusion.

From fig. 3.15, we observe that changing matrix has a minimal impact on T_1^{-1} when in the solid state. Solvents introduce local variations such as different solvent size or viscosity that mildly affect spin-lattice relaxation, while deuteration of the matrix seems to have an even smaller effect. Therefore, we describe spin-lattice relaxation mostly due to intramolecular modes with limited effects from the environment. The trends of T_1^{-1} vs T show the presence of several dominant mechanisms for various temperature regimes and different matrix conditions. In the low temperature regime we fit the d_8Tol results with the same expression of eq. (3.5), with the results referring to the mono-hydrogenated species.

Above the melting points of the solvent, the spin-lattice relaxation is dominated by tumbling. We fit the d_8Tol data for **2-4** with a model developed for nitroxyl radicals that includes contribution of three different phenomena [300, 301]:

$$\frac{1}{T_1} = \frac{1}{T_1^{SR}} + \frac{1}{T_1^{END}} + \frac{1}{T_1^{SD}}. \tag{3.14}$$

The first term describes the relaxation due to modulation of g-anisotropy due to tumbling:

$$\frac{1}{T_1^{SR}} = \frac{\Delta g}{9\tau_c}; \quad \Delta g = (g_x - g_e)^2 + (g_y - g_e)^2 + (g_z - g_e)^2 \tag{3.15}$$

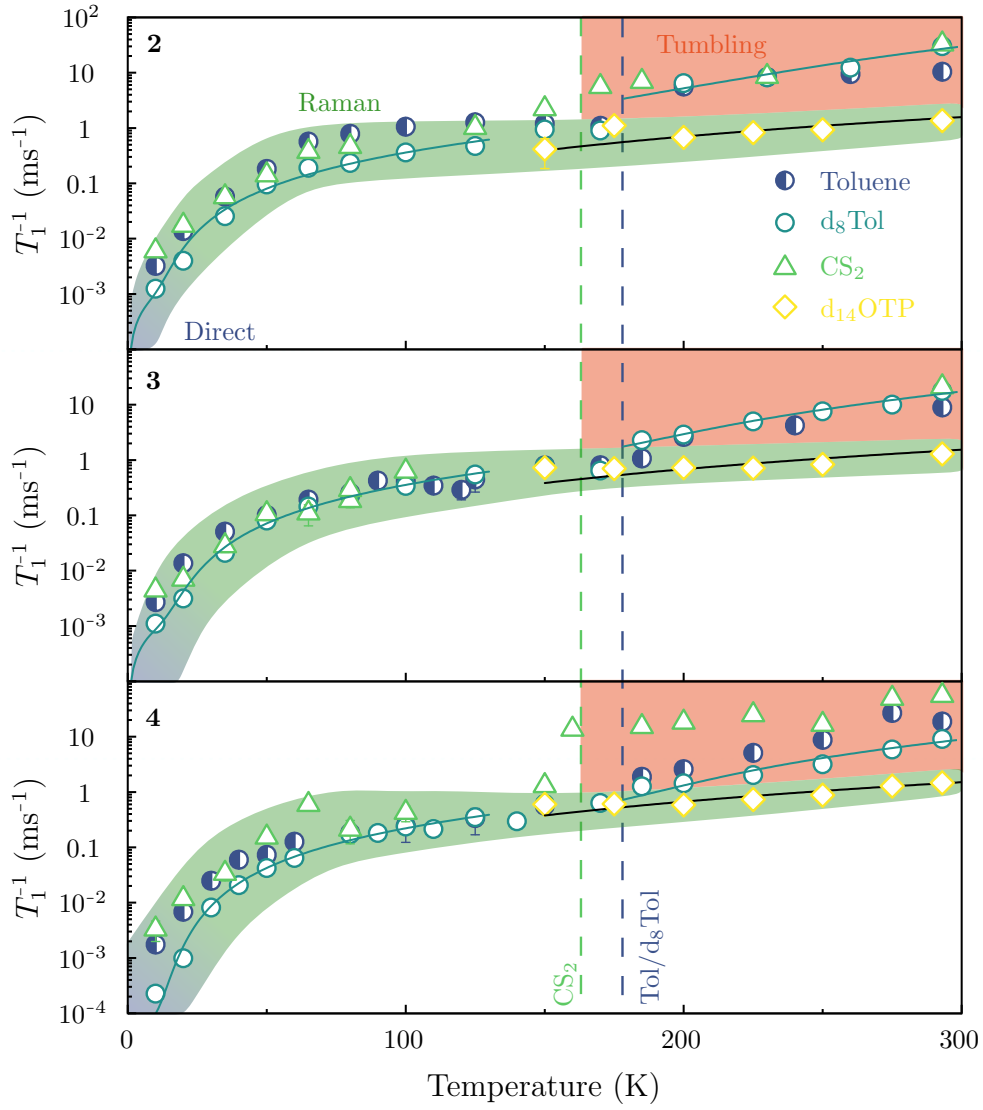


Figure 3.15: Spin-lattice relaxation rate for **2** (top), **3** (middle), and **4** (bottom). Half-circles are toluene, empty circles d_8Tol, empty triangles CS_2, and empty diamond d_{14}OTP. Solid lines are fit to the model described in text. Dashed lines indicate the melting point of the solvents. Shaded areas refer to main relaxation mechanisms.

where g_e is the free electron value, and τ_c the tumbling correlation time that can be expressed using Einstein-Stoke equation depending on the hydrodynamic volume of the molecule V and the viscosity of the solvent η:

$$\tau_c = \frac{V\eta}{k_{\mathrm{B}}T}. \tag{3.16}$$

The second term describes relaxation due to modulation of anisotropic hyperfine coupling:

$$\frac{1}{T_1^{END}} = \Delta A \frac{\tau_c}{1+(\tau_c\omega_e)^2}; \quad \Delta A = (A_x - A_{\mathrm{iso}})^2 + (A_y - A_{\mathrm{iso}})^2 + (A_z - A_{\mathrm{iso}})^2. \tag{3.17}$$

The third term describes the diffusion of the electron spin through the nuclei of the solvent:

$$\frac{1}{T_1^{SD}} = R_{SD}\left(\frac{2\omega_e\tau_c}{1+(\omega_e\tau_c)^{3/2}}\right)^{1/4}, \tag{3.18}$$

where R_{SD} is a rate constant. We fit the model with two free parameters: R_{SD} and V. We calculate Δg and ΔA from EPR parameters of DFT calculations. We use published data for the viscosity of toluene [302]:

$$\eta(T) = 554.2 \times 10^{-6}\exp\left(-5.2203 + \frac{8.964}{T/293.15} - \frac{5.834}{(T/293.15)^2} + \frac{2.089}{(T/293.15)^3}\right) \tag{3.19}$$

which was obtained by measurements at ambient pressure. If we take the dimensions of the simulated geometry from DFT and assume, in first approximation, that the hydrodynamic volume of the molecules can be approximated as a sphere, we can heuristically check if the fit parameter V gives a reasonable value. From the values in table 3.3 we see that there is a difference of roughly a factor 10 between V and V_{sphere}. Since our samples are degassed and flame sealed to a base pressure of 1×10^{-2} Pa, the viscosity of the solvent will likely be overestimated by eq. (3.19), that reflects in underestimating the free fit parameter V. Nonetheless, the fit results are consistent with $V_2 < V_3 < V_4$.

For d_{14}OTP we can explore the effects on T_1 in a solid matrix at high temperature. For all samples in d_{14}OTP, T_1 is only weakly temperature-dependent at $T > 150$ K. We obtain a good fit with the model of the Raman process at temperatures above the Debye temperature [301]:

$$T_1^{-1} = C_{\mathrm{Ram}}T^2 \tag{3.20}$$

	2	**3**	**4**
$\Delta g^{\dagger}$	4.36×10^{-7}	8.41×10^{-7}	8.63×10^{-7}
$\Delta A^{\dagger}$ (Hz^2)	149×10^{12}	164×10^{12}	163×10^{12}
$V^{\dagger}_{\text{sphere}}$ (m^3)	277×10^{-30}	645×10^{-30}	920×10^{-30}
V^{*} (m^3)	$13(3) \times 10^{-30}$	$45(6) \times 10^{-30}$	$91(12) \times 10^{-30}$
R^{*}_{SD} (Hz)	$2.7(1.5) \times 10^{3}$	$1.6(0.7) \times 10^{3}$	$6.5(4.0) \times 10^{2}$
C^{*}_{Ram} (Hz K^{-2})	0.018(3)	0.017(3)	0.017(2)

Table 3.3: Parameters used for T_1^{-1} fit with the expression in text, and fit results. † from DFT calculations; * from fit.

where C_{Ram} is a free parameter. This indicates that, radicaloids display no contribution from local or Orbach modes, and the main process for T_1 remains a Raman one up to room temperature. More importantly, a T_1 of around 1 ms is observed up until room temperature in an immobilised matrix without any particular engineering of the molecule. This is at least two orders of magnitude larger than the best metal-centre molecular qubits reported in the literature. We argue that carbon-based radicaloids present a naturally optimal structure to achieve very large T_1 even at high temperatures. The presence of light elements (C, H) limits the contributions of spin-orbit coupling that mediates the spin-phonon exchange, and despite the presence of a curvature, that might enhance the g-anisotropy, the g value for all molecules is both very close to the free electron value of 2.0023 and also largely isotropic.

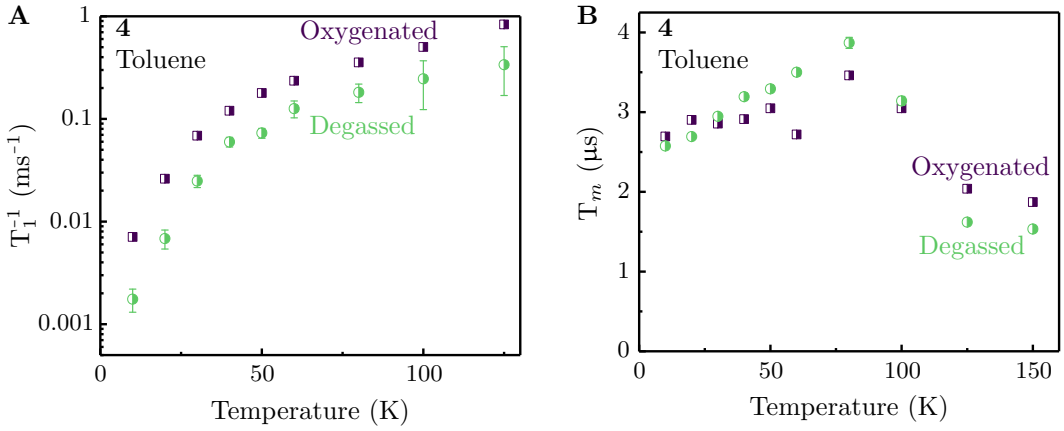


Figure 3.16: (A) T_1^{-1} comparison between ambient pressure oxygenated sample (half squares) and degassed and flame sealed sample (half circles) for compound **4** in toluene. (B) T_{m} comparison between oxygenated and degassed sample.

Comparing the results **1**-**4**, we observe that at low temperature T_1 for **1** is roughly one order of magnitude faster than in the other molecules. This is due to the fact that the samples of **1** were not degassed. As it can be seen in fig. 3.16 for **4** in toluene, degassing contribute to a factor 10 in T_1,

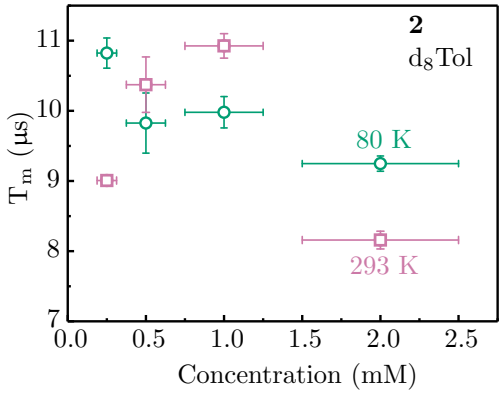


Figure 3.17: Concentration dependence of T_m for **2** in d_8Tol at 80 K and 293 K.

while it does not affect T_m. In addition to this, the samples of **1** in OTP and d_{14}OTP were degassed and their T_1 is analogous to **2**-**4**.

3.4.3 Coherence Time

We fit all the Hahn echo traces with a monoexponential decay except for the ones in CS_2. CS_2 is not a glass-forming solvent, crystallisation with separation of phases is possible and it has been reported before in the EPR literature [79, 303]. We observe a very quick initial decay that we fit with a bi-exponential to include the aggregate and the completely dissolved molecules:

$$Y(2\tau) = A\left(0.8e^{-2\tau/T_{\text{fast}}} + 0.2e^{-2\tau/T_m}\right). \tag{3.21}$$

The use of fixed coefficients for the two decays is only to facilitate comparison amongst different compounds. However, we note that the aggregate part has a much higher weight hiding the true decay which makes the CS_2 data less meaningful.

As said above, the solutions were prepared with concentration of 2.0 ± 0.5 mM, which can in general be high for such measurements. However, we have to consider the following. First, as seen from the SQUID, not all the molecules are in the magnetic state. Second, even for the molecules in the magnetic state, at any temperature, a majority will still be in the singlet ground state. Therefore, 2 mM is only a nominal concentration, while the true spin concentration could well be one order of magnitude smaller and variable with temperature. Nonetheless, as seen with CS_2 it might be possible that there are aggregates of molecules that contribute to lower the coherence. We tested this hypothesis for **2** in d_8Tol as shown in fig. 3.17. It can be seen that effectively the higher concentration

has the lowest coherence time. However, the increase is not monotonic and only about 10-20%. In general, it seems that the effect of concentration is not striking, while the reduction in signal-to-noise ratio was conspicuous. Therefore, we chose not to lower the concentration.

In fig. 3.18 we show variable temperature characterisation of T_m. For measurements in Tol, d_8Tol, and CS_2, T_m is largely constant in the range 10-60 K and presents a peak around 80 K. We attribute this trend to tunnelling of frozen methyl groups as discussed for **1**. Between 80-170 K the coherence has a non-monotonic trend with a minimum at 130 K and an increase at higher temperature until the melting point of the solvent. As the minimum is common to all three solvents, decoherence is more likely be attributed to intramolecular motions which might be facilitated by the softening of the matrix.

Here the steep decay in T_m and the recover above 130 K are to be attributed to molecular motions of methyl groups. A 120° rotation of a methyl group around the C-C bond brings a proton in the position of another proton. Since the three protons of a methyl group are generally inequivalent, the change of position also produces a change in hyperfine coupling. The EPR literature has showed that when the rotation rate is equivalent to the difference in anisotropic hyperfine interaction upon position switch, the decoherence is maximum. This was observed for instance in Cr complexes [304], Cu complexes [305], and organic radicals [255, 306], which all see a minimum of T_m in the range 100-140 K due to motional degrees of freedom that become available [307].

Here, we used the DFT simulation of hyperfine couplings to calculate the average difference in anisotropic hyperfine couplings of the methyl groups. For example, **2** has 9 methyl groups, following the approach of Barbon *et al.* [308], we can calculate the hyperfine coupling difference between proton i and proton j in a methyl group:

$$\Delta A = \sqrt{(A_i^x - A_j^x)^2 + (A_i^y - A_j^y)^2 + (A_i^z - A_j^z)^2}. \tag{3.22}$$

By averaging over all the difference in all the methyl groups we get for **2**: $\Delta\bar{A} = 0.4 \pm 0.2$ MHz. If we consider an Arrhenius behaviour, a rotation of a methyl has a time constant of $\tau_R = \tau_0 \exp(E_a/k_B T)$. Maximum decoherence is obtained when the rotation rate is equal to the anisotropic hyperfine difference, therefore we have that at 130 K $\tau_R^{-1} \approx 2\pi\Delta\bar{A} \approx 2.5$ MHz. Assume that τ_0 is the correlation time at infinite temperature we can reasonably approximate $\tau_0 \approx 10^{-12}$ s, and from the Arrhenius equation we find the energy barrier of the process $E_a \approx 3.3$ kcal/mol which is comparable with

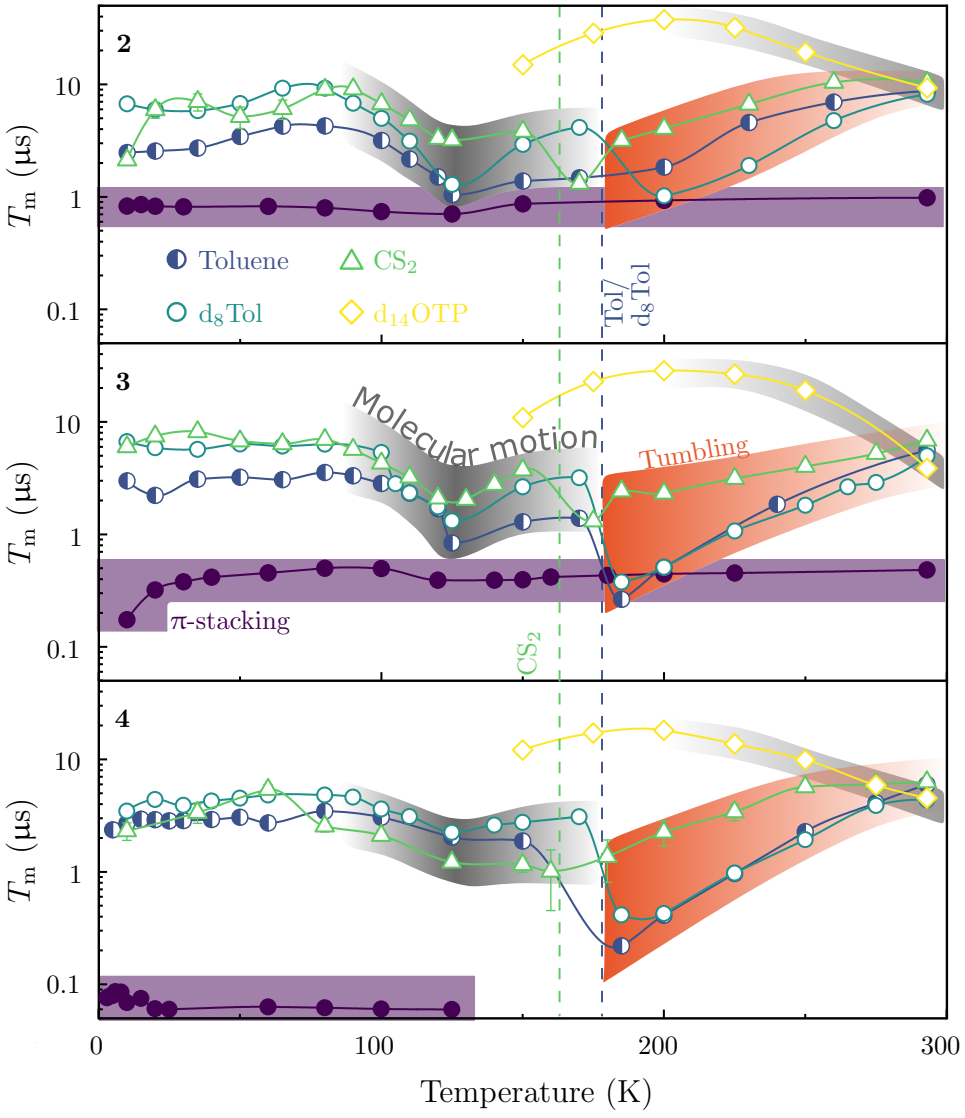


Figure 3.18: Coherence time for **2** (top), **3** (middle), and **4** (bottom). Full circles are powders, half-circles toluene, empty circles d_8Tol, empty triangles CS_2, and empty diamonds d_{14}OTP. Lines are guides for the eye. Dashed lines indicate the melting point of the solvents. Shaded areas refer to main relaxation mechanisms.

literature data [304, 309].

In the liquid state, at higher T, the decoherence is dominated by tumbling. We can use the tumbling correlation time τ_c extracted from the T_1 fit to understand the T_m trend in this regime. In the viscous regime, just above the melting point of the solvent, we obtain that $\tau_c \approx 1/\omega_S$. As the tumbling occurs on the same timescale of the spin precession, its effect is maximized, and coherence is low. With increasing temperature tumbling becomes faster and off-resonance with spin precession, hence the coherence time increases monotonically. This phenomenon is commonly seen in CW spectra of some organic radicals and denoted motional narrowing. When dynamics processes become faster than the timescale of electron resonance, the linewidth of the EPR signal narrows. This argument is quantitatively supported by three observation. First, coherence times in toluene and $d_8$tol are largely similar if not the same since they have analogous viscosity and therefore produce analogous correlation times. Second, T_m is always larger in CS_2 because it is less viscous than toluene, hence the correlation time is faster, and the molecule enters the fast tumbling regime at lower temperatures. Third, T_m of **2** is larger than **3** and **4** because its dimensions yield a smaller hydrodynamic volume that consequently produce a faster correlation time.

In-solution trends have little applications in quantum information processing, but they might prove useful for biological use. Nevertheless, a solid proof of the performance of the radicaloids in solid state up to room temperature is provided by the data in d_{14}OTP. In a solid deuterated matrix we observe a peak at 200 K, record T_m of 38 µs for **2** at 200K, an unprecedented result for molecular systems that can only be equaled by the high temperature coherence of N@C_{60} [310]. The steep decrease in coherence time at higher temperature bears again the fingerprint of molecular motions. Since the matrix has no methyl groups, we can restrict molecular motion effects to the graphenoids only. While methyl rotations are already too fast and averaged out at this temperature, bulkier mesityl groups might become free to rotate around the C-C bond, similar to the effect of phenyl groups in polystyrene around its glass transition [311].

3.5 Outlook

In this chapter, we studied the magnetism and quantum properties of 4 molecules with a common core unit and a similar saddle shape produced by the inclusion of pentagonal defects in their lattice. We showed that topological inclusion of five-membered rings in a honeycomb lattice results in the

availability of free pairs of spins. As also showed by another recent paper in the literature [312], defect engineering in GNRs is a viable tool to tailor the bandgap, and the magnetism of carbon structures.

In terms of magnetic properties, we can use the open-shell character index, y to compare the molecules. The index can be calculated from quantum chemistry simulations [313]:

$$y = 1 - \frac{2T}{1+T^2}, \tag{3.23}$$

where T is the orbital overlap between the highest occupied molecular orbital (HOMO) and lowest unoccupied molecular orbital (LUMO) of the singlet state:

$$T = \frac{n_{\mathrm{HOMO}} - n_{\mathrm{LUMO}}}{2}, \tag{3.24}$$

where n_i are natural orbital occupation numbers that can be calculated with DFT or Hartree-Fock theory. An analogous definition can be extended for polyradical character considering higher occupied orbitals. The index describes the contribution of the open-shell structure to the final wavefunction, for example $y = 1$ indicates a completely open-shell molecule. From our collaborator's simulations, we have that the biradical character are in order: 0.69, 0.17, 0.21 and 0.22; while the tetraradical character for **3** and **4** are 0.08 and 0.21 respectively. In the SQUID we had related this property to the value of the mass correcting parameter n, and effectively we observe that **2** and **3** have very weak open-shell characters. In addition to this, **1** has the lowest J coupling which means that at any reasonable temperature its triplet state will be much more populated than the other three molecules. Overall, from magnetic experiments, we conclude that **1** is the most performing molecules of the 4.

Even though **2**, **3**, and **4** are weakly magnetic, they do allow proof of principle and understanding of the change in quantum properties. In terms of T_1, it is hard to make comparison across the entire set since the majority of **1** samples were not degassed. Nonetheless, the 4 d_{14}OTP samples were all degassed and they work as a good testbed. Comparing the spin lattice relaxation time for **1** in fig. 3.10 and for **2**, **3**, **4** in fig. 3.15 we observe that the trend is analogous and all 4 molecules reach T_1 of about 1 ms at room temperature.

In terms of coherence time, d_{14}OTP is again a good platform for comparison. If we fix the observation at 200 K, where we generally hit the peak in T_{m}, we can produce a ranking of longest

coherence time, in order: **2**, **1**, **3**, and **4**. The differences are not dramatic but we can explain them in relations to the two main channels of decoherence: nuclear spin diffusion and molecular motion.

First, discussing NSD, **1** and **2** have the lowest number of hydrogen atoms: 44 and 46 respectively, while **3** and **4** have 90 and 86. The mere number of components of the nuclear bath is not the only criterion to explain the strength of nuclear spin diffusion. Indeed, as discussed in chapter 1, the strength of the hyperfine coupling plays a role in blocking nuclear flip-flops: nuclei that are more strongly coupled will flip-flop less often. An intuition already expressed in the literature of molecular spin systems is the presence of a nuclear spin diffusion barrier. The nuclei closer to the spin center are so strongly coupled to the spin that they are less likely to produce flip-flops leading to decoherence. And we can see this is the situation for example for **1** and **2** first and **3** and **4** then. Molecule **2** achieves better coherence than **1** despite having 2 more nuclei, because the nuclei are closer and therefore more strongly coupled to the spin. Molecule **3** achieves better coherence than **4** despite having 4 more nuclei, because the spin density is less delocalised and the active nuclei are closer to it.

Second, we have argued in length that molecular motion effects are mainly related to mobile methyl and mesithyl groups. Molecule **1** has 6 methyl groups and 2 mesithyl, **2** has 9 and 2, **3** and **4** have 18 and 4. Motions are responsible of the decrease of coherence in the 200-293 K range. We observe that at 293 K, **1** and **2** roughly display same $T_m \approx 8$ µs as they were equally affected, while for **3** and **4**, $T_m \approx 4$ µs.

These observations confirm experimentally the possibility of superior quantum performance in carbon-based nanostructures where spins can be included by topological defects. The investigation of the different T regions reveals that intramolecular motions of the side-appendages are most detrimental to spin coherence, which is never found to be limited by T_1, in contrast to most previous literature. Fusion or dimerization of the individual units is much less significant than expected, and its effects are modulated by a nuclear spin diffusion barrier effects as well as the different delocalization of the spin density. Counterintuitively, residual σ-bonds are not found to hamper the coherence, so that synthetic approaches that allow a certain extent of incomplete conjugation, but still preserve the desired quantum properties, appear accessible. Chemical inclusion into conducting nanostructures, such as nanoribbons and graphene sheets, or fusing several molecules into double and multiple quantum dots, opens the path to using quantum effects in the next generation of optoelectronic, electric, and bioactive systems. In this sense, it is crucial that these observations offer

a rational synthetic pathway to add any desired functionality to a graphene quantum unit, opening up an unprecedented multitude of options for the optics and magnetism of quantum nanomaterials.

3.6 Project Overview

This project was carried out in collaboration with Prof Xinliang Feng's group at Technische Universität Dresden. The synthesis of the compounds was performed by Dr Ji Ma under direct supervision of Dr Junzhi Liu. All the EPR measurements were carried out at the Centre for Advanced ESR (CAESR) with the collaboration of Dr William Myers, and for molecule **1** also of Alessandro Lodi. The SQUID measurements in Figure 3.11 were carried out by Dr Dimitris Alexandropolous who also helped for the analysis.

Zigzag Segments

4.1 Introduction

A lot of effort has been put into understanding electronic transport in single molecules. Single units can be grafted on a surface to be operated by an STM tip, or in a junction as single-electron transistors. These setups both represent a way to obtain high quality fundamental spectroscopic information on the molecule: Franck-Condon blockade, vibrational effects, and Kondo effect; but they are also proof of principle of devices for future electronics [314]. For short molecules, the conductivity decreases exponentially with the length, since direct tunnelling represents the main conductivity channels. However, there is evidence that for long conjugated molecules with length above 3 nm the conduction regime shifts towards hopping achieving conduction that is similar to metallic wires [315]. In particular, such molecular wires should be fully conjugated, and with a moderate bandgap [316].

Graphene nanoribbons (GNRs) fulfill the previous requirements. In addition to the extraordinary mechanical strength and carrier mobility of graphene, they also possess more exotic electronic and magnetic properties that depend on the topology of their edge [141, 142]. Armchair GNRs have semiconducting or metallic behavior according to their width, making them suitable as electrical components in molecular circuits. Similarly, numerous studies suggested that zigzag GNRs are semiconducting or metallic and they present a large density of states at the zigzag edges. This energy configuration is responsible for antiferromagnetic spin polarization at the opposite edges. Therefore, in principle zigzag GNRs could be used for spintronics applications [144]. Experimental studies on zigzag nanoribbons have been scarce with respect to the large body of theoretical work, and with respect to the work for amrchair ribbons. However, recent progress in bottom-up synthesis of atomically precise ribbons have allowed wider experimental investigations [170]. Scanning tunnelling [167] and magnetic resonance [15] spectroscopies provided evidence of the energy states, the band

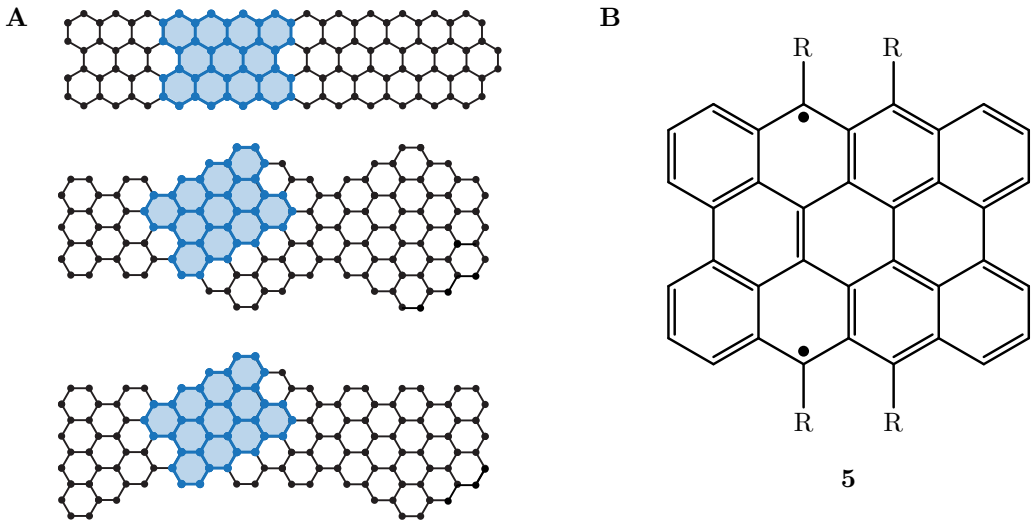


Figure 4.1: (A) Peri-tetracene seen as fundamental unit or segment of longer nanoribbons from literature (from top to bottom [167, 177, 178]). (B) Chemical structure of peri-tetracene in its open-shell diradical configuration.

gap and the magnetic activity of zigzag graphene nanoribbons validating many of the theoretical claims.

Such large interest in GNRs fuelled more studies in polycyclic hydrocarbons whose properties are also affected by the edge topology. For instance, polyacenes can be thought as the narrowest zigzag GNRs, and similarly rylenes [220] corresponds to armchair GNRs. Peri-acenes extend the width of acenes, and can be studied as individual segments of longer graphene nanoribbons structures (fig. 4.1). Simulations show that peri-tetracene is the smallest component that could show an open-shell behaviour [317] and no magnetic activity has been reported for perylene and bisanthene, which are the two smaller members of the family. However, there is a significant chemical challenge in designing such molecules because of their extreme reactivity. Recently, it was possible to synthesize and characterize peri-tetracene, while unsubstituted peri-pentacene was only isolated on surface [318, 319].

Peri-tetracene confirmed the theoretical expectations showing a large open-shell singlet diradical character with antiferromagnetic coupling at the opposite edges. In this chapter, we further the studies of the spin properties of peri-tetracene (**5**).

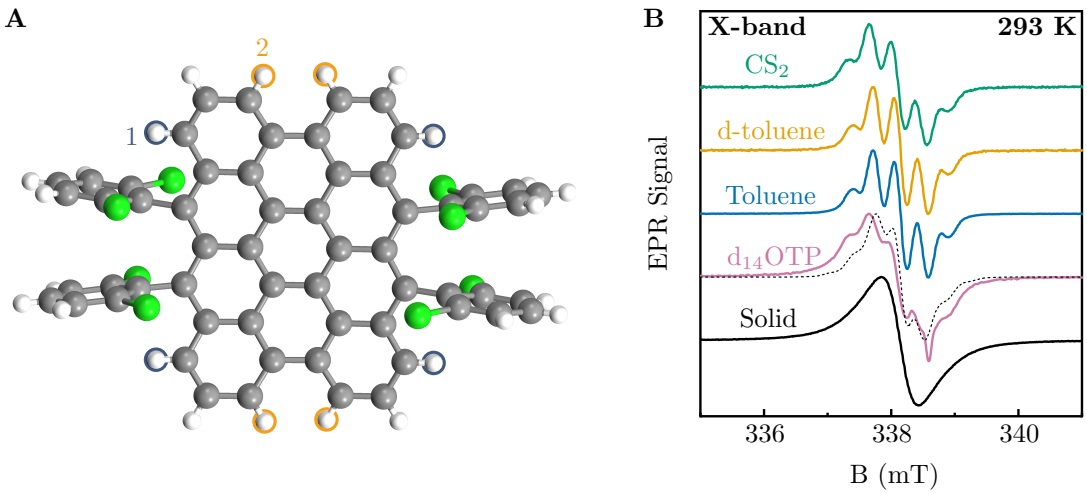


Figure 4.2: (A) X-ray structure of peri-tetracene as reported from [320]. Highlighted are the nuclei responsible for hyperfine coupling. (B) Room-temperature CW EPR of peri tetracene in 3 different solutions (CS_2, d_8-toluene, and toluene), a diamagnetic solid matrix (d_{14}OTP), and powders. The dashed line is a simulation with the parameters in table 4.1.

4.2 Magnetic Properties

Peri-tetracene powders were received in a sealed NMR tube. Upon arrival the sample was measured at CW EPR for magnetic activity showing the powder spectrum in fig. 4.2B. The tube was opened in the glovebox where we prepared four 1 mM solutions in toluene, deuterated toluene ($d_8$tol), carbon disulfide (CS_2), and deuterated ortho-terphenyl (d_{14}OTP). All tubes were degassed and flame sealed. We measured the CW spectra in all conditions as seen from fig. 4.2B. The spectra in solution completely agree with what published [320], therefore we concluded that despite the sensitivity of the sample shipping of the powders and transfer to the tube was successful and did not affect the properties of the radical.

Standard magnetic characterisation was carried out already in the synthetic paper, including SQUID, CW EPR in THF and variable temperature EPR in THF [320]. It was found that the molecule is in a singlet ground state with a singlet-triplet gap of -1258 K. Here we extend the measurements to new solvents and matrices and we further the discussion on the EPR parameters of the molecule that was only superficial in the first paper.

In fig. 4.2B we show the CW spectra of peri-tetracene in the four different matrices and in a polycrystalline powder. The spectra in toluene, d-toluene, and CS_2 are in a liquid solution and they are analogous to the one already reported in THF [320]. In liquid solution all anisotropic behaviours are averaged by fast molecular tumbling and the splitting is only produced by isotropic hyperfine

coupling. Differently, the spectrum in d_{14}OTP is in a solid matrix. Indeed, the main features are still the same of the solution spectra, but the linewidth is increased due to the effect of anisotropy. The effect of anisotropic hyperfine coupling is even accentuated in the solid sample where hyperfine strain due to absence of dilution produces a large linewidth that hides all the features.

The dashed line in fig. 4.2B is a simulation with the Hamiltonian of eq. (3.4) here simplified as:

$$\hat{H} = \mu_{\mathrm{B}} g B \hat{S}_z + \sum_{i=1}^{8} \hat{\mathbf{S}} \mathbf{A}_i \hat{\mathbf{I}}_i \tag{4.1}$$

with the formalism defined before and the summation over the 8 highlighted hydrogen nuclei in fig. 4.2A. Given the large exchange coupling that was reported, peri-tetracene is in the high exchange limit for which microwaves cannot drive transitions from the singlet state to the triplet state. While the system is in a triplet state, the effect of dipolar coupling is not observed in the d_{14}OTP or solid spectrum since the interaction is too small as reported already in chapter 3 and in several other delocalised carbon systems in the literature, therefore it was neglected in the Hamiltonian. No difference is observed in the CW spectra at Q-band because the g-factor is largely isotropic and its anisotropic features could probably appear only at very high fields, while the hyperfine contribution that determines the splitting is field-independent.

To better define the magnetic properties of the sample we carried out extensive DFT calculations using the B3LYP and PBE0 hybrid functionals and the basis sets 6-31G**, EPR-II, and SVP. In all cases we used the geometry obtained by X-ray from [320]. In fig. 4.3 we show the calculated spin densities for all cases with iso value 0.02, highlighted are the the two sets of four equivalent hydrogen nuclei that contribute the most to hyperfine coupling. In table 4.1 we report the relevant calculated EPR parameters. From fig. 4.3 we can see that all the different calculations are in excellent agreement, locating the great majority of the spin density at the edge of the molecule. Using the same functional, there is almost no difference across the various basis sets. A small systematic difference can be seen when switching the two functionals: B3LYP places a larger spin density in the centre of the molecule, while with PBE0 the density is more pronounced at the edge. This difference becomes clearer when we observe the hyperfine parameters in table 4.1 which are larger in PBE0 with respect to B3LYP.

Here, the g-factor depends on the spin-orbit coupling. It is common for carbon radicaloids to have g-factor close to the free electron g-value of 2.0023. This is because the intrinsic spin-orbit coupling

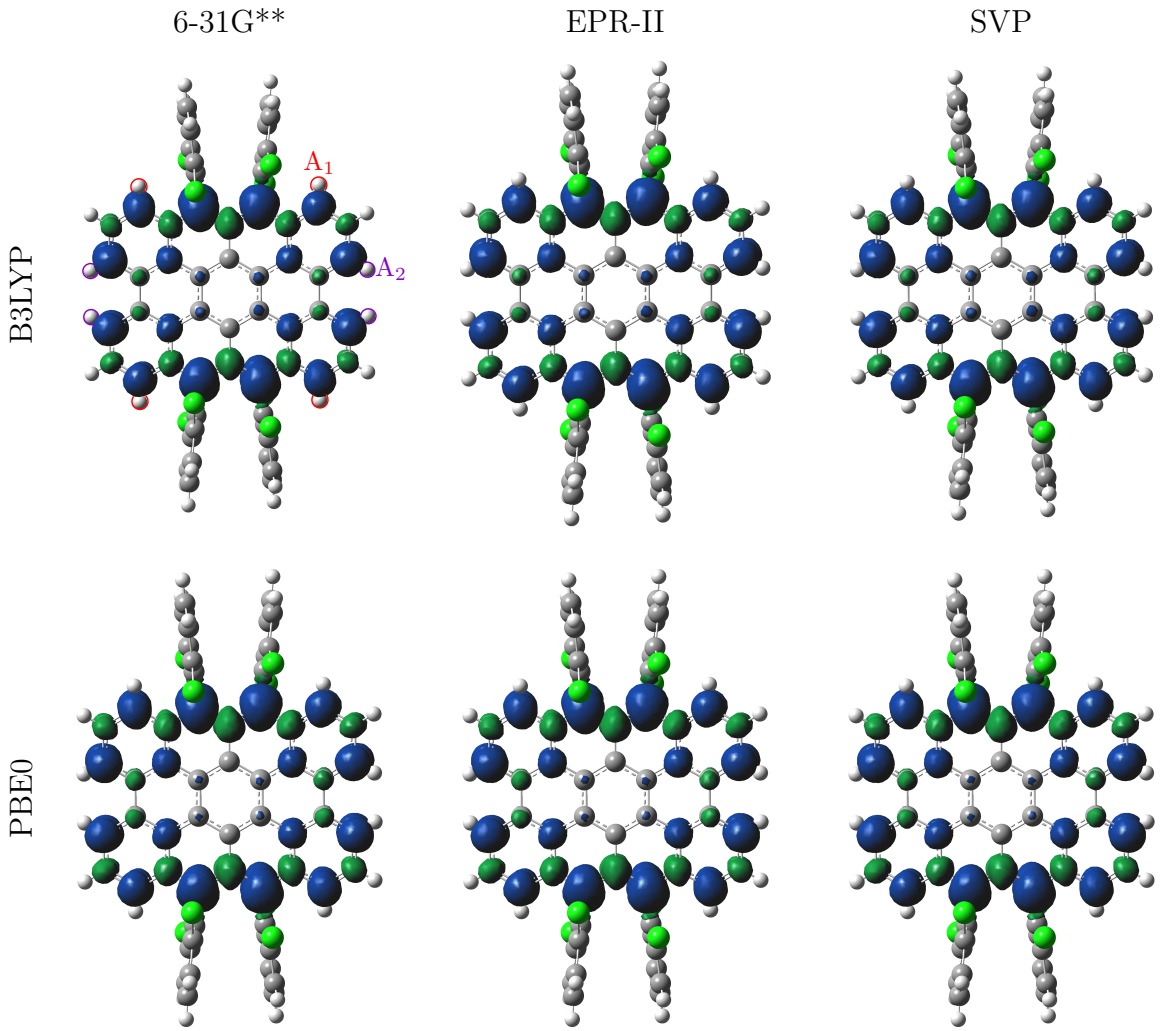


Figure 4.3: Computed spin densities using different combinations of functional/basis sets for peri-tetracene using the fixed geometry obtain from X-Ray [320]. The 8 highlighted hydrogen atoms in the first structure indicate the nuclei responsible for hyperfine coupling and their parameters are reported in table 4.1 for each combination.

given by light elements as carbon and hydrogen is notoriously low. However, what is remarkable for peri-tetracene is how close to isotropic are g_{xx}, g_{yy}, g_{zz}. Several theoretical works have shown that local curvature has a very large contribution to spin-orbit coupling and extremely large g-anisotropies have been found for carbon nanotubes [321, 322] and fullerenes [323], which would, otherwise, have a very small intrinsic spin-orbit interaction. However, as the structure of peri-tetracene is almost perfectly planar, this represents an excellent model system where the contribution of spin-orbit coupling is reduced to its minimum.

In fig. 4.1 we showed how peri-tetracene can be thought of as a building block for longer and more complex GNRs featuring zigzag edges. Here, we calculated the spin densities of several GNRs

Functional	Basis		xx	yy	zz
B3LYP	6-31G**	g	2.0029	2.0030	2.0031
		A_1 (MHz)	2.1	5.0	7.5
		A_2 (MHz)	2.0	5.0	8.7
	EPR-II	g	2.0023	2.0026	2.0034
		A_1 (MHz)	1.7	4.7	7.2
		A_2 (MHz)	1.6	4.7	8.4
	SVP	g	2.0031	2.0031	2.0031
		A_1 (MHz)	1.5	4.7	6.9
		A_2 (MHz)	1.4	4.8	8.1
PBE0	6-31G**	g	2.0029	2.0030	2.0031
		A_1 (MHz)	3.0	5.8	8.7
		A_2 (MHz)	2.9	5.9	9.9
	EPR-II	g	2.0023	2.0026	2.0034
		A_1 (MHz)	2.2	5.3	8.1
		A_2 (MHz)	2.1	5.3	9.4
	SVP	g	2.0030	2.0031	2.0031
		A_1 (MHz)	2.3	5.2	8.0
		A_2 (MHz)	2.2	5.2	9.2
Experiment		g	2.0029	2.0030	2.0031
		A_1 (MHz)	2.7	6.3	9.4
		A_2 (MHz)	2.5	6.3	10.9

Table 4.1: EPR parameters as calculated from DFT. The experimental line indicates the parameters used for the d_{14}OTP simulation in fig. 4.2B.

that were synthesised in the literature, and of relevant nanographenes with zigzag edges. Most of these structures were already discussed in chapter 1. In fig. 4.4 and 4.5 we present simulations at the B3LYP/6-31G** level of theory. We can clearly note that all the molecules have very large spin densities in correspondence of their zigzag edge. There is also a direct correspondence between the location of the spin density and the presence of localised edge states near to the Fermi level. This can clearly see by comparing the spin densities to the STM images in the literature. Some of them were reported in chapter 1, in particular it is possible to compare fig. 4.4A and fig. 1.7B, or fig. 4.4D and fig. 1.8D. All these structures were synthesised on surface, which allowed probing of their band structures via STM. However, no experimental hints of their magnetic properties or quantum properties was obtainable. In view of the considerable similarity of spin localisation, we argue that peri-tetracene can be taken as a simple model of longer ribbons, and the results achieved can be, in first approximation, extended to structures with at least three consecutive zigzag edges.

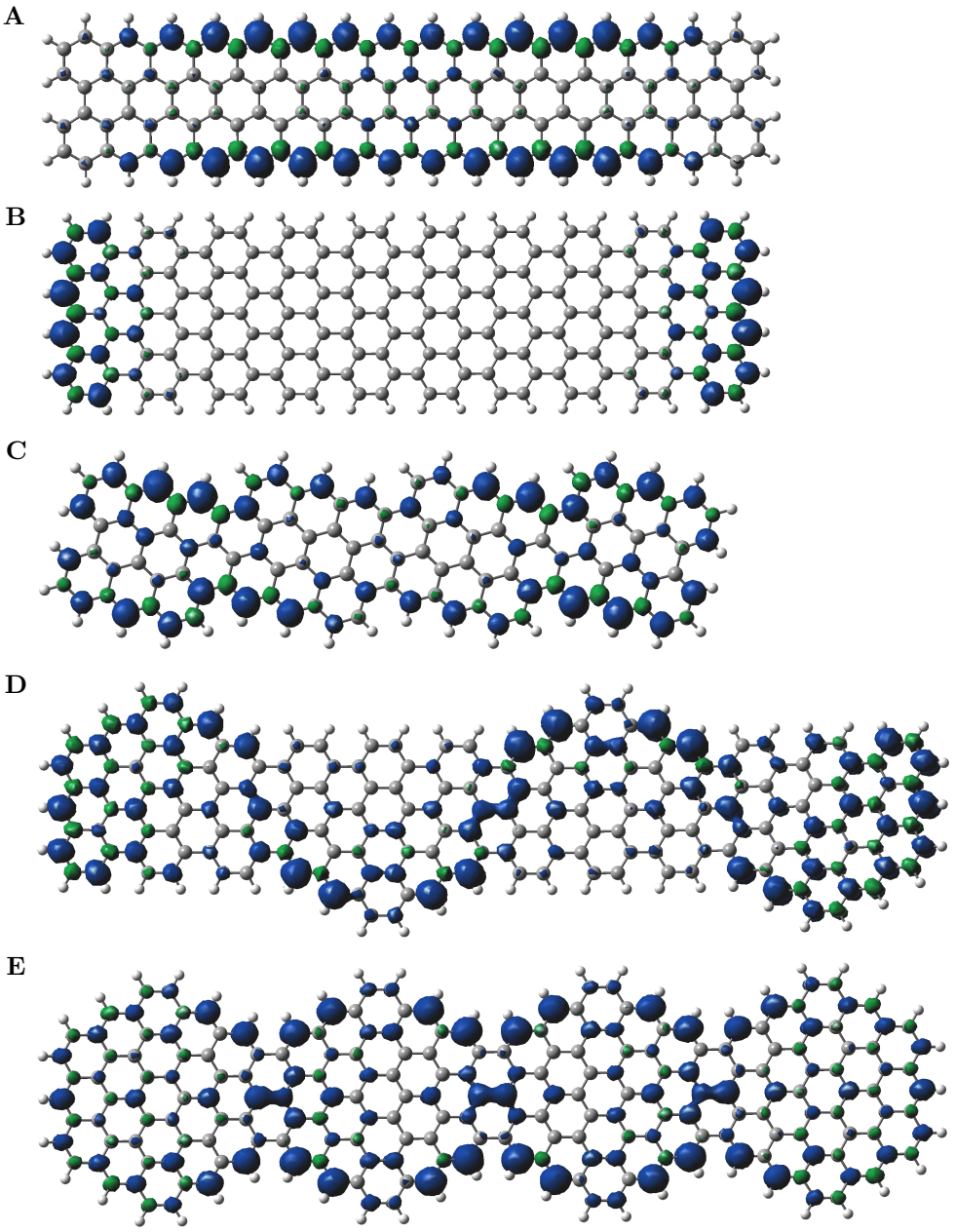


Figure 4.4: All spin densities were obtained at the B3LYP/6-31G** level of theory and are showed with iso value 0.002. (A) Extension of the zigzag edge of peri-tetracene. Synthesis and characterisation on surface from [167]. (B) Extension of the armchair edge of peri-tetracene, all the spin density concentrated at the zigzag termini. Synthesis and characterisation of 9-AGNR from [161]. (C) Chiral GNR, synthesis and characterisation from [324]. (D-E) Staggered 7-AGNR and in-line staggered 7-AGNR from [178].

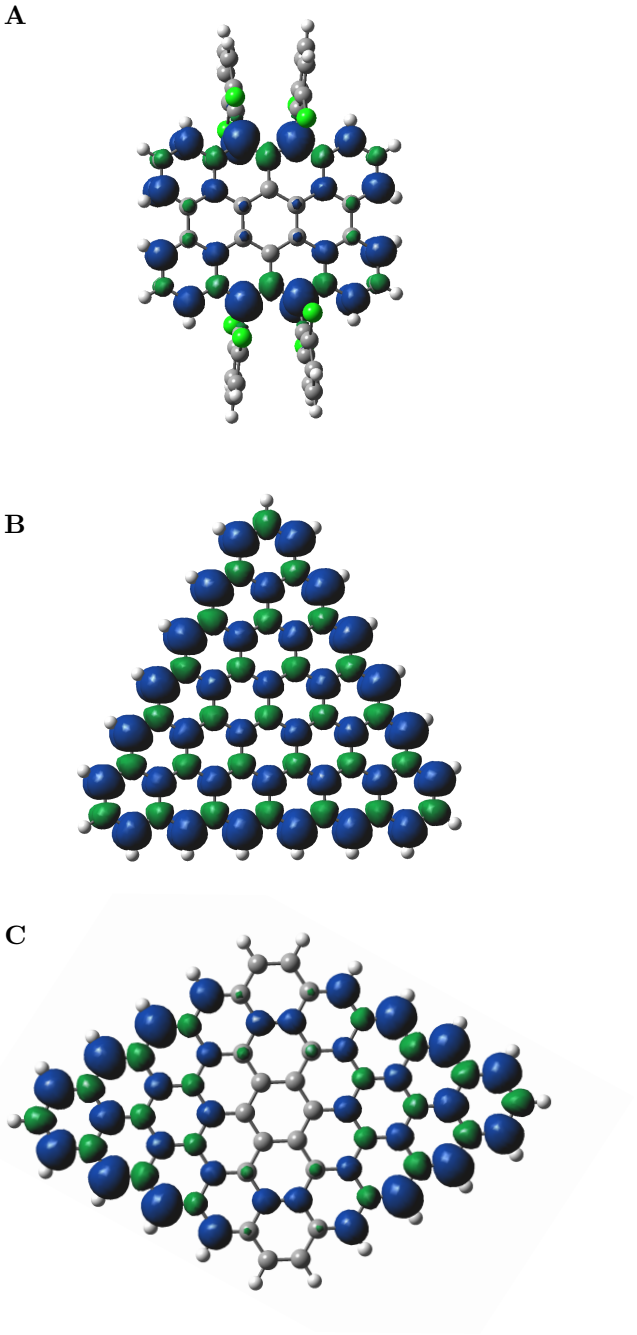


Figure 4.5: Comparison between the spin density of peri-tetracene and other zigzag-edged nanographene molecules. All spin densities shown were obtained at the B3LYP/6-31G** level of theory and are showed with iso value 0.002. (A) Spin density of peri-tetracene, repeated for convenience. (B) [6]triangulene, yet to be isolated, but [4] and [5]triangulene were observed in [227, 228]. (C) Rhomboid nanographene [325].

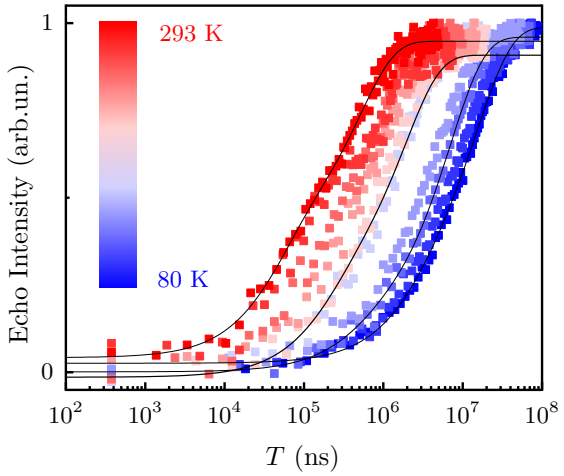


Figure 4.6: Experimental traces of the spin-lattice recovery as measured with a Picket Fence sequence, at different temperatures (80, 100, 120, 140, 160, 180, 200, 220, 240, 293 K). Black lines are fit with a bi-exponential model for certain temperatures (80, 100, 180, 293 K).

4.3 Spin-lattice relaxation

We measured spin-lattice relaxation time using a Picket Fence sequence and fitting with a biexponential as in eq. (2.7). In fig. 4.7, we present the summary of the spin-lattice relaxation rate T_1^{-1} at different temperatures, in X-band and Q-band. The relaxation rate increases monotonically with temperature in all conditions because at higher temperature more phonon modes become available. A large increase is observed above the melting temperature of the solvents because of relaxation due to molecular tumbling [254]. Here, we focus on spin-lattice couplings in immobilised samples. The trend of T_1^{-1} in solution is reminiscent of the behaviour of **2**-**4**, and the same analysis of chapter 3 would be appropriate, although not of interest. The sample in d_{14}OTP grants the possibility of studying the properties in a large temperature range with only the glass transition at 243 K. It appears, nonetheless, that the microscopic reorganisation above the glass temperature does not introduce sudden jumps in T_1^{-1}. Likewise, it emerges from fig. 4.7 that the trend of the spin-lattice relaxation rate is not affected by the type of solvents, although local variations are evident especially at X-band. Therefore, the results in d_{14}OTP can be extended to all other solvents.

A key in the interpretation of the data in fig. 4.7 is that the relaxation rate is not affected by the change in magnetic field. The main processes that are magnetic field independent are Raman and Orbach, both involving two-phonon absorption. We find excellent agreement of the data fitting with

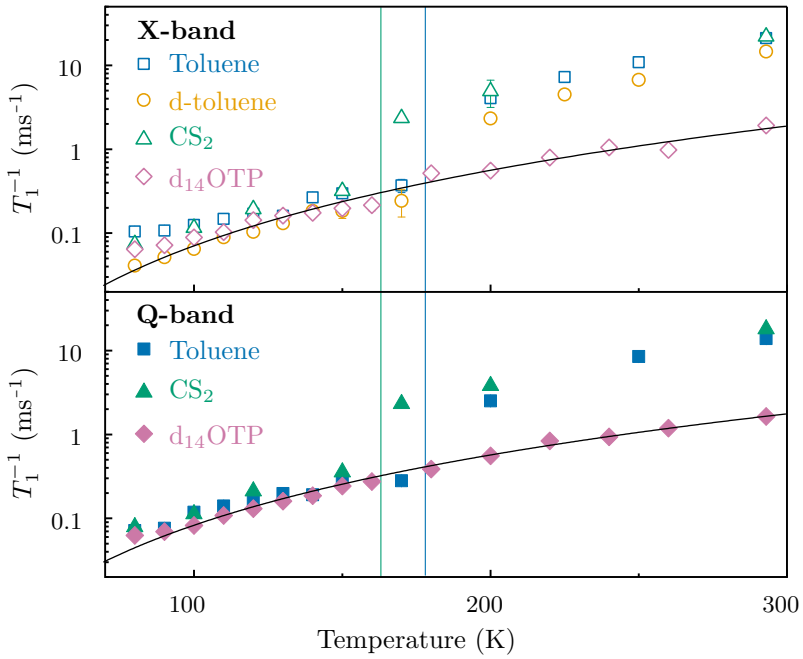


Figure 4.7: X-band (top) and Q-band (bottom) spin-lattice relaxation rate vs T diagram for peri-pentacene in different matrices: toluene (squares), $d_8$toluene (circles), CS_2 (triangles), d_{14}OTP (rhombi). Empty symbols refer to X-band, full symbols to Q-band. The vertical lines mark the melting temperature of CS_2 (163 K) and toluene (178 K). The black lines are fit to the expression in text.

the model

$$T_1^{-1} = CT^n, \tag{4.2}$$

with $n = 2.7-3$, which is indicator of a Raman process. A much worse fit is obtained modelling it with the Orbach equation. Therefore, we conclude that for $T > 80$ K the dominating channel is a Raman process. This is analogous to previous results in chapter 3, and to numerous publications of single metal-centre molecular systems [97, 99, 326], particularly measurements in vanadyl complexes also yielded $n \approx 3$ [81, 118, 327]. Besides, the Raman process was also the main process at intermediate temperatures for functionalised GNRs, which were affected by local modes at higher temperatures [15]. In that particular case the local mode was interpreted as a result of C-N vibrations, which is not present in peri-tetracene.

We compare our results to a published theory on the spin relaxation of graphene nanoribbons [328, 329]. The theoretical paper focuses on a long GNR in which a single electron is electrically confined in a smaller segment of the system. Starting from a phonon distribution based on vibrational modes of graphene and previous results, they calculate spin-phonon coupling mediated by spin-orbit coupling and they show the dependence of the spin-lattice relaxation time at different fields for a

length/width ration equals to 5, considering only single phonon processes. With these assumptions, Droth and Burkard [328] find that T_1 varies between 1 s and 10 ms for magnetic field below 1.5 T with a magnetic field dependence $T_1 \propto B^{-5}$, and T_1 depends on the length/width ratio increasing when reducing the ratio.

The experimental conditions in peri-tetracene are different to a certain degree: the length/width ratio is roughly 1, being an isolated molecule all the states are bound with no wavefunction extending past the geometry (while there would be extended states in a portion of a GNR confined in a longer geometry), and the results are field independent. A more suitable experimental condition to probe single-phonon process would be at $T < 20$ K, but this is not possible with a singlet diradical since the molecules would be in the $S = 0$ state. Albeit we miss experimental evidence for that regime, results from chapter 3 and from longer GNRs in powder [15] suggest that peri-tetracene would likely fall into the direct process. Nonetheless, if high temperature applications of GNRs are to be studied, calculations should be adapted to include the dominant effect of two-phonon processes.

A more direct comparison can be done with results in nitrogen vacancy (NV) centres. It is reported that, at low magnetic fields, they are affected by the direct process for $T < 1$ K, and by the Orbach and Raman processes for $T > 20$ K, with the latter dominating in the high temperature regime [330]. In particular at room temperature, bulk NV centres reach T_1 in the range 5-10 ms that is 1 order of magnitude larger than the 0.6 ms of peri-tetracene. On the other hand, shallow NV defects are affected by surface related noise and their performance is comparable if not worse than **5** [331].

4.4 Spin coherence

We measured the coherence time in all four matrices with a Hahn echo decay sequence. For toluene, CS_2, and d_{14}OTP we recorded data in both X-band and Q-band, while for d-toluene we only used X-band because it appeared that measuring also at Q-band would have not yielded additional information.

In fig. 4.8, we show traces at 80 K for all samples and both frequency ranges. In X-band (fig. 4.8 left panels), we can observe the ESEEM modulation superimposed to the time decay. In the right part of the figure, we display the Fourier analysis of the modulation which shows two main peaks for toluene, $d_8$tol, and d_{14}OTP. In all these cases, the highest peak is centred at the Larmor frequency

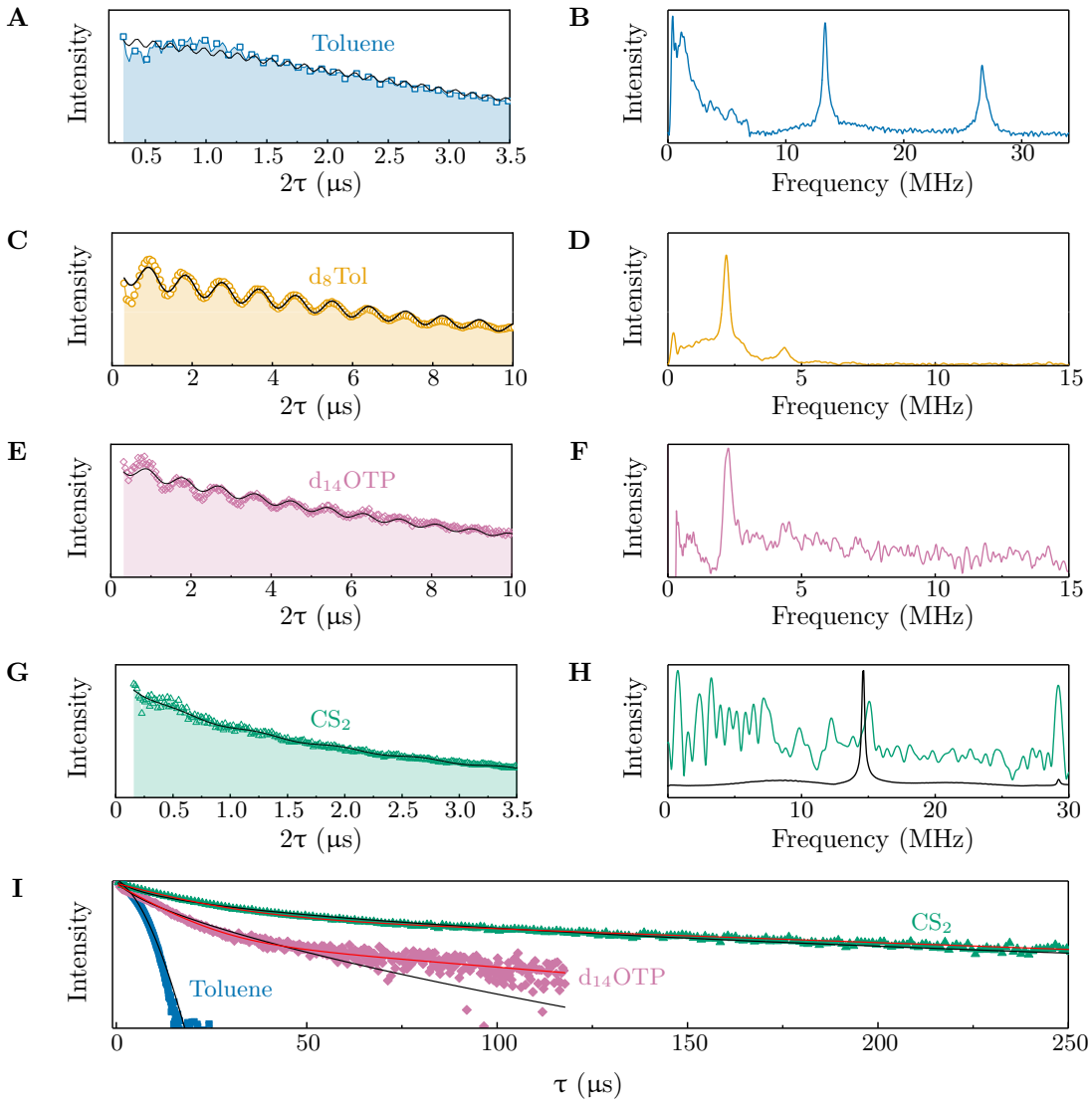


Figure 4.8: All traces are taken at 80 K. Empty symbols refer to X-band, full symbols to Q-band. (A) Toluene decay with fit. (B) FT of the modulation in toluene. (C) d_8Tol decay with fit. (D) FT of the modulation in d_8Tol. (E) d_{14}OTP decay with fit. (F) FT of the modulation in d_{14}OTP. (G) CS_2 decay and fit. (H)FT of the modulation in CS_2, black line is an Easyspin simulation that takes into account all the hydrogens at the edge of the molecule. (I) Q-band decay in toluene (squares), d_{14}OTP (rhombi), and CS_2 (triangles). In the time decay traces, red lines are fit with a bi-exponential decay, black line are fit with a stretched exponential decay.

of the most abundant nuclei in the matrix H (14.8 MHz), D (2.27 MHz), and the lowest peak at the second harmonic of the Larmor frequency, 29 MHz and 4.5 MHz respectively. A different discussion should be dedicated to the sample in CS_2, because the matrix is nuclear free. Hence, the modulation only depends on the nuclei of isolated molecules. It can be immediately noted that the modulation depth is remarkably weaker than in the other matrices, because the number of nuclei involved is much smaller: 24 H, 8 Cl, and some rare ^{13}C from the molecule or matrix, versus the hundreds of

nuclei surrounding the molecule in toluene, $d_8$tol, and d_{14}OTP. The associated Fourier analysis is representative of the molecule only and we simulated it with the DFT-calculated hyperfine couplings for the hydrogen only (black line in fig. 4.8H). The simulation shows good agreement in the peak positions, but not in the intensity. It is indeed strange that the second harmonics presents such a large peak. An additional series of peaks at lower frequency can be seen, possibly hidden in the noise, which we can attribute to Cl isotopes, ^{13}C, and their combination frequencies. In the bottom panel (fig. 4.8I), we also display the traces at 80 K in Q-band. In this case, the modulation has disappeared because of the increase in Larmor frequency (the dependence of the modulation depth with the Larmor frequency was summarised in fig. 2.10).

Here we present two different models for different matrices: a stretched exponential model with the following equation

$$Y(2\tau) = A\exp\left\{-\left(\frac{2\tau}{T_{\mathrm{m}}}\right)^{\beta}\right\}, \tag{4.3}$$

and a bi-exponential model:

$$Y(2\tau) = Ae^{-2\tau/T_{\mathrm{m}}} + Be^{-2\tau/T_{\mathrm{f}}}. \tag{4.4}$$

In toluene and d-toluene the stretched exponential model always produces a better fit than the bi-exponential model, T_{m} constants for these two matrices are summarised in fig. 4.9A-B together with their exponential stretch parameter β. The situation is different for CS_2 and d_{14}OTP, and it is harder to choose the best fitting model. We highlight that there is no *a priori* way to make the choice, as both models are based on phenomenological explanations. We establish the quality of a fit visually, looking at the residuals, and mathematically looking at the R^2. Both models produce a good visual fit for the initial part of the decay, but they tend to diverge at the decay tail. However, the tail is also the part where there is less signal and the experiment is more prone to noise fluctuations. It is also tricky to evaluate the fit based on the highest R^2, first because both models generally present $R^2 > 0.99$, second because R^2 depends on the number of free parameters. The stretched exponential model has 3 free parameters, while the bi-exponential has 4. In theory a higher number of parameters should always lead to a higher R^2, but often parameters are inter-dependent and therefore cannot be considered fully free. It could be possible to employ a machine learning approach for which we randomly divide the experimental data in three sets: training set (60%), test set (20%), and cross-validation set (20%). The fit would be performed on the training set and then evaluated on the other two sets. However, due to the exponential shape, the result of this procedure would

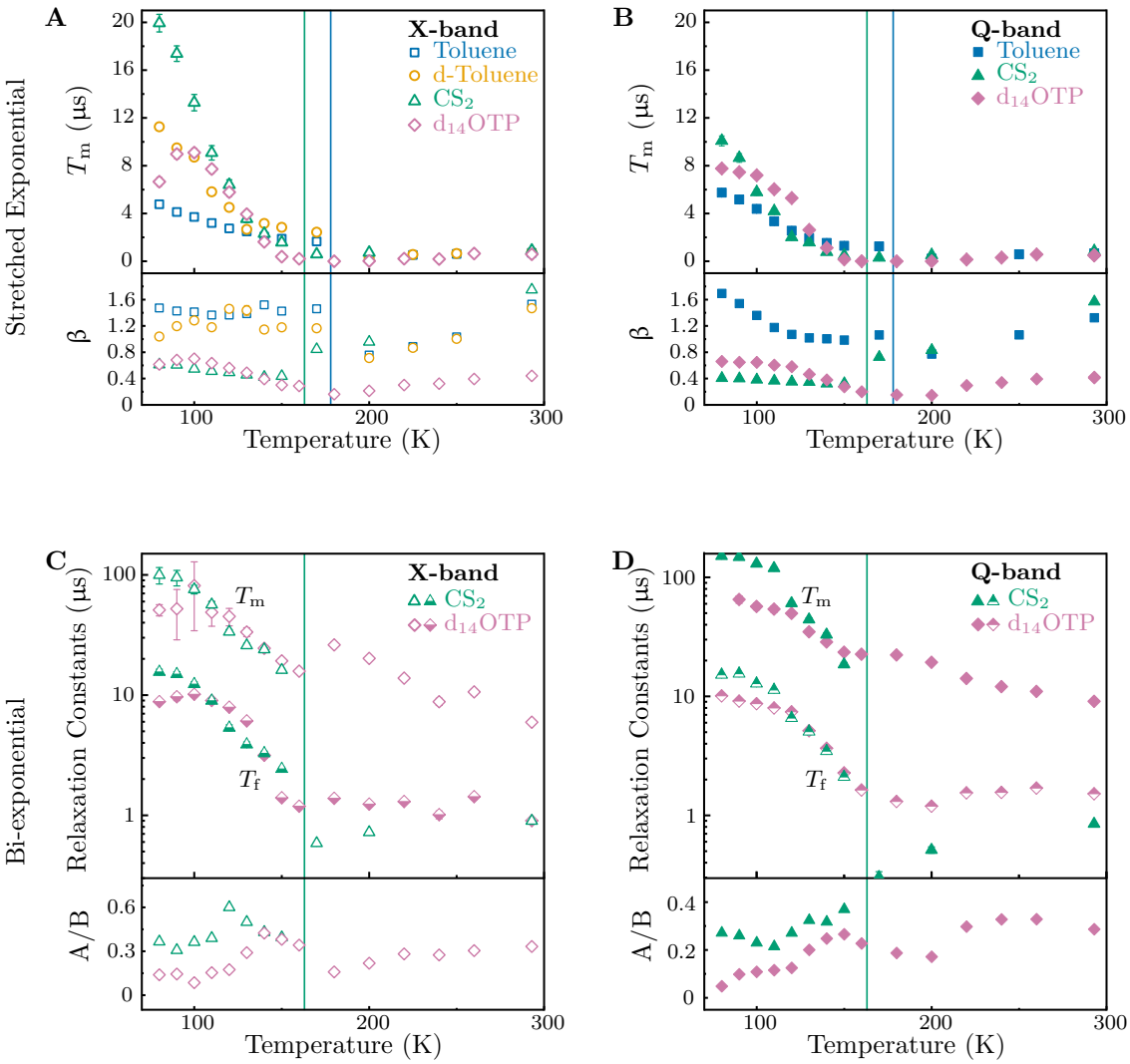


Figure 4.9: (Top) Parameters obtained fitting with a stretched exponential model. (A) X-band results. (B) Q-band results. In all graphs different matrices are represented by symbols: toluene (squares), d-toluene (circles), CS_2 (triangles), d_{14}OTP (rhombi). Empty symbols refer to X-band, full symbols to Q-band. (Bottom) Parameters obtained fitting with a bi-exponential. (C) X-band results. (D) Q-band results. Triangles are CS_2, and rhombi d_{14}OTP. Empty symbols refer to T_m in X-band and full symbols to Q-band. Half-filled symbols represent T_f. Vertical lines mark the melting point of CS_2 (163 K) and toluene (178 K).

depend strongly on which points are assigned in each set: i.e. initial part or tail. Therefore, we deemed this approach inappropriate. Overall, we observe that the bi-exponential model has always highest R^2 in the 80-120 K, while the stretched exponential performs better at higher temperatures. Additionally, the stretched exponential is clearly a better in solution phase for CS_2.

In fig. 4.9 we summarise all the results for both models: the time constant for the stretched exponential is presented with the parameter β, while for the bi-exponential both T_m and T_f are shown, together with the ratio of their weights A/B. For the stretched exponential fitting we observe

values for CS_2 and d_{14}OTP that are consistently below 0.5 with a minimum of 0.15. This stretch parameter represents a remarkably fast decay at early time and extremely long tails. We have not found any steadily similar behaviour in the literature where most of the times $\beta > 1$. These values also contrast other measurements described in this thesis, for which, in the same matrices, $\beta > 0.65$ (see **1** in chapter 3, **6** and **7** in chapter 5). It would be possible to constrain β, but this would decrease the quality of the fit, therefore favouring the bi-exponential fit.

On the other hand, the use of a bi-exponential is well documented in the literature in very similar situations: for deuterated solfuric acid [94], for CS_2 [79], and for d_{14}OTP [255]. These solvents have in common that they do not form good glassy matrices, thus aggregation is possible depending on the structure of the molecule, which favours intermolecular dipolar couplings. Thus, T_f represents the coherence time when limited by dipolar coupling by aggregates or neighbour molecules, while T_m is the true coherence time of isolated molecules. We also highlight that T_f is always larger than any T_m reported for toluene and d-toluene, which indicates that even if there were aggregates in those matrices, the environmental effect would be still larger than the average dipolar coupling, and therefore it is sensible to use a stretched exponential.

Overall, we conclude that the parameters extracted by the stretched exponential fit for CS_2 and d_{14}OTP are not representative of a true physical behaviour and are merely a mathematical artefact, and we favour the use of the bi-exponential fit. Nonetheless, it is clear from fig. 4.9 that, while the time constants might differ even by an order of magnitude, the temperature trend is roughly analogous for the two treatments. Similarly for T_1 discussion, the behaviour above the melting point of the matrix is dominated by molecular tumbling, here we focus on immobilised matrices only. As expected, the coherence time increases going from toluene to d-toluene and d_{14}OTP and to CS_2 because of lower gyromagnetic ratio of the nuclear environment or absence of nuclei. In all matrices, T_m almost monotonically decreases when increasing the temperature while in the solid state. The increased decoherence is to be attributed to self-translation and rotation of the molecule or any molecular groups that modulate the anisotropic hyperfine coupling at a rate comparable with the interaction itself. A quantitative modelling of this behaviour would require simulation of the dynamics of the molecule in the matrix at different temperatures. Here we qualitatively connect the effect to motions of the chloro-mesityl groups at the edge of peri tetracene. With increasing temperature, we can expect full or partial rotations of the mesityl group around the C-C bond to be possible as well as rotation around the plane of the molecule and stretching of the bond. Any of

these movements would change the position of the chlorines with respect to molecule. Given the very large spin density localised at the carbons bonded to the mesityl groups, motion of the chlorine would likely have a very large impact on their hyperfine coupling. Since the mesityl groups play an important role in the chemical stabilisation of the molecule it is not possible to simply remove them.

The molecular motion effect is analogous to what described in length in chapter 3. However we can see a clear difference: for **2**, **3**, and **4** the motions were matched by a minimum at around 130 K followed by a retrieval of coherence, while for **5** the decay appears to be monotonic, or possibly with a minimum at temperatures higher than what was probed. For **2**, **3**, and **4** we had attributed the minimum to methyl groups, but **5** has no methyl groups, which are instead substituted by chlorines. Qualitatively, if we compare the molecular weight of a methyl group with a single chlorine atom, we have $m(\text{methyl}) = 15$ u while $m(\text{Cl}) = 35.5$ u, but the chlorine is much less bulky than the methyl group. Therefore, the inertia of the bulk is shifted, but also the degree of freedoms available are modified, which explains the different behaviour.

Theoretical predictions of coherence in zigzag edges of confined systems provide values of $T_\text{m} \approx 10 - 80$ µs, when the source of decoherence is the hyperfine coupling with ^{13}C [45, 332]. Our zigzag fragment should display faster decoherence because, in addition to ^{13}C coupling, the electron spin also couples to edge hydrogens, nuclei in the solvent, and molecular motions. Nonetheless, at 80 K in CS_2, the T_m value of 100 µs at 9 GHz already exceeds the predictions, and as it will be seen in chapter 6 the performance can be further improved. It is possible that theoretical predictions were off of order of magnitudes with respect what is achievable. Indeed, they were based only on the static effect of hyperfine coupling and possibly the hyperfine coupling of ^{13}C was overestimated. Better predictions should consider the dynamic effect, which means that decoherence is not driven only by single nuclei coupled to the electron spin, but by the dynamics of the nuclear bath, and in particular it is the intrabath dynamic stregth that affects it the most.

4.5 ^{13}C Isotropic hyperfine coupling

Multiple theoretical papers downgrade the hyperfine interaction with ^{13}C suggesting that this in major part, if not completely, a dipolar interaction with no isotropic component [45, 332, 333]. The intuitive explanation of this argument is that graphene or graphenoids electrons are delocalised in p orbitals. The electron density of a p orbital at the nucleus is 0, therefore the isotropic interaction,

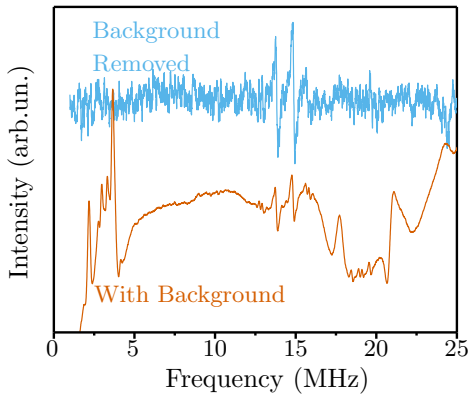


Figure 4.10: CW-ENDOR of **5** in CS_2 at 293 K. In the top line the off-resonance background has been removed, while it is still present in the bottom line.

intended as the spin density on the nucleus, must also be 0. However, this is not generally true. Early EPR literature suggest that in metals, even if the spin density is in p or d orbitals, an isotropic hyperfine effect might arise from spin polarisation coming from s orbitals [334]. In addition to this, our DFT calculations show presence of isotropic coupling, and they do include polarisation from different orbitals.

To try to observe isotropic hyperfine coupling we prepared a room temperature CW ENDOR experiment in solution using a Bruker EN 801 ENDOR cavity. In solution all dipolar couplings are averaged by the molecular tumbling and only isotropic ones are left. We carried out the experiment twice: the first time we did not produce an off-resonance background reading, while the second time we did not achieve the signal-to-noise ratio (SNR) we hoped for. As can be seen from fig. 4.10 while the SNR was very good and a fine structure can be appreciated, the large background does not allow to correctly identify the peaks except for the ones of the hydrogen. On the other hand, only the hydrogens are resolved for the low SNR trace. Overall, we were not able to conclusively find any ^{13}C isotropic hyperfine interaction. The natural abundance of ^{13}C is 1.3 % therefore its signal is very low for a molecule with 60 carbon atoms. To improve the SNR the experiment shall be repeated allowing more averaging (that still took 24 hours for the low SNR measurement), using a more concentrated sample, and using liquid nitrogen to keep the temperature constant. Indeed, high energy RF radiation heats up the sample significantly modifying the resonance conditions. Ultimately, an isotopically enriched sample would be necessary to prove the presence of isotropic coupling.

4.6 Outlook

These results reveal that the potential of carbon nanostructures with zigzag edges, although highly anticipated, is still underestimated. The exceedingly small spin-orbit coupling, achieved by eliminating any curvature, makes spin-phonon process particularly inefficient, and gives rise to extremely long T_1 times. Contrary to predictions for transverse vibrational modes, the relaxation channel is field-independent, and mainly the result of Raman processes involving two phonons and a virtual state. New calculations that include the dominant effect of two-phonon and nonlinear processes are thus necessary to establish applicability above liquid nitrogen temperatures. The observed T_m times, much higher than predictions, are still two orders of magnitude below the intrinsic limit of $T_\mathrm{m} < T_1$, and even longer times are within reach by chemical engineering of the nuclear bath, and by investigating a single edge, instead of a randomly-oriented ensemble. An appealing geometry consists of a zigzag nanosystem deposited onto a silicon/silicon oxide surface with graphene contacts, to form a single-molecule-transistor. Both graphene and silicon have a very weak nuclear bath since ^{13}C (1.3%) and ^{29}Si (4.7%) are present in low percentage and they can easily be removed with isotopic enrichment, as demonstrated for NV centres in diamonds [62] and donors in silicon [63]. Multiple dots in series are also within reach of chemical synthesis, as they can be produced by joining together two molecules with aklyl chains. Such device would thus achieve an extremely low nuclear bath, with electrical control of the spin degree of freedom.

Recently, we have also collaborated with Prof Xingliang Feng's group at TU Dresden for the magnetic characterisation of peri-heptacene which is an extension of **5** to a molecule 7-carbon ring long. While the synthesis of peri-heptacene was confirmed through standard chemical characterisation and Raman spectroscopy,[1] the extreme reactivity of the compound made it available only in solution, and mixed with its precursor and the reaction agent DDQ (2,3-Dichloro-5,6-dicyano-1,4-benzoquinone). We observed that the reaction produced large quantity of anionic DDQ that is spin-active. Therefore, the EPR signal was completely dominated by DDQ^-, with an incredibly smaller signal that could be attributed to peri-heptacene, although such attribution could be strongly contested, given the intensity of the signal. Such sample was deemed unsuitable for further EPR characterisation. For now peri-tetracene remains the only magnetic-interesting poly-acene that can be synthesised and purified with solution chemistry, but in the near future optimisation of peri-heptacene's synthesis

[1] M. R. Ajayakumar *et al.*, Angew. Chem. Int. Ed., Submitted (2021)

might make it available for pulse EPR analysis.

4.7 Project Overview

The project on peri-tetracene was carried out with the group of Prof Jishan Wu at the National University of Singapore. The synthesis and chemical characterisation of peri-tetracene was published in [320]. The synthesis of the sample we used was done by Dr Yong Ni at NUS. All the EPR experiments were carried out in Oxford at CAESR. Dr Will Myers carried out one ENDOR measurement and provided aid for the second one.

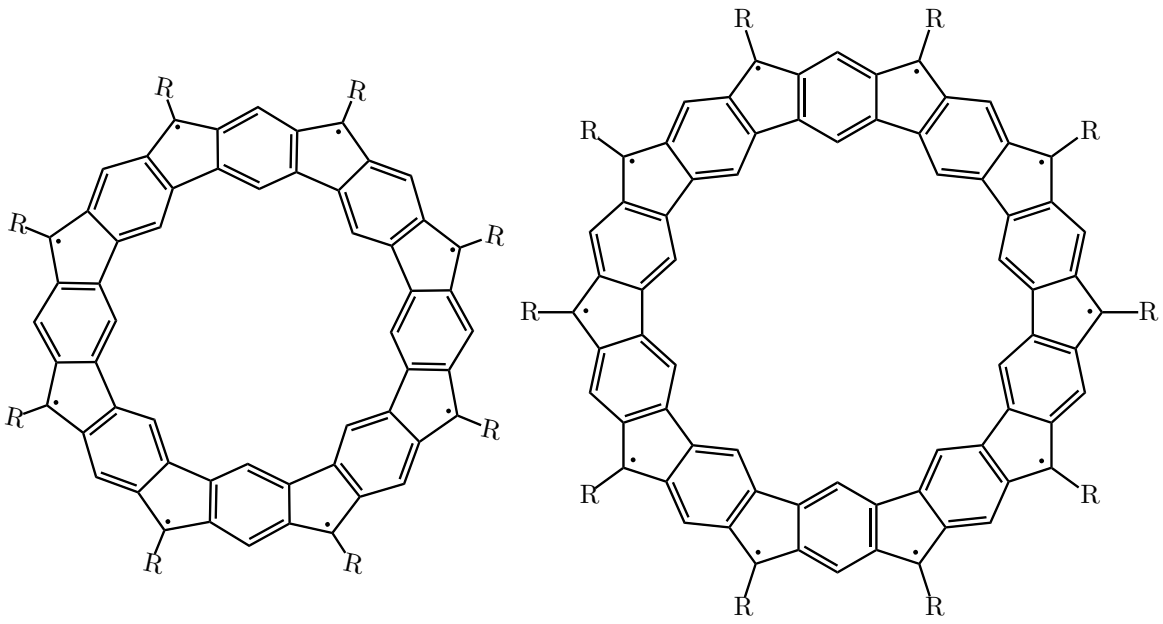
Ring Shaped Graphenoids

5.1 Introduction

There is a vast activity in chemistry towards cyclic and macro-cyclic molecules since they serve as testbed for aromatic theories. Aromaticity is an omnipresent concept in organic chemistry: from the first lecture of a chemistry curriculum, to the most advanced research papers, its origins and implications are object of debate. Aromaticity is at the same time a very practical and abstract concept: it plays a crucial role in chemical reactions and molecule stabilization, but it is not directly a physical observable, therefore it cannot be easily defined. For example, a popular first-year undergraduate chemistry textbook [335] attempts at explaining it via enunciation of Huckel's rule: "Planar, fully conjugated, monocyclic systems with $(4n+2)$ π electrons have a closed shell of electrons all in bonding orbitals and are exceptionally stable. Such systems are said to be aromatic", but immediately limits the scope: "This is not a strict definition of aromaticity: it is actually very difficult to define aromaticity precisely, but all aromatic systems obey Huckel's rule".

In chemistry, the presence of aromaticity (or antiaromaticity) is often related to persistent ring currents under an external magnetic field. This concept was strongly debated in the early days of the theory [336], but it has become more and more established thanks to NMR experimental results. A persistent ring current flowing in the conjugated π electron is generated when applying a magnetic field to an (anti)aromatic molecule. In turn, the current will generate its own magnetic field whose direction depends on the direction of the current itself and it is opposite in aromatic and antiaromatic molecules. This last concept is simply related to Ampere's law:

$$\boldsymbol{\nabla} \times \mathbf{B} = \mu_0 \mathbf{J} \tag{5.1}$$



6 **7**

Figure 5.1: Structure of 8MC-R (**6**) and 10MC-R (**7**) in the resonance structures that allow the largest number of unpaired spins.

where **J** represents the density of the ring current. The magnetic field generated by the ring current, albeit weak, modifies the shielding of hydrogens in the molecule and can be observed and studied through NMR. Excellent results have been obtained for porphyrin macrocycles where aromatic and antiaromatic behaviour could be switched by changing the oxidation state of the nanoring [337, 338].

There is also a great physical interest towards ring-like structures. Persistent ring currents have been found in Al single rings with ≈ 400 nm radius [339]. Such inorganic rings can be grown on surfaces with a reasonable control on their sizes, but they cannot surpass the control achievable through synthetic chemistry. Molecular nanorings achieve much higher atomic precision and can be fabricated with radii of the order of nm, which can be beneficial since the intensity of the persistent current is thought to increase with decreasing circumference length. Porphyrin nanoring arrays on Ag surface have been demonstrated to show interesting coherence states [340]. Additionally, rings display remarkable properties for molecular electronics and spintronics. In a molecular circuit, electrons entering a ring component would have two different paths available, i.e. right half and left half. The concept of quantum interference can be applied to this situation and complex patterns can arise from the superposition of the two paths. In particular, it was demonstrated for a conjugated macrocycle in a single molecule transistor, that the conductance is more than the sum of the individual conductance

of the two paths [341]. A similar result was also observed at EPR for a porphyrin nanoring: the exchange coupling between the central spin active copper ions depended on the availability of the two paths, and clear constructive interference could be obtained [342].

Given the interesting properties of (macro)cyclic molecules, a large effort in Wu's group was devoted to synthetise graphenoids with a ring shape and compare aromaticity with the presence of persistent spins [343–346]. Their idea was to produce molecules with an inner and an outer ring that could be defined as "an annulene within an annulene". In a way, we can also see the ring as a thin graphene nanoribbon that forms a closed loop. Non-linearities in the geometry are introduced by pentagonal defects that, as seen in chapter 3, have the ability of introducing local curvature. In this chapter, we study the spin properties of two cyclic molecules of different size: **6** and **7**.

5.2 Magnetic Properties

Powders of **6** and **7** were received in sealed NMR tubes. Upon arrival the samples were measured at CW EPR for magnetic activity, showing the solid state spectra in fig. 5.2. The tubes were opened in the glovebox where we prepared solutions in carbon disulfide (CS_2), and deuterated ortho-terphenyl (d_{14}OTP). All tubes were degassed and flame sealed.

The samples were mostly large flakes, given the electrostatics and the fact that we were using a glovebox it was very hard to measure mg quantities. A scale of UV/Vis absorption depending on the concentration was also not available. Therefore, we are unable to provide a measurement of the concentration and we expect it in the 1-5 mM range. Although it was hard to measure concentration, for CS_2 we could produce different solutions with known concentration ratio. For example, we prepared a solution of **7** in CS_2 and then diluted 8 times. The resulting samples labelled as "high conc" and "low conc" displayed the same CW EPR, and it appeared there were no concentration effects on the quantum properties from fig. 5.5. On the other hand, since d_{14}OTP is not liquid at room temperature and we could not warm it up in the glovebox, we were unable to produce a similar set of data. Later in chapter 6, we present measurements on **6** and **7** that show a degree of instantaneous diffusion (fig. 6.6), which suggests it is likely that concentration had an effect on the properties of the d_{14}OTP samples.

We measured the CW spectra in all conditions as seen from fig. 5.2. The spectra in solution completely agree with what published [347], therefore we concluded that, despite the sensitivity of

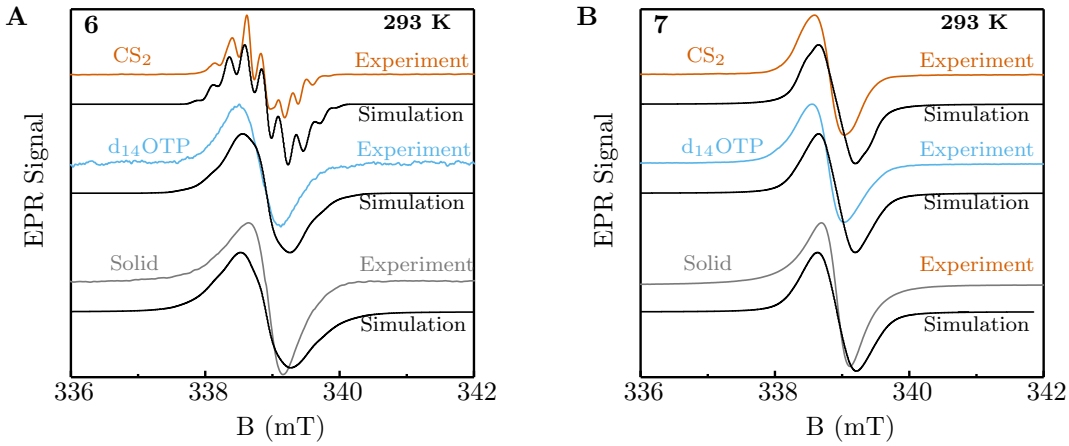


Figure 5.2: (A) Room-temperature CW-EPR of **6** in CS_2 solution, dOTP matrix, and powders. (B) Room-temperature CW-EPR of **7** in CS_2 solution, dOTP matrix, and powders. Black lines are simulations with the model in text.

the samples, shipping of the powders and transfer to the tubes were successful and did not affect the properties of the radicals.

From previous measurements [347] it is known that **6** is in a singlet ground state with singlet-triplet energy gap of -1539 K, while **7** is a triplet ground state with an energy gap of +15 K. We model the CW spectra in fig. 5.2 with the following Hamiltonian:

$$\hat{H} = \mu_B g B \hat{S}_z + \sum_{i=1}^{N} \hat{\mathbf{S}} \mathbf{A}_i \hat{\mathbf{I}}_i \tag{5.2}$$

where N runs among the labelled hydrogen atoms in fig. 5.3 and fig. 5.4.

We use DFT at the CAM-B3LYP/EPR-II level of theory to extract the EPR parameters for **6** and **7**. We include the values for ^{13}C hyperfine coupling as this will be observed later with higher resolution spectroscopic techniques, but they do not play a role in the CW EPR. Any splitting observed is only attributed to hydrogen hyperfine coupling.

We obtain an extremely good simulation of the CS_2 data for **6** using DFT in the triplet state with the parameters in table 5.1. In appendix B.3 we also show spin densities and EPR parameters from DFT calculations for the quintet state and the septet state. The shape of the experimental spectrum can be reproduced quite well in these two cases, but it requires scaling all the hyperfine parameters by constant factors and manually adjust the linewidth (which cannot be predicted by DFT). Therefore, it appears that the CW spectrum more likely points towards a triplet state as also observed by SQUID measurements in [347].

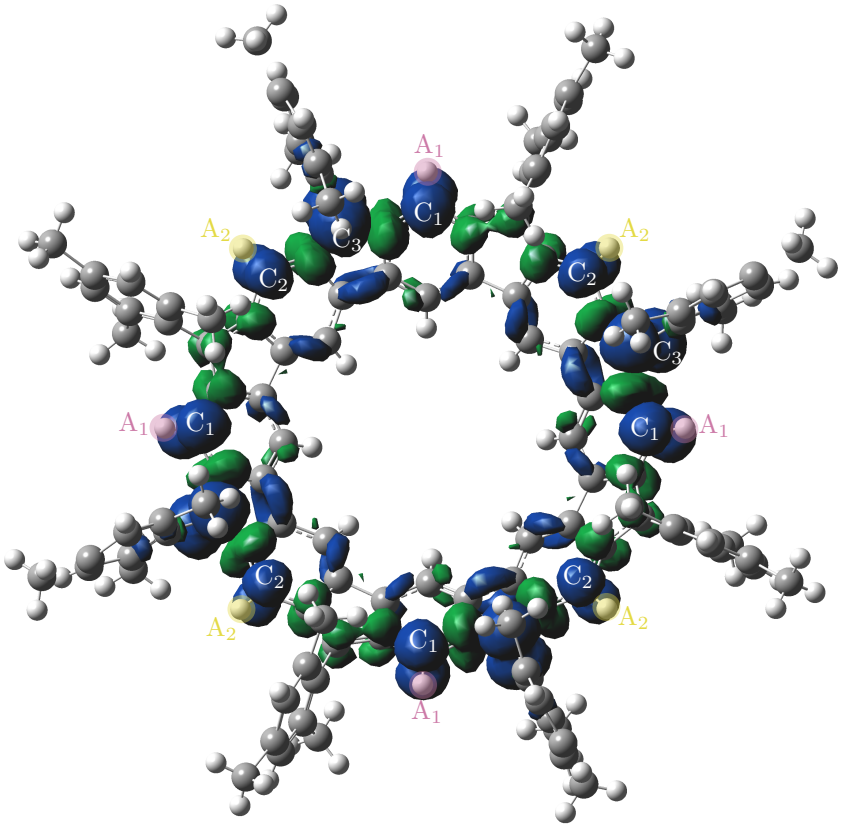


Figure 5.3: Spin density for the triplet state of **6** calculated at the CAM-B3LYP/EPR-II level of theory. Highlighted and labelled are the nuclei with the largest spin density.

Similarly, for **7** we also obtain a good simulation of the solution spectrum from the DFT parameters. However, in the absence of any structure it is not possible to check if the simulation parameters are correct. A more in depth discussion of this will be provided below using more sensitive hyperfine spectroscopy techniques.

For both **6** and **7** no structure is observed in solid state or in d_{14}OTP matrix due to anisotropic hyperfine coupling. However a structure is observed for **6** in solution, but no structure for **7**. This result is comparable to the discussion about **2**, **3**, and **4** in chapter 3, where we argued that the width of the spectrum depends on the strength of the hyperfine coupling which in order is a fingerprint of spin delocalisation. Here, **6** should show a larger hyperfine coupling because the carbon backbone is less extended than in **7** and therefore should show smaller delocalisation, as can also be seen by comparison of the hyperfine parameters in table 5.1 and 5.2.

We observe that the higher symmetry of **6** with respect to **7** is reflected in the spin density maps

6		xx	yy	zz
	S		1	
	g	2.0025	2.0029	2.0029
	A_1 (MHz)	3.01	7.57	13.56
CAM-B3LYP/EPR-II	A_2 (MHz)	2.15	5.10	8.76
	C_1 (MHz)	0.60	0.87	29.02
	C_2 (MHz)	0.84	0.86	19.62
	C_3 (MHz)	3.49	3.87	62.82

Table 5.1: Simulation parameters for **6** from DFT calculations

7		xx	yy	zz
	S		1	
	g	2.0025	2.0027	2.0029
	A_1 (MHz)	2.7	5.4	7.7
	A_2 (MHz)	2.5	4.5	5.5
	A_3 (MHz)	4.2	8.3	11.2
	A_4 (MHz)	3.3	6.4	8.6
	A_5 (MHz)	2.2	4.1	6.1
	A_6 (MHz)	1.2	2.7	3.7
CAM-B3LYP/6-31G**	C_1 (MHz)	22.1	22.4	71.6
	C_2 (MHz)	12.1	12.2	35.9
	C_3 (MHz)	9.7	9.8	27.8
	C_4 (MHz)	9.3	9.3	27.4
	C_5 (MHz)	12.5	12.7	39.0
	C_6 (MHz)	6.8	6.8	18.3
	C_7 (MHz)	8.4	8.7	25.7
	C_8 (MHz)	8.2	8.2	24.9

Table 5.2: Simulation parameters for **7** from DFT calculations. The parameters used for simulating experiments are obtained by multiplying the calculated parameters by a factor 0.85.

in fig. 5.3 and 5.4 and in the hyperfine parameters. For example, **6** has a pair of four equivalent hydrogen nuclei and three sets of four equivalent carbons, while four different hyperfine constants are used to describe the hydrogen in the outer ring of **7** plus two more constants for the inner ring. Overall, there are more inequivalent atoms in **7** than in **6**. This symmetry and topology considerations seem very important because **6** and **7** have extremely different J coupling, since the former is in a singlet ground state and the latter in a triple ground state.

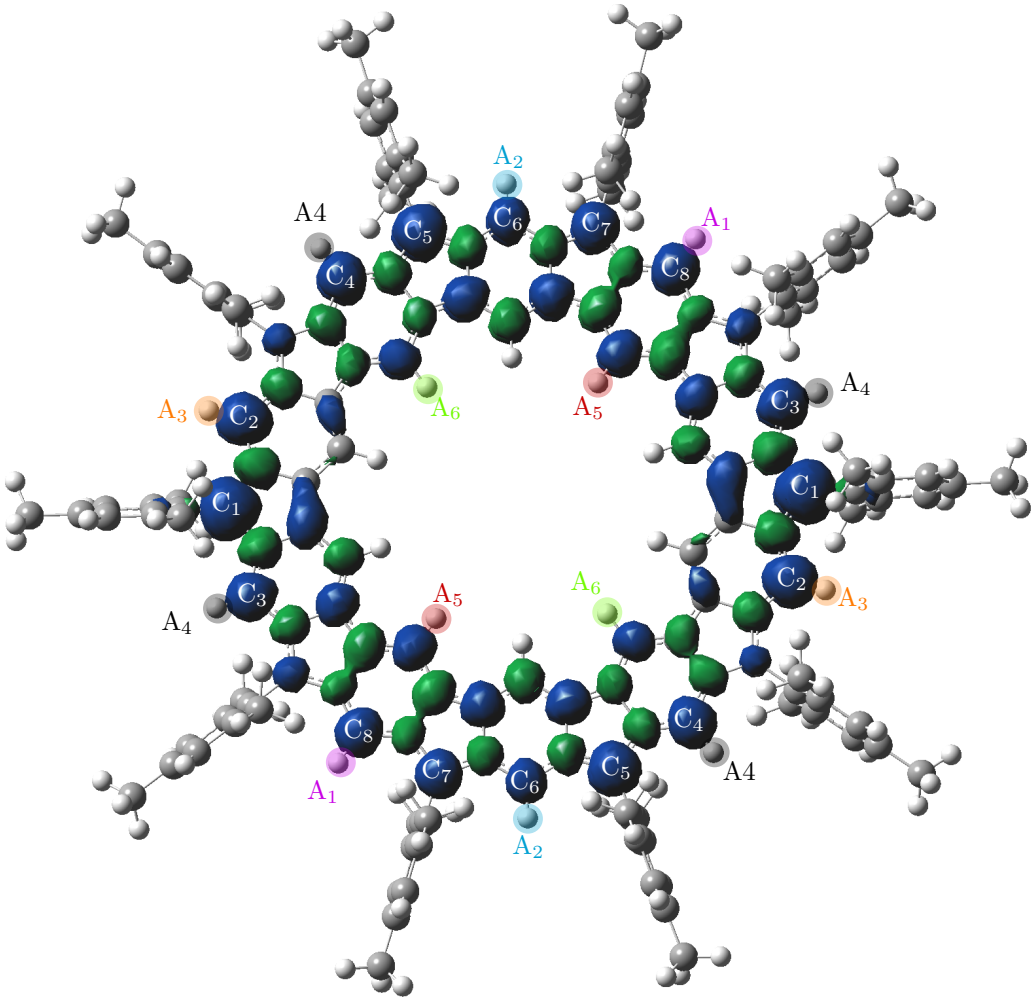


Figure 5.4: Spin density for the triplet state of **7**. Highlighted and labelled are the nuclei with the largest hyperfine coupling.

5.3 Quantum Properties

We measured the quantum properties of **6** and **7** using inversion recovery for T_1 and the Hahn echo sequence for T_m. Spin-lattice relaxation traces were fit with the following bi-exponential

$$Y(T) = A_1 e^{T/T_1} + A_\mathrm{sd} e^{T/T_\mathrm{sd}} + y_0, \tag{5.3}$$

while echo decay traces were fit with a stretched exponential:

$$Y(2\tau) = A \exp\left\{ -\left(\frac{2\tau}{T_\mathrm{m}}\right)^{\beta} \right\}. \tag{5.4}$$

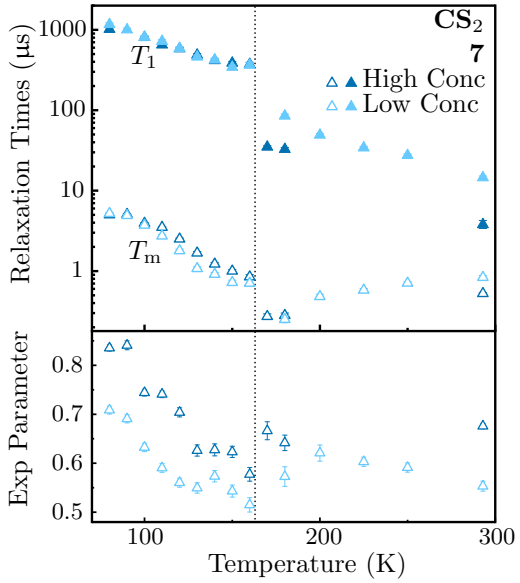


Figure 5.5: Relaxation times comparison between two different samples of **7** in CS_2.

In fig. 5.6 we show the summary of the relaxation constants for both molecules in CS_2 and d_{14}OTP. The spin lattice relaxation rate T_1^{-1} increases monotonically in all conditions with a large jump after the melting point of CS_2 due to change in regime in liquid solution. No differences are observed for T_1^{-1} in the immobilised state for the two matrices used. Conversely, there are differences in the T_m behaviour for the two matrices. In CS_2 T_m decreases almost monotonically between 80 - 160 K due to softening of the matrix, it then increases above the melting point of the solvent because of motional narrowing effects, similarly to what seen in both the previous chapters. In d_{14}OTP, T_m peaks at around 150 K and then decreases. We observe a very sharp decrease above the glass transition temperature of the matrix (243 K). This behaviour is analogous to **1-4** and different from **5**.

It immediately catches the eye that in any condition, **6** consistently outperforms **7**, despite having the same trend. We could qualitatively related their difference in spin-lattice relaxation time to the geometry of the molecules: **6** being bowl-shaped and **7** being fully planar. Nonetheless, it is surprising and against previous arguments that the bowl-shaped molecule presents a slower relaxation than the planar one. Regarding the coherence time, as we are using a stretched exponential, we need to take into consideration both constants. Indeed, we also see that at mostly all temperatures the stretch factor of **6** is larger than the stretch factor in **7**. From a mathematical point of view the two parameters are dependent when doing the fit. This means that by lowering β, the extracted T_m

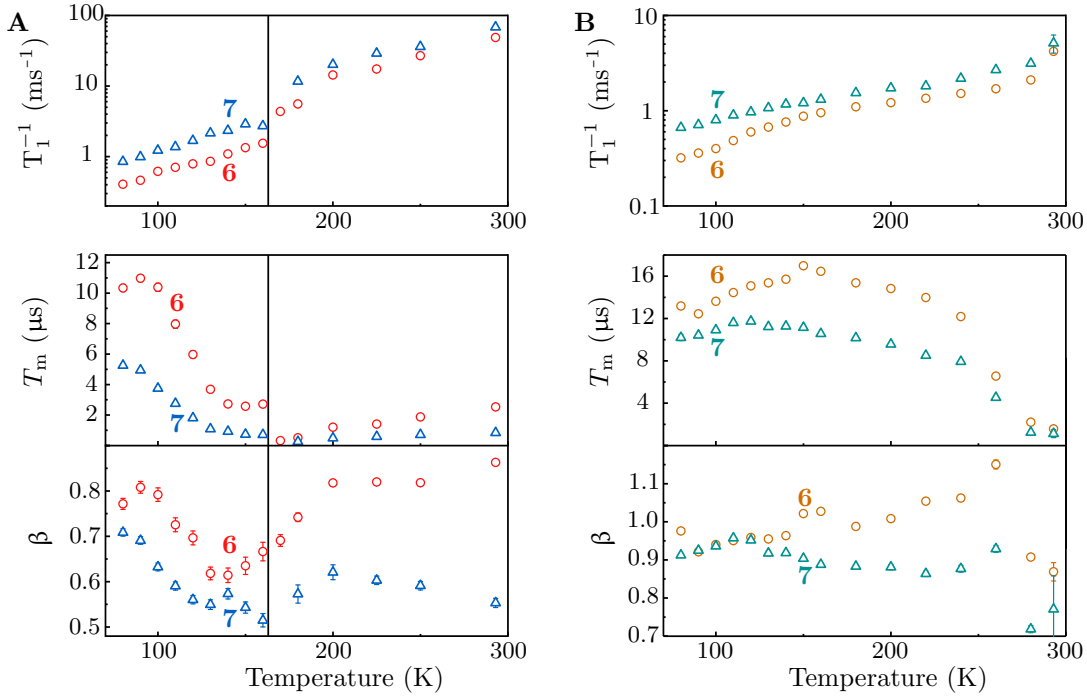


Figure 5.6: (A) Summary of T_1, T_m, and the stretch parameter β for **6** (circles) and **7** (triangles) in CS_2. (B) Summary of T_1, T_m, and the stretch parameter β for **6** (circles) and **7** (triangles) in d_{14}OTP.

will also be lower. The physical reason between the difference in coherence can be attributed to the larger number of bulky mesityl groups in **7** which has two more than **6**. This has a two-fold effect: first, the number of active nuclei in **7** is larger than in **6**; second, the additional mesityl groups will also contribute to molecular motions. On the other hand, we have already pointed out the visible difference in the symmetry of the spin densities of the two compounds. It could be that the edge states in **6** are protected by the higher symmetry with respect to **7**, presenting superior quantum properties.

In fig. 5.7 we present a more in depth analysis of T_1^{-1} in d_{14}OTP and its trend. For both samples around 200 K there is a switch in regime for which the fast recovery starts having a larger weight in the exponential than the slower recovery. With this regime it is hard to uniquely attribute the value of T_1 to the slower decay. Indeed, we observe a change in gradient of the plotted T_1^{-1} data in fig. 5.7A-B. We argue that this means that above 200 K the parameter T_1 is not representative of the spin-lattice recovery of the molecules because it is not the majority channel any more. The predominance of the fast decay could be seen as an artefact of the inversion recovery technique that is usually prone to spectral diffusion. However, even using Picket Fence we did not observe any kind

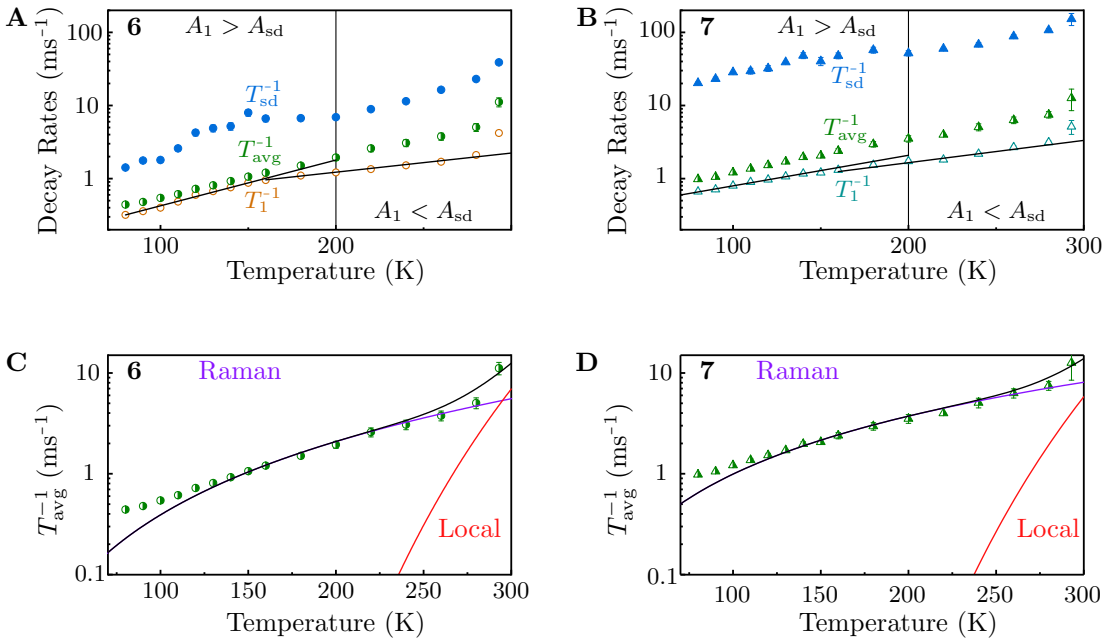


Figure 5.7: (A-B) Trend of T_{sd}^{-1}, T_{avg}^{-1}, and T_1^{-1} for **6** (circles) and **7** (triangles) in d_{14}OTP. The vertical lines mark the temperature difference between the two regimes of $A_1 > A_{sd}$ and $A_1 < A_{sd}$, where A_1 and A_{sd} are weights in the bi-exponential fit. Solid black lines are linear fits to the data. (C-D) Fit of T_{avg}^{-1} for **6** (circles) and **7** (triangles) with the model discussed in text (black line), which is further broken down in the two components: Raman (purple), and local (red).

of improvement. Instead of using T_1^{-1} to fit the behaviour of the spin-lattice relaxation time to a model, we use T_{avg} which we define as the weighted average of the two time constant:

$$T_{avg} = \frac{A_1 T_1 + A_{sd} T_{sd}}{A_1 + A_{sd}}. \tag{5.5}$$

As seen from fig. 5.7, $T_{avg} \approx T_1$ for T< 200 K but it diverges above that temperature. Nonetheless, the trend of T_{avg} remain more constant and therefore it might be more appropriate for fitting.

We find very good fit T_{avg}^{-1} with a model that includes both a Raman process and local modes:

$$T_{avg}^{-1} = CT^n + A_{loc} \frac{e^{\Delta_{loc}/T}}{(e^{\Delta_{loc}/T} - 1)^2} \tag{5.6}$$

where Δ_{loc} is the vibration energy of the bond involved in the process. We also tried the fit with an Orbach process instead of the Raman one, but we obtained a much worse result. The best fit parameters are reported in table 5.3. We find the exponent of the Raman model to be between 2-3 in line with the results obtained in chapter 3 and 4. Differently from all the previous graphenoids, we identify a local mode that contributes to spin-lattice relaxation. We lack infrared spectroscopy

	6	**7**
C (ms^{-1})	5.7×10^{-6}	1.5×10^{-4}
n	2.4	1.9
A_{loc} (ms^{-1})	3.9×10^{7}	2.9×10^{7}
Δ_{loc} (cm^{-1})	3243	3215

Table 5.3: Fit parameters for the curves in fig. 5.7 for **6** and **7**.

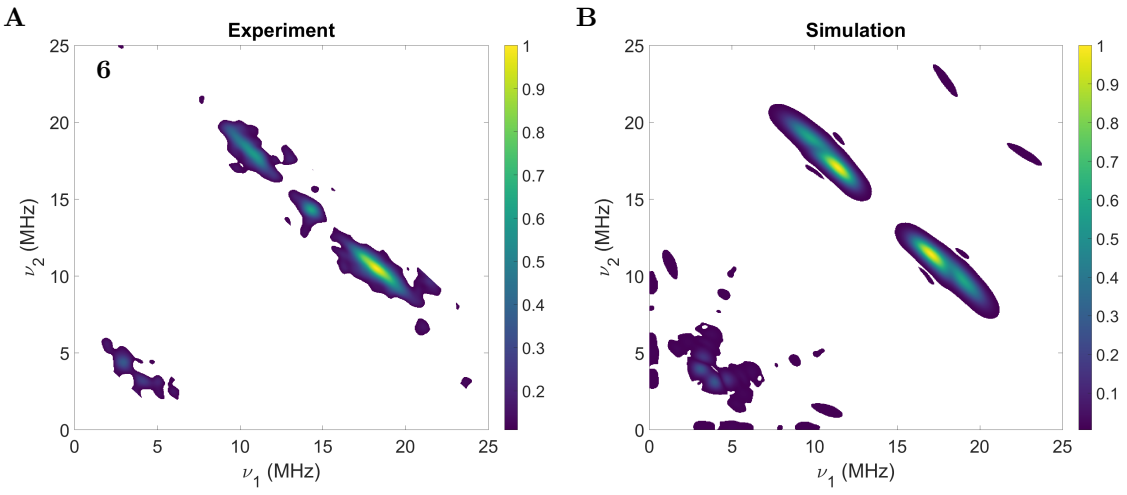


Figure 5.8: (A) HYSCORE experiment for **6** in CS_2 at 80 K. (B) Simulations using the parameters in table 5.1 .

measurements or frequency calculations for **6** and **7**, but from general infrared spectroscopy literature, we found that an asymmetric stretch at wavenumber 2962 cm^{-1} is characteristic of CH_3 groups. Effectively, the number of methyl groups for **6** and **7** is larger than for the graphenoids in the previous chapters. For example, **6** has 24 methyl groups, **7** has 30, **3** has 18, and **5** has 0. The difference between **6** and **3** is not enormous but possibly significant so that no local mode is observed in **3**.

5.4 Hyperfine Spectroscopy

We carried out HYSCORE on **6** and **7** in CS_2 to have a better understanding of the hyperfine structure of the molecules. We used the DFT parameters from table 5.1 and 5.2 to simulate the results.

In fig. 5.8 and 5.9, we show the results at 80 K and the simulations. The results were obtained in the time domain and then transformed into the frequency domain. Processing of the raw data included in order: subtraction of a third order polynomial baseline, apodization with a Hamming

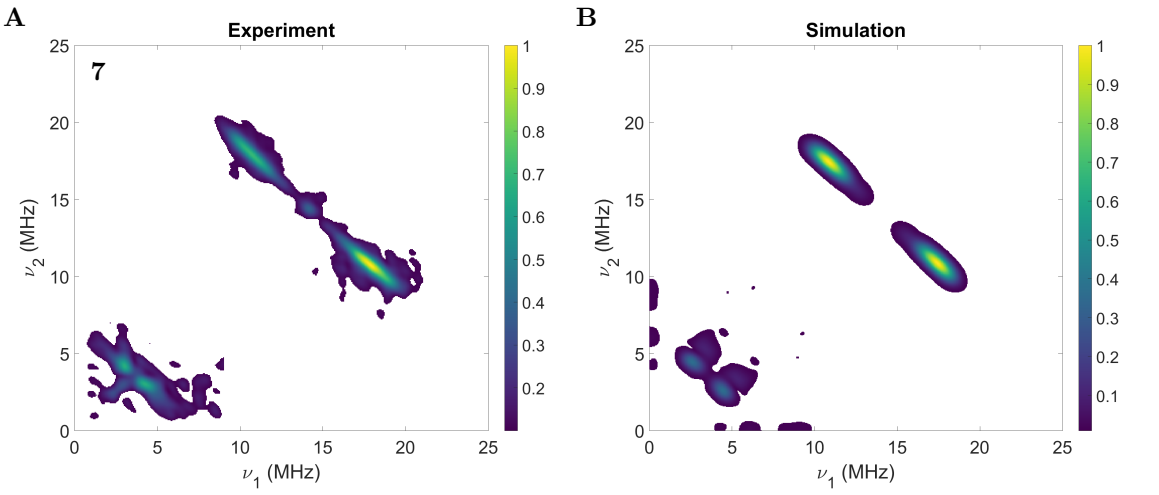


Figure 5.9: (A) HYSCORE experiment for **7** in CS_2 at 80 K. (B) Simulations using the experimental parameters in table 5.2.

function, zero filling to 2048 points, discrete 2D Fourier transformation, and absolute value extraction. Additionally, for clarity, all points that had intensity below 10% of the maximum were rejected and appear as blank. Simulations were obtained by separately calculating the time domain response of the hydrogens (at 14 MHz) and the carbons (at 3.7 MHz), the same processing of the experimental data was applied, and the two Fourier diagrams were then added up. As the intensity of the simulations were strongly imbalanced the carbon intensity was multiplied by a factor of 20. As described in chapter 2, the intensity of the features depends on a numerous factors such as number of nuclei involved, Larmor frequency, and magnitude of the coupling, here we focus more on the position of the peaks instead of their intensity, therefore the arbitrary scaling of the carbon features will not affect the analysis.

The features relative to the hydrogen nuclei are made of two components. A single peak on the diagonal of the quadrant and two peaks symmetric with respect to the diagonal. The single peak can be related to hydrogens with hyperfine coupling < 1 MHz, which are all the nuclei belonging to the methyl groups plus some of the hydrogens in the inner ring. The two broader features are representative of the hydrogens bearing the largest hyperfine coupling that are also those labelled in fig. 5.3 and 5.4. We have not included the very weakly coupled nuclei in the simulation as their low contribution does not allow resolution of their values.

It is more difficult to assess the effect of ^{13}C nuclei. The DFT parameters suggest that the carbons are strongly coupled. Strongly coupled nuclei should show features in the fourth quadrant at

negative ν_1 and positive ν_2, whereas no particular signal is observed in the fourth quadrant except for artefacts of the π pulse. Even though the simulations represent the carbon feature quite well in the first quadrant (the one showed in fig. 5.8 and 5.9), it does not necessarily mean that those are effectively the active carbons. Indeed, it could well be the signal of other more weakly coupled nuclei in the molecule or even, more likely, weakly dipolarly coupled nuclei from the solvent.

We repeated the HYSCORE measurement at 150 K for both samples as well. We were interested in seeing if at higher temperatures averaging of nuclear hyperfine coupling due to molecular motion would produce a different trace, therefore confirming the role and nature of such motions. However as can be seen in appendix B.3, the HYSCORE data at 150 K are analogous to the ones at 80 K but with less resolution due to reduced signal-to-noise ratio at higher temperature. We are unable to observe a difference because the nuclei responsible for the broad features are not involved in molecular motions. The hydrogens in methyl groups, which are more likely going to average out, only contribute to the central blob that also include all other very weakly coupled nuclei for which we lack resolution. Since the hydrogen nuclei are so numerous and with such close hyperfine constants, it is unlikely that any other technique, for example ENDOR, would be able to shine light on this problem.

5.5 Outlook

In this chapter, we studied the quantum properties of graphenoid macrocycles with pentagonal defects that allow a polyradical character. With DFT and hyperfine spectroscopy we assessed that the majority of the spin density is concentrated on the outer ring. Differently from the other graphenoids in this thesis, we found out that the spin-lattice relaxation time at high temperature is affected by a sharp increase which we attributed to local modes of methyl groups.

The different topology of the two compounds give rise to different symmetries of the spin density. This can be clearly seen in fig. 5.3 and 5.4. We suggested that this is the reason why the two compounds show such different properties. First, **6** is in the singlet ground state, while **7** is in the triplet ground state. Second, the quantum properties of **6** are superior with respect to **7**. At this point, this has only descriptive value, but we are collaborating to obtain more quantitative theories on the effect of topology in the two molecules.

5.6 Project Overview

This project was carried out in collaboration with the group of Prof Jishan Wu at the National University of Singapore. The synthesis of the molecules here presented was published in [347]. The synthesis of the samples used for the measurements was carried out by Dr Fan Wei at NUS. All EPR measurements were carried out at CAESR.

Improving Coherence

6.1 Introduction

Current limitations to the performance of molecular graphenoids are to be attributed to environmental nuclei that are strongly detrimental to electron spin coherence. There are numerous approaches that can be used to mitigate the decohering effect of nuclei, namely: isotopic enrichment, clock transitions, and dynamical decoupling. The first approach is intuitively the most effective [62, 63, 348, 349], but it is also highly costly. In addition to this, not all elements have nuclear-spin free isotopes. For example, hydrogen, which is ubiquitous in graphenoids, does not have a spin-free isotope, although deuterium has a much lower gyromagnetic ratio.

Clock transitions are special avoided crossing points where the magnetic field becomes insensitive to fluctuations in first order. In numerous systems, working around clock transitions has resulted in strong increase of coherence [66, 68, 69]. Nevertheless, clock transitions are not present in all complexes: they are usually related to systems with strong hyperfine couplings or zero field splittings, and it is usually very challenging to rationally synthesise systems with these properties [350].

Both previous methods require engineering on the fabrication or chemical composition of the device. On the other hand, dynamical decoupling (that can also be used in conjunction with any of the previous two ideas) shifts the engineering on the control instead than the system itself. Dynamical decoupling consists in applying a sequence of n π pulses at times t_k in order to reverse the destructive effect of the environment on quantum coherence. Decoupling sequences were initially developed for ensemble magnetic resonance experiments in order to refocus the signal and eliminate inhomogeneous broadening, and only in recent years quantum theory was applied to rationalise their effect of preserving coherence [70, 351].

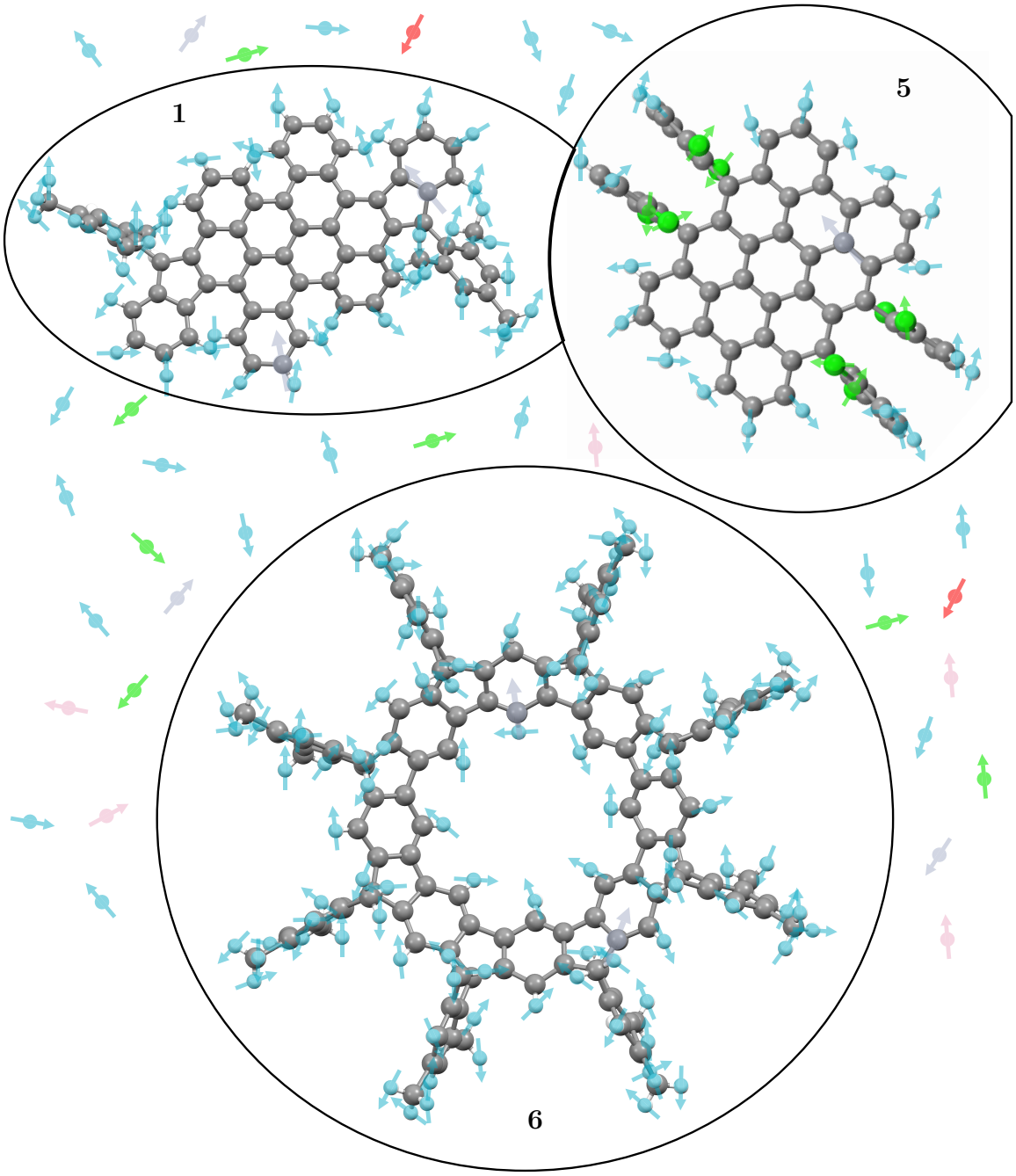


Figure 6.1: Nuclear spins are ubiquitous and destructive to quantum coherence. Homonuclear flip-flops modulate the local magnetic field perceived by the electron spin. The large density of nuclear spins at the edges of the molecules studied in this thesis is the main channel of decoherence. Additional interactions are provided by the environmental nuclei in the host or matrix. In the figure, different nuclei are represented by different colors, for example H = cyan, Cl = green, and ^{13}C = gray.

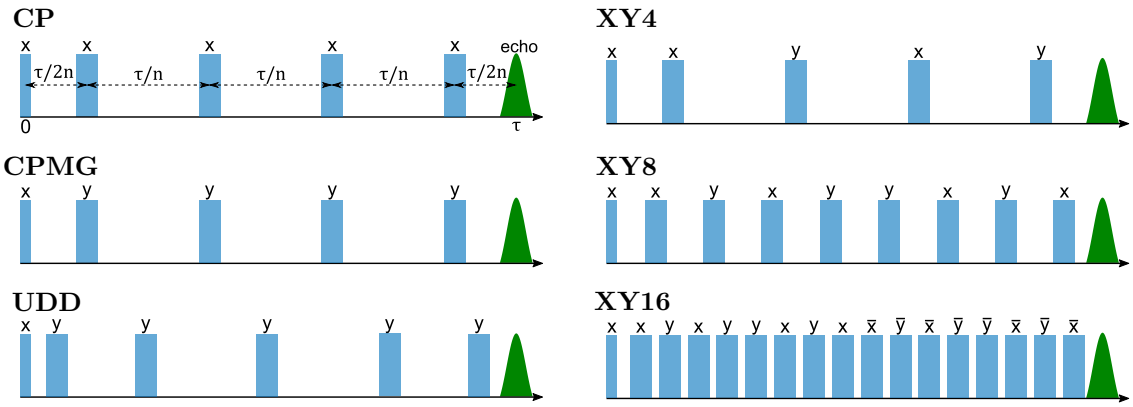


Figure 6.2: Dynamical decoupling sequences: the first pulse is a $\pi/2$, while the decoupling train is made of π pulses. The letters above the pulses indicate the channel used.

The simplest dynamical decoupling sequence is the Hahn echo that applies a single refocusing π pulse [253], which is sufficient to remove any static noise. The CP (Carr-Purcell) sequence increases the number of π pulses to arbitrary n [352], while the Carr-Pucell-Meiboom-Gill (CPMG) sequence improved CP by modifying the phase of the π pulses in order to be perpendicular to the first pulse [353]. Having a fix phase difference of 90° between the initial $\pi/2$ pulse and the decoupling pulses removes pulse formation errors, and several experiments established that CPMG always outperforms CP [354]. Further improvements were obtained by alternating multiple phase pulses with XY4, XY8, XY16 [355, 356]. The sequences of the XY family do not require a stringent phase condition between the first pulse and the train of π pulses due to the multi-axis decoupling, and they were demonstrated to be robust against any initial condition [354].

All the previous sequences have in common that the interpulse spacing is kept constant in the sequence (fig. 6.2), so that they are often referred as periodic dynamical decoupling (PDD). Theoretical understanding of dynamical decoupling led to the development of sequences with unevenly spaced pulses whose positions can be optimised to increase the coherence. Ühring analytically constructed a new sequence (UDD) [357] to maximise the perfomance in a bosonic environment. Later the UDD sequence was demonstrated to be universal [60]. Concatenated dynamical decoupling (CDD) was showed to be able to naturally correct pulse formation errors arising in PDD by concatenating blocks of pulses up to higher orders [358]. An alternative approach to a pulsed control is provided by continuous dynamical decoupling, where a continuous drive is used to produce long lived dressed states [359]. More recently, such approach has been also used in contingency with pulsed control [360]. Nonetheless, the complexity added by uneven spacing or continuous microwave fields is not

always matched by substantial performance increase with respect to PDD [354]. Therefore, most of the experimental results still rely on the less sophisticate CPMG which produced exciting results in a plethora of quantum systems such as NV centres [348, 361, 362], trapped ions [363], and GaAs quantum dots [364].

In the previous chapters we have recognised and described the effect of nuclei on the coherence of the different graphenoids we studied. In this chapter, we retrieve some of the molecules discussed before, namely **1**, **5**, **6**, and **7**, and we apply dynamical decoupling sequences to improve their coherence. First, we present a semi-classical model that describes nuclear noise as a random classical variable. Second, we discuss possible complications when using dynamical decoupling in ensemble EPR. Finally, we perform CPMG on the four compounds mentioned. We analyse how coherence improves at different temperatures and in different matrices and we use a unified model to refer the decay rate to the main channels of decoherence.

6.2 Theoretical Modelling

For all the systems in this thesis we have defined an analogous Hamiltonian that we repeat here:

$$\hat{H} = \hat{H}_S + \hat{H}_{SB} + \hat{H}_B = J\hat{\mathbf{S}}_\mathbf{1}\hat{\mathbf{S}}_\mathbf{2} + \mu_\mathrm{B} g B \hat{S}_z + \hat{\mathbf{S}}_\mathbf{1}\mathbf{D}\hat{\mathbf{S}}_\mathbf{2} + \sum_{i=1}^{N} \hat{\mathbf{S}}\mathbf{A}_i\hat{\mathbf{I}}_i + \sum_{i}^{N} g_\mathrm{n}^{(i)}\mathbf{B}\hat{\mathbf{I}}_i + \sum_{i,j}^{N} \hat{\mathbf{I}}_i\mathbf{P}_{i,j}\hat{\mathbf{I}}_j. \quad (6.1)$$

We can exclude some terms from the Hamiltonian using the knowledge that we have for these molecules: the large exchange coupling J places the systems in the high-exchange regime; at the magnetic field of our experiments, the Zeeman term dominates the dipolar one by several orders of magnitude. Therefore, the spin can be considered quantised on the axis of the magnetic field and the system Hamiltonian can be simplified as:

$$\hat{H}_S = \Omega \hat{S}_z, \quad (6.2)$$

where we considered the experiment in a rotating framework so that $\Omega = \omega_S - \omega_{MW}$.

The system-bath (hyperfine term) and bath Hamiltonians (nuclear Zeeman and nuclear-nuclear dipolar coupling) can also be simplified assuming a pure dephasing regime [365, 366], which is true since for all molecules we observed $T_1 \gg T_\mathrm{m}$ in the diluted solid state. Thus, the total Hamiltonian

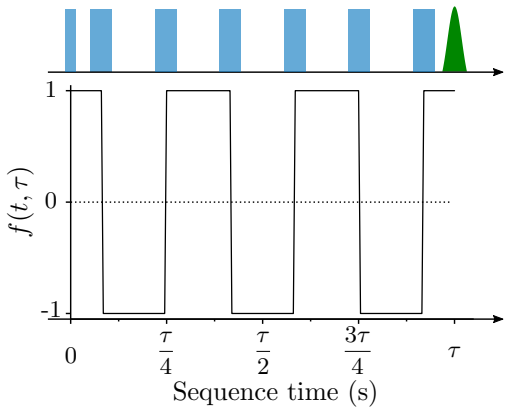


Figure 6.3: Shape of the time domain filter function for a CPMG6 decoupling sequence

can be written as:

$$\hat{H}(t) = [\Omega + \beta(t)]\hat{S}_z, \tag{6.3}$$

where $\beta(t)$ is a classical random variable. This semi-classical model describes the effect of the bath as a fluctuating modulation of the resonant frequency of the spin system. It can be related to the Overhauser field produced by flip-flop of neighbour nuclear spins, which modify the local magnetic field perceived by the central spin. Therefore, the quantum origin of this classical noise can be fully mapped in the intra-bath dynamics [367].

Here, we assume $\beta(t)$ to be Gaussian. Such assumption relies on the pure dephasing regime, on the fact that the noise is produced by an ensemble of weakly interacting systems, and it has been theoretically validated before [368]. Effects arising from a non-Gaussian behaviour of $\beta(t)$ are discussed in [369] and will be disregarded here. Therefore, we can write:

$$\langle \beta(t) \rangle = 0, \tag{6.4}$$

$$\langle \beta(t)\beta(t+t') \rangle = g(t'), \tag{6.5}$$

where g is the autocorrelation function. The Fourier transform of g is the spectral density function that completely describes the noise spectrum of the nuclear bath

$$S(\omega) = \int_{-\infty}^{+\infty} g(t) e^{-i\omega t} \mathrm{d}t. \tag{6.6}$$

It was showed [365, 366] that for a spin system under the general noise spectrum of $S(\omega)$, the

effect of a π pulse in the control sequence is to flip the sign of the phase accumulation. For n arbitrary pulses we can write the evolution of the phase as:

$$f(t,\tau) = \sum_{k=0}^{n} (-1)^k \Theta(t - t_k)\Theta(t_{k+1} - t), \tag{6.7}$$

where $t_0 = 0$, $t_k = \frac{(k-1/2)\tau}{n}$, $t_{n+1} = \tau$, and $\Theta(t)$ is the Heaviside step function. An example of this function for CPMG6 is presented in fig. 6.3. We can then write the Fourier transform of eq. (6.7) to obtain the equation of a filter function, which behaves as a high pass filter that cancels out low frequency noise. Such filter is centred at $\omega_0 = \pi n/\tau$, with a width of π/τ and higher harmonics components that let high frequency noise through. Nonetheless, assuming that $S(\omega)$ goes to 0 at high frequency, the filter can become very efficient by decreasing τ and increasing n that corresponds to a bang-bang control regime. The decoherence behaviour of the system will then depend on the convolution between the characteristic spectral density and the filter function of the applied control:

$$\chi(\tau) = \frac{1}{2\pi} \int_0^\infty S(\omega) \left| \widetilde{f}(\tau,\omega) \right|^2 \mathrm{d}\omega \tag{6.8}$$

$$= \frac{1}{\pi} \int_0^\infty S(\omega) \frac{F(\tau,\omega)}{\omega^2} \mathrm{d}\omega, \tag{6.9}$$

where $\widetilde{f}(\tau,\omega)$ is the Fourier transform of $f(t,\tau)$. Therefore, for any value τ

$$W(\tau) = e^{-\chi(\tau)}. \tag{6.10}$$

6.3 Methods Discussion

We deem the discussion of methods relevant since the magnetic-resonance literature presents some uncertainty for the results of CPMG. In NMR, Dementyev et al. and Li et al. observed a long tail decay for Si nuclei in solid state undergoing CPMG, which was considered very surprising [153, 370, 371]. After thorough calculations, such a long decay, which also included an even/odd effect, was attributed to the non-ideality of π pulses that have a finite length during which the system's time-dependent Hamiltonian is active [153, 371]. The problem of non-ideality should be much less relevant in EPR than in NMR, because the pulses used are $\sim$ 10 ns long, while in NMR they are in the order of µs. On the other hand, the EPR literature suggest that a CPMG sequence can lead to a

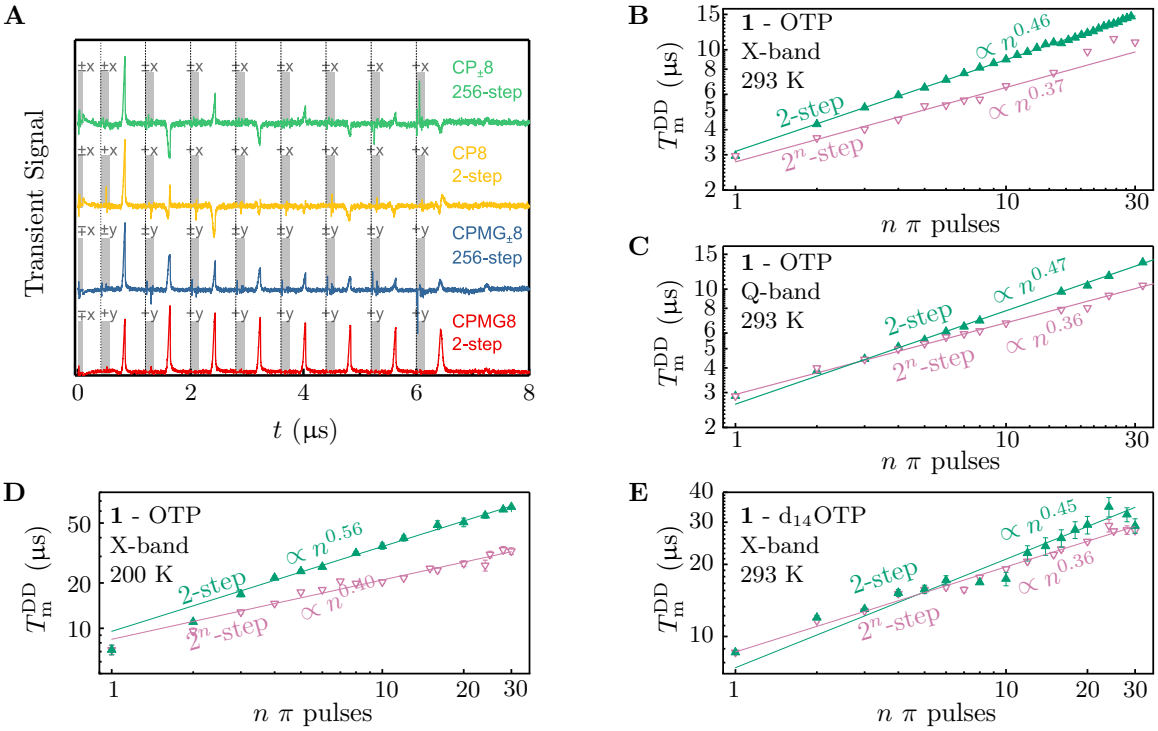


Figure 6.4: (A) Recording of the echo signals for CP and CPMG decoupling sequences using a phase cycling on the first pulse only and on all pulses (indicated with ±), at 293 K for **1** in OTP. The pulse positions are indicated in gray, together with their channel and the phase cycling used. (B) Results for the 2-step (up triangles) and 2^n-step (down triangles) phase cycling for **1** in OTP at 293 K at X-band. (C) Results for the 2-step (up triangles) and 2^n-step (down triangles) phase cycling for **1** in OTP at 293 K at Q-band. (D) Results for the 2-step (up triangles) and 2^n-step (down triangles) phase cycling for **1** in OTP at 200 K at X-band. (E) Results for the 2-step (up triangles) and 2^n-step (down triangles) phase cycling for **1** in d_{14}OTP at 293 K at X-band.

spurious signal that overlaps with the echo when the bandwidth of the pulses is not sufficient to excite the entirety of the spectrum [372], which in contrast does not happen in NMR. In order to avoid this occurrence, several EPR papers have proposed more advanced cycling of the pulse phases [255, 373, 374]. However, here we deal with molecules that have spectra roughly 1.5 mT wide, while the bandwidth of a 16 ns rectangular pulse is 1.33 mT, which should be enough to excite the large majority of the spectrum. Additionally, we also tried 8 ns pulses obtaining the same results.

Bearing in mind the discussion in the EPR literature, we clarify the CPMG results in our samples that have a very narrow spectrum. Here, we compare a situation where a 2-step phase cycling is used (standard CPMG), i.e. only phasing the first pulse on the $\pm x$ channel, and a 2^n-step phase cycling (n is the number of π pulses in the decoupling train) where all pulses are phased on their ± channel except the last one, so that all possible phase relationships are covered,[1] we refer to the latter as

[1]There are limitations to the number of steps that can be performed, with each additional pulse increasing the measurement time exponentially. We determined that reasonable measurement times would be obtained up until a

$CPMG_{\pm}$. We tested their difference for **1** in two different matrices, at different temperatures, and at different microwave frequencies.

In fig. 6.4A, we compare the transient echoes of the different phase cycling for both CP and CPMG in an 8-pulse decoupling sequence with the same interpulse spacing (analogously to $CPMG_{\pm}$ we have called $CP_{\pm}$ the sequence entailing a 2^n phase cycling based on CP). When one observes the decay of the echo intensity at different times, the results show that the CPMG sequence with a 2-step phase cycling presents the slowest decay, the CP with 2-step phase cycling the fastest decay, and the two sequences with 256-step cycling are in the middle with the exact same decay trend, but different sign of the echoes. It is established that a CP sequence performs worse than CPMG [354], this is because having the pulse axis longitudinal (phase y) removes the pulse errors that are otherwise present with the pulse axis transverse (phase x) with respect to the spin vector. However, it is surprising that by introducing a more complete phase cycling, not only we remove the possible spurious signal but we also equalise CP and CPMG. In a way, the results show that the 2^n-step phase cycling makes the sequence more robust to the initial condition but less performing.

Figure 6.4B-E prove that the difference between the 2-step and the 2^n-step is consistent even when varying the number of pulses. The two set of data can be fit with a polynomial function based on the number n of π pulses:

$$T_{\mathrm{m}}^{DD}(n) = T_{\mathrm{m}} n^{\gamma} \tag{6.11}$$

where T_{m} and γ are free parameters. We discuss the performance of a pulse sequence looking at the term n^{γ} which we refer to as enhancement factor: the larger γ, the higher performing the sequence. Keeping the temperature constant we do not obtain any difference even going to higher magnetic fields and frequencies (Q-band is 34 GHz). Even changing the temperature to 200 K or switching samples to the d_{14}OTP matrix, the result is always that the CPMG prolongs the coherence time more than $CPMG_{\pm}$. On the other hand, the performance of the $CPMG_{\pm}$ experiment in terms of the γ exponent is analogous to the XY sequences. There are multiple instances in the literature where CPMG is found to offer better decoupling than XY, but with stronger dependence on the initial conditions [354, 375]. Therefore, we conclude that, for a sample with a narrow spectrum that is well excited by a short $\pi/2$ pulse, a 2-step pulse cycling is sufficient to remove spurious signals, while

256-step phase cycling, but anything above would become cumbersome. Therefore, we established a cycled approach for which we decompose a sequence of $n > 8$ pulses into equal blocks of 3, 4, or 5 π pulses, for which we apply an 8-step, 16-step, and 32-step phase cycling. While this is not the same as a 2^n-step phase cycling, the results in fig. 6.4B-C for $n > 8$ are coherent with what observed for the full phase cycling.

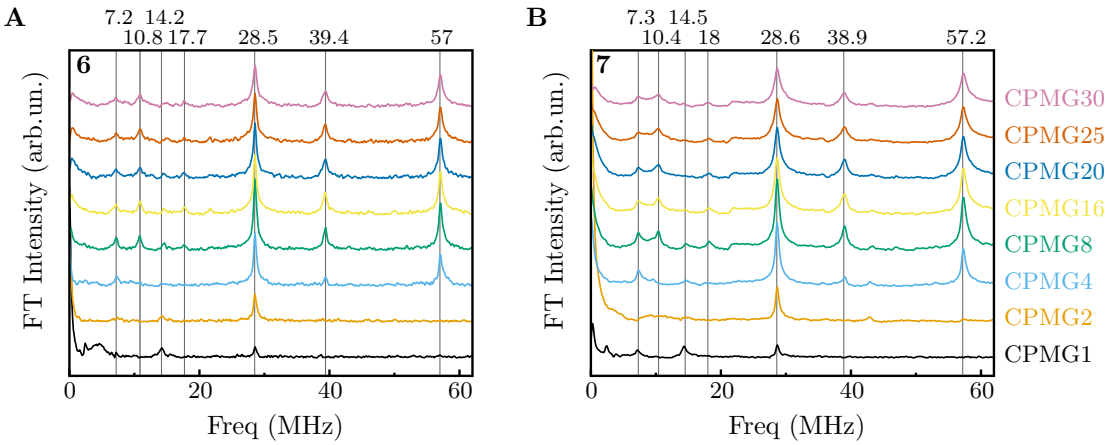


Figure 6.5: (A) Fourier Transform intensity of the modulation of the time decay for **6** in CS_2 at 80 K as a function of the number of pulses applied. (B) Fourier Transform intensity of the modulation of the time decay for **7** in CS_2 at 80 K as a function of the number of pulses applied.

the 2^n-step cycling removes dependency on the initial condition mimicking the effect of pulses on both axis, but at the cost of a reduced performance. Additionally, the 2^n-step phase cycling is more costly than the XY sequences, which can achieve the same result but without the complexity of large number of cycles. In the following, we omit the results related to $CPMG_{\pm}$ as we deem them redundant with respect to XY sequences.

While measuring the increase in coherence when using a larger number of decoupling pulses, we also observed that the modulation depth was varying depending on the number of pulses. In particular, CPMG sequences are still prone to ESEEM modulation and they are even able to amplify it, which had already been reported and studied in [374]. In fig. 6.5, we show the increase of modulation depth for a train of pulses for **6** and **7** in CS_2 at 80 K. The label CPMG1 corresponds to the Hahn echo sequence, for which the modulation is very weak since CS_2 is mostly nuclear free, hydrogen modulation is only produced by the nuclei in the molecule, and some ^{13}C modulation is visible. Increasing the number of pulses, the modulation depth increases monotonically up until CPMG8 and then it slowly decreases. Overall, the spectrum of frequencies obtained is not very informative: as for the 2-pulse ESEEM, the spectrum is sensitive to higher harmonics and combination frequencies, which makes it very hard to deconvolute.

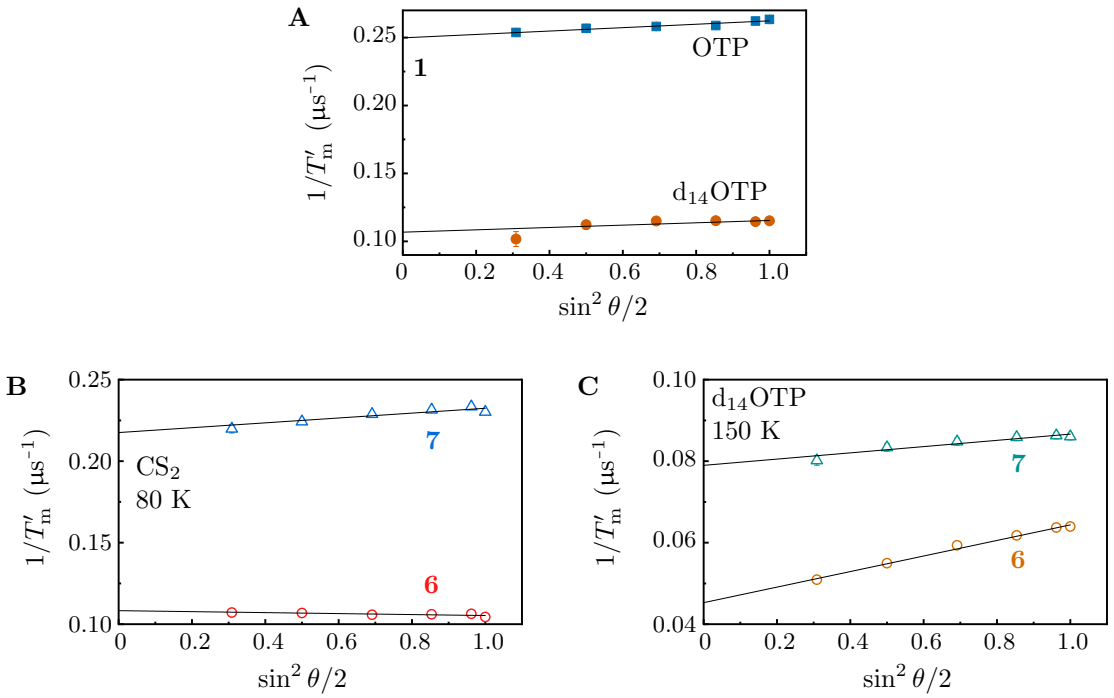


Figure 6.6: (A) Effect of instantaneous diffusion on the coherence time of **1** in OTP (squares) and d_{14}OTP (circles) at 293 K. (B) Effect of instantaneous diffusion on the coherence time of **6** (circles) and **7** (triangles) in CS_2 at 80 K. (C) Effect of instantaneous diffusion on the coherence time of **6** (circles) and **7** (triangles) in d_{14}OTP at 150 K. θ refers to the turning angle of the second pulse in the echo sequence, $\theta = 180°$ corresponds to a π pulse. Black lines are linear fit, the coherence time in absence of instantaneous diffusion is obtained by the y intercept of the linear regression.

6.4 Results

6.4.1 Instantaneous Diffusion

In the previous chapters, when discussing quantum coherence, we have disregarded instantaneous diffusion, which, in the case of a spin ensemble, can contribute to lower T_m. In the Hahn echo sequence, the application of the second pulse can lead to spin flip-flops for coupled electron spin pairs, implying that the local resonant field of the excited spin will be different before and after the pulse, which is a source of decoherence. The rate of instantaneous diffusion is proportional to the concentration of electron spin and to the turning angle of the second pulse:

$$\Gamma_{id} = C\frac{\pi}{9\sqrt{3}}\frac{\mu_0 g_1 g_2 \mu_B^2}{\hbar}\sin^2\frac{\theta}{2} \tag{6.12}$$

where C is the concentration, θ the turning angle, and the other parameters follow previous definitions [26, 254].

Generally, instantaneous diffusion should not be a problem for our molecules since the nominal concentration is usually in the 1-2 mM range, but being singlet ground states the electron spin concentration is much lower. Nonetheless, we can check for instantaneous diffusion. Let's consider that in an experiment we are able to extract a coherence time that we will name T'_{m}, if we take its reciprocal, we obtain the decoherence rate, which in turn is just the sum of the rate of "true" decoherence (T_{m}) plus the rate of instantaneous diffusion as defined in eq. (6.12):

$$\frac{1}{T'_{\mathrm{m}}} = \frac{1}{T_{\mathrm{m}}} + C\frac{\pi}{9\sqrt{3}}\frac{\mu_0 g_1 g_2 \mu_{\mathrm{B}}^2}{\hbar}\sin^2\frac{\theta}{2}. \tag{6.13}$$

Since the true coherence time T_{m} should be constant, and all the parameters of the sample are constant, the previous equation can be written in a more concise linear fashion:

$$\frac{1}{T'_{\mathrm{m}}} = \frac{1}{T_{\mathrm{m}}} + m\sin^2\frac{\theta}{2}, \tag{6.14}$$

which shows that we can measure T'_{m} at different turning angles and then extrapolate for $\theta = 0$, obtaining the true coherence time T_{m}.

Figure 6.6 shows instantaneous diffusion measurements for **1**, **6**, and **7**. We can see very mild effects of instantaneous diffusion in **1** in OTP and d_{14}OTP, and in **6** and **7** in CS_2, that amount to roughly 7% increase of T_{m}. Reducing the turning angle of the second pulse also produces a sharp decrease in signal which implies a larger error on the determination of the coherence time, which might be larger than the reported increase. However, a sharp increase of more than 50% is observed for **6** and **7** in d_{14}OTP (fig. 6.6C). As mentioned in chapter 5 these two samples were very high concentrated, therefore they show large contribution of instantaneous diffusion.

6.4.2 Decoupling

In fig. 6.7 we show the results at 200 K and 293 K for **1** in OTP and d_{14}OTP, all time constants were obtained fitting a stretched exponential decay keeping the exponential factor constant when varying the number of pulses. We used sample **1** as a test of all the periodic decoupling sequences. We observe that pulses in the XY family perform very similarly and all of them below CPMG. This is compatible with what demonstrated by the literature [354], therefore for all the other samples we only used CPMG sequences since they allow the largest decoupling.

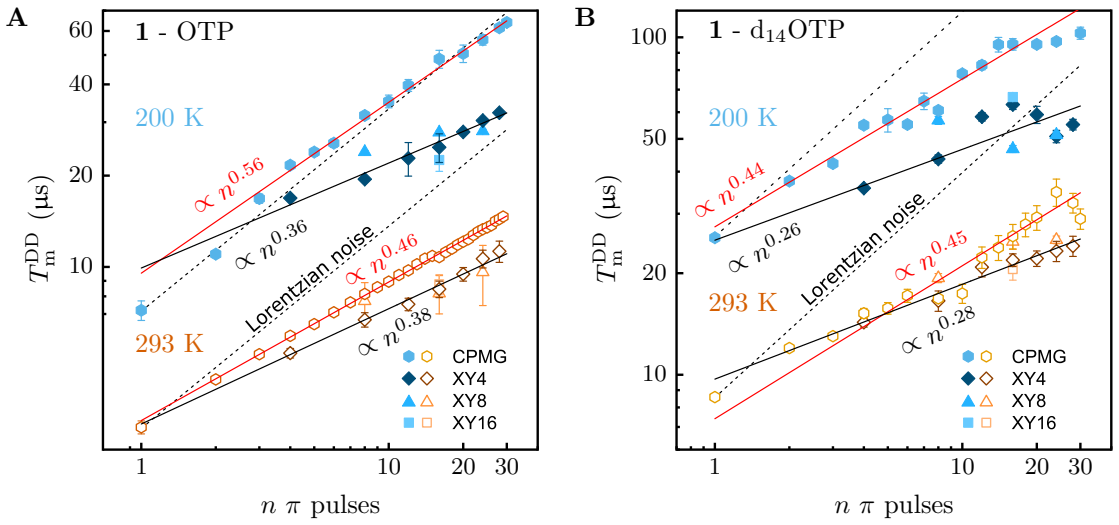


Figure 6.7: (A) Summary of the decay times for different sequences for **1** in OTP at 200 and 293 K. (B) Summary of the decay times for different sequences for **1** in d_{14}OTP at 200 and 293 K. Solid lines are fit to the data with the model in eq. (6.11). Dashed line marks the time constant scaling with an enhancement factor $n^{2/3}$.

In fig. 6.8 we show the results for **5** at X-band and Q-band in CS_2. As done also in chapter 4 we present both the results of stretched exponential fitting and bi-exponential fitting. For fig. 6.8A the stretched parameter was kept constant when changing the number of pulses. Due to the nature of the two models used, the magnitudes of the parameters extracted are very different, but the trend observed with respect to the number of pulses is analogous.

In fig. 6.9 we show results for **6** and **7** in CS_2 at 80 K and d_{14}OTP at 150 K. The time constants were extracted with a stretched exponential with the stretched parameter constant when varying the number of pulses.

6.5 Discussion

In the previous chapters we have discussed the decoherence channels that affect our graphenoids, here we tie up together all results and explain the decoherence rate Γ in terms of a sum of four contributions:

$$\Gamma = \Gamma_{NSD} + \Gamma_{motion} + \Gamma_{id} + \frac{1}{2T_1}, \tag{6.15}$$

where Γ_{NSD} refers to nuclear spin diffusion (NSD), Γ_{motion} is the contribution of molecular motions, and Γ_{id} of instantaneous diffusion. We have already mentioned that $T_1 \gg T_m$ so we can disregard the latter term at any temperature, as per assumption of pure dephasing. We know that the NSD

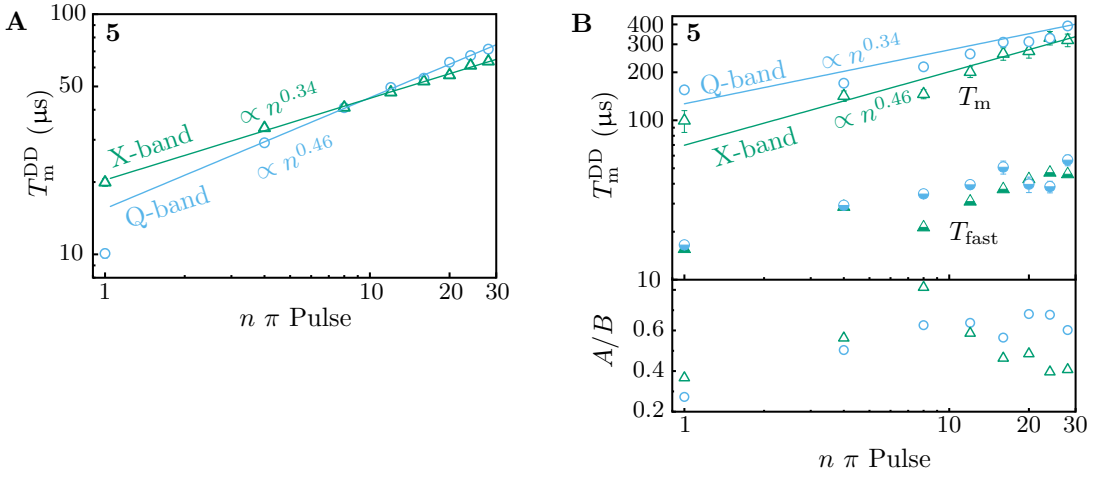


Figure 6.8: (A) Summary of the decay times for different sequences for **5** when fit with a stretched exponential decay. (B) Summary of the decay times for different sequences for **5** when fit with a bi-exponential decay. The two models and their significance are discussed in chapter 4

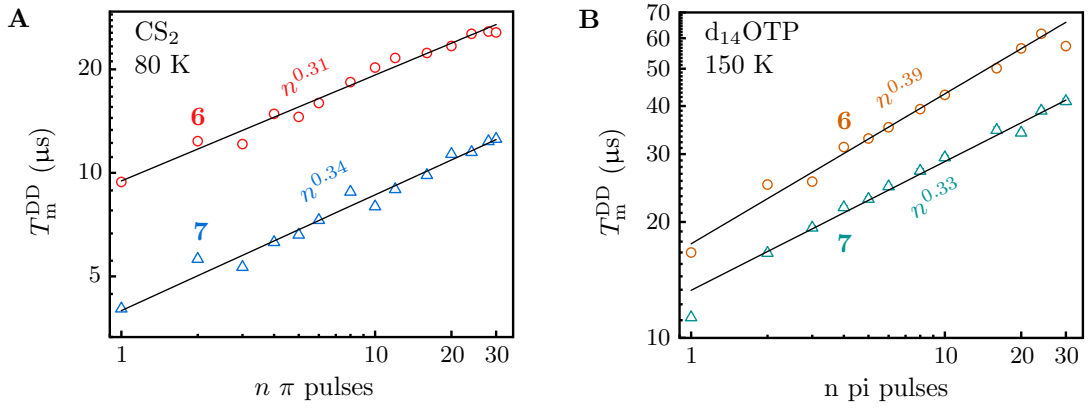


Figure 6.9: (A) Summary of the decay times of **6** and **7** in CS_2 at 80K. (B) Summary of the decay times of **6** and **7** in d_{14}OTP at 150 K.

term is temperature independent, while the motion term is strongly temperature dependent. We have checked for instantaneous diffusion in the previous section demonstrating that we can disregard it except for **6** in d_{14}OTP. Therefore, we are left with only the first two terms that we can further break down into contributions from matrix-related and system-related effects:

$$\begin{aligned}\Gamma &= \Gamma_{NSD} + \Gamma_{motion} \\ &= \Gamma^{\mathrm{m}}_{NSD} + \Gamma^{\mathrm{s}}_{NSD} + \Gamma^{\mathrm{m}}_{motion} + \Gamma^{\mathrm{s}}_{motion}.\end{aligned} \tag{6.16}$$

The edge hydrogens are the main source of $\Gamma^{\mathrm{s}}_{NSD}$, much weaker contributions are provided by ^{13}C and occasionally other substitutional nuclei such as Cl. In a protonated matrix, system and

matrix nuclear baths are the same and Γ_{NSD} dominates the decoherence. However if we remove the protons in the matrix, either by deuterium substitution or by switching to CS_2, the matrix contribution to the nuclear bath decreases substantially. For example, the EPR literature estimate a decrease of NSD of 10-30 times upon deuteration [26, 254], therefore $\Gamma^{\mathrm{s}}_{NSD} \gg \Gamma^{\mathrm{m}}_{NSD}$, and in first approximation we can completely neglect matrix contributions. In general, we can disregard the $\Gamma^{\mathrm{m}}_{motion}$ in the solid state, but this term becomes more and more important above the glass transition temperature and in the viscous regime just below the melting point.

In light of the arguments above, we can interpret the main results about coherence time in this work. In protonated matrices Γ_{NSD} is the main decoherence channel at low temperatures, this is confirmed by stretched parameters $\beta > 1.5$ as registered for **1** in OTP and **5** in toluene. Molecular motion effects come into play around the glass transition temperature and are augmented by presence of methyl groups in the matrix. Therefore, we expect higher coherence time in OTP (no methyl groups) than toluene (which is what we see in **1**).

In deuterated or nuclear free matrices the effect of $\Gamma^{\mathrm{m}}_{NSD}$ is virtually 0, and relaxation is strongly affected by molecular motions. This is corroborated by $\beta \leq 1$ in **1**, **6** and **7** in d_{14}OTP and CS_2 and by the fact coherence time in d_{14}OTP is often larger than in CS_2, even though the latter is nuclear-free. Indeed, molecular motions affect CS_2 more, because its melting point is lower. d_{14}OTP is also less affected by $\Gamma^{\mathrm{m}}_{motion}$ with respect to $d_8$tol, since the latter has methyl groups. Additionally, the deuterium concentration per unit volume of d_{14}OTP is lower than $d_8$tol.

In rationalising the effect of dynamical decoupling, EPR literature [376] argued that the enhancement factor due to a pulse train would be described by $T^{DD}_{\mathrm{m}} = T_{\mathrm{m}} n^{(1-1/\beta)}$, where β is the stretched parameter of the Hahn echo fit. The previous statement would imply that a coherence time enhancement can only be obtained when $\beta > 1$, hence when nuclear spin diffusion is the dominant factor. Contrary to this, here we demonstrate that the coherence time always increases with the number of pulses even for $\beta < 1$ which is the case for **1** in d_{14}OTP at 200 K, **6** and **7** in CS_2 at 80 K, and if we think about the stretch exponential treatment in fig. 4.9A also **5** in CS_2.

There are other theories that connect the enhancement factor with the shape of the spectral density function. For example, de Lange and coworkers [361] showed that an enhancement factor $n^{2/3}$ would be obtained when the spectral density function is Lorentzian representing a bath noise

modelled by an Ornstein-Uhlenbeck process [361]:

$$S(\omega) = \frac{\Delta\tau_c}{\pi}\frac{1}{1+(\omega\tau_c)^2}, \tag{6.17}$$

where Δ is the average inter-bath coupling strength, and τ_c the bath correlation time related to the flip-flop time. Indeed, a very good match with this theory is found in several single NV centres [361, 362]. While the Ornstein-Uhlenbeck process describes very well the noise in NV centres because they are affected by individual nuclear spins in their vicinity, in a more general situation the central spin is perturbed by a collection of nuclei. In this case, the Lorentzian distribution is well approximated for $\omega \gg 0$ by a $1/f$ noise: $S(\omega) \propto \omega^{-\alpha}$. The two distributions do not differ very much in their high frequency tails, therefore, in an experimental setting where it is hard to obtain high-quality low frequency components of the spectral density, it would become non-trivial to clearly distinguish them. Analogous scaling with n is found in several other systems: for example $n^{0.72}$ is observed in spin qubits in GaAs [377], and $n^{0.6}$ for an ensemble of malonic acid radicals in the solid state [373]. Overall, it appears that for several systems where the bath is made of nuclear spins: N and ^{13}C for NV centres, Ga and As nuclei for GaAs quantum dots, ^{13}C and H for malonic acid, a trend of n^{γ} with $\gamma \approx 0.6 - 0.7$ is found.

For our graphenoids, the value of the enhancement factor is strongly affected by the type of fit used, but we can reliably say that γ is consistently in the range $0.35 - 0.45$. In fig. 6.7, the dashed line represents an ideal trend assuming the enhancement factor was $n^{2/3}$ with $S(\omega)$ as in eq. (6.17). In all cases except **1** in OTP at 200 K, the molecular graphenoids underperform with respect to a Lorentzian noise, and in general with respect to the quantum systems mentioned above. We interpret this result using the break-down of the decoherence rate provided in eq. (6.16). Dynamical decoupling is efficient when acting on the Γ_{NSD} term: when this is the dominant term, the maximum performance is obtained, as in **1** in OTP 200 K, which can be related to the Ornstein-Uhlenbeck picture. On the other hand, the sequence is much less efficient when Γ_{motion} term dominates, yielding $\gamma \approx 0.35 - 0.45$ for different matrices at different temperature. Indeed, the main difference with the quantum systems mentioned above is that they are not affected by any kind of internal motion.

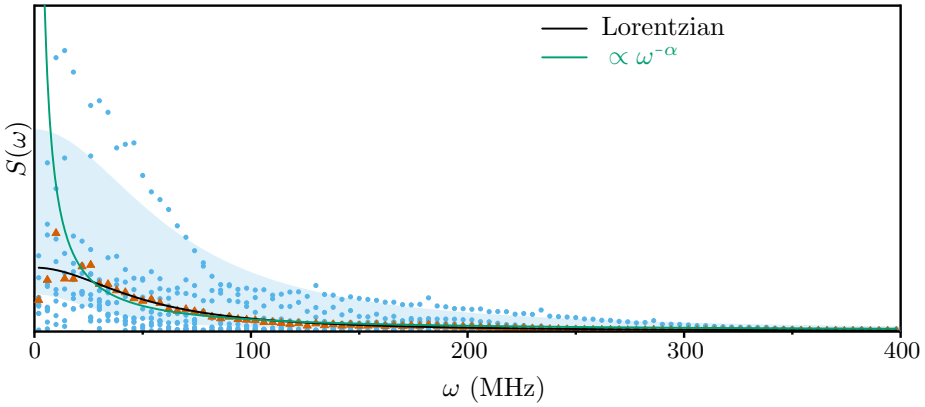


Figure 6.10: $S(\omega)$ from the spectral deconvolution of CPMG data in OTP at 200 K. The blue dots are the spectral density function for individual traces, while the orange triangles are their mean. Solid lines are fit with the models discussed in text. The shaded area includes the Lorentzian fitting to the individual CPMG traces.

6.5.1 Spectral decomposition

Noticing the similarity between the sample in OTP at 200 K and the pure Lorentzian noise, we proceeded with spectral deconvolution of the noise density function $S(\omega)$ following the method of [362]. We approached the integral in eq. (6.8) as a sum of discrete terms. For CPMG with even number n of pulses, the filter function is:

$$F(\omega, \tau, n) = 8 \sin^2\left(\frac{\omega\tau}{2}\right) \frac{\sin^4 \frac{\omega\tau}{4n}}{\cos^2 \frac{\omega\tau}{2n}}. \tag{6.18}$$

For each CPMG trace, we used $\omega_{\text{step}} = 0.1$ MHz and frequency cutoff $\omega_{\text{cutoff}} = 400$ MHz to produce a matrix of $M = F(\omega, \tau, n)/\omega^2$ with the experimental τ values as rows, the ω as columns, and n fixed depending on the sequence. We solved the problem $\chi = MS$ using a least-squares approach and then we binned the values of the extracted $S(\omega)$ into 100 bins with $0 < \omega < 400$ MHz fixed at the centre of every bin. The values of $S(\omega)$ at every ω for every CPMG sequence used are represented by the blue dots in fig. 6.10. Finally, we calculated the mean of all the sequences at each ω value (orange triangles) and fit it with both with a Lorentzian and a $1/f$ noise. From the results in fig. 6.10 it appears that the Lorentzian is a better fit than the $1/f$ noise at low frequencies. Additionally, it is a better physical representation to assume that $S(\omega)$ goes to a finite value at $\omega = 0$ than to infinity. From the Lorentzian fit we obtain a value for the correlation time from eq. (6.17) $\tau_c = 20 \pm 1$ ns. Such a parameter is about 500 times faster than what observed in [362] for NV centres, which is fully representative of the much higher concentration and faster dynamics of hydrogen nuclei in our

sample, compared with ^{13}C nuclei.

6.6 Outlook

In this chapter we demonstrated that it is possible to extend the performance of molecular graphenoids using dynamical decoupling pulse sequences. In particular, we showed that given a specific initial condition CPMG sequence is the most performing, while XY sequences are more robust to random initialisation. We used a semi-classical model to interpret the data, assigning to the nuclear bath a classical random noise character. We observed that the enhancement due to the decoupling is roughly the same for the different molecules that we used. This is because the molecules share the same nuclear bath (hydrogens) and are affected by analogous molecular motions. In particular, the decoupling is more efficient when facing large nuclear spin diffusion, while it is less efficient when in the presence of molecular motions.

6.7 Project Overview

This chapter compared dynamical decoupling results for the molecules discussed in chapter 3, 4, and 5. Large part of the measurements for **1** discussed here were carried out at the Helmholtz-Zentrum Berlin collaborating with Prof Boris Naydenov and with the help of Michele Segantini. All the other measurements were done at CAESR. Ming-Yee Tsang wrote the code for the spectral density deconvolution.

Conclusions and Perspectives

In this thesis, we have, for the first time, applied pulsed Electron Paramagnetic Resonance (EPR) to characterize the quantum properties of open-shell molecular graphenoids. All the molecules studied showed superb properties in diluted diamagnetic solid matrices.

We demonstrated that the spin-lattice relaxation time, T_1, is several orders of magnitude larger than in any other molecular qubit, and competitive with the best qubit candidates in the literature, such as NV centres. We attributed this extraordinary result to the intrinsically low and isotropic spin-orbit coupling that characterizes non-curved carbon nanostructures. We were also able to fit the temperature trend of T_1 with known models, identifying that the main process is a Raman mechanism. A further step would be to match the spin-lattice relaxation time with specific bond types and structures in the molecules, through theoretical calculations or more specific phonon measurements. For example, we found out that local modes affect ring structures (**6** and **7**) only, hence it would be interesting to understand the root cause of this effect.

We studied the coherence time, T_m, and found out that it is much more dependent on the environment than T_1. We obtained very large variations from powders and in different matrices. We also used different models to fit and understand the behaviour of the coherence, which makes it difficult to directly compare the performances amongst different molecules, although coherence was always above 10 μs at 80 K and more. This is again a record in the high temperature regime for molecular qubits, while other molecular complexes achieved $T_\mathrm{m} > 100$ μs at 10 K [79].

Overall, we find that the main decoherence channels are given by the effect of the nuclear bath and molecular motions. In nuclear-free or deuteraterad matrices, the decoherence could be linked directly to the molecule. The size, shape, and topology of the molecules do affect the decoherence channels but their effect is not dramatic. Larger molecules are always less performing due to the increase in the number of hydrogen nuclei and the number of substituents affected by motions. We

also discussed the concept of spin-diffusion barrier for which the number of nuclei only does not strictly determine the coherence, but their hyperfine coupling too, with more strongly coupled nuclei contributing less to decoherence.

The analysis of T_{m} was mostly qualitative. In chapter 6, we briefly discussed a model breaking down the decoherence rate into its fundamental components: Γ_{NSD} and Γ_{motion}. It would be interesting to calculate their effect. The CCE is a suitable technique that was already used in the EPR field to quantify decoherence in several systems [67, 92, 378], which could be used to calculate Γ_{NSD}. We believe that it would be more difficult to calculate the effect of Γ_{motion}, since the theory on molecular motions is much less developed than the effect of the nuclear bath. Nonetheless, molecular dynamics techniques have become very successful even for large systems in the last few years [379]. Therefore, mapping the motion of substituents at a certain frequency and in a specific matrix appears within reach of current technology.

As we put so much focus on the role of hydrogen nuclei, it would be very interesting to repeat the experiments with molecules that are hydrogen-free. In talks with our collaborators, it was discussed if this was feasible. It appears that deuteration of the molecules would be a challenging and costly process. However, it should be practical and reasonably quick to chlorinate all the edges. Possibly, such new molecule would have increased reactivity and it might be difficult to handle them. Yet, we would expect a two-fold effect from chlorination. First, ^{35}Cl and ^{37}Cl have gyromagnetic ratios about 10 times lower than H, which means dipolar coupling would decrease 100 times. Second, the mass of Cl is 35 times the mass of H which will have a dramatic effect on the motions, although we are not able to predict if this will be increasing T_{m} or decreasing it.

Finally, we highlight a set of three problems and open questions that emerged from this work and should be considered in future research. All the molecules studied in this thesis, except for **7**, were in their singlet ground state. This can be problematic because only a fraction of molecules will be in their paramagnetic state at any temperature. A solution to this would be to try to pump the molecules in their paramagnetic state, possibly with light excitation. While tuning of the singlet-triplet splitting was not discussed deeply in this thesis, several chemistry groups already apply advanced chemical and theoretical methods to understand the structural features that mostly affect exchange coupling [299].

An open question remains the role of dipolar coupling D in the poly-radicaloids. We never saw any traces of dipolar coupling in any molecules even when trying more advanced pulse EPR

techniques. Moreover, the role of D is largely overlooked in most of the literature as many other molecules do not show any splitting nor any half-field line. Therefore, it needs to be understood if and how the multiple spins couple to each others and whether they could be addressed individually.

Ultimately, exploitations of quantum properties cannot be relegated to ensemble studies. A device must bear the opportunity to address a single quantum unit at a time and couple multiple units. Several architectures are available to study single molecules: the most promising are single molecules in a transistor [20] or on a surface [19], which are already routinely performed [380]. It would also be intriguing to place a single molecule in a superconducting resonator [381, 382]. Current technologies allow coupling down to a few hundreds molecules with a resonator [383], and single spin sensitivity might be achieved in the next few years.

EPR on Charge Transfer Tryads

A.1 Introduction

In a three-terminal single-molecule transistor, a molecule comprising one or multiple active metals is deposited between two leads. The gate voltage acts to shift the energy levels of the molecules, while the bias voltage drives a current through the molecule if the resonant conditions of the energy levels are respected. This is a spectroscopy tool that can finely probe the energy levels of the molecule, including its vibrational state. If the central metal is spin active, the transistor is a prototype of a spintronic device where spin states can be controlled through an electric current.

Nevertheless, the experiments highlighted major issues: difficulty in determining if the structure of the molecule is preserved after deposition; coupling with the leads perturbing the magnetic state of spins; loss of spin dynamics information. A chemical approach could be used to combine the coherence time measurements with the electrical transport. Indeed, it is possible to mimic a transport experiment if a spin centre is chemically functionalised with a donor and an acceptor. After shining light, we can observe a charge transfer between the two functional groups through or in proximity of the spin active bridge. This is an analogous set up of a transport experiment between two electrodes in a single electron fashion, but it provides the certainty that the molecule retains its structure and a clean coupling.

The experiment described can be realised in an EPR spectrometer combining laser excitation with microwaves. Indeed, this set up is well-known in biology where it is used to study photosynthesis [386, 387] and for photovoltaics [388]. Chernick *et al.* [384, 385] studied the spin dynamics in a donor–bridge–acceptor molecule with different radicals attached on the bridging group. The nitroxyl radical ($NN^{\cdot}$) in **18** was chosen because the spin is strongly localised on the two N-O without injection into the bridge. After shining a 100 fs laser pulse at 420 nm the compound undergoes

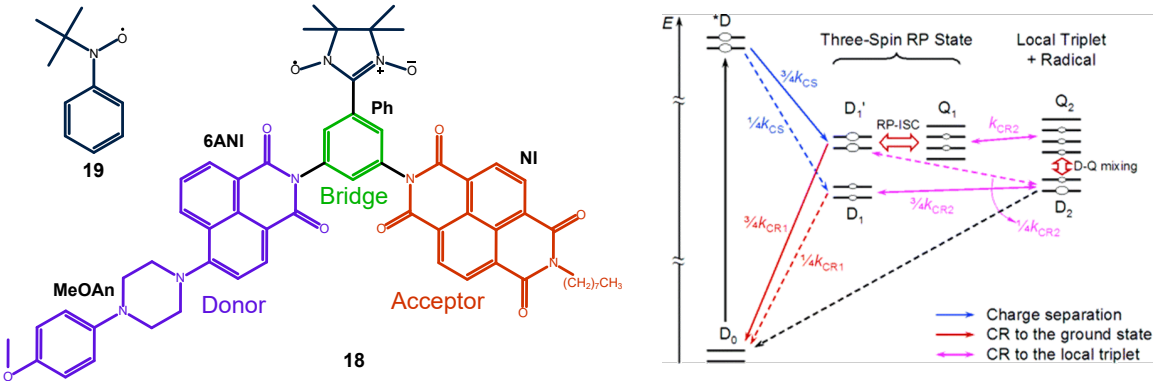


Figure A.1: **18** MeOAn-6ANI-Ph(NN$^{\cdot}$)-NI, where MeOAn = p -methoxyaniline, 6ANI = 4-(N-piperidinyl)-naphthalene-1,8-dicarboximide, Ph = phenyl, and NI = naphthalene-1,8:4,5-bis(dicarboximide) [384]. **19** Substitution of the NN radical with a BPNO$^{\cdot}$ radical [385]. Mechanism of enhanced intersystem crossing (EISC) in presence of the nitroxil radical. The *D represents the excited state ^{2}(MeOAn$^{-\cdot}$–Ph(NN$^{\cdot}$)–NI$^{-\cdot}$). The magnetic field introduced by the radical produces a strong mixing between a doublet and quartet state. In addition to this it is possible to produce a local triplet on the NI group that can be written as ^{2,4}(MeOAn–Ph(NN$^{\cdot}$)–^{*3}NI) from which is harder to obtain charge recombination and it represents the key point in increasing the lifetime of the system (reproduced from [384]).

photogenerated radical pairs formation MeOAn$^{\cdot+}$-6ANI$^{\cdot-}$-Ph(NN$^{\cdot}$)-NI and charge transfer MeOAn$^{\cdot+}$-6ANI-Ph(NN$^{\cdot}$)-NI$^{\cdot-}$ with timescales of less than 100 ps. Since charge separation and transfer are on a faster timescale than spin interactions they are not influenced by the presence of the NN$^{\cdot}$. In the absence of the NN$^{\cdot}$, an external magnetic field splits up the triplet state of the photogenerated radical pair introducing a path for intersystem crossing (RP-ISC). The magnetic fields modulated the rate of RP-ISC peaking when the Zeeman splitting equals twice the singlet-triplet splitting. The presence of a third spin complicates the situation since there are three different exchange coupling MeOAn$^{\cdot+}$–NI$^{\cdot-}$ (J_{12}), MeOAn$^{\cdot+}$–NN$^{\cdot}$ (J_{13}) and NI$^{\cdot-}$–NN$^{\cdot}$ (J_{23}). As seen in fig. A.1 the nitroxyl radical produces a strong doublet quartet mixing without influencing J_{12} resulting in a increased intersystem crossing $Q_1 \rightarrow Q_2$ and therefore slower charge recombination. The same authors studied also an analogous complex using a BPNO$^{\cdot}$ radical that has a much larger spin injection on the phenyl group [385]. More D-B-A structures can be synthesised exploiting for instance strong electron acceptors as fullerenes [389] and transition metal or lanthanide spin centres instead of radicals.

In this chapter, we present the measurements on a set of donor–metal–acceptor tryads used to mimic the behaviour of molecules in a transistor. The donor is a Zn-porphyirin, the central metal is bridged by two terpyridine ligands, and the acceptor is Naphthalenetetracarboxylic diimide (NDI). Three central metals were considered: Zn, Cu, and Co, because they show different spin multiplicity, respectively $S = 0$, $S = 1/2$, and $S = 1$. The aim of the project is to observe the effect of the charge transfer on the coherence of the central metal. This requires, first, to establish if the charge transfer

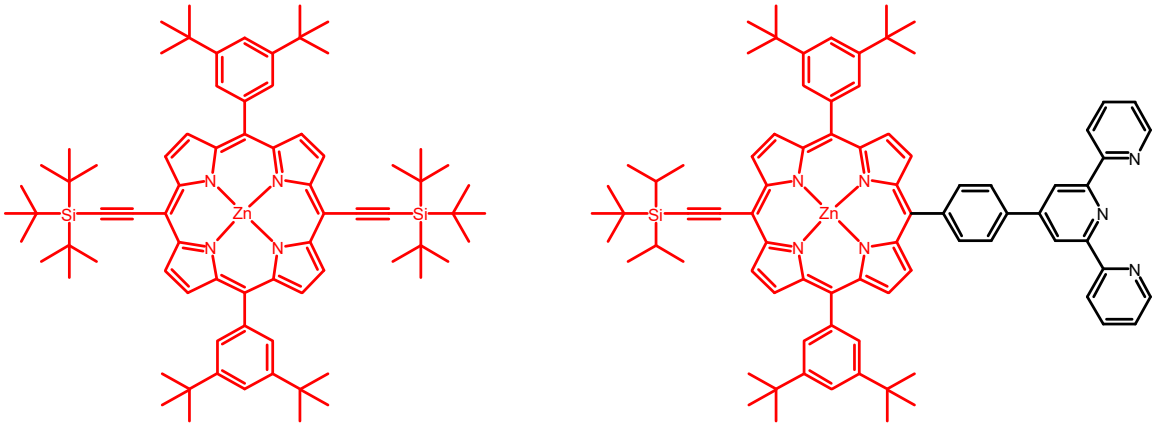


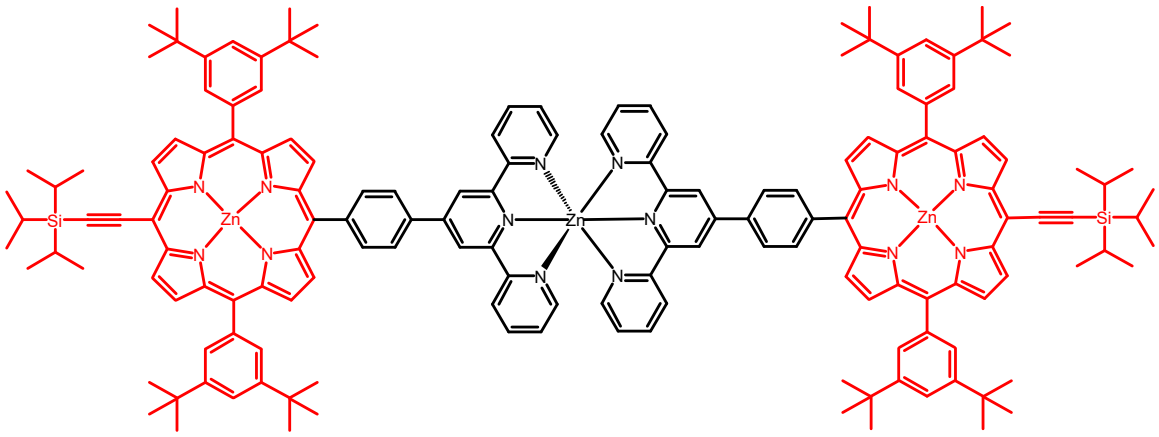
Figure A.2: Chemical structures of the building blocks of the donor–acceptor tryad. **20** is the donor zinc porphyrin. **21** is the donor plus one terpyridine group.

is successful. Before presenting the result of the tryads, we analyse its building blocks in order to break down the problem and find differences that could help the study.

A.2 Experimental Methods

All measurements were carried out at cryogenic temperatures. All samples were dissolved in deuterated toluene, put in 4 mm outer diameter quartz glass tubes, and degassed with 5 cycles of freeze-pump-thaw before flame-sealing. Degassing improves significantly the signal because intersystem crossing to triplet oxygen is a relaxation channel. All measurements were carried out on a Bruker E680 equipped with an EN 4118X-MD4 Bruker ENDOR resonator with an optical window. 10 ns laser pulses were provided by a Quanta-Ray Nd:Yag laser, with 20 Hz shot frequency and $\sim$ 1 mJ energy. Power oscillations are expected since the measurement time was 24 h per sample.Therefore, all measurements were obtained as sum of four identical intervals of 6 hours in order to average out the drift of the laser power.

We used transient EPR (TrEPR) to record the CW spectra of all the samples. The magnetic field was swept, and for every magnetic field point the transient response of the system was recorded. In order to increase time resolution down to 10 ns, the lock-in amplifier was disconnected. This means that the resulting spectra are not prime derivative but they refer to absorption and emission. Moreover, removing the lock-in amplifier implies that the measurement is insensitive to all permanent paramagnetic species in the sample, or any paramagnetic background signal from the resonator. Light



22

Figure A.3: Chemical structure of the donor–metal–donor tryad. The same molecule could be synthesised with Cu as a central metal.

excitation results in very large spin polarisation that allows to overcome the population difference problem discussed in chapter 2.

Nonetheless, the measurement is sensitive to artefacts due to the dielectric effect of the laser. In order to remove these artefacts, we set the laser trigger to include an 800 ns delay between the beginning of the measurement and the laser pulse so that the initial delay could be used for laser background removal in the data processing. Additionally, the magnetic field range was chosen to have at least 40 points in regions where no signal is expected so that a linear regression could be used to remove any baseline.

The results are presented as 2D color plot with the time on the x axis, the magnetic field on the y axis, and the intensity color coded. Positive intensity corresponds to absorption and negative to emission. We also show the results as a more traditional EPR field sweep for clarity. We selected time windows of 100 ns over which we integrated over the traces in order to improve SNR. Furthermore, it would be possible to select field window to study the time decay and obtain relevant decay constant, but we chose not to show those results.

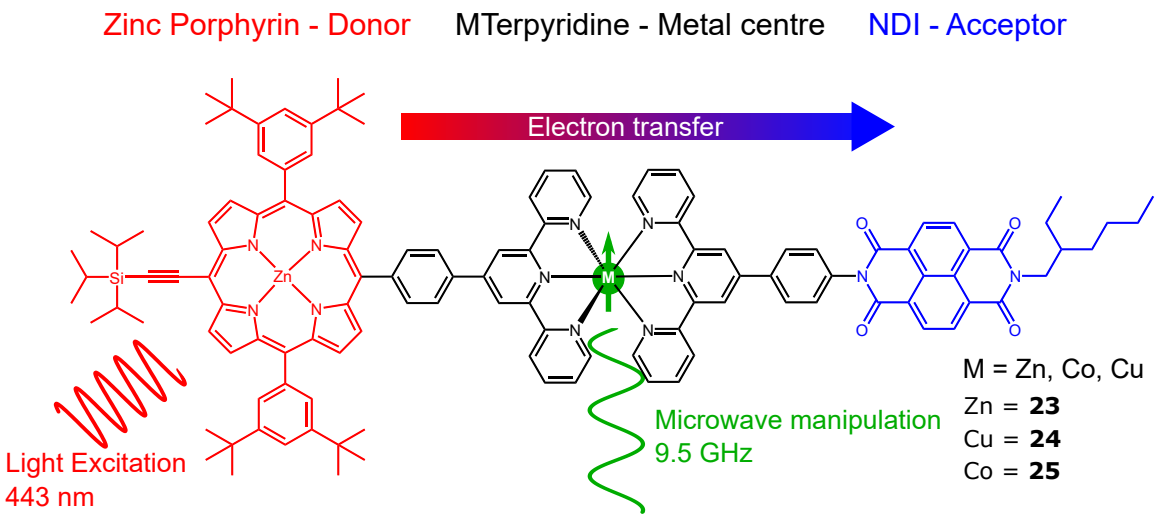


Figure A.4: Chemical structure of the donor–metal–acceptor tryad. Excitation is provided by external light pulses, while spin control is achieved through microwaves. Three different compounds are available with central metal: Zn, Cu, and Co.

A.3 Results

A.3.1 UV-Vis Spectroscopy

In fig. A.6 the UV/Vis spectroscopy of the building blocks and the tryads is presented. We highlight that the absorption band of the NDI is clearly separated from the one of the donor Zn-porphyrin. This means that upon light excitation at 443 nm we can be sure that we are exciting the donor.

A.3.2 EPR

Building Blocks

In fig. A.7 we show the TrEPR result for **20** and **21**. The two are presented together due to the similarity in their spectra. Indeed, the terpyridine is not highly conjugated with respect to the Zn porphyrin. Therefore, we expect the excited triplet to be mostly localised on the porphyrin ring.

Donor-Metal-Donor Tryad

In fig. A.8 we show the results at 5 K for **22**. From comparison with **20** and **21** we see a different spectrum. We believe that the presence of the complete central metal with the two terpyridine provides an additional level for the excited state to separate.

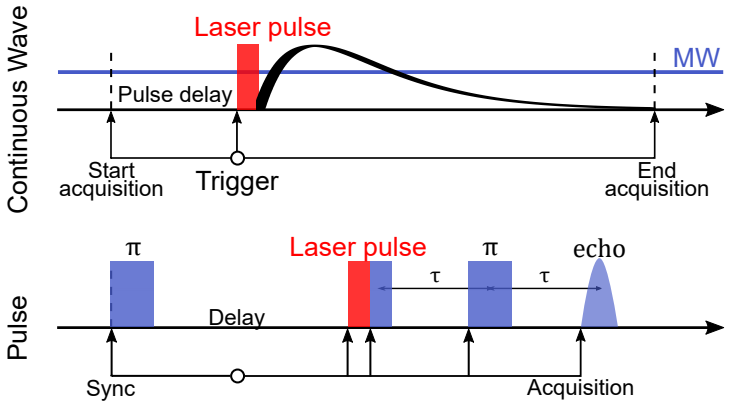


Figure A.5: (Top) Schematics of transient EPR (TrEPR), a transient signal is generated by the light pulse and the magnetic field is swept. (Bottom) Schematics of pulse EPR with light excitation. Any MW pulse can be used before light excitation to depolarise any background signal. After pulse excitation any pulse sequence can be used to study the

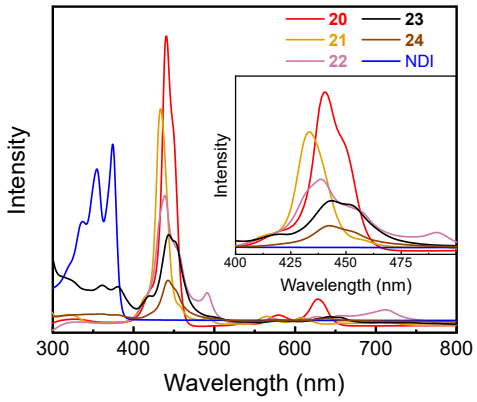


Figure A.6: UV/Vis spectroscopy of the tryads and the building blocks in toluene at room temperature.

Donor-Metal-Acceptor Tryads

In fig. A.9 and A.10 we show the results for the two tryads with Zn and Cu. We do not have yet results for Co due to problems in the synthesis. The figures show that the two spectra are very similar to each others and completely different to what seen beforehand. Therefore, the two tryads must be subjected to the same charge transfer process that seems independent from the choice of the central metal.

A.4 Outlook

In this chapter we briefly commented the results obtained with TrEPR on donor–metal–acceptor tryads. Due to time limitations we were not able to finish the project, and therefore we cannot

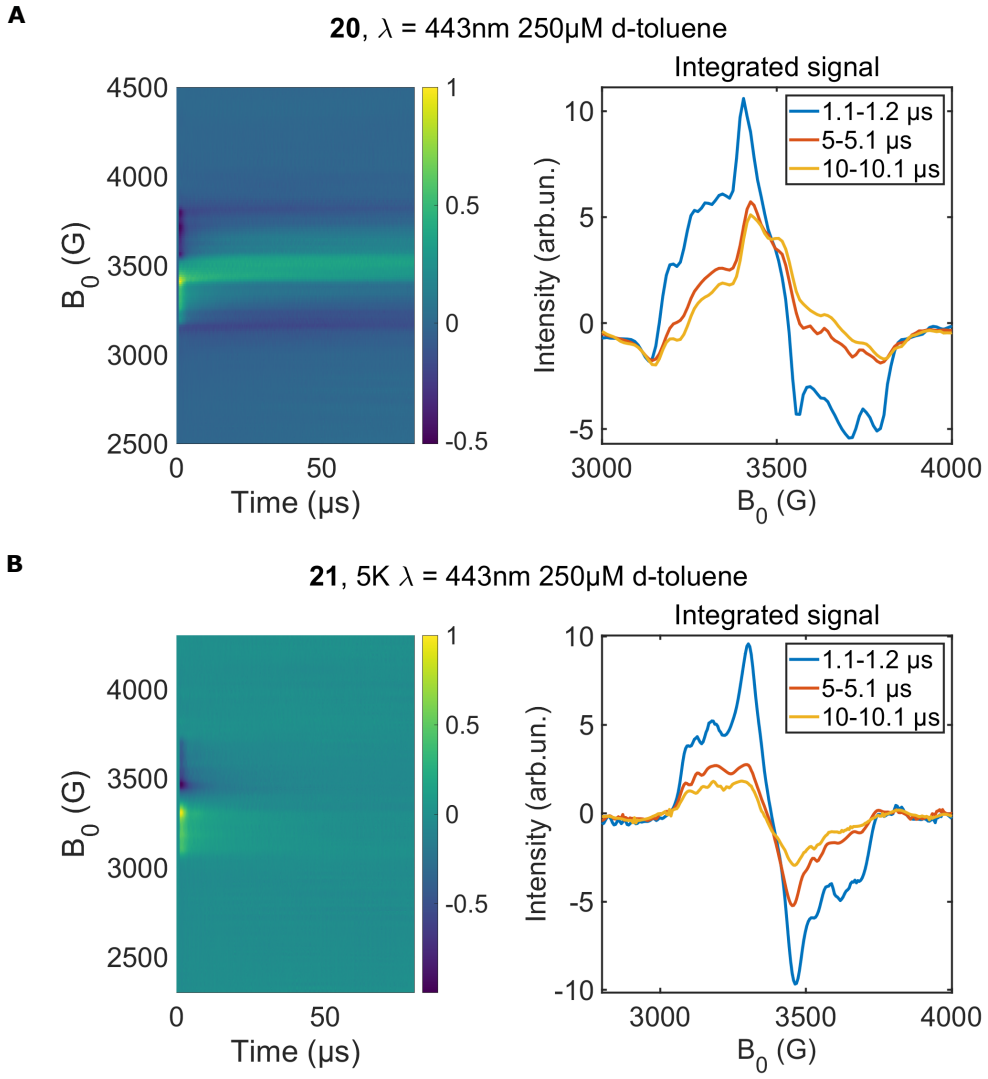


Figure A.7: (A) TrEPR of **20** at 5 K. (B) TrEPR of **21** at 5 K.

present a conclusive outlook. However, we discuss here current problems and future steps.

The main limitation in the interpretation of the spectra is given by the multiple interactions that can appear, namely: hyperfine coupling with N and the metals, and zero field splitting or dipolar interactions between radical pairs, which would be complicated by the presence of the third spin on the central metal. The idea of the building blocks was initiated to unravel all these contributions. Furthermore, we are now collaborating to obtain transient absorption spectroscopy of the samples. Initial measurements (not showed here) for **23** highlighted a rich dynamics in the ps region with a long lived state in the ns timescale. Since we have no resolution at the EPR for the ps region, we are only able to observe the long lived species. Additional information about this species can be

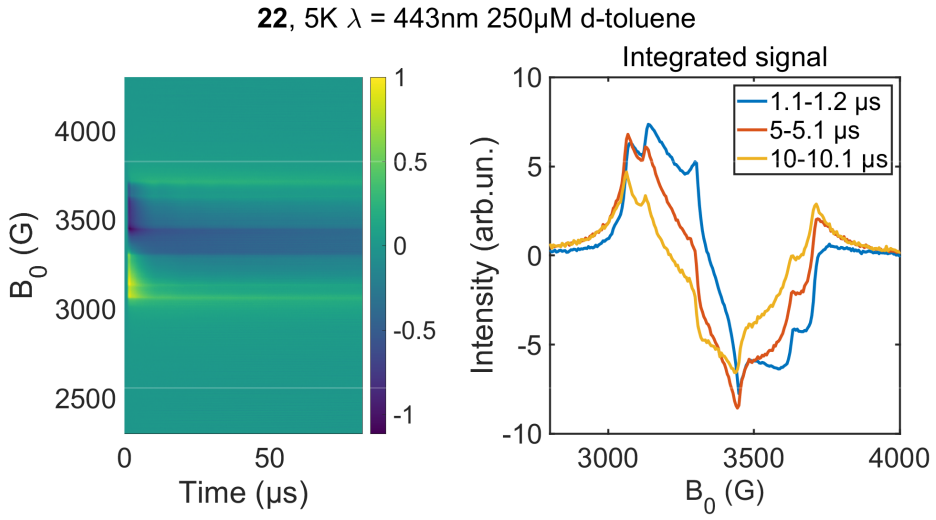


Figure A.8: TrEPR of **22** at 5 K.

obtained with ns transient absorption spectroscopy or even using electrochemistry to analyse the oxidation and reduction states of the tryad.

While we are still unable to interpret the spectra with clear EPR simulations, the raw data show a clear difference between the building blocks, **22**, and the two tryads. Intuitively, this means that the electron cannot be constrained to the porphyrin ring, but it needs to be subjected to a cascade.

A.5 Project Overview

The tryads (**23**, **24**, and **25**) discussed in this project were originally designed and synthesised by Dr Jennifer le Roy. The synthesis was then taken over by Dr Dimitrios Alexandropolous who also synthesised all the building blocks (**20**-**22**). Help in setting up the laser measurements was provided by Dr Michael Slota and Dr William Myers. Ongoing collaborations with the group of Dr Olof Johansson at University of Edinburgh are producing transient absorption spectroscopy measurements carried out by Kyle Barlow.

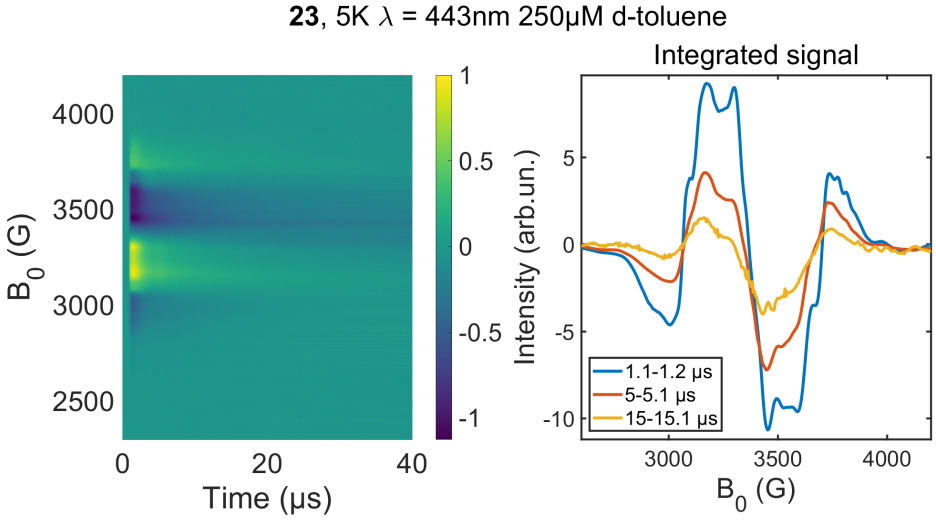


Figure A.9: TrEPR of **23** at 5 K.

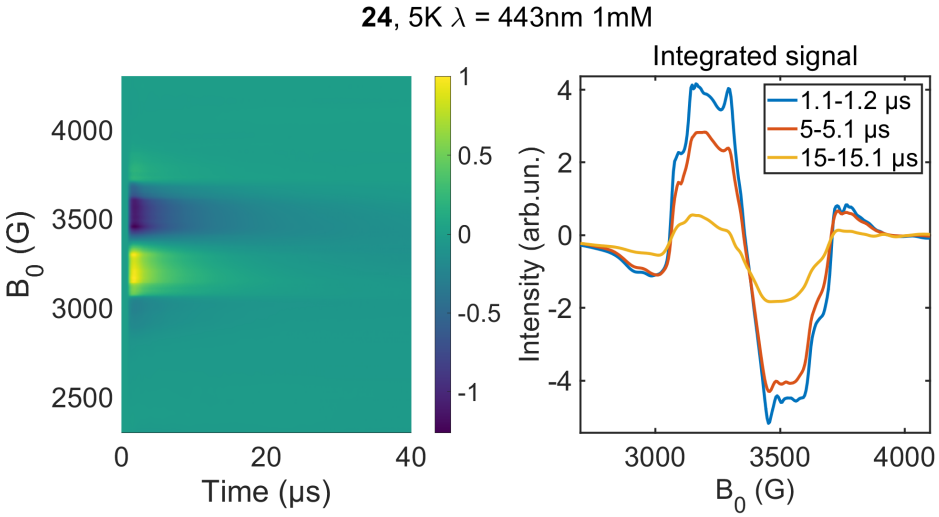


Figure A.10: TrEPR of **24** at 5 K.

Additional Data

B.1 Pentagonal units in graphenoids

HYSCORE and 2D Mims ENDOR measurements of **2**-**4** were recorded at 150 K in solid states. For **2** and **3** we performed HYSCORE at two different τ values to avoid blindspots, but no particular differences are observed. Therefore, only one τ value was taken for **4**.

Simulations were obtained with Easyspin using the function *saffron*. There are computational limitations to the maximum number of atoms that can be included into a calculation. In all cases, simulations were obtained as sum of three individual simulations: one simulations including one hydrogen nucleus with hyperfine values A_1; one simulation including one hydrogen nucleus with hyperfine values A_2; one simulation including remaining nuclei with constant $A_3 - A_5$ (see table B.1). A fourth simulation was added for HYSCORE to take into consideration ^{13}C contribution. The individual simulations were then summed together using arbitrary weights to represent the intensity ratio observed in the experiment. This approach is justified because the three sets of nuclei are independent.

As the measurements were carried out in powders the observed contributions come for a variety of sources. We attribute the hyperfine constant A_1 to far away nuclei that are only weakly dipolar coupled to the central electron spin. We attribute A_2 to nuclei of nearby molecules that are weakly coupled both isotropically and dipolarly due to extension of the wavefunction in a π stack. Finally we attribute A_3-A_5 to the nuclei in the molecule. We obtain the value of these constants from DFT calculations.

The most striking factor is that the hyperfine coupling are comparable in **2** and **3**, but much weaker in **4**. Such difference was already observed in the comparison of CW signal in fig. 3.14. This is additional confirmation that the spin density in **4** is more distributed over the entire molecule

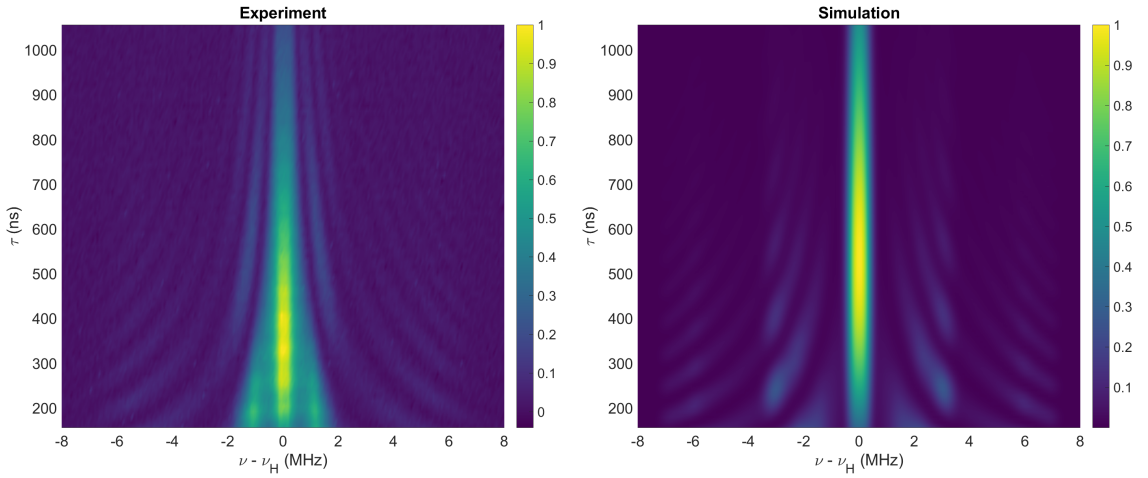


Figure B.1: 2D Mims ENDOR at 150 K in powders for **2**.

due to the larger conjugation, while in **3** it is more concentrated in one lobe and resembles the distribution of **2**.

	2			**3**			**4**		
A_1 (MHz)	-0.3	-0.3	0.6	-0.2	-0.2	0.4	-0.2	-0.2	0.4
A_2 (MHz)	0.4	0.4	2.8	0.4	0.4	2.8	0.8	0.8	2.6
A_3 (MHz)	5.4	11.9	14.3	5.3	11.6	15.8			
A_4 (MHz)	2.5	6	6.8	2.5	5.7	6.3			
A_5 (MHz)	1.3	4.5	6.4						

Table B.1: Hydrogen hyperfine coupling used in ENDOR and HYSCORE simulations.

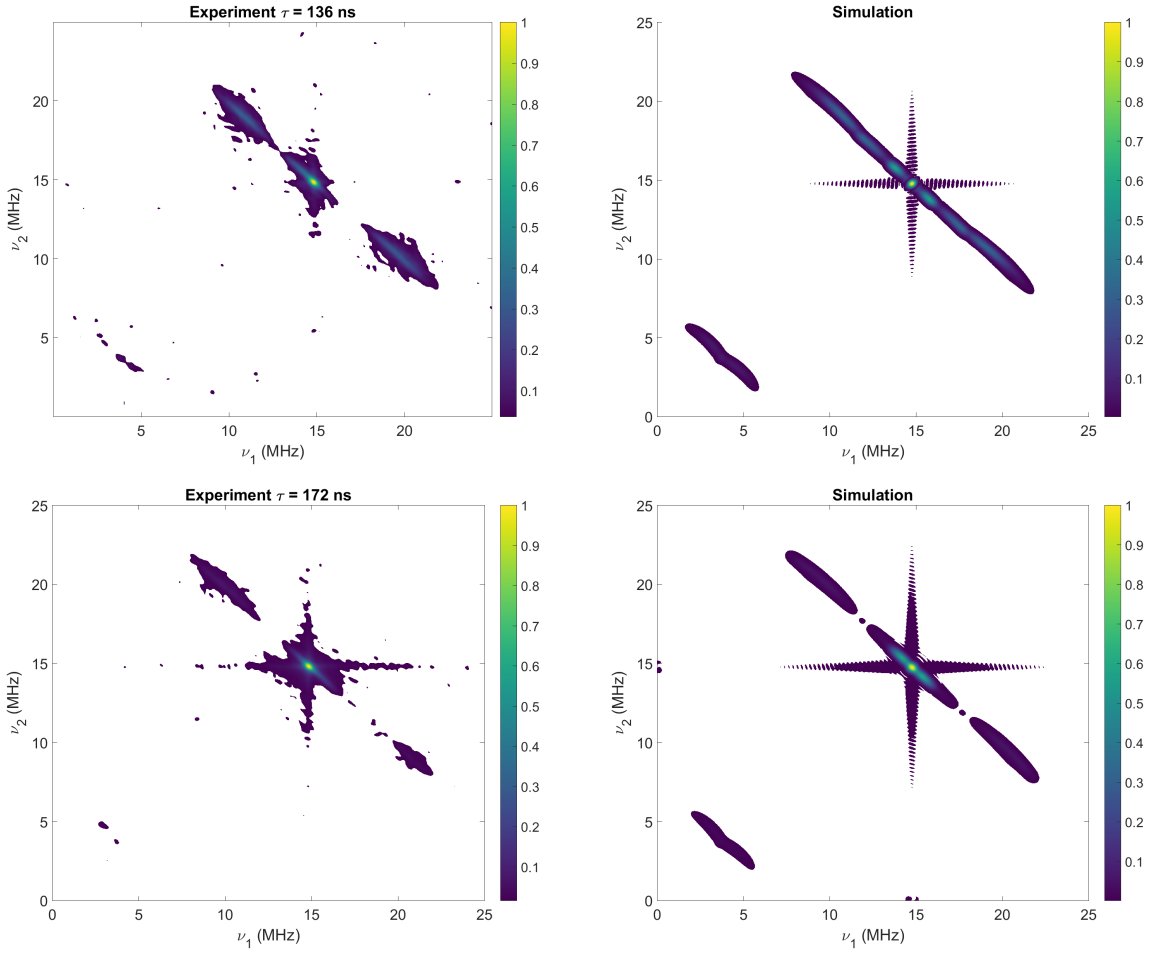


Figure B.2: (Top) HYSCORE and simulation of **2** at 150 K in powder $\tau = 136$ ns. (Bottom) HYSCORE and simulation of **2** at 150 K in powder $\tau = 172$ ns.

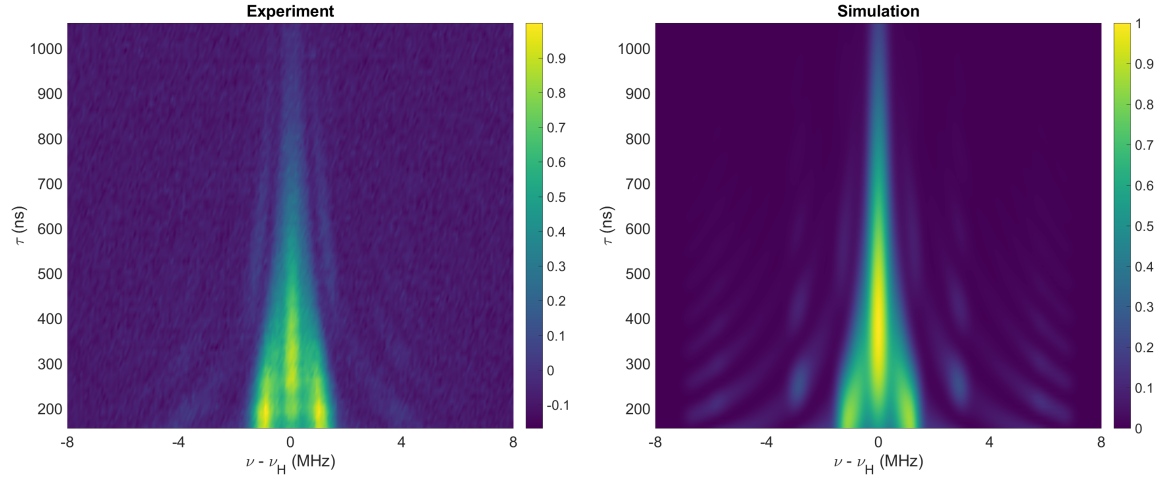


Figure B.3: 2D Mims ENDOR at 150 K in powders for **3**.

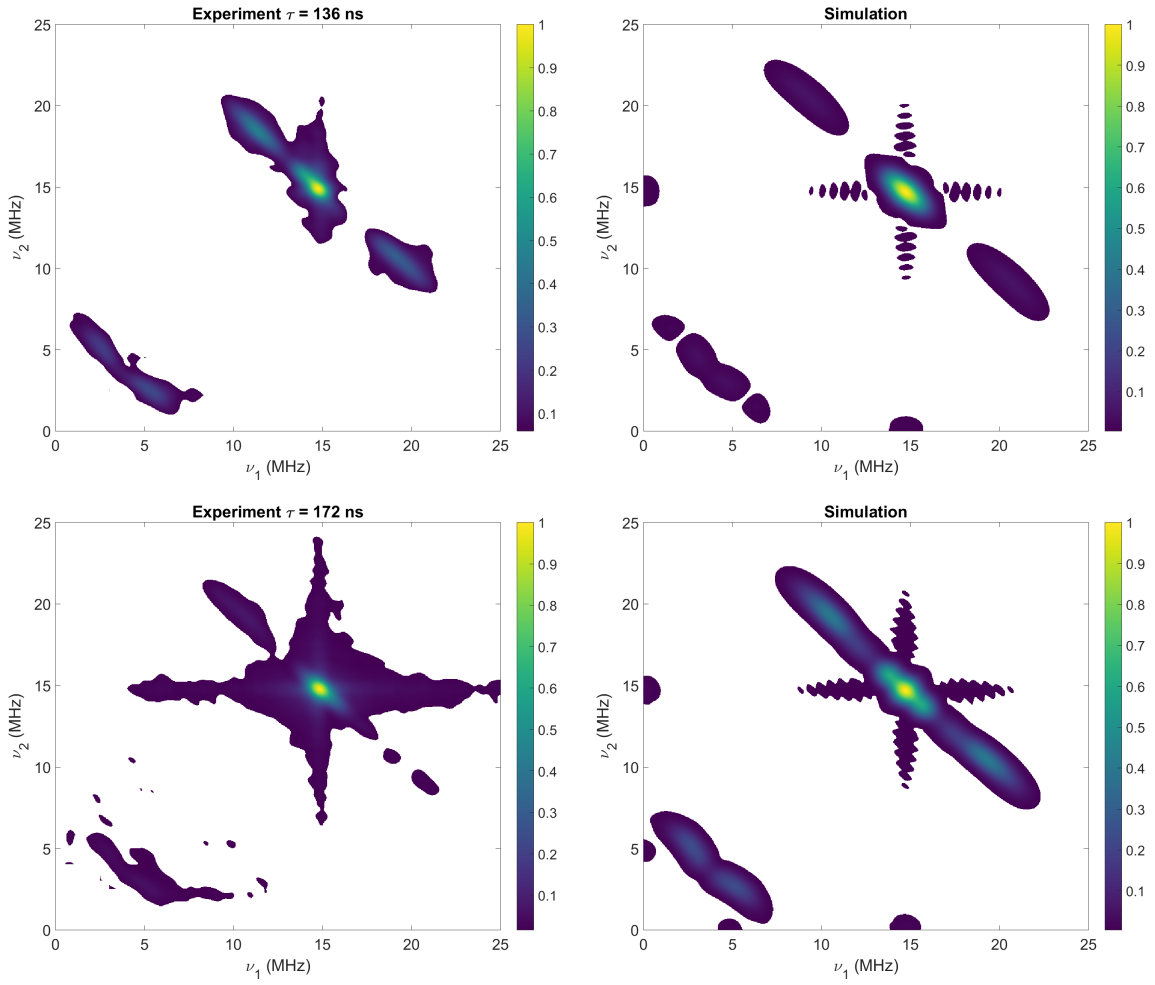


Figure B.4: (Top) HYSCORE and simulation of **3** at 150 K in powder $\tau = 136$ ns. (Bottom) HYSCORE and simulation of **3** at 150 K in powder $\tau = 172$ ns.

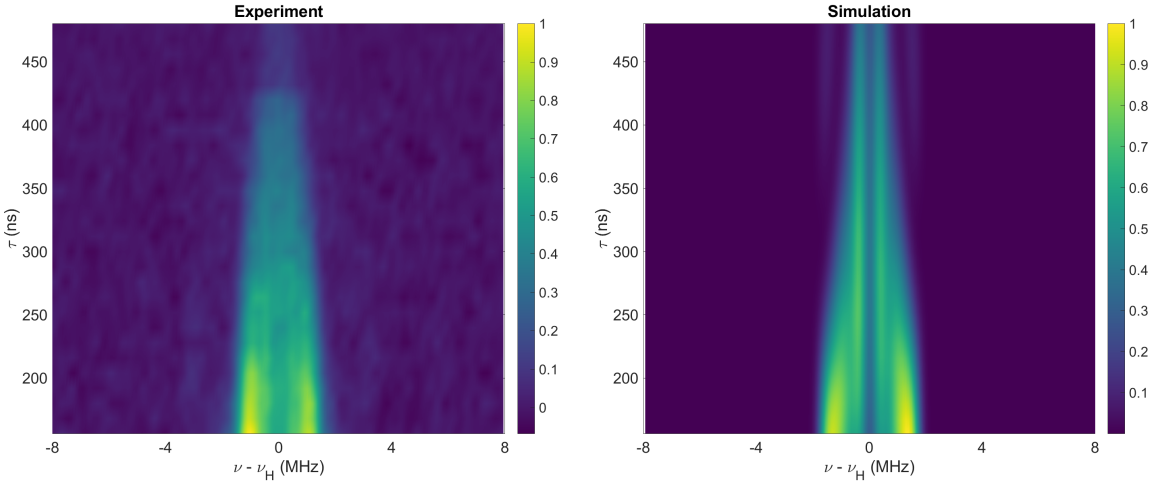


Figure B.5: 2D Mims ENDOR at 150 K in powders for **4**.

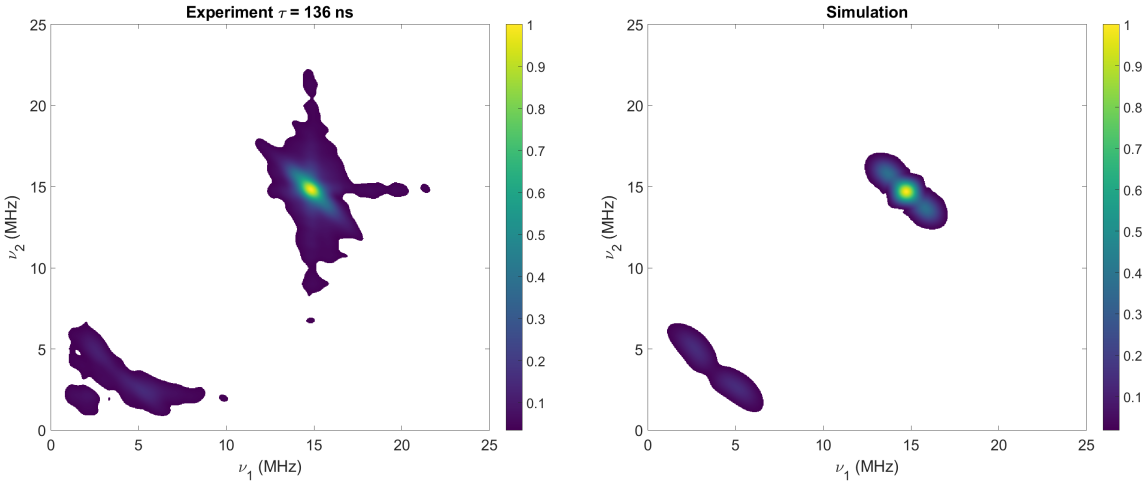


Figure B.6: HYSCORE and simulation of **4** at 150 K in powder $\tau = 136$ ns.

B.2 Zigzag graphenoids

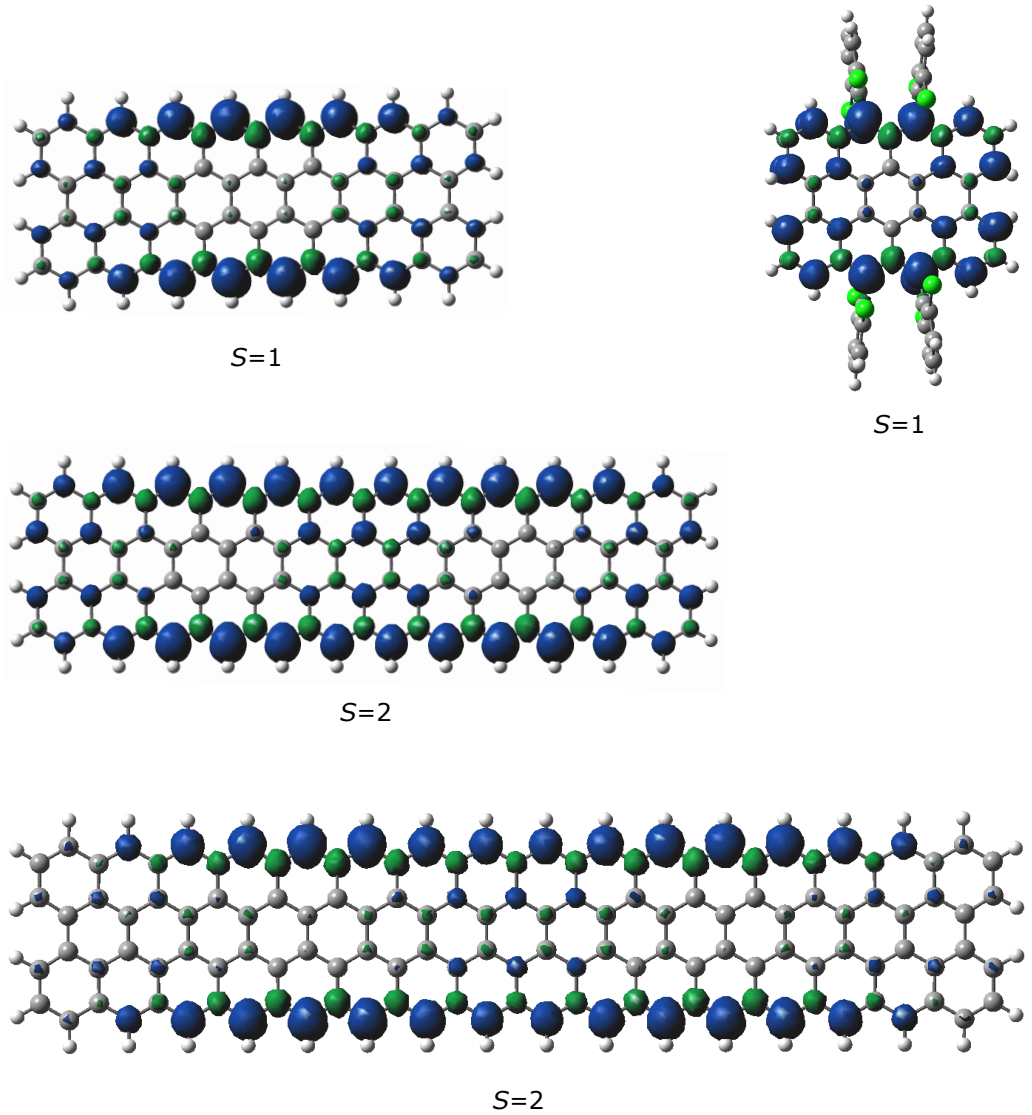


Figure B.7: Comparison of the DFT calculated spin density of **5** with longer zigzag nanoribbons. All simulations were carried out with the combination B3LYP/6-31G**. The spin state is indicated below the structure.

B.3 Ring shaped graphenoids

	xx	yy	zz
S		2	
g	2.0024	2.0028	2.0029
A_1 (MHz)	1.7	4.5	7.5
A_2 (MHz)	1.6	4.2	6.7
A_3 (MHz)	1.1	2.8	4.8
A_4 (MHz)	0.4	1.4	1.9
lw		0.1	

Table B.2: EPR parameters for the quintet state of **6** from DFT calculations. All hyperfine couplings refer to the hydrogen hyghlighted in fig. B.8. The simulation curve in fig. B.8 is obtained by multiplying all hyperfine constants by a scaling factor 1.6.

	xx	yy	zz
S		3	
g	2.0028	2.0029	2.0034
A_1 (MHz)	1.3	3.7	5.9
A_2 (MHz)	1.3	3.5	5.7
A_3 (MHz)	0.8	2.6	3.8
lw		0.14	

Table B.3: EPR parameters for the septet state of **6** from DFT calculations. All hyperfine couplings refer to the hydrogen hyghlighted in fig. B.9. The simulation curve in fig. B.9 is obtained by multiplying all hyperfine constants by a scaling factor 1.8.

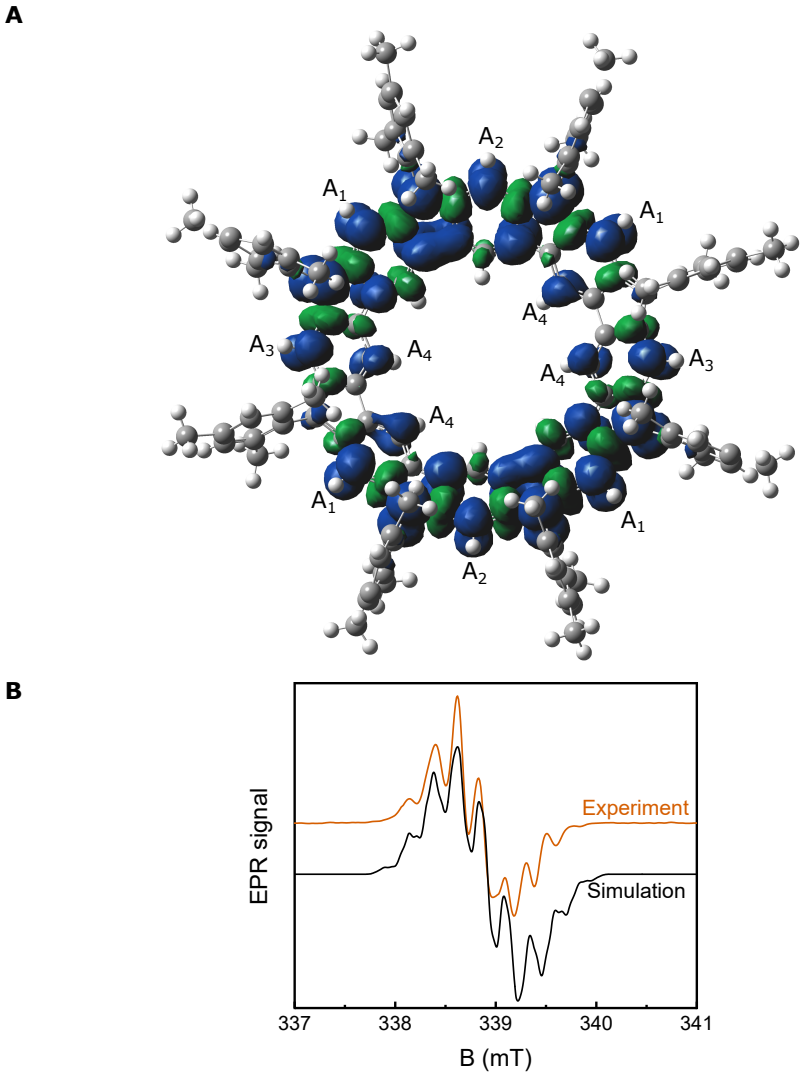


Figure B.8: (A) DFT calculated spin density of **6** in the quintet state (B3LYP/EPRII). (B) EPR simulation of **6** in solution at room temperature considering the quintet state hyperfine constants.

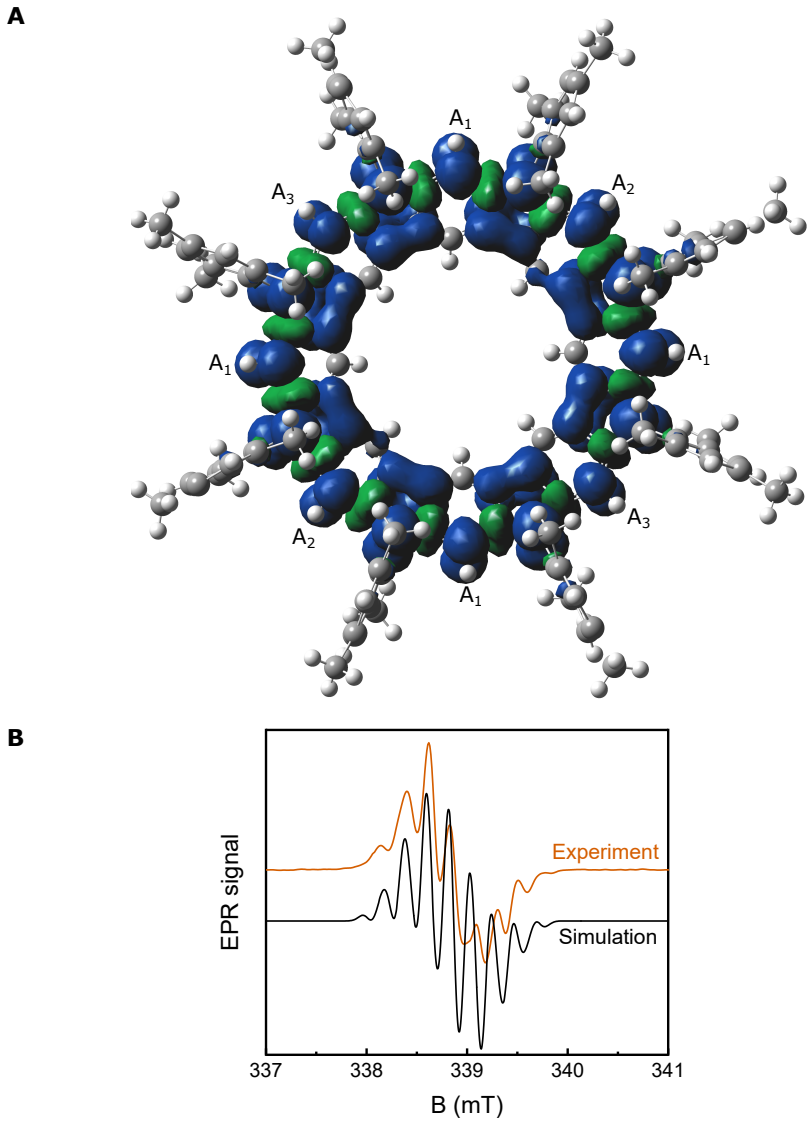


Figure B.9: (A) DFT calculated spin density of **6** in the septet state (B3LYP/EPRII). (B) EPR simulation of **6** in solution at room temperature using the septet state hyperfine constants.

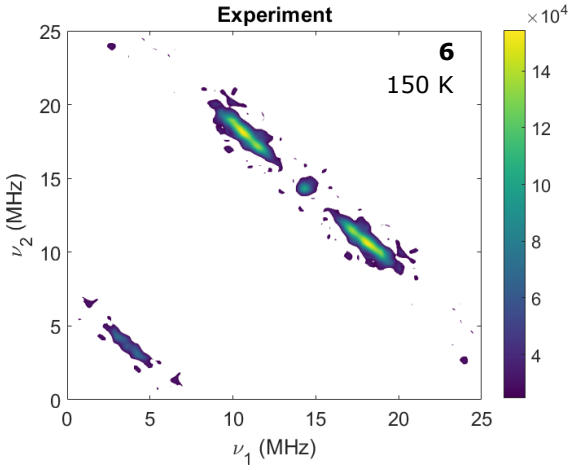


Figure B.10: HYSCORE measurement of **6** at 150 K in CS_2.

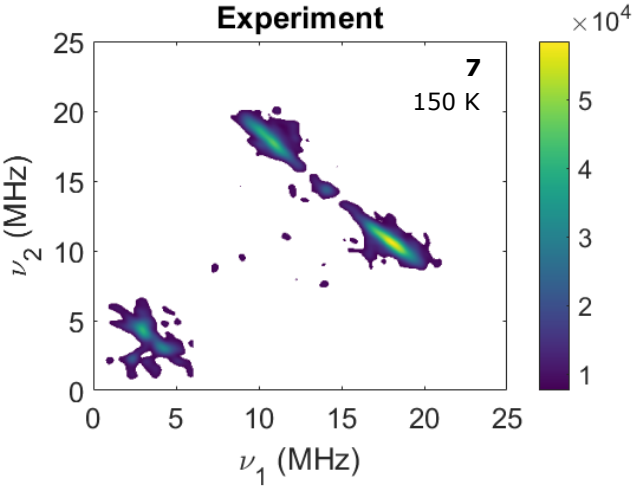


Figure B.11: HYSCORE measurement of **7** at 150 K in CS_2.

Acronyms

AFM Atomic Force Microscopy. 26, 28, 30, 166, 167

AGNR armchair GNR. 25, 27, 30, 95, 166, 167, 172

ARPES Angle Resolved PhotoEmission Spectroscopy. 26, 27

AWG Arbitrary Wave Generator. 41

CAESR Centre for Advanced ESR. 88

CCE Cluster Correlation Expansion. 16, 140

CNOT Controlled NOT. 10, 11, 35, 165

CPMG Carr-Pucell-Meiboom-Gill. 124, 125, 127, 128, 129, 130

CW Continuous Wave. 37, 38, 39, 41, 44, 46, 50, 51, 57, 69, 85, 91, 111, 145, 152, 167

DFT Density Functional Theory. 41, 52, 53, 54, 55, 56, 57, 64, 77, 86, 101, 111, 118, 178

EDNMR ELDOR-detected NMR. 47

ENDOR Electron Nuclear DOuble Resonance. 47, 50, 51, 69, 105, 120, 145, 152, 153, 154, 155, 173, 177

EPR Electron Paramagnetic Resonance. ii, 3, 22, 28, 37, 38, 39, 40, 41, 42, 43, 44, 46, 51, 52, 56, 57, 61, 62, 63, 74, 75, 82, 83, 85, 88, 91, 92, 111, 125, 127, 128, 139, 140, 168, 170

ESEEM Electron Spin Echo Envelope Modulation. 47, 48, 51, 68, 99, 130, 169

ESR Electron Spin Resonance. 37, 88, 162

eZ electron Zeeman. 5, 8, 39, 46

FID Free Induction Decay. 42, 43, 44, 168

FT Fourier Transform. 41, 100, 173

GNR Graphene Nanoribbon. 2, 3, 25, 26, 27, 28, 29, 30, 31, 34, 86, 89, 90, 93, 95, 98, 99, 162, 164, 165, 166, 172

GTO Gaussian-Type Orbital. 55

HF hyperfine. 7, 46

HOMO highest occupied molecular orbital. 86

HYSCORE HYperfine Sublevel CORrElation. 50, 118, 119, 120, 152, 154, 155, 156, 174, 177

KS Kohn-Sham. 53, 54

LDA-DFT local density approximation density functional theory. 30

LUMO lowest unoccupied molecular orbital. 86

MOF metal-organic framework. 21

MW microwave. 38, 50, 51, 61, 62, 70, 148, 167, 176

NMR Nuclear Magnetic Resonance. 7, 12, 41, 44, 47, 50, 51, 63, 109, 127, 162

NSD nuclear spin diffusion. 13, 15, 16, 72, 87

NV nitrogen vacancy. 99

nZ nuclear Zeeman. 8, 46

OWP Optimal Working Point. 16

PAH Polycyclic aromatic hydrocarbon. 32, 33

qubit quantum bit. 9, 10, 11, 12, 17, 19

RF radio frequency. 50, 51

SD spin diffusion. 13

SH spin Hamiltonian. 5, 7, 41, 54

SMM Single Molecule Magnet. 2, 17, 19

SNR signal-to-noise ratio. 105

SOC spin-orbit coupling. 19

SQUID Superconducting QUantum Interference Device. 73, 74, 75, 86, 91, 111

STM Scanning Tunnelling Microscopy. 21, 22, 26, 27, 30, 31, 32, 34, 89, 94, 166, 167

STO Slater-Type Orbital. 55

STS Scanning Tunnelling Spectroscopy. 26, 28, 34, 36

TEM Transmission Electron Microscope. 32

TrEPR transient EPR. 145, 147, 148, 149, 150, 151, 176, 177

TWTA Travelling Wave Tube Amplifier. 42, 57, 168

ZFS Zero Field Splitting. 6

ZGNR zigzag GNR. 25, 28, 166

List of Figures

1 Carbon-based nanostructures are generally diamagnetic, but different strategies have been devised to include and manipulate spins. It is possible to electrically confine single electron spins in carbon nanotubes but their performance is limited at mK temperature and hindered by spin-orbit coupling [13]. Single or multiple magnetic elements can be included inside the cage of fullerenes, but their synthesis is extremely inefficient, and it is hard to link different fullerenes with each other [14]. An intriguing strategy is to functionalise GNRs with spin active components in order to inject spin density into their edge and make use of their magnetic properties [15]. The different structures are showed together with their characteristic coherence time T_{m}, which we will assess for our molecules in the experimental part of this thesis. 2

1.1 (Top) Matrix representation of the Hadamard gate, a single qubit gate that generates a superposition of states where the states $|0\rangle$ and $|1\rangle$ have equal probability. It is easy to demonstrate $H^{\dagger}H = I$. (Middle) Matrix representation of the CNOT gate and its schematic: $|A\rangle$ is the control qubit and $|B\rangle$ is the target one which is flipped only if $|A\rangle = |1\rangle$. (Bottom) reparation of Bell states with a Hadamard gate and a CNOT gate, they represent the most simple entanglement between multiple qubits. 11

1.2 Visual representation of the central spin model. An electron spin is coupled to a nuclear bath, only the nuclei within a certain radius contribute to the decoherence, while the ones too far can be discarded. Here, the spin-bath interaction ($\hat{H}_{hf}$), and the intrabath dipolar interaction ($\hat{H}^{\mathrm{B}}_{n--n}$) are highlighted. 14

1.3 (A) Cr_7Ni, counterion omitted (C = gray, H = white, F = light green, O = red, Cr = blue, Ni = green) [77]. (B) Er polyoxometalate, part of the molecule omitted for clarity (O = red, W = blue, Er = green) [78]. (C) $V(C_8S_8)_3$ counterion omitted (C = gray, S = yellow, V = green) [79]. (D) $Cu(mnt)_2$ counterion omitted (C = gray, S = yellow, N = blue, Cu = amber) [80]. (E) VO phthalocyanine (C = gray, H = white, O = red, N = blue, V = green) [81]. (F) Tb bis-phthalocyanine (C = gray, H = white, O = red, N = blue, Tb = cyan) [82]. 18

1.4 (A) Geometry of the hexagonal lattice of graphene. (B) First Brillouin zone of the honeycomb lattice. (C) Graphene band dispersion calculated with the Hubbard model with nearest neighbour hopping energy 2.7 eV, and next-nearest neighbour hopping energy -0.54 eV. The inset shows the Dirac cones at a K point. Adapted from [127]. 22

1.5 Different geometries of graphene nanoribbons. Armchair and zigzag nanoribbons can be thought of as stripes cut from a graphene sheet with the cutting directions differing of a 30° angle. Armchair are usually referred to by their width counting the carbon atoms on the shorter edge, while zigzag by counting the number of horizontal carbon lines. For example, in the figure they would be 7-AGNR and 4-ZGNR. Cove GNRs are zigzag ribbons in which there is a carbon vacancy that produces the fjord. Chevron GNRs can be seen as two armchair ribbons fused at an angle. 25

1.6 (A) High-resolution STM image of 5-AGNR on a gold surface. Adapted from [158]. (B) High-resolution STM image of a heterojunction between 7- and 13-AGNR. Adapted from [159]. (C) ARPES image of the occupied bands of a 7-AGNR on a gold surface. White arrows indicate the top of each band, and the highest band is the valence band. The red circle on the right are peak positions of the valence band that are fit with a parabolic dispersion to yield the effective mass of the charge carrier $m \approx 0.21m_0$ (m_0 is the rest mass of an electron). The white curve refers to the average carrier velocity on the right axis. Adapted from [160]. 27

1.7 (A) Non-contact AFM image of 6-ZGNR on gold surface. (B) Differential conductance map of filled (left) and empty states (right) on the edge of the graphene nanoribbons. The top panels are experimental data, and the bottom panels are simulations with a DFT local density of states approach. Scale bars are 1 nm. Adapted from [167]. . . 28

1.8 (A) Bond-resolved STM image of an heterojunction between 7-AGNR and 9-AGNR. (B) Experiment and simulation of constant current $\mathrm{d}I/\mathrm{d}V$ maps at different voltages for the 7/9-AGNR heterojunction. The local density of states is obtained via a density functional theory calculations. The different states are attributed to different bands of the global heterostructure: conduction band (CB), unoccupied topologically-induced band (UTB), occupied topologically-induced band (OTB), and valence band (VB). Experimental STM images in A-B were taken at 4 K. Adapted from [177]. (C) Non contact AFM image of a 7-AGNR-S (S for staggered). Scale bar is 1 nm. (D) Experiment and simulation of constant current $\mathrm{d}I/\mathrm{d}V$ maps at different voltages for the 7-AGNR-S. C-D adapter from [178] 30

1.9 Examples of topological defects: Stone-Wales defect (55-77), inverse Stone-Wales defect (7557), and a reconstructed double vacancy that yields a pentagon pair and an octagon (5-8-5). 31

1.10 Examples of zig zag edge nanographene molecules: nonacene **11** in its closed shell form, phenalenyl **12**, Clar's goblet **13**, and [3]triangulene **14** in their open-shell structure. 33

1.11 Examples of nanographene molecules bearing topological defects: difluoreno[1,9,8-*alkj*:1',9',8'-*gfed*] heptalene **15**, *para*-quinodimethane embedded indenofluorene **16**, *para*-quinodimethane bridged biphenalenyl **17**, 9,10-bis(4-bromo-2,6- dimethylphenyl)anthracene **18**. 35

2.1 Schematics of a CW microwave bridge, and setup of an experiment. The microwave bridge includes the solid state MW source, and the electronics necessary to amplify and phase it. A set of waveguides directs the MW excitation towards the resonator. The circulator allows the MW to go only in one direction, for example counterclockwise, and is necessary to measure the reflection of the signal. The resonator is equipped with side coils that generate the modulation fields and are connected to the lock-in amplifier. Adapted from [246]. 38

2.2 (A) Q-band spectrum of a spin $S = 1/2$ with g anisotropy, $g = (1.9987\ 2.0007\ 2.0043)$ in a powder. (B) X-band spectrum of a copper $S = 1/2$ sample in a slow-tumbling solution. The electron spin is coupled to the copper nucleus, both ^{63}Cu and ^{65}Cu have spin $I = 3/2$ which explains the $2I + 1 = 4$ lines of the spectrum. The distance between the lines gives indication of the isotropic hyperfine coupling, while the y-axis values depend on the tumbling time, here 5 ns. (C) X-band spectrum of an $S = 1$ powder sample with zero-field splitting $D = 40$ MHz, the spectrum is the derivative of the famous Pake pattern. All simulations were produced with the Matlab package Easyspin [247]. The EPR linewidth was 0.2 mT of Lorentzian shape for all three graphs. 39

2.3 EPR line amplitude as a function of the square root of the microwave power as in eq. (2.2). The two regimes are highlighted. In the calculation we used $P_{1/2} = 24.8$ mW, $b = 1.44$, adapted from [250]. 40

2.4 Simplified schematics of a pulse EPR setup. Pulses are generated through PIN (P-type Intrinsic N-type) diode switches. In the drawing, 4 channels (+X, +Y, -X, -Y) are shown with fixed amplitudes, whereas the majority of the instruments have 4 additional channels that can be adjusted. The pulses produced are low power and they need to be amplified by a TWTA. The amplified pulses are so high power that the pulses reflected from the resonator could easily destroy the detection system, therefore a defence pulse protects the detector. A Low Noise Amplifier (LNA) is used to amplify the signal before the quadrature detection. The output is visualised as real and imaginary and allows full reconstruction of the phase and amplitude of the signal. Adapted from R. T. Weber, E580 Pulse EPR Course, Bruker Biospin Manual, 2007. 42

2.5 Single pulse FID generation and Bloch sphere representation. (I) At the thermal equilibrium the magnetisation is parallel to the z-axis, (II) the magnetisation is flipped by a $\pi/2$ pulse to the y-axis. (III) Only a certain number of spin packets are resonant with the excitation while the others have a frequency difference $\Delta\omega$ with respect to the rotating frame that determines their precession around z. (IV) After a certain time the spin packets are incoherent and the FID is extinguished. 43

2.6 Pulse sequence and Bloch sphere representation for the Hahn echo. (I) At equilibrium the magnetisation vector is parallel to the external field on z, (II) the $\pi/2$ pulse rotates the magnetisation in the xy-plane. (III) Spin packets with $\Delta\omega \neq 0$ gain a phase difference, (IV) then their precession frequency is flipped by the π pulse, (V) and in the free precession the phase difference is refocused (VI) until the spin packets come together and emit an echo signal that is detected at a time 2τ from the initial pulse. 44

2.7 In the inversion recovery sequence, the first π pulse reverses the population of the spin level. The magnetisation will the precess towards equilibrium during the time T and its state will be detected with an Hahn echo. In picket fence recovery, a train of π pulses demagnetises the sample, and similarly the recovery of the magnetisation is followed varying T. 45

2.8 Level schematics of a spin $S = 1/2$ coupled to one nucleus $I = 1/2$, assuming $A > 0,\ g_n > 0$ and weakly coupled system. The arrows indicate the spin number for electron spin and nuclear spin respectively. 47

2.9 (Top) General schematics of ESEEM techniques, involving preparation of coherent superposition, evolution and mixing of nuclear and electron coherence, and detection of electron coherence [258]. (Middle) Schematics of a 3-pulse ESEEM sequence. In a typical experiment τ is fixed and T is varied. (Bottom) Schematics of a HYSCORE sequence. In a typical experiment the π pulse has same length of the $\pi/2$ pulses but double power. 48

2.10 Trend of the modulation depth with respect to the external magnetic field for a 2-pulse ESEEM experiment on a system of spin $S = 1/2$ coupled to one hydrogen ($A = 3$ MHz, $B = 2.1$ MHz), one deuterium ($A = 1.5$ MHz, $B = 0.7$ MHz), one ^{13}N ($A = 5$ MHz, $B = 0.7$ MHz), and one ^{14}N ($A = 3.5$, $B = 1.1$). The computation follows the expression for modulation depth from [258]. The vertical lines mark the typical magnetic field for experiments at X-band and Q-band. 49

2.11 Sequence for Mims ENDOR, MW pulses are in red while RF pulses are in blue. . . 51

3.1 Schematics of the synthesis of **1**, for reaction conditions we refer to publications. In the last step of the synthesis, partial de-hydrogenation can result in production of **1b** at impurity levels. 60

3.2 Molecular structures and relationship between monomer **2** and the two dimers **3** and **4**. For each molecule both the non-magnetic and the magnetic resonant structures are shown. 60

3.3 Equivalency of the Lieb's theorem and Clar's rule for the explanation of the magnetism of **1**. 61

3.4 (A) Room-temperature CW spectra of **1** in powders and solution. (B) Temperature dependence of the integrated signal multiplied by the temperature and fit with the Bleaney-Bower's equation, and a combination of the Curie law and the Bleaney-Bowers' equation as discussed in the text. The inset shows the variation of the contribution of the EPR signal by **1** and **1b**. 62

3.5 Room–temperature EPR spectra of **1** in powder and toluene solution. Black lines are simulations with the Hamiltonian in text. 63

3.6 (A) Simulated geometry of **1** at the B3LYP/6-31G** level of theory. (B) Calculated spin density for a triplet state, iso value 0.002. 64

3.7 (A) Inversion recovery traces in toluene at different temperatures. Black lines are fit to the data with a bi-exponential recovery. (B) Hahn echo decay at 100 K in d_8-toluene. Black line is a fit with the model in text. 66

3.8 Summary of the relaxation times for **1** and **1b**. (Top) Trend of the spin-lattice relaxation rate with temperature. Solid symbols are powders, half-empty symbols toluene, and empty symbols are d_8Tol. The solid line is a fit to eq. (3.5). The dashed line marks the melting spot of toluene/d_8Tol. (Bottom) Trend of coherence time with temperature. Pentagons refer to the coherence time of **1b** while empty circles are for **1** in d_8Tol and CS_2. Lines are guide for the eye. 67

3.9 (Top) Sequence for detection of Rabi oscillations. (A) Examples of Rabi oscillations at 80 K in $d_8$tol. Different traces refer to different power attenuation used. Lines are fit to the data. (B) Fourier transform of the time traces in (A). The dashed line is a fit of the Rabi frequency with respect to the power used. The peak at 14.8 MHz refers to the Larmor frequency of hydrogen nuclei at the field of the experiment. . . 69

3.10 (A) Echo detected field sweep of **1** in OTP and d_{14}OTP at 293K. (B) Relaxation constants T_1 (empty symbols) and T_m (full symbols) in OTP (squares) and d_{14}OTP (circles) at different temperatures. 71

3.11 SQUID magnetometry $\chi_m T$ vs T for **2** and **3** at 3000 Oe. The red line is a fit to the equation in text. The data is cut at 100 K because low temperature measurements present an oxygen artefact. 73

3.12 Measurements of integrated EPR signal times temperature at different temperature for sample **4** in powders. The solid line is a fit with the Bleaney-Bower equation from eq. (3.2). 75

3.13 (A) Calculated spin density of **3** in the triplet state, iso value 0.002. (B) Simulated geometry of **3**, highlighted in red are the hydrogens that contribute to methyl rotation, in green the hydrogen that contribute to mesithyl rotation, and in blue the hydrogens that do not participate to molecular motions. (C) Calculated spin density of **3** in the triplet state, iso value 0.002. (D) Calculated spin density of **3** in the quintet state, iso value 0.002. (E) Calculated spin density of **4** in the triplet state, iso value 0.002. (F) Calculated spin density of **4** in the quintet state, iso value 0.002. 76

3.14 (A) CW spectra of **2**-**4** in powders and toluene solution with respective simulations. (B) Direct comparison of the solution spectra of **2**-**4**. The different width of the spectra is a consequence of different hyperfine couplings in the three molecules. **2** has the largest hyperfine coupling constants and the widest spectrum, while **4** has the smallest couplings and the narrowest spectrum. 77

3.15 Spin-lattice relaxation rate for **2** (top), **3** (middle), and **4** (bottom). Half-circles are toluene, empty circles d_8Tol, empty triangles CS_2, and empty diamond d_{14}OTP. Solid lines are fit to the model described in text. Dashed lines indicate the melting point of the solvents. Shaded areas refer to main relaxation mechanisms. 79

3.16 (A) T_1^{-1} comparison between ambient pressure oxygenated sample (half squares) and degassed and flame sealed sample (half circles) for compound **4** in toluene. (B) T_m comparison between oxygenated and degassed sample. 81

3.17 Concentration dependence of T_m for **2** in d_8Tol at 80 K and 293 K. 82

3.18 Coherence time for **2** (top), **3** (middle), and **4** (bottom). Full circles are powders, half-circles toluene, empty circles d_8Tol, empty triangles CS_2, and empty diamonds d_{14}OTP. Lines are guides for the eye. Dashed lines indicate the melting point of the solvents. Shaded areas refer to main relaxation mechanisms. 84

4.1 (A) Peri-tetracene seen as fundamental unit or segment of longer nanoribbons from literature (from top to bottom [167, 177, 178]). (B) Chemical structure of peri-tetracene in its open-shell diradical configuration. 90

4.2 (A) X-ray structure of peri-tetracene as reported from [320]. Highlighted are the nuclei responsible for hyperfine coupling. (B) Room-temperature CW EPR of peri tetracene in 3 different solutions (CS_2, d_8-toluene, and toluene), a diamagnetic solid matrix (d_{14}OTP), and powders. The dashed line is a simulation with the parameters in table 4.1. 91

4.3 Computed spin densities using different combinations of functional/basis sets for peri-tetracene using the fixed geometry obtain from X-Ray [320]. The 8 highlighted hydrogen atoms in the first structure indicate the nuclei responsible for hyperfine coupling and their parameters are reported in table 4.1 for each combination. 93

4.4 All spin densities were obtained at the B3LYP/6-31G** level of theory and are showed with iso value 0.002. (A) Extension of the zigzag edge of peri-tetracene. Synthesis and characterisation on surface from [167]. (B) Extension of the armchair edge of peri-tetracene, all the spin density concentrated at the zigzag termini. Synthesis and characterisation of 9-AGNR from [161]. (C) Chiral GNR, synthesis and characterisation from [324]. (D-E) Staggered 7-AGNR and in-line staggered 7-AGNR from [178]. . . 95

4.5 Comparison between the spin density of peri-tetracene and other zigzag-edged nanographene molecules. All spin densities shown were obtained at the B3LYP/6-31G** level of theory and are showed with iso value 0.002. (A) Spin density of peri-tetracene, repeated for convenience. (B) [6]triangulene, yet to be isolated, but [4] and [5]triangulene were observed in [227, 228]. (C) Rhomboid nanographene [325]. 96

4.6 Experimental traces of the spin-lattice recovery as measured with a Picket Fence sequence, at different temperatures (80, 100, 120, 140, 160, 180, 200, 220, 240, 293 K). Black lines are fit with a bi-exponential model for certain temperatures (80, 100, 180, 293 K). 97

4.7 X-band (top) and Q-band (bottom) spin-lattice relaxation rate vs T diagram for peri-pentacene in different matrices: toluene (squares), $d_8$toluene (circles), CS_2 (triangles), d_{14}OTP (rhombi). Empty symbols refer to X-band, full symbols to Q-band. The vertical lines mark the melting temperature of CS_2 (163 K) and toluene (178 K). The black lines are fit to the expression in text. 98

4.8 All traces are taken at 80 K. Empty symbols refer to X-band, full symbols to Q-band. (A) Toluene decay with fit. (B) FT of the modulation in toluene. (C) d_8Tol decay with fit. (D) FT of the modulation in d_8Tol. (E) d_{14}OTP decay with fit. (F) FT of the modulation in d_{14}OTP. (G) CS_2 decay and fit. (H)FT of the modulation in CS_2, black line is an Easyspin simulation that takes into account all the hydrogens at the edge of the molecule. (I) Q-band decay in toluene (squares), d_{14}OTP (rhombi), and CS_2 (triangles). In the time decay traces, red lines are fit with a bi-exponential decay, black line are fit with a stretched exponential decay. 100

4.9 (Top) Parameters obtained fitting with a stretched exponential model. (A) X-band results. (B) Q-band results. In all graphs different matrices are represented by symbols: toluene (squares), d-toluene (circles), CS_2 (triangles), d_{14}OTP (rhombi). Empty symbols refer to X-band, full symbols to Q-band. (Bottom) Parameters obtained fitting with a bi-exponential. (C) X-band results. (D) Q-band results. Triangles are CS_2, and rhombi d_{14}OTP. Empty symbols refer to T_m in X-band and full symbols to Q-band. Half-filled symbols represent T_f. Vertical lines mark the melting point of CS_2 (163 K) and toluene (178 K). 102

4.10 CW-ENDOR of **5** in CS_2 at 293 K. In the top line the off-resonance background has been removed, while it is still present in the bottom line. 105

5.1 Structure of 8MC-R (**6**) and 10MC-R (**7**) in the resonance structures that allow the largest number of unpaired spins. 109

5.2 (A) Room-temperature CW-EPR of **6** in CS_2 solution, dOTP matrix, and powders. (B) Room-temperature CW-EPR of **7** in CS_2 solution, dOTP matrix, and powders. Black lines are simulations with the model in text. 111

5.3 Spin density for the triplet state of **6** calculated at the CAM-B3LYP/EPR-II level of theory. Highlighted and labelled are the nuclei with the largest spin density. 112

5.4 Spin density for the triplet state of **7**. Highlighted and labelled are the nuclei with the largest hyperfine coupling. 114

5.5 Relaxation times comparison between two different samples of **7** in CS_2. 115

5.6 (A) Summary of T_1, T_m, and the stretch parameter β for **6** (circles) and **7** (triangles) in CS_2. (B) Summary of T_1, T_m, and the stretch parameter β for **6** (circles) and **7** (triangles) in d_{14}OTP. 116

5.7 (A-B) Trend of T_{sd}^{-1}, T_{avg}^{-1}, and T_1^{-1} for **6** (circles) and **7** (triangles) in d_{14}OTP. The vertical lines mark the temperature difference between the two regimes of $A_1 > A_{sd}$ and $A_1 < A_{sd}$, where A_1 and A_{sd} are weights in the bi-exponential fit. Solid black lines are linear fits to the data. (C-D) Fit of T_{avg}^{-1} for **6** (circles) and **7** (triangles) with the model discussed in text (black line), which is further broken down in the two components: Raman (purple), and local (red). 117

5.8 (A) HYSCORE experiment for **6** in CS_2 at 80 K. (B) Simulations using the parameters in table 5.1 118

5.9 (A) HYSCORE experiment for **7** in CS_2 at 80 K. (B) Simulations using the experimental parameters in table 5.2. 119

6.1 Nuclear spins are ubiquitous and destructive to quantum coherence. Homonuclear flip-flops modulate the local magnetic field perceived by the electron spin. The large density of nuclear spins at the edges of the molecules studied in this thesis is the main channel of decoherence. Additional interactions are provided by the environmental nuclei in the host or matrix. In the figure, different nuclei are represented by different colors, for example H = cyan, Cl = green, and ^{13}C = gray. 123

6.2 Dynamical decoupling sequences: the first pulse is a $\pi/2$, while the decoupling train is made of π pulses. The letters above the pulses indicate the channel used. 124

6.3 Shape of the time domain filter function for a CPMG6 decoupling sequence 126

6.4 (A) Recording of the echo signals for CP and CPMG decoupling sequences using a phase cycling on the first pulse only and on all pulses (indicated with ±), at 293 K for **1** in OTP. The pulse positions are indicated in gray, together with their channel and the phase cycling used. (B) Results for the 2-step (up triangles) and 2^n-step (down triangles) phase cycling for **1** in OTP at 293 K at X-band. (C) Results for the 2-step (up triangles) and 2^n-step (down triangles) phase cycling for **1** in OTP at 293 K at Q-band. (D) Results for the 2-step (up triangles) and 2^n-step (down triangles) phase cycling for **1** in OTP at 200 K at X-band. (E) Results for the 2-step (up triangles) and 2^n-step (down triangles) phase cycling for **1** in d_{14}OTP at 293 K at X-band. . . 128

6.5 (A) Fourier Transform intensity of the modulation of the time decay for **6** in CS_2 at 80 K as a function of the number of pulses applied. (B) Fourier Transform intensity of the modulation of the time decay for **7** in CS_2 at 80 K as a function of the number of pulses applied. 130

6.6 (A) Effect of instantaneous diffusion on the coherence time of **1** in OTP (squares) and d_{14}OTP (circles) at 293 K. (B) Effect of instantaneous diffusion on the coherence time of **6** (circles) and **7** (triangles) in CS_2 at 80 K. (C) Effect of instantaneous diffusion on the coherence time of **6** (circles) and **7** (triangles) in d_{14}OTP at 150 K. θ refers to the turning angle of the second pulse in the echo sequence, $\theta = 180°$ corresponds to a π pulse. Black lines are linear fit, the coherence time in absence of instantaneous diffusion is obtained by the y intercept of the linear regression. 131

6.7 (A) Summary of the decay times for different sequences for **1** in OTP at 200 and 293 K. (B) Summary of the decay times for different sequences for **1** in d_{14}OTP at 200 and 293 K. Solid lines are fit to the data with the model in eq. (6.11). Dashed line marks the time constant scaling with an enhancement factor $n^{2/3}$. 133

6.8 (A) Summary of the decay times for different sequences for **5** when fit with a stretched exponential decay. (B) Summary of the decay times for different sequences for **5** when fit with a bi-exponential decay. The two models and their significance are discussed in chapter 4 134

6.9 (A) Summary of the decay times of **6** and **7** in CS_2 at 80K. (B) Summary of the decay times of **6** and **7** in d_{14}OTP at 150 K. 134

6.10 $S(\omega)$ from the spectral deconvolution of CPMG data in OTP at 200 K. The blue dots are the spectral density function for individual traces, while the orange triangles are their mean. Solid lines are fit with the models discussed in text. The shaded area includes the Lorentzian fitting to the individual CPMG traces. 137

A.1 **18** MeOAn-6ANI-Ph($NN^{\cdot}$)-NI, where MeOAn = p -methoxyaniline, 6ANI = 4-(N-piperidinyl)-naphthalene-1,8-dicarboximide, Ph = phenyl, and NI = naphthalene-1,8:4,5-bis(dicarboximide) [384]. **19** Substitution of the NN radical with a $BPNO^{\cdot}$ radical [385]. Mechanism of enhanced intersystem crossing (EISC) in presence of the nitroxil radical. The *D represents the excited state ^{2}(MeOAn$^{-\cdot}$–Ph($NN^{\cdot}$)–NI$^{-\cdot}$). The magnetic field introduced by the radical produces a strong mixing between a doublet and quartet state. In addition to this it is possible to produce a local triplet on the NI group that can be written as ^{2,4}(MeOAn–Ph($NN^{\cdot}$)–^{*3}NI) from which is harder to obtain charge recombination and it represents the key point in increasing the lifetime of the system (reproduced from [384]). 144

A.2 Chemical structures of the building blocks of the donor–acceptor tryad. **20** is the donor zinc porphyrin. **21** is the donor plus one terpyridine group. 145

A.3 Chemical structure of the donor–metal–donor tryad. The same molecule could be synthesised with Cu as a central metal. 146

A.4 Chemical structure of the donor–metal–acceptor tryad. Excitation is provided by external light pulses, while spin control is achieved through microwaves. Three different compounds are available with central metal: Zn, Cu, and Co. 147

A.5 (Top) Schematics of TrEPR, a transient signal is generated by the light pulse and the magnetic field is swept. (Bottom) Schematics of pulse EPR with light excitation. Any MW pulse can be used before light excitation to depolarise any background signal. After pulse excitation any pulse sequence can be used to study the 148

A.6 UV/Vis spectroscopy of the tryads and the building blocks in toluene at room temperature. 148

A.7 (A) TrEPR of **20** at 5 K. (B) TrEPR of **21** at 5 K. 149

A.8 TrEPR of **22** at 5 K. 150

A.9 TrEPR of **23** at 5 K. 151

A.10 TrEPR of **24** at 5 K. 151

B.1 2D Mims ENDOR at 150 K in powders for **2**. 153

B.2 (Top) HYSCORE and simulation of **2** at 150 K in powder $\tau = 136$ ns. (Bottom) HYSCORE and simulation of **2** at 150 K in powder $\tau = 172$ ns. 154

B.3 2D Mims ENDOR at 150 K in powders for **3**. 154

B.4 (Top) HYSCORE and simulation of **3** at 150 K in powder $\tau = 136$ ns. (Bottom) HYSCORE and simulation of **3** at 150 K in powder $\tau = 172$ ns. 155

B.5 2D Mims ENDOR at 150 K in powders for **4**. 155

B.6 HYSCORE and simulation of **4** at 150 K in powder $\tau = 136$ ns. 156

B.7 Comparison of the DFT calculated spin density of **5** with longer zigzag nanoribbons. All simulations were carried out with the combination B3LYP/6-31G**. The spin state is indicated below the structure. 157

B.8 (A) DFT calculated spin density of **6** in the quintet state (B3LYP/EPRII). (B) EPR simulation of **6** in solution at room temperature considering the quintet state hyperfine constants. 159

B.9 (A) DFT calculated spin density of **6** in the septet state (B3LYP/EPRII). (B) EPR simulation of **6** in solution at room temperature using the septet state hyperfine constants. 160

B.10 HYSCORE measurement of **6** at 150 K in CS_2. 161

B.11 HYSCORE measurement of **7** at 150 K in CS_2. 161

List of Tables

3.1 EPR parameters used for simulations of powder and solution spectra. All the hyperfine couplings and the g-factor are obtained by DFT calculations. 65

3.2 Isotropic hyperfine parameters for **2** and **3** from DFT and used in the simulation of the experiment. 77

3.3 Parameters used for T_1^{-1} fit with the expression in text, and fit results. † from DFT calculations; * from fit. 81

4.1 EPR parameters as calculated from DFT. The experimental line indicates the parameters used for the d_{14}OTP simulation in fig. 4.2B. 94

5.1 Simulation parameters for **6** from DFT calculations 113

5.2 Simulation parameters for **7** from DFT calculations. The parameters used for simulating experiments are obtained by multiplying the calculated parameters by a factor 0.85. 113

5.3 Fit parameters for the curves in fig. 5.7 for **6** and **7**. 118

B.1 Hydrogen hyperfine coupling used in ENDOR and HYSCORE simulations. 153

B.2 EPR parameters for the quintet state of **6** from DFT calculations. All hyperfine couplings refer to the hydrogen hyghlighted in fig. B.8. The simulation curve in fig. B.8 is obtained by multiplying all hyperfine constants by a scaling factor 1.6. 158

B.3 EPR parameters for the septet state of **6** from DFT calculations. All hyperfine couplings refer to the hydrogen hyghlighted in fig. B.9. The simulation curve in fig. B.9 is obtained by multiplying all hyperfine constants by a scaling factor 1.8. . . 158

Bibliography

[1] X.-Y. Wang, A. Narita, and K. Müllen. "Precision synthesis versus bulk-scale fabrication of graphenes". *Nature Reviews Chemistry* 2 (2018), 1–10. DOI: 10.1038/s41570-017-0100 (cit. on p. 1).

[2] X. Y. Wang, X. Yao, and K. Müllen. "Polycyclic aromatic hydrocarbons in the graphene era". *Science China Chemistry* 62 (2019), 1099–1144. DOI: 10.1007/s11426-019-9491-2 (cit. on pp. 1, 32).

[3] W. Zeng and J. Wu. "Open-Shell Graphene Fragments". *Chem* 7 (2020), 358–386. DOI: 10.1016/j.chempr.2020.10.009 (cit. on pp. 1, 32, 33).

[4] J. Liu and X. Feng. "Synthetic Tailoring of Graphene Nanostructures with Zigzag-Edged Topologies: Progress and Perspectives". *Angewandte Chemie - International Edition* 59 (2020), 23386–23401. DOI: 10.1002/anie.202008838 (cit. on p. 1).

[5] M. A. Nielsen and I. Chuang. *Quantum computation and quantum information*. Cambridge University Press, 2010 (cit. on pp. 1, 10, 12).

[6] V. Scarani et al. "The security of practical quantum key distribution". *Reviews of modern physics* 81 (2009), 1301 (cit. on p. 1).

[7] C. L. Degen, F. Reinhard, and P. Cappellaro. "Quantum sensing". *Reviews of Modern Physics* 89 (2017), 1–39. DOI: 10.1103/RevModPhys.89.035002 (cit. on pp. 1, 12).

[8] F. Arute et al. "Quantum supremacy using a programmable superconducting processor". *Nature* 574 (2019), 505–510. DOI: 10.1038/s41586-019-1666-5 (cit. on p. 1).

[9] V. Cerletti et al. "Recipes for spin-based quantum computing". *Nanotechnology* 16 (2005), R27 (cit. on p. 1).

[10] J. L. O'brien, A. Furusawa, and J. Vučković. "Photonic quantum technologies". *Nature Photonics* 3 (2009), 687–695 (cit. on pp. 1, 2).

[11] F. A. Zwanenburg et al. "Silicon quantum electronics". *Reviews of modern physics* 85 (2013), 961 (cit. on p. 2).

[12] D. D. Awschalom et al. "Quantum technologies with optically interfaced solid-state spins". *Nature Photonics* 12 (2018), 516–527. DOI: 10.1038/s41566-018-0232-2 (cit. on pp. 2, 17).

[13] E. A. Laird et al. "Quantum transport in carbon nanotubes". *Reviews of Modern Physics* 87 (2015), 703 (cit. on p. 2).

[14] W. Harneit. "Fullerene-based electron-spin quantum computer". *Physical Review A* 65 (2002), 032322 (cit. on p. 2).

[15] M. Slota et al. "Magnetic edge states, spin dynamics and coherent manipulation of molecular graphene nanoribbons". *Nature* 557 (2018), 691. DOI: 10.1038/s41586-018-0154-7 (cit. on pp. 2, 28, 89, 98, 99).

[16] D. Gatteschi, R. Sessoli, and J. Villain. *Molecular Nanomagnets*. Vol. 5. Oxford University Press, 2006 (cit. on pp. 2, 19).

[17] G. Aromı et al. "Design of magnetic coordination complexes for quantum computing". *Chemical Society Reviews* 41 (2012), 537–546 (cit. on p. 2).

[18] C.-J. Yu et al. "A Molecular Approach to Quantum Sensing". *ACS Central Science* (2021) (cit. on p. 3).

[19] M. Mannini et al. "Quantum tunnelling of the magnetization in a monolayer of oriented single-molecule magnets". *Nature* 468 (2010), 417–421. DOI: 10.1038/nature09478 (cit. on pp. 3, 17, 22, 141).

[20] L. Bogani and W. Wernsdorfer. "Molecular spintronics using single-molecule magnets". *Nature Materials* 7 (2008), 179–186 (cit. on pp. 3, 22, 141).

[21] M. Warner et al. "Potential for spin-based information processing in a thin-film molecular semiconductor". *Nature* 503 (2013), 504–508. DOI: 10.1038/nature12597 (cit. on pp. 3, 19).

[22] W. Han et al. "Graphene spintronics". *Nature nanotechnology* 9 (2014), 794–807 (cit. on pp. 3, 24).

[23] F. Neese. "Quantum Chemistry and EPR Parameters". In: *EPR spectroscopy: fundamentals and methods*. Ed. by D. Goldfarb and S. Stoll. John Wiley & Sons, 2018 (cit. on pp. 5, 57).

[24] J. Telser. "EPR Interactions – Zero-field Splittings". In: *EPR spectroscopy: fundamentals and methods*. Ed. by D. Goldfarb and S. Stoll. John Wiley & Sons, 2018 (cit. on p. 6).

[25] J. A. Weil and J. R. Bolton. *Electron paramagnetic resonance: elementary theory and practical applications*. John Wiley & Sons, 2007 (cit. on pp. 6, 7).

[26] A. Schweiger and G. Jeschke. *Principles of pulse electron paramagnetic resonance*. Oxford University Press on Demand, 2001 (cit. on pp. 6, 12, 13, 41, 43, 46, 51, 70, 131, 135).

[27] A. Abragam and B. Bleaney. *Electron paramagnetic resonance of transition ions*. OUP Oxford, 2012 (cit. on p. 6).

[28] R. Horodecki et al. "Quantum entanglement". *Reviews of Modern Physics* 81 (2009), 865–942. DOI: 10.1103/RevModPhys.81.865 (cit. on p. 10).

[29] D. McMahon. *Quantum computing explained*. John Wiley & Sons, 2007 (cit. on p. 10).

[30] S. Lloyd. "Almost any Quantum Gate is universal". *Physical Review Letters* 75 (1995), 346. DOI: 10.1103/PhysRevLett.75.346 (cit. on p. 10).

[31] A. Barenco et al. "Elementary gates for quantum computation". 52 (1995) (cit. on p. 10).

[32] D. Deutsch and R. Jozsa. "Rapid solution of problems by nuclear-magnetic-resonance quantum computation". *Proceedings of the Royal Society of London. Series A: Mathematical and Physical Sciences* 439 (1992), 553–558 (cit. on p. 10).

[33] P. W. Shor. "Algorithms for quantum computation: discrete logarithms and factoring". *Proceedings 35th annual symposium on foundations of computer science*. Ieee, 1994, 124–134 (cit. on p. 10).

[34] L. K. Grover. "Quantum mechanics helps in searching for a needle in a haystack". *Physical review letters* 79 (1997), 325 (cit. on p. 10).

[35] J. Preskill. "Quantum computing and the entanglement frontier". *arXiv preprint arXiv:1203.5813* (2012) (cit. on p. 10).

[36] J. Preskill. "Quantum Computing in the NISQ era and beyond". *Quantum* 2 (2018), 79. DOI: 10.22331/q-2018-08-06-79 (cit. on p. 10).

[37] D. P. DiVincenzo. "Quantum Computation". *Science* 270 (1995), 255–261. DOI: 10.1126/science.270.5234.255 (cit. on p. 10).

[38] E. Knill, R. Laflamme, and G. J. Milburn. "A scheme for efficient quantum computation with linear optics". *Nature* 409 (2001), 46–52. DOI: 10.1038/35051009 (cit. on p. 11).

[39] M. H. Devoret and R. J. Schoelkopf. "Superconducting circuits for quantum information: An outlook". *Science* 339 (2013), 1169–1174. DOI: 10.1126/science.1231930 (cit. on p. 11).

[40] D. P. DiVincenzo. "The physical implementation of quantum computation". *Fortschritte der Physik* 48 (2000), 771–783. DOI: 10.1002/1521-3978(200009)48:9/11<771::AID-PROP771>3.0.CO;2-E (cit. on p. 11).

[41] P. C. E. Stamp and A. Gaita-Ariño. "Spin-based quantum computers made by chemistry: hows and whys". *J. Mater. Chem.* 19 (2009), 1718–1730. DOI: 10.1039/B811778K (cit. on p. 11).

[42] T. D. Ladd et al. "Quantum computers". *Nature* 464 (2010), 45–53. DOI: 10.1038/nature08812 (cit. on p. 11).

[43] I. L. Chuang et al. "Bulk quantum computation with nuclear magnetic resonance: theory and experiment". *Proceedings of the Royal Society of London. Series A: Mathematical, Physical and Engineering Sciences* 454 (1998), 447–467 (cit. on p. 12).

[44] D. Loss and D. P. DiVincenzo. "Quantum computation with quantum dots". *Physical Review A* 57 (1998), 120–126. DOI: 10.1103/PhysRevA.57.120 (cit. on p. 12).

[45] B. Trauzettel et al. "Spin qubits in graphene quantum dots". *Nature Physics* 3 (2007), 192–196. DOI: 10.1038/nphys544 (cit. on pp. 12, 104).

[46] B. E. Kane. "A silicon-based nuclear spin quantum computer". *Nature* 393 (1998), 133–137. DOI: 10.1038/30156 (cit. on p. 12).

[47] L. Childress and R. Hanson. "Diamond NV centers for quantum computing and quantum networks". *MRS Bulletin* 38 (2013), 134–138. DOI: DOI:10.1557/mrs.2013.20 (cit. on p. 12).

[48] M. N. Leuenberger and D. Loss. "Quantum computing in molecular magnets". *Nature* 410 (2001), 789–793 (cit. on pp. 12, 17).

[49] I. L. Chuang et al. "Quantum computers, factoring, and decoherence". *Science* 270 (1995), 1633–1635. DOI: 10.1126/science.270.5242.1633 (cit. on p. 12).

[50] W. H. Zurek. "Decoherence, einselection, and the quantum origins of the classical". *Reviews of modern physics* 75 (2003), 715 (cit. on p. 12).

[51] M. A. Schlosshauer. *Decoherence: and the quantum-to-classical transition*. Springer Science & Business Media, 2007 (cit. on p. 12).

[52] B. Herzog and E. Hahn. "Transient nuclear induction and double nuclear resonance in solids". *Physical Review* 103 (1956), 148 (cit. on p. 14).

[53] J. Klauder and P. Anderson. "Spectral Diffusion Decay in Spin Resonance Experiments". *Physical Review* 125 (1962), 912–932. DOI: 10.1103/PhysRev.125.912 (cit. on p. 14).

[54] R. de Sousa and S. Das Sarma. "Theory of nuclear-induced spectral diffusion: Spin decoherence of phosphorus donors in Si and GaAs quantum dots". *Physical Review B - Condensed Matter and Materials Physics* 68 (2003), 1153221–11532213. DOI: 10.1103/PhysRevB.68.115322 (cit. on p. 14).

[55] R. de Sousa and S. Das Sarma. "Electron spin coherence in semiconductors: Considerations for a spin-based solid-state quantum computer architecture". *Physical Review B - Condensed Matter and Materials Physics* 67 (2003), 1–4. DOI: 10.1103/PhysRevB.67.033301 (cit. on p. 14).

[56] W. M. Witzel, R. De Sousa, and S. Das Sarma. "Quantum theory of spectral-diffusion-induced electron spin decoherence". *Physical Review B - Condensed Matter and Materials Physics* 72 (2005), 1–4. DOI: 10.1103/PhysRevB.72.161306 (cit. on p. 16).

[57] W. M. Witzel and S. Das Sarma. "Quantum theory for electron spin decoherence induced by nuclear spin dynamics in semiconductor quantum computer architectures: Spectral diffusion of localized electron spins in the nuclear solid-state environment". *Physical Review B - Condensed Matter and Materials Physics* 74 (2006), 1–24. DOI: 10.1103/PhysRevB.74.035322 (cit. on p. 16).

[58] W. Yao, R. B. Liu, and L. J. Sham. "Theory of electron spin decoherence by interacting nuclear spins in a quantum dot". *Physical Review B - Condensed Matter and Materials Physics* 74 (2006), 1–11. DOI: 10.1103/PhysRevB.74.195301 (cit. on p. 16).

[59] S. K. Saikin, W. Yao, and L. J. Sham. "Single-electron spin decoherence by nuclear spin bath: Linked-cluster expansion approach". *Physical Review B - Condensed Matter and Materials Physics* 75 (2007). DOI: 10.1103/PhysRevB.75.125314 (cit. on p. 16).

[60] W. Yang and R. B. Liu. "Quantum many-body theory of qubit decoherence in a finite-size spin bath". *Physical Review B - Condensed Matter and Materials Physics* 78 (2008), 1–13. DOI: 10.1103/PhysRevB.78.085315 (cit. on pp. 16, 124).

[61] W. Yang and R. B. Liu. "Quantum many-body theory of qubit decoherence in a finite-size spin bath. II. Ensemble dynamics". *Physical Review B - Condensed Matter and Materials Physics* 79 (2009), 1–7. DOI: 10.1103/PhysRevB.79.115320 (cit. on p. 16).

[62] G. Balasubramanian et al. "Ultralong spin coherence time in isotopically engineered diamond". *Nature Materials* 8 (2009), 383–387. DOI: 10.1038/nmat2420 (cit. on pp. 16, 106, 122).

[63] A. M. Tyryshkin et al. "Electron spin coherence exceeding seconds in high-purity silicon". *Nature Materials* 11 (2012), 143–147. DOI: 10.1038/nmat3182 (cit. on pp. 16, 106, 122).

[64] D. Vion et al. "Manipulating the quantum state of an electrical circuit". *Science* 296 (2002), 886–889 (cit. on p. 16).

[65] R. Harding et al. "Spin Resonance Clock Transition of the Endohedral Fullerene $^{15}N@C_{60}$". *Physical review letters* 119 (2017), 140801 (cit. on p. 16).

[66] G. Wolfowicz et al. "Atomic clock transitions in silicon-based spin qubits". *Nature Nanotechnology* 8 (2013), 561–564. DOI: 10.1038/nnano.2013.117 (cit. on pp. 16, 122).

[67] G. W. Morley et al. "Quantum control of hybrid nuclear-electronic qubits". *Nature Materials* 12 (2013), 103–107. DOI: 10.1038/nmat3499 (cit. on pp. 16, 140).

[68] M. Shiddiq et al. "Enhancing coherence in molecular spin qubits via atomic clock transitions". *Nature* 531 (2016), 348–351. DOI: 10.1038/nature16984 (cit. on pp. 16, 20, 122).

[69] J. M. Zadrozny et al. "A Porous Array of Clock Qubits". *Journal of the American Chemical Society* 139 (2017), 7089–7094. DOI: 10.1021/jacs.7b03123 (cit. on pp. 16, 20, 122).

[70] L. Viola, E. Knill, and S. Lloyd. "Dynamical decoupling of open quantum systems". *Physical Review Letters* 82 (1999), 2417–2421 (cit. on pp. 17, 122).

[71] A. Chatterjee et al. "Semiconductor qubits in practice". *Nature Reviews Physics* 3 (2021), 157–177. DOI: 10.1038/s42254-021-00283-9 (cit. on p. 17).

[72] M. Atatüre et al. “Material platforms for spin-based photonic quantum technologies”. *Nat. Rev. Mat.* 3 (2018), 38–51. DOI: 10.1038/s41578-018-0008-9 (cit. on p. 17).

[73] A. Gaita-Ariño et al. “Molecular spins for quantum computation”. *Nature Chemistry* 11 (2019), 301–309. DOI: 10.1038/s41557-019-0232-y (cit. on p. 17).

[74] M. Atzori and R. Sessoli. “The Second Quantum Revolution: Role and Challenges of Molecular Chemistry”. *Journal of the American Chemical Society* 141 (2019), 11339–11352. DOI: 10.1021/jacs.9b00984 (cit. on p. 17).

[75] D. Aravena and E. Ruiz. “Spin dynamics in single-molecule magnets and molecular qubits”. *Dalton Transactions* 49 (2020), 9916–9928. DOI: 10.1039/d0dt01414a (cit. on p. 17).

[76] E. Coronado. “Molecular magnetism: from chemical design to spin control in molecules, materials and devices”. *Nature Reviews Materials* 5 (2020), 87–104. DOI: 10.1038/s41578-019-0146-8 (cit. on p. 17).

[77] A. Ardavan et al. “Will Spin-Relaxation Times in Molecular Magnets Permit Quantum Information Processing?” *Physical Review Letters* 98 (2007), 057201. DOI: 10.1103/PhysRevLett.98.057201 (cit. on pp. 18, 19).

[78] J. Lehmann et al. “Spin qubits with electrically gated polyoxometalate molecules”. *Nature Nanotechnology* 2 (2007), 312–317. DOI: 10.1038/nnano.2007.110 (cit. on pp. 18, 21).

[79] J. M. Zadrozny et al. “Millisecond Coherence Time in a Tunable Molecular Electronic Spin Qubit”. *ACS Central Science* 1 (2015), 488–492. DOI: 10.1021/acscentsci.5b00338 (cit. on pp. 18, 19, 82, 103, 139).

[80] K. Bader et al. “Room temperature quantum coherence in a potential molecular qubit”. *Nature Communications* 5 (2014), 1–5. DOI: 10.1038/ncomms6304 (cit. on pp. 18, 19).

[81] M. Atzori et al. “Quantum Coherence Times Enhancement in Vanadium(IV)-based Potential Molecular Qubits: The Key Role of the Vanadyl Moiety”. *Journal of the American Chemical Society* 138 (2016), 11234–11244. DOI: 10.1021/jacs.6b05574 (cit. on pp. 18, 19, 98).

[82] S. Thiele et al. “Electrically driven nuclear spin resonance in single-molecule magnets”. *Science* 344 (2014) (cit. on pp. 18, 22).

[83] C. J. Wedge et al. “Chemical Engineering of Molecular Qubits”. *Physical Review Letters* 108 (2012), 107204 (cit. on p. 19).

[84] C. Schlegel et al. “Direct Observation of Quantum Coherence in Single-Molecule Magnets”. *Physical Review Letters* 101 (2008), 147203. DOI: 10.1103/PhysRevLett.101.147203 (cit. on p. 19).

[85] S. Takahashi et al. “Coherent Manipulation and Decoherence of S = 10 Single-Molecule Magnets”. *Physical Review Letters* 102 (2009), 087603. DOI: 10.1103/PhysRevLett.102.087603 (cit. on p. 19).

[86] S. Takahashi et al. “Decoherence in crystals of quantum molecular magnets”. *Nature* 476 (2011), 76–79. DOI: 10.1038/nature10314 (cit. on p. 19).

[87] J. M. Zadrozny et al. “Multiple quantum coherences from hyperfine transitions in a vanadium(IV) complex”. *Journal of the American Chemical Society* 136 (2014), 15841–15844. DOI: 10.1021/ja507846k (cit. on p. 19).

[88] M. J. Martínez-Pérez et al. “Gd-based single-ion magnets with tunable magnetic anisotropy: Molecular design of spin qubits”. *Physical Review Letters* 108 (2012), 1–5. DOI: 10.1103/PhysRevLett.108.247213 (cit. on p. 19).

[89] C.-J. Yu et al. “Long Coherence Times in Nuclear Spin-Free Vanadyl Qubits”. *Journal of the American Chemical Society* 138 (2016), 14678–14685. DOI: 10.1021/jacs.6b08467 (cit. on pp. 19, 20).

[90] M. Atzori et al. “Room-Temperature Quantum Coherence and Rabi Oscillations in Vanadyl Phthalocyanine: Toward Multifunctional Molecular Spin Qubits”. *Journal of the American Chemical Society* 138 (2016), 2154–2157. DOI: 10.1021/jacs.5b13408 (cit. on p. 19).

[91] K. Bader et al. “Molecular qubits based on potentially nuclear-spin-free nickel ions”. *Physical Chemistry Chemical Physics* 19 (2017), 2525–2529. DOI: 10.1039/c6cp08161d (cit. on pp. 19, 45).

[92] S. Lenz et al. “Quantitative prediction of nuclear-spin-diffusion-limited coherence times of molecular quantum bits based on copper(II)”. *Chem. Commun.* 53 (2017), 4477–4480. DOI: 10.1039/C6CC07813C (cit. on pp. 19, 140).

[93] S. Lenz et al. “Chromium(iii)-based potential molecular quantum bits with long coherence times”. *Physical Chemistry Chemical Physics* 21 (2019), 6976–6983. DOI: 10.1039/c9cp00745h (cit. on p. 19).

[94] K. Bader, M. Winkler, and J. Van Slageren. "Tuning of molecular qubits: Very long coherence and spin-lattice relaxation times". *Chemical Communications* 52 (2016), 3623–3626. DOI: 10.1039/c6cc00300a (cit. on pp. 19, 45, 103).

[95] M. J. Graham et al. "Influence of electronic spin and spin-orbit coupling on decoherence in mononuclear transition metal complexes". *Journal of the American Chemical Society* 136 (2014), 7623–7626. DOI: 10.1021/ja5037397 (cit. on p. 19).

[96] D. Kaminski et al. "Quantum spin coherence in halogen-modified Cr7Ni molecular nanomagnets". *Physical Review B - Condensed Matter and Materials Physics* 90 (2014), 1–4. DOI: 10.1103/PhysRevB.90.184419 (cit. on p. 20).

[97] M. J. Graham et al. "Synthetic Approach To Determine the Effect of Nuclear Spin Distance on Electronic Spin Decoherence". *Journal of the American Chemical Society* 139 (2017), 3196–3201. DOI: 10.1021/jacs.6b13030 (cit. on pp. 20, 98).

[98] J. Chen et al. "Decoherence in Molecular Electron Spin Qubits: Insights from Quantum Many-Body Simulations". *Journal of Physical Chemistry Letters* 11 (2020), 2074–2078. DOI: 10.1021/acs.jpclett.0c00193 (cit. on p. 20).

[99] C. E. Jackson et al. "Nuclear-spin-pattern control of electron-spin dynamics in a series of V(iv) complexes". *Chemical Science* 10 (2019), 8447–8454. DOI: 10.1039/c9sc02899d (cit. on pp. 20, 98).

[100] S. H. Johnson, C. E. Jackson, and J. M. Zadrozny. "Programmable Nuclear-Spin Dynamics in Ti(IV) Coordination Complexes". *Inorganic Chemistry* 59 (2020), 7479–7486. DOI: 10.1021/acs.inorgchem.0c00244 (cit. on p. 20).

[101] M. Atzori et al. "Structural Effects on the Spin Dynamics of Potential Molecular Qubits". *Inorganic Chemistry* 57 (2018), 731–740. DOI: 10.1021/acs.inorgchem.7b02616 (cit. on p. 20).

[102] A. M. Ariciu et al. "Engineering electronic structure to prolong relaxation times in molecular qubits by minimising orbital angular momentum". *Nature Communications* 10 (2019), 1–8. DOI: 10.1038/s41467-019-11309-3 (cit. on p. 20).

[103] E. Garlatti et al. "Unveiling phonons in a molecular qubit with four-dimensional inelastic neutron scattering and density functional theory". *Nature Communications* 11 (2020), 1–10. DOI: 10.1038/s41467-020-15475-7 (cit. on p. 20).

[104] A. Albino et al. "First-Principles Investigation of Spin-Phonon Coupling in Vanadium-Based Molecular Spin Quantum Bits". *Inorganic Chemistry* 58 (2019), 10260–10268. DOI: 10.1021/acs.inorgchem.9b01407 (cit. on p. 20).

[105] F. Troiani et al. "Molecular engineering of antiferromagnetic rings for quantum computation". *Physical Review Letters* 94 (2005), 1–4. DOI: 10.1103/PhysRevLett.94.207208 (cit. on p. 20).

[106] M. Affronte et al. "Linking Rings through Diamines and Clusters: Exploring Synthetic Methods for Making Magnetic Quantum Gates". *Angewandte Chemie* 117 (2005), 6654–6658. DOI: 10.1002/ange.200502505 (cit. on p. 21).

[107] G. A. Timco et al. "Engineering the coupling between molecular spin qubits by coordination chemistry". *Nature Nanotechnology* 4 (2009), 173–178. DOI: 10.1038/nnano.2008.404 (cit. on p. 21).

[108] A. Candini et al. "Entanglement in supramolecular spin systems of two weakly coupled antiferromagnetic rings (purple-Cr7Ni)". *Physical Review Letters* 104 (2010), 1–4. DOI: 10.1103/PhysRevLett.104.037203 (cit. on p. 21).

[109] G. A. Timco et al. "Linking heterometallic rings for quantum information processing and amusement". *Chemical Society Reviews* 40 (2011), 3067–3075. DOI: 10.1039/c0cs00151a (cit. on p. 21).

[110] A. Chiesa et al. "Molecular nanomagnets with switchable coupling for quantum simulation". *Scientific Reports* 4 (2014), 1–8. DOI: 10.1038/srep07423 (cit. on p. 21).

[111] A. Ardavan et al. "Engineering coherent interactions in molecular nanomagnet dimers". *npj Quantum Information* 1 (2015), 1–7. DOI: 10.1038/npjqi.2015.12 (cit. on p. 21).

[112] F. Luis et al. "Molecular prototypes for spin-based CNOT and SWAP quantum gates". *Physical Review Letters* 107 (2011), 1–5. DOI: 10.1103/PhysRevLett.107.117203 (cit. on p. 21).

[113] D. Aguilá et al. "Heterodimetallic [LnLn'] lanthanide complexes: Toward a chemical design of two-qubit molecular spin quantum gates". *Journal of the American Chemical Society* 136 (2014), 14215–14222. DOI: 10.1021/ja507809w (cit. on p. 21).

[114] S. Nakazawa et al. "A synthetic two-spin quantum bit: G-engineered exchange-coupled biradical designed for controlled-NOT gate operations". *Angewandte Chemie - International Edition* 51 (2012), 9860–9864. DOI: 10.1002/anie.201204489 (cit. on p. 21).

[115] J. Ferrando-Soria et al. "A modular design of molecular qubits to implement universal quantum gates". *Nature Communications* 7 (2016). DOI: 10.1038/ncomms11377 (cit. on p. 21).

[116] M. Atzori et al. "A two-qubit molecular architecture for electron-mediated nuclear quantum simulation". *Chemical Science* 9 (2018), 6183–6192. DOI: 10.1039/c8sc01695j (cit. on p. 21).

[117] A. Urtizberea et al. "A Porphyrin Spin Qubit and Its 2D Framework Nanosheets". *Advanced Functional Materials* 28 (2018), 1–15. DOI: 10.1002/adfm.201801695 (cit. on p. 21).

[118] T. Yamabayashi et al. "Scaling Up Electronic Spin Qubits into a Three-Dimensional Metal-Organic Framework". *Journal of the American Chemical Society* 140 (2018), 12090–12101. DOI: 10.1021/jacs.8b06733 (cit. on pp. 21, 98).

[119] C. J. Yu et al. "A concentrated array of copper porphyrin candidate qubits". *Chemical Science* 10 (2019), 1702–1708. DOI: 10.1039/c8sc04435j (cit. on p. 21).

[120] M. D. Jenkins et al. "A scalable architecture for quantum computation with molecular nanomagnets". *Dalton Transactions* 45 (2016), 16682–16693. DOI: 10.1039/c6dt02664h (cit. on p. 22).

[121] S. Baumann et al. "Electron paramagnetic resonance of individual atoms on a surface". *Science* 350 (2015), 417–420 (cit. on p. 22).

[122] P. Willke et al. "Probing quantum coherence in single-atom electron spin resonance". *Science advances* 4 (2018), eaaq1543 (cit. on p. 22).

[123] P. Willke et al. "Hyperfine interaction of individual atoms on a surface". *Science* 362 (2018), 336–339 (cit. on p. 22).

[124] P. Willke et al. "Magnetic resonance imaging of single atoms on a surface". *Nature Physics* 15 (2019), 1005–1010 (cit. on p. 22).

[125] R. Vincent et al. "Electronic read-out of a single nuclear spin using a molecular spin transistor". *Nature* 488 (2012), 357 (cit. on p. 22).

[126] C. Godfrin et al. "Operating Quantum States in Single Magnetic Molecules: Implementation of Grover's Quantum Algorithm". *Physical Review Letters* 119 (2017), 1–5. DOI: 10.1103/PhysRevLett.119.187702 (cit. on p. 22).

[127] A. H. C. Neto et al. "The electronic properties of graphene". *Reviews of Modern Physics* 81 (2009). DOI: 10.1103/RevModPhys.81.109 (cit. on pp. 22–24).

[128] A. K. Geim and K. S. Novoselov. "The rise of graphene". *Nature Materials* 6 (2007), 183–191. DOI: 10.1038/nmat1849 (cit. on pp. 23, 24).

[129] D. Akinwande et al. "A review on mechanics and mechanical properties of 2D materials—Graphene and beyond". *Extreme Mechanics Letters* 13 (2017), 42–77 (cit. on p. 23).

[130] S. Pang et al. "Graphene as transparent electrode material for organic electronics". *Advanced Materials* 23 (2011), 2779–2795 (cit. on p. 23).

[131] K. S. Novoselov et al. "A roadmap for graphene". *Nature* 490 (2012), 192–200. DOI: 10.1038/nature11458 (cit. on p. 24).

[132] Z. Li et al. "Field and temperature dependence of intrinsic diamagnetism in graphene: Theory and experiment". *Physical Review B - Condensed Matter and Materials Physics* 91 (2015), 1–5. DOI: 10.1103/PhysRevB.91.094429 (cit. on p. 24).

[133] M. Sepioni et al. "Limits on intrinsic magnetism in graphene". *Physical Review Letters* 105 (2010), 1–4. DOI: 10.1103/PhysRevLett.105.207205 (cit. on p. 24).

[134] Y. Wang et al. "Room-temperature ferromagnetism of graphene." *Nano letters* 9 (2009), 220–4. DOI: 10.1021/nl802810g (cit. on p. 24).

[135] H. S. Ramakrishna Matte, K. S. Subrahmanyam, and C. N. Rao. "Novel magnetic properties of graphene: Presence of both ferromagnetic and antiferromagnetic features and other aspects". *Journal of Physical Chemistry C* 113 (2009), 9982–9985. DOI: 10.1021/jp903397u (cit. on p. 24).

[136] E. H. Lieb. "Two theorems on the Hubbard model". *Physical Review Letters* 62 (1989), 1201 (cit. on p. 24).

[137] O. V. Yazyev. "Emergence of magnetism in graphene materials and nanostructures". *Rep. Prog. Phys.* 73 (2010). DOI: 10.1088/0034-4885/73/5/056501 (cit. on p. 24).

[138] J. J. Palacios and F. Ynduráin. "Critical analysis of vacancy-induced magnetism in monolayer and bilayer graphene". *Physical Review B - Condensed Matter and Materials Physics* 85 (2012), 1–8. DOI: 10.1103/PhysRevB.85.245443 (cit. on p. 24).

[139] R. R. Nair et al. "Spin-half paramagnetism in graphene induced by point defects". *Nature Physics* 8 (2012), 199–202. DOI: 10.1038/nphys2183 (cit. on p. 24).

[140] A. C. Ferrari et al. "Science and technology roadmap for graphene, related two-dimensional crystals, and hybrid systems". *Nanoscale* 7 (2015), 4598–4810 (cit. on p. 24).

[141] K. Nakada et al. "Edge state in graphene ribbons: Nanometer size effect and edge shape dependence". *Physical Review B - Condensed Matter and Materials Physics* 54 (1996), 17954–17961. DOI: 10.1103/PhysRevB.54.17954 (cit. on pp. 25, 89).

[142] M. Fujita et al. "Peculiar Localized State at Zigzag Graphite Edge". *Journal of the Physical Society of Japan* 65 (1996), 1920–1923. DOI: 10.1143/JPSJ.65.1920 (cit. on pp. 25, 26, 89).

[143] V. Barone, O. Hod, and G. E. Scuseria. "Electronic structure and stability of semiconducting graphene nanoribbons". *Nano Letters* 6 (2006), 2748–2754. DOI: 10.1021/nl0617033 (cit. on p. 25).

[144] Y. W. Son, M. L. Cohen, and S. G. Louie. "Energy gaps in graphene nanoribbons". *Physical Review Letters* 97 (2006), 1–4. DOI: 10.1103/PhysRevLett.97.216803 (cit. on pp. 25, 26, 89).

[145] L. Brey and H. A. Fertig. "Electronic states of graphene nanoribbons studied with the Dirac equation". *Physical Review B - Condensed Matter and Materials Physics* 73 (2006), 2–6. DOI: 10.1103/PhysRevB.73.235411 (cit. on p. 25).

[146] H. Lee et al. "Magnetic ordering at the edges of graphitic fragments: Magnetic tail interactions between the edge-localized states". *Physical Review B - Condensed Matter and Materials Physics* 72 (2005), 1–8. DOI: 10.1103/PhysRevB.72.174431 (cit. on p. 26).

[147] Y. W. Son, M. L. Cohen, and S. G. Louie. "Half-metallic graphene nanoribbons". *Nature* 444 (2006), 347–349. DOI: 10.1038/nature05180 (cit. on p. 26).

[148] M. Y. Han et al. "Energy band-gap engineering of graphene nanoribbons". *Physical Review Letters* 98 (2007), 1–4. DOI: 10.1103/PhysRevLett.98.206805 (cit. on p. 26).

[149] Z. Chen et al. "Graphene nano-ribbon electronics". *Physica E: Low-Dimensional Systems and Nanostructures* 40 (2007), 228–232. DOI: 10.1016/j.physe.2007.06.020 (cit. on p. 26).

[150] D. V. Kosynkin et al. "Longitudinal unzipping of carbon nanotubes to form graphene nanoribbons". *Nature* 458 (2009), 872–876. DOI: 10.1038/nature07872 (cit. on p. 26).

[151] L. Jiao et al. "Narrow graphene nanoribbons from carbon nanotubes". *Nature* 458 (2009), 877–880. DOI: 10.1038/nature07919 (cit. on p. 26).

[152] C. Tao et al. "Spatially resolving edge states of chiral graphene nanoribbons". *Nature Physics* 7 (2011), 616–620. DOI: 10.1038/nphys1991 (cit. on pp. 26, 28).

[153] X. Li et al. "Chemically Derived Ultramooth Graphene Nanoribbon Semiconductors". *Science* 319 (2008), 1229–1232. DOI: 10.1126/science.1150878 (cit. on pp. 26, 127).

[154] A. Narita et al. "Synthesis of structurally well-defined and liquid-phase-processable graphene nanoribbons". *Nature Chemistry* 6 (2014), 126–132. DOI: 10.1038/nchem.1819 (cit. on pp. 26, 28).

[155] L. Grill et al. "Nano-architectures by covalent assembly of molecular building blocks". *Nature Nanotechnology* 2 (2007), 687–691. DOI: 10.1038/nnano.2007.346 (cit. on p. 26).

[156] J. Cai et al. "Atomically precise bottom-up fabrication of graphene nanoribbons". *Nature* 466 (2010), 470–473. DOI: 10.1038/nature09211 (cit. on p. 26).

[157] L. Grill and S. Hecht. "Covalent on-surface polymerization". *Nature chemistry* 12 (2020), 115–130 (cit. on p. 26).

[158] A. Kimouche et al. "Ultra-narrow metallic armchair graphene nanoribbons". *Nature Communications* 6 (2015), 1–6. DOI: 10.1038/ncomms10177 (cit. on p. 27).

[159] Y. C. Chen et al. "Molecular bandgap engineering of bottom-up synthesized graphene nanoribbon heterojunctions". *Nature Nanotechnology* 10 (2015), 156–160. DOI: 10.1038/nnano.2014.307 (cit. on p. 27).

[160] P. Ruffieux et al. "Electronic structure of atomically precise graphene nanoribbons". *ACS Nano* 6 (2012), 6930–6935. DOI: 10.1021/nn3021376 (cit. on p. 27).

[161] Y. C. Chen et al. "Tuning the band gap of graphene nanoribbons synthesized from molecular precursors". *ACS Nano* 7 (2013), 6123–6128. DOI: 10.1021/nn401948e (cit. on pp. 27, 95).

[162] L. Talirz et al. "On-Surface Synthesis and Characterization of 9-Atom Wide Armchair Graphene Nanoribbons". *ACS Nano* 11 (2017), 1380–1388. DOI: 10.1021/acsnano.6b06405 (cit. on p. 27).

[163] M. Koch et al. "Voltage-dependent conductance of a single graphene nanoribbon". *Nature Nanotechnology* 7 (2012), 713–717. DOI: 10.1038/nnano.2012.169 (cit. on p. 27).

[164] J. Cai et al. "Graphene nanoribbon heterojunctions". *Nature Nanotechnology* 9 (2014), 896–900. DOI: 10.1038/nnano.2014.184 (cit. on p. 27).

[165] G. D. Nguyen et al. "Atomically precise graphene nanoribbon heterojunctions from a single molecular precursor". *Nature Nanotechnology* 12 (2017), 1077–1082. DOI: 10.1038/nnano.2017.155 (cit. on p. 27).

[166] D. J. Rizzo et al. "Length-Dependent Evolution of Type II Heterojunctions in Bottom-Up-Synthesized Graphene Nanoribbons". *Nano Letters* 19 (2019), 3221–3228. DOI: 10.1021/acs.nanolett.9b00758 (cit. on p. 27).

[167] P. Ruffieux et al. "On-surface synthesis of graphene nanoribbons with zigzag edge topology". *Nature* 531 (2016), 489–492. DOI: 10.1038/nature17151 (cit. on pp. 28, 89, 90, 95).

[168] T. H. Vo et al. "Large-scale solution synthesis of narrow graphene nanoribbons". *Nature Communications* 5 (2014), 1–8. DOI: 10.1038/ncomms4189 (cit. on p. 28).

[169] J. Liu et al. "Toward Cove-Edged Low Band Gap Graphene Nanoribbons". *Journal of the American Chemical Society* 137 (2015), 6097–6103. DOI: 10.1021/jacs.5b03017 (cit. on p. 28).

[170] A. Narita et al. "New advances in nanographene chemistry". *Chem. Soc. Rev.* 44 (2015), 6616–6643. DOI: 10.1039/C5CS00183H (cit. on pp. 28, 89).

[171] M. Z. Hasan and C. L. Kane. "Colloquium: Topological insulators". *Reviews of Modern Physics* 82 (2010), 3045–3067. DOI: 10.1103/RevModPhys.82.3045 (cit. on p. 29).

[172] Kitaev, A.Yu. "Fault-tolerant quantum computation by anyons". *Annals of Physics* 303 (2002), 2–30 (cit. on p. 29).

[173] D. Hsieh et al. "A topological Dirac insulator in a quantum spin Hall phase". *Nature* 452 (2008), 970–974 (cit. on p. 29).

[174] T. Cao, F. Zhao, and S. G. Louie. "Topological Phases in Graphene Nanoribbons: Junction States, Spin Centers, and Quantum Spin Chains". *Physical Review Letters* 119 (2017), 1–5. DOI: 10.1103/PhysRevLett.119.076401 (cit. on p. 29).

[175] J. Zak. "Berrys phase for energy bands in solids". *Physical Review Letters* 62 (1989), 2747–2750. DOI: 10.1103/PhysRevLett.62.2747 (cit. on p. 29).

[176] M. V. Berry. "Quantal phase factors accompanying adiabatic changes". *Proceedings of the Royal Society of London. A. Mathematical and Physical Sciences* 392 (1984), 45–57 (cit. on p. 29).

[177] D. J. Rizzo et al. "Topological band engineering of graphene nanoribbons". *Nature* 560 (2018), 204–208. DOI: 10.1038/s41586-018-0376-8 (cit. on pp. 30, 90).

[178] O. Gröning et al. "Engineering of robust topological quantum phases in graphene nanoribbons". *Nature* 560 (2018), 209–213 (cit. on pp. 30, 31, 90, 95).

[179] K. S. Lin and M. Y. Chou. "Topological Properties of Gapped Graphene Nanoribbons with Spatial Symmetries". *Nano Letters* 18 (2018), 7254–7260. DOI: 10.1021/acs.nanolett.8b03417 (cit. on p. 30).

[180] Y. L. Lee et al. "Topological Phases in Cove-Edged and Chevron Graphene Nanoribbons: Geometric Structures, Z 2 Invariants, and Junction States". *Nano Letters* 18 (2018), 7247–7253. DOI: 10.1021/acs.nanolett.8b03416 (cit. on p. 30).

[181] J. Li et al. "Topological phase transition in chiral graphene nanoribbons: from edge bands to end states" (2021), 1–12 (cit. on p. 30).

[182] J. Jiang and S. G. Louie. "Topology Classification using Chiral Symmetry and Spin Correlations in Graphene Nanoribbons". *Nano Letters* 21 (2021), 197–202. DOI: 10.1021/acs.nanolett.0c03503 (cit. on p. 30).

[183] F. Banhart, J. Kotakoski, and A. V. Krasheninnikov. "Structural defects in graphene". *ACS Nano* 5 (2011), 26–41. DOI: 10.1021/nn102598m (cit. on pp. 31, 59).

[184] A. Hashimoto et al. "Direct evidence for atomic defects in graphene layers". *Nature* 430 (2004), 870–873. DOI: 10.1038/nature02817 (cit. on p. 32).

[185] J. Ma et al. "Stone-Wales defects in graphene and other planar sp2-bonded materials". *Physical Review B - Condensed Matter and Materials Physics* 80 (2009), 1–4. DOI: 10.1103/PhysRevB.80.033407 (cit. on p. 32).

[186] M. T. Lusk and L. D. Carr. "Nanoengineering defect structures on graphene". *Physical Review Letters* 100 (2008), 1–4. DOI: 10.1103/PhysRevLett.100.175503 (cit. on p. 32).

[187] O. V. Yazyev and S. G. Louie. "Topological defects in graphene: Dislocations and grain boundaries". *Physical Review B - Condensed Matter and Materials Physics* 81 (2010), 1–7. DOI: 10.1103/PhysRevB.81.195420 (cit. on p. 32).

[188] A. Cortijo and M. A. H. Vozmediano. "Effects of topological defects and local curvature on the electronic properties of planar graphene". *Nuclear Physics B* 763 (2007), 293–308. DOI: 10.1016/j.nuclphysb.2006.10.031 (cit. on p. 32).

[189] O. V. Yazyev and L. Helm. "Defect-induced magnetism in graphene". *Physical Review B - Condensed Matter and Materials Physics* 75 (2007), 1–5. DOI: 10.1103/PhysRevB.75.125408 (cit. on p. 32).

[190] M. P. López-Sancho, F. De Juan, and M. A. Vozmediano. "Magnetic moments in the presence of topological defects in graphene". *Physical Review B - Condensed Matter and Materials Physics* 79 (2009), 1–5. DOI: 10.1103/PhysRevB.79.075413 (cit. on p. 32).

[191] Z. Lin et al. "Defect engineering of two-dimensional transition metal dichalcogenides". *2D Materials* 3 (2016). DOI: 10.1088/2053-1583/3/2/022002 (cit. on p. 32).

[192] A. Gottscholl et al. "Initialization and read-out of intrinsic spin defects in a van der Waals crystal at room temperature". *Nature Materials* 19 (2020), 540–545. DOI: 10.1038/s41563-020-0619-6 (cit. on p. 32).

[193] S. Kumar et al. "Recent Advances in Organic Radicals and Their Magnetism". *Magnetochemistry* 2 (2016), 42. DOI: 10.3390/magnetochemistry2040042 (cit. on pp. 32, 33, 61).

[194] M. Stepien et al. "Heterocyclic nanographenes and other polycyclic heteroaromatic compounds: synthetic routes, properties, and applications". *Chemical reviews* 117 (2017), 3479–3716. DOI: 10.1021/acs.chemrev.6b00076 (cit. on p. 32).

[195] Y. G. Tullimi et al. "From open-shell singlet diradicaloids to polyradicaloids". *Chemical Communications* 54 (2018), 2186–2199. DOI: 10.1039/C7CC09949E (cit. on pp. 32, 33).

[196] L. Dou et al. "Low-bandgap near-IR conjugated polymers/molecules for organic electronics". *Chemical reviews* 115 (2015), 12633–12665 (cit. on p. 32).

[197] J. Messelberger et al. "Carbene derived diradicaloids-building blocks for singlet fission?" *Chemical Science* 9 (2018), 6107–6117. DOI: 10.1039/c8sc01999a (cit. on p. 32).

[198] K. Kamada et al. "Strong two-photon absorption of singlet diradical hydrocarbons". *Angewandte Chemie International Edition* 46 (2007), 3544–3546 (cit. on p. 32).

[199] Y. Morita et al. "Synthetic organic spin chemistry for structurally well-defined open-shell graphene fragments". *Nature Chemistry* 3 (2011), 197–204. DOI: 10.1038/nchem.985 (cit. on pp. 32, 34).

[200] V. A. Dediu et al. "Spin routes in organic semiconductors". *Nature materials* 8 (2009), 707–716 (cit. on p. 32).

[201] E. Clar. *Aromatic sextet*. New York, Wiley, 1972 (cit. on p. 33).

[202] M. Treier et al. "Surface-assisted cyclodehydrogenation provides a synthetic route towards easily processable and chemically tailored nanographenes". *Nature Chemistry* 3 (2011), 61–67. DOI: 10.1038/nchem.891 (cit. on p. 33).

[203] M. Abe. "Diradicals". *Chemical Reviews* 113 (2013), 7011–7088. DOI: 10.1021/cr400056a (cit. on p. 33).

[204] M. Bendikov et al. "Oligoacenes: Theoretical prediction of open-shell singlet diradical ground states". *Journal of the American Chemical Society* 126 (2004), 7416–7417. DOI: 10.1021/ja048919w (cit. on p. 33).

[205] J. Hachmann et al. "The radical character of the acenes: A density matrix renormalization group study". *Journal of Chemical Physics* 127 (2007). DOI: 10.1063/1.2768362 (cit. on p. 33).

[206] Z. Qu et al. "Open-shell ground state of polyacenes: A valence bond study". *Journal of Physical Chemistry A* 113 (2009), 7909–7914. DOI: 10.1021/jp9015728 (cit. on p. 33).

[207] S. S. Zade and M. Bendikov. "Heptacene and beyond: the longest characterized acenes". *Angewandte Chemie International Edition* 49 (2010), 4012–4015 (cit. on p. 34).

[208] H. F. Bettinger and C. Toenshoff. "The longest acenes". *The Chemical Record* 15 (2015), 364–369 (cit. on p. 34).

[209] M. Watanabe et al. "The synthesis, crystal structure and charge-transport properties of hexacene". *Nature chemistry* 4 (2012), 574 (cit. on p. 34).

[210] R. Einholz et al. "Heptacene: characterization in solution, in the solid state, and in films". *Journal of the American Chemical Society* 139 (2017), 4435–4442 (cit. on p. 34).

[211] R. Zuzak et al. "Higher Acenes by On-Surface Dehydrogenation: From Heptacene to Undecacene". *Angewandte Chemie - International Edition* 57 (2018), 10500–10505. DOI: 10.1002/anie.201802040 (cit. on p. 34).

[212] J. I. Urgel et al. "On-surface light-induced generation of higher acenes and elucidation of their open-shell character". *Nature Communications* 10 (2019), 1–9. DOI: 10.1038/s41467-019-08650-y (cit. on p. 34).

[213] F. Eisenhut et al. "Dodecacene generated on surface: reopening of the energy gap". *ACS nano* 14 (2019), 1011–1017 (cit. on p. 34).

[214] B. Cirera et al. "Tailoring topological order and π-conjugation to engineer quasi-metallic polymers". *Nature Nanotechnology* 15 (2020), 437–443. DOI: 10.1038/s41565-020-0668-7 (cit. on p. 34).

[215] J. L. Zafra et al. "Zethrene biradicals: How pro-aromaticity is expressed in the ground electronic state and in the lowest energy singlet, triplet, and ionic states". *Journal of Chemical Physics* 140 (2014). DOI: 10.1063/1.4863557 (cit. on p. 34).

[216] Z. Sun, Z. Zeng, and J. Wu. "Zethrenes, extended p-quinodimethanes, and periacenes with a singlet biradical ground state". *Accounts of Chemical Research* 47 (2014), 2582–2591. DOI: 10.1021/ar5001692 (cit. on p. 34).

[217] Y. C. Hsieh et al. "Zethrene and dibenzozethrene: Masked biradical molecules". *Angewandte Chemie - International Edition* 54 (2015), 3069–3073. DOI: 10.1002/anie.201410316 (cit. on p. 34).

[218] P. Hu and J. Wu. "Modern zethrene chemistry". *Canadian Journal of Chemistry* 95 (2017), 223–233. DOI: 10.1139/cjc-2016-0568 (cit. on pp. 34, 61).

[219] M. Melle-Franco. "Uthrene, a radically new molecule?" *Chemical Communications* 51 (2015), 5387–5390. DOI: 10.1039/c5cc01276g (cit. on p. 34).

[220] W. Zeng et al. "Rylene Ribbons with Unusual Diradical Character". *Chem* 2 (2017), 81–92. DOI: 10.1016/j.chempr.2016.12.001 (cit. on pp. 34, 61, 75, 90).

[221] J. Fernández-Rossier and J. J. Palacios. "Magnetism in graphene nanoislands". *Physical Review Letters* 99 (2007), 1–4. DOI: 10.1103/PhysRevLett.99.177204 (cit. on p. 34).

[222] W. L. Wang, S. Meng, and E. Kaxiras. "Graphene NanoFlakes with large spin". *Nano Letters* 8 (2008), 244–245. DOI: 10.1021/nl072548a (cit. on p. 34).

[223] P. Potasz, A. Güçlü, and P. Hawrylak. "Zero-energy states in triangular and trapezoidal graphene structures". *Physical Review B* 81 (2010), 033403 (cit. on p. 34).

[224] Z. Mou et al. "Evidence of σ- And π-dimerization in a series of Phenalenyls". *Journal of the American Chemical Society* 136 (2014), 18009–18022. DOI: 10.1021/ja509243p (cit. on p. 34).

[225] G. Allinson et al. "ESR Spectrum of a Stable Triplet π Biradical: Trioxytriangulene". *Journal of the American Chemical Society* 115 (1993), 2062–2064. DOI: 10.1021/ja00058a076 (cit. on p. 34).

[226] J. Inoue et al. "The first detection of a Clar's hydrocarbon, 2,6,10-tri-tert-butyltriangulene: A ground-state triplet of non-kekulé polynuclear benzenoid hydrocarbon". *Journal of the American Chemical Society* 123 (2001), 12702–12703. DOI: 10.1021/ja016751y (cit. on p. 34).

[227] N. Pavliček et al. "Synthesis and characterization of triangulene". *Nature Nanotechnology* 12 (2017), 308–311. DOI: 10.1038/nnano.2016.305 (cit. on pp. 34, 96).

[228] S. Mishra et al. "Synthesis and characterization of π-extended triangulene". *Journal of the American Chemical Society* 141 (2019), 10621–10625 (cit. on pp. 34, 96).

[229] M. Telychko et al. "Ultrahigh-yield on-surface synthesis and assembly of circumcoronene into a chiral electronic Kagome-honeycomb lattice". *Science Advances* 7 (2021), 1–8. DOI: 10.1126/sciadv.abf0269 (cit. on p. 35).

[230] W. L. Wang et al. "Topological frustration in graphene nanoflakes: Magnetic order and spin logic devices". *Physical Review Letters* 102 (2009), 1–4. DOI: 10.1103/PhysRevLett.102.157201 (cit. on p. 35).

[231] S. Mishra et al. "Topological frustration induces unconventional magnetism in a nanographene". *Nature Nanotechnology* 15 (2020), 22–28. DOI: 10.1038/s41565-019-0577-9 (cit. on p. 35).

[232] K. Ohashi et al. "4,8,12,16-tetra-tert-butyl-s-indaceno[1,2,3-cd:5,6,7-c'd'] diphenalene: A four-stage amphoteric redox system". *Journal of the American Chemical Society* 120 (1998), 2018–2027. DOI: 10.1021/ja970961m (cit. on pp. 35, 63).

[233] T. Kubo et al. "Synthesis, intermolecular interaction, and semiconductive behavior of a delocalized singlet biradical hydrocarbon". *Angewandte Chemie - International Edition* 44 (2005), 6564–6568. DOI: 10.1002/anie.200502303 (cit. on p. 35).

[234] T. S. Cameron et al. "Characterisation of the thermally accessible spin triplet state in dimers of the 7π ClCNSSS+. in the solid state". *Chemical Communications* 2 (2006), 2277–2279. DOI: 10.1039/b602843h (cit. on p. 35).

[235] T. Kubo et al. "Singlet biradical character of phenalenyl-based Kekulé hydrocarbon with naphthoquinoid structure". *Organic Letters* 9 (2007), 81–84. DOI: 10.1021/ol062604z (cit. on p. 35).

[236] A. Konishi et al. "Open-shell and antiaromatic character induced by the highly symmetric geometry of the planar heptalene structure: Synthesis and characterization of a nonalternant isomer of bisanthene". *Journal of the American Chemical Society* 141 (2019), 10165–10170. DOI: 10.1021/jacs.9b04080 (cit. on p. 35).

[237] A. Shimizu et al. "Indeno[2,1-b]fluorene: A 20-π-electron hydrocarbon with very low-energy light absorption". *Angewandte Chemie - International Edition* 52 (2013), 6076–6079. DOI: 10.1002/anie.201302091 (cit. on p. 35).

[238] D. Luo et al. "Indolo[2,3-b]carbazoles with tunable ground states: How Clar's aromatic sextet determines the singlet biradical character". *Chemical Science* 5 (2014), 4944–4952. DOI: 10.1039/c4sc01843e (cit. on p. 35).

[239] S. Nobusue et al. "Tetracyclopenta[def,jkl,pqr,vwx]tetraphenylene: A potential tetraradicaloid hydrocarbon". *Angewandte Chemie - International Edition* 54 (2015), 2090–2094. DOI: 10.1002/anie.201410791 (cit. on p. 35).

[240] G. E. Rudebusch et al. "Diindeno-fusion of an anthracene as a design strategy for stable organic biradicals". *Nature Chemistry* 8 (2016), 753–759. DOI: 10.1038/nchem.2518 (cit. on p. 35).

[241] Y. Zheng et al. "Engineering of Magnetic Coupling in Nanographene". *Physical Review Letters* 124 (2020), 147206. DOI: 10.1103/PhysRevLett.124.147206 (cit. on p. 35).

[242] S. Mishra et al. "Topological Defect-Induced Magnetism in a Nanographene". *Journal of the American Chemical Society* (2020). DOI: 10.1021/jacs.9b09212 (cit. on p. 36).

[243] Y. Fei et al. "Defective Nanographenes Containing Seven-Five-Seven (7–5–7)-Membered Rings". *Journal of the American Chemical Society* 20 (2021). DOI: 10.1021/jacs.0c12116 (cit. on p. 36).

[244] C. Chaolumen et al. "Construction of Heptagon-Containing Molecular Nanocarbons". *Angewandte Chemie* (2021). DOI: 10.1002/ange.202100260 (cit. on p. 36).

[245] I. R. Márquez et al. "Synthesis of distorted nanographenes containing seven- and eight-membered carbocycles". *Chemical Communications* 54 (2018), 6705–6718. DOI: 10.1039/c8cc02325e (cit. on p. 36).

[246] J. H. Golbeck and A. van der Est. "Electron Paramagnetic Resonance Spectroscopy". In: *Molecular Biophysics for the Life Sciences*. Ed. by N. Allewell, L. O. Narhi, and I. Rayment. Springer, 2013 (cit. on p. 38).

[247] S. Stoll and A. Schweiger. "EasySpin, a comprehensive software package for spectral simulation and analysis in EPR". *Journal of Magnetic Resonance* 178 (2006), 42–55. DOI: 10.1016/j.jmr.2005.08.013 (cit. on pp. 39, 41, 57).

[248] G. R. Eaton and S. S. Eaton. "Rapid-scan EPR". In: *EPR spectroscopy: fundamentals and methods*. Ed. by D. Goldfarb and S. Stoll. John Wiley & Sons, 2018. Chap. 23, 503–520 (cit. on p. 39).

[249] M. Brustolon and E. Giamello. *Electron Paramagnetic Resonance: A Practitioners Toolkit*. John Wiley & Sons, 2009 (cit. on pp. 40, 61).

[250] A. van der Est. "Continuous-Wave EPR". In: *EPR spectroscopy: fundamentals and methods*. Ed. by D. Goldfarb and S. Stoll. John Wiley & Sons, 2018. Chap. 1, 3–16 (cit. on p. 40).

[251] H. Hogben et al. "Spinach a software library for simulation of spin dynamics in large spin systems". *Journal of Magnetic Resonance* 208 (2011), 179–194 (cit. on p. 41).

[252] S. Stoll. "Pulse EPR". In: *EPR spectroscopy: fundamentals and methods*. Ed. by D. Goldfarb and S. Stoll. John Wiley & Sons, 2018. Chap. 23, 503–520 (cit. on pp. 42, 43).

[253] E. L. Hahn. "Spin echoes". *Physical review* 80 (1950), 580 (cit. on pp. 44, 124).

[254] S. S. Eaton and G. R. Eaton. "Relaxation Times of Organic Radicals and Transition Metal Ions". In: *Distance measurements in biological systems by EPR*. Ed. by L. J. Berliner, S. S. Eaton, and G. R. Eaton. Vol. 19. Springer Science & Business Media, 2006 (cit. on pp. 45, 66, 68, 97, 131, 135).

[255] J. Soetbeer et al. "Dynamical decoupling of nitroxides in: O-terphenyl: A study of temperature, deuteration and concentration effects". *Physical Chemistry Chemical Physics* 20 (2018), 1615–1628. DOI: 10.1039/c7cp07074h (cit. on pp. 45, 68, 83, 103, 128).

[256] G. R. Eaton and S. S. Eaton. "Relaxation Mechanisms". In: *EPR spectroscopy: fundamentals and methods*. Ed. by D. Goldfarb and S. Stoll. John Wiley & Sons, 2018. Chap. 9 (cit. on p. 46).

[257] M. Bennati. "EPR Interactions – Hyperfine Couplings". In: *EPR spectroscopy: fundamentals and methods*. Ed. by D. Goldfarb and S. Stoll. John Wiley & Sons, 2018. Chap. 5 (cit. on p. 47).

[258] S. V. Doorslaer. "Sabine Van Doorslaer". In: *EPR spectroscopy: fundamentals and methods*. Ed. by D. Goldfarb and S. Stoll. John Wiley & Sons, 2018. Chap. 18 (cit. on pp. 48, 49, 52).

[259] J. R. Harmer. "Hyperfine Spectroscopy – ENDOR". In: *EPR spectroscopy: fundamentals and methods*. Ed. by D. Goldfarb and S. Stoll. John Wiley & Sons, 2018. Chap. 16, 332 (cit. on pp. 51, 52).

[260] R. G. Parr and Y. W. Yang. *Density-Functional Theory of Atoms and Molecules*. Oxford University Press, 1989 (cit. on p. 52).

[261] F. Neese. "Prediction of molecular properties and molecular spectroscopy with density functional theory: From fundamental theory to exchange-coupling". *Coordination Chemistry Reviews* 253 (2009), 526–563 (cit. on pp. 52, 55, 56).

[262] F. Jensen. *Introduction to computational chemistry*. John wiley & sons, 2017 (cit. on p. 52).

[263] M. Kaupp, M. Buhl, and V. G. Malkin. *Calculation of NMR and EPR Parameters*. Wiley Online Library, 2004 (cit. on pp. 52, 54).

[264] P. Hohenberg and W. Kohn. "Inhomogeneous electron gas". *Physical review* 136 (1964), B864 (cit. on p. 53).

[265] W. Kohn and L. J. Sham. "Self-consistent equations including exchange and correlation effects". *Physical review* 140 (1965), A1133 (cit. on p. 53).

[266] A. D. Becke. "Density-functional thermochemistry. I. The effect of the exchange-only gradient correction". *The Journal of chemical physics* 96 (1992), 2155–2160 (cit. on p. 55).

[267] J. P. Perdew, M. Ernzerhof, and K. Burke. "Rationale for mixing exact exchange with density functional approximations". *The Journal of chemical physics* 105 (1996), 9982–9985 (cit. on p. 55).

[268] C. Adamo and V. Barone. "Toward reliable density functional methods without adjustable parameters: The PBE0 model". *The Journal of chemical physics* 110 (1999), 6158–6170 (cit. on p. 55).

[269] V. N. Staroverov et al. "Comparative assessment of a new nonempirical density functional: Molecules and hydrogen-bonded complexes". *The Journal of chemical physics* 119 (2003), 12129–12137 (cit. on p. 55).

[270] T. Yanai, D. P. Tew, and N. C. Handy. "A new hybrid exchange–correlation functional using the Coulomb-attenuating method (CAM-B3LYP)". *Chemical physics letters* 393 (2004), 51–57 (cit. on p. 55).

[271] W. J. Hehre, R. Ditchfield, and J. A. Pople. "Self—consistent molecular orbital methods. XII. Further extensions of Gaussian—type basis sets for use in molecular orbital studies of organic molecules". *The Journal of Chemical Physics* 56 (1972), 2257–2261 (cit. on p. 55).

[272] A. Schäfer, H. Horn, and R. Ahlrichs. "Fully optimized contracted Gaussian basis sets for atoms Li to Kr". *The Journal of Chemical Physics* 97 (1992), 2571–2577 (cit. on p. 55).

[273] A. Schäfer, C. Huber, and R. Ahlrichs. "Fully optimized contracted Gaussian basis sets of triple zeta valence quality for atoms Li to Kr". *The Journal of Chemical Physics* 100 (1994), 5829–5835 (cit. on p. 55).

[274] S. Patchkovskii and G. Schreckenbach. "Calculation of EPR g-Tensors with Density Functional Theory". In: *Calculation of NMR and EPR Parameters*. Ed. by M. Kaupp, M. Buhl, and V. G. Malkin. John Wiley & Sons, 2004 (cit. on p. 55).

[275] R. Improta and V. Barone. "Interplay of Electronic, Environmental, and Vibrational Effects in Determining the Hyperfine Coupling Constants of Organic Free Radicals". *Chemical Reviews* 104 (2004), 1231–1254. DOI: 10.1021/cr960085f (cit. on pp. 55–57).

[276] F. Neese. "Efficient and accurate approximations to the molecular spin-orbit coupling operator and their use in molecular g-tensor calculations". *Journal of Chemical Physics* 122 (2005). DOI: 10.1063/1.1829047 (cit. on p. 55).

[277] M. L. Munzarova. "DFT Calculations of EPR Hyperfine Coupling Tensors". In: *Calculation of NMR and EPR Parameters*. Ed. by M. Kaupp, M. Buhl, and V. G. Malkin. John Wiley & Sons, 2004 (cit. on p. 56).

[278] B. Engels. "Ab Initio Post-Hartree–Fock Calculations of Hyperfine Coupling Tensors and Their Comparison with DFT Approaches". In: *Calculation of NMR and EPR Parameters*. Ed. by M. Kaupp, M. Buhl, and V. G. Malkin. John Wiley & Sons, 2004 (cit. on p. 56).

[279] S. Kossmann, B. Kirchner, and F. Neese. *Molecular Physics* (). DOI: 10.1080/00268970701604655 (cit. on p. 56).

[280] S. Sinnecker and F. Neese. "Spin- Spin Contributions to the Zero-Field Splitting Tensor in Organic Triplets, Carbenes and Biradicals A Density Functional and Ab Initio Study". *The Journal of Physical Chemistry A* 110 (2006), 12267–12275 (cit. on p. 56).

[281] S. Perumal, B. Minaev, and H. Ågren. "Spin-spin and spin-orbit interactions in nanographene fragments: A quantum chemistry approach". *Journal of Chemical Physics* 136 (2012). DOI: 10.1063/1.3687002 (cit. on p. 56).

[282] K. Yamaguchi et al. "A spin correction procedure for unrestricted Hartree-Fock and Møller-Plesset wavefunctions for singlet diradicals and polyradicals". *Chemical Physics Letters* 149 (1988), 537–542. DOI: 10.1016/0009-2614(88)80378-6 (cit. on p. 56).

[283] F. Neese. "The ORCA program system". *Wiley Interdisciplinary Reviews: Computational Molecular Science* 2 (2012), 73–78 (cit. on p. 57).

[284] F. Weigend. "Accurate Coulomb-fitting basis sets for H to Rn". *Physical chemistry chemical physics* 8 (2006), 1057–1065 (cit. on p. 57).

[285] J. Lahiri et al. "An extended defect in graphene as a metallic wire". *Nature nanotechnology* 5 (2010), 326 (cit. on p. 59).

[286] F. Lombardi et al. “Quantum units from the topological engineering of molecular graphenoids”. *Science* 366 (2019), 1107–1110 (cit. on p. 59).

[287] F. Lombardi et al. “Synthetic Tuning of Quantum Properties of Open-shell Radicaloids”. *Chem* (2021). DOI: 10.1016/j.chempr.2021.03.024 (cit. on p. 59).

[288] J. Ma et al. “Wave-shaped polycyclic hydrocarbons with controlled aromaticity”. *Chemical Science* 10 (2019), 4025–4031. DOI: 10.1039/C8SC05416A (cit. on pp. 59, 74, 75).

[289] R. Huang et al. “Higher Order π-Conjugated Polycyclic Hydrocarbons with Open-Shell Singlet Ground State: Nonazethrene versus Nonacene”. *Journal of the American Chemical Society* 138 (2016), 10323–10330. DOI: 10.1021/jacs.6b06188 (cit. on p. 61).

[290] B. Bleaney and K. D. Bowers. “Anomalous paramagnetism of copper acetate” (1952), 451–466. DOI: 10.1098/rspa.1952.0181 (cit. on p. 62).

[291] X. Zhu et al. “Air- and heat-stable planar tri-p-quinodimethane with distinct biradical characteristics”. *Journal of the American Chemical Society* 133 (2011), 16342–16345. DOI: 10.1021/ja206060n (cit. on p. 63).

[292] S. Clough and F. Poldy. “Tunnelling rotation rate of a weakly hindered methyl group”. *Journal of Physics C: Solid State Physics* 6 (1973), 1953–1964. DOI: 10.1088/0022-3719/6/11/020 (cit. on p. 69).

[293] A. R. Sørnes et al. “Effect of isotopic substitution on the electron spin dynamics of the CH3$\dot{\text{C}}$(COOH)2 radical in X-irradiated methyl malonic acid powder: Intrinsic potentials and activation energies”. *Journal of Physical Chemistry A* 101 (1997), 8987–8994. DOI: 10.1021/jp972067n (cit. on p. 69).

[294] R. Glenn et al. “Analytical study of spin-dependent transition rates within pairs of dipolar and strongly exchange coupled spins with s= 1 2 during magnetic resonant excitation”. *Physical Review B* 87 (2013), 165205 (cit. on p. 70).

[295] S. Hediger et al. “NMR cross polarization by adiabatic passage through the Hartmann—Hahn condition (APHH)”. *Chemical physics letters* 223 (1994), 283–288 (cit. on p. 70).

[296] A. V. Astashkin and A. Schweiger. “Electron-spin transient nutation: a new approach to simplify the interpretation of ESR spectra”. *Chemical Physics Letters* 174 (1990), 595–602. DOI: 10.1016/0009-2614(90)85493-V (cit. on p. 71).

[297] F. Fujara et al. "Translational and rotational diffusion in supercooled orthoterphenyl close to the glass transition". *Zeitschrift für Physik B Condensed Matter* 88 (1992), 195–204. DOI: 10.1007/BF01323572 (cit. on p. 72).

[298] M. D. Ediger, C. A. Angell, and S. R. Nagel. "Supercooled liquids and glasses". *Journal of Physical Chemistry* 100 (1996), 13200–13212. DOI: 10.1021/jp953538d (cit. on p. 72).

[299] J. J. Dressler et al. "Diindenoanthracene Diradicaloids Enable Rational, Incremental Tuning of Their Singlet-Triplet Energy Gaps". *Chem* 6 (2020), 1353–1368. DOI: 10.1016/j.chempr.2020.02.010 (cit. on pp. 75, 140).

[300] B. H. Robinson, D. A. Haas, and C. Mailer. "Molecular dynamics in liquids: Spin-lattice relaxation of nitroxide spin labels". *Science* 263 (1994), 490–493. DOI: 10.1126/science.8290958 (cit. on p. 78).

[301] H. Sato et al. "Electron spin-lattice relaxation of nitroxyl radicals in temperature ranges that span glassy solutions to low-viscosity liquids". *Journal of Magnetic Resonance* 191 (2008), 66–77. DOI: 10.1016/j.jmr.2007.12.003 (cit. on pp. 78, 80).

[302] F. J. Santos et al. "Standard reference data for the viscosity of toluene". *Journal of physical and chemical reference data* 35 (2006), 1–8 (cit. on p. 80).

[303] J. J. Morton et al. "Environmental effects on electron spin relaxation in N@C_{60}". *Physical Review B - Condensed Matter and Materials Physics* 76 (2007). DOI: 10.1103/PhysRevB.76.085418 (cit. on p. 82).

[304] K. Nakagawa et al. "Electron-spin relaxation times of chromium(V)". *Journal of Magnetic Resonance (1969)* 98 (1992), 81–91. DOI: 10.1016/0022-2364(92)90111-J (cit. on pp. 83, 85).

[305] J. Du, G. R. Eaton, and S. S. Eaton. "Temperature and Orientation Dependence of Electron-Spin Relaxation Rates for Bis (diethyldithiocarbamato) copper (II)". 72 (1995), 67–72 (cit. on p. 83).

[306] J. Goslar, S. K. Hoffmann, and S. Lijewski. "Dynamics of 4-oxo-TEMPO-d16-15N nitroxide-propylene glycol system studied by ESR and ESE in liquid and glassy state in temperature range 10-295 K". *Journal of Magnetic Resonance* 269 (2016), 162–175. DOI: 10.1016/j.jmr.2016.06.006 (cit. on p. 83).

[307] I. M. Brown. "Electron spin-echo envelope decays and molecular motion: rotational and translational diffusion". *The Journal of Chemical Physics* 4930 (1974), 4930–4938. DOI: 10.1063/1.1681005 (cit. on p. 83).

[308] A. Barbon et al. "Dynamics and spin relaxation of tempone in a host crystal. An ENDOR, high field EPR and electron spin echo study". *Physical Chemistry Chemical Physics* 1 (1999), 4015–4023. DOI: 10.1039/a903380g (cit. on p. 83).

[309] Y. D. Tsvetkov and S. A. Dzuba. "Pulsed ESR and molecular motions". *Applied Magnetic Resonance* 1 (1990), 179–194. DOI: 10.1007/BF03166154 (cit. on p. 85).

[310] J. J. Morton et al. "Electron spin relaxation of N@C_{60} in CS_2". *Journal of Chemical Physics* 124 (2006). DOI: 10.1063/1.2147262 (cit. on p. 85).

[311] W. Gronski and N. Murayama. "The phenyl group motion in polystyrene and a model of restricted internal rotation". *Die Makromolekulare Chemie* 179 (1978), 1521–1529. DOI: 10.1002/macp.1978.021790610 (cit. on p. 85).

[312] D. J. Rizzo et al. "Inducing metallicity in graphene nanoribbons via zero-mode superlattices". *Science* 369 (2020), 1597–1603 (cit. on p. 86).

[313] S. Yamanaka et al. "EHF theory of chemical reactions part 4. UNO CASSCF, UNO CASPT2 and R (U) HF coupled-cluster (CC) wavefunctions". *Journal of Molecular Structure* 310 (1994), 205–218 (cit. on p. 86).

[314] M. L. Perrin, E. Burzurí, and H. S. J. Van Der Zant. "Single-molecule transistors". *Chem. Soc. Rev* 44 (2015), 835–1030. DOI: 10.1039/C4CS00231H (cit. on p. 89).

[315] S. H. Choi, B. Kim, and C. D. Frisbie. "Electrical resistance of long conjugated molecular wires". *Science* 320 (2008), 1482–1486 (cit. on p. 89).

[316] L. Lafferentz et al. "Conductance of a single conjugated polymer as a continuous function of its length". *Science* 323 (2009), 1193–1197 (cit. on p. 89).

[317] D. E. Jiang, B. G. Sumpter, and S. Dai. "First principles study of magnetism in nanographenes". *Journal of Chemical Physics* 127 (2007), 1–6. DOI: 10.1063/1.2770722 (cit. on p. 90).

[318] C. Rogers et al. "Closing the Nanographene Gap: Surface-Assisted Synthesis of Peripentacene from 6, 6-Bipentacene Precursors". *Angewandte Chemie International Edition* 54 (2015), 15143–15146 (cit. on p. 90).

[319] A. Sánchez-Grande et al. "Unravelling the Open-Shell Character of Peripentacene on Au(111)". *Journal of Physical Chemistry Letters* 12 (2021), 330–336. DOI: 10.1021/acs.jpclett.0c02518 (cit. on p. 90).

[320] Y. Ni et al. "A Peri-tetracene Diradicaloid: Synthesis and Properties". *Angewandte Chemie - International Edition* 57 (2018), 9697–9701 (cit. on pp. 91–93, 107).

[321] J. S. Jeong and H. W. Lee. "Curvature-enhanced spin-orbit coupling in a carbon nanotube". *Physical Review B - Condensed Matter and Materials Physics* 80 (2009), 1–5. DOI: 10.1103/PhysRevB.80.075409 (cit. on p. 93).

[322] F. Pei et al. "Large spin-orbit coupling in carbon nanotubes". *Nature Communications* 4 (2013), 1573–1577. DOI: 10.1038/ncomms2584 (cit. on p. 93).

[323] D. Huertas-Hernando, F. Guinea, and A. Brataas. "Spin-orbit coupling in curved graphene, fullerenes, nanotubes, and nanotube caps". *Physical Review B - Condensed Matter and Materials Physics* 74 (2006). DOI: 10.1103/PhysRevB.74.155426 (cit. on p. 93).

[324] D. G. De Oteyza et al. "Substrate-Independent Growth of Atomically Precise Chiral Graphene Nanoribbons". *ACS Nano* 10 (2016), 9000–9008. DOI: 10.1021/acsnano.6b05269 (cit. on p. 95).

[325] S. Mishra et al. "Large magnetic exchange coupling in rhombus-shaped nanographenes with zigzag periphery". *Nature Chemistry* (2021), 1–6 (cit. on p. 96).

[326] M. S. Fataftah et al. "Metal-ligand covalency enables room temperature molecular qubit candidates". *Chemical Science* 10 (2019), 6707–6714. DOI: 10.1039/c9sc00074g (cit. on p. 98).

[327] L. Tesi et al. "Quantum coherence in a processable vanadyl complex: new tools for the search of molecular spin qubits". *Chemical Science* 7 (2016), 2074–2083. DOI: 10.1039/C5SC04295J (cit. on p. 98).

[328] M. Droth and G. Burkard. "Electron spin relaxation in graphene nanoribbon quantum dots". *Physical Review B - Condensed Matter and Materials Physics* 87 (2013), 1–10 (cit. on pp. 98, 99).

[329] M. Droth and G. Burkard. "Spintronics with graphene quantum dots". *Physica Status Solidi - Rapid Research Letters* 10 (2016), 75–90 (cit. on p. 98).

[330] A. Jarmola et al. “Temperature- and magnetic-field-dependent longitudinal spin relaxation in nitrogen-vacancy ensembles in diamond”. *Physical Review Letters* 108 (2012), 1–5. DOI: 10.1103/PhysRevLett.108.197601 (cit. on p. 99).

[331] T. Rosskopf et al. “Investigation of surface magnetic noise by shallow spins in diamond”. *Physical Review Letters* 112 (2014), 1–5. DOI: 10.1103/PhysRevLett.112.147602 (cit. on p. 99).

[332] J. Fischer, B. Trauzettel, and D. Loss. “Hyperfine interaction and electron-spin decoherence in graphene and carbon nanotube quantum dots”. *Physical Review B - Condensed Matter and Materials Physics* 80 (2009), 1–9 (cit. on p. 104).

[333] M. Fuchs, V. Rychkov, and B. Trauzettel. “Spin decoherence in graphene quantum dots due to hyperfine interaction”. *Physical Review B - Condensed Matter and Materials Physics* 86 (2012) (cit. on p. 104).

[334] B. R. McGarvey. “The isotropic hyperfine interaction”. *The Journal of Physical Chemistry* 71 (1967), 51–66 (cit. on p. 105).

[335] J. Clayden et al. *Organic chemistry*. Second. Oxford university press Oxford, 2012 (cit. on p. 108).

[336] J. A. N. F. Gomes and R. B. Mallion. “Aromaticity and ring currents”. *Chemical Reviews* 101 (2001), 1349–1383. DOI: 10.1021/cr990323h (cit. on p. 108).

[337] M. D. Peeks, T. D. Claridge, and H. L. Anderson. “Aromatic and antiaromatic ring currents in a molecular nanoring”. *Nature* 541 (2017), 200–203. DOI: 10.1038/nature20798 (cit. on p. 109).

[338] M. Rickhaus et al. “Global aromaticity at the nanoscale”. *Nature Chemistry* 12 (2020), 236–241. DOI: 10.1038/s41557-019-0398-3 (cit. on p. 109).

[339] A. C. Bleszynski-Jayich et al. “Persistent currents in normal metal rings”. *Science* 326 (2009), 272–275. DOI: 10.1126/science.1178139 (cit. on p. 109).

[340] C. J. Judd et al. “Molecular Quantum Rings Formed from a π -Conjugated Macrocycle”. *Physical Review Letters* 125 (2020), 206803. DOI: 10.1103/PhysRevLett.125.206803 (cit. on p. 109).

[341] Z. Li et al. "Towards graphyne molecular electronics". *Nature Communications* 6 (2015), 6321. DOI: 10.1038/ncomms7321 (cit. on p. 110).

[342] "Constructive quantum interference in a bis-copper six-porphyrin nanoring". *Nature Communications* 8 (2017), 1–5. DOI: 10.1038/ncomms14842 (cit. on p. 110).

[343] X. Lu et al. "Fluorenyl Based Macrocyclic Polyradicaloids". *Journal of the American Chemical Society* 139 (2017), 13173–13183. DOI: 10.1021/jacs.7b07335 (cit. on p. 110).

[344] G. Li et al. "From Open-Shell Singlet Diradicaloid to Closed-Shell Global Antiaromatic Macrocycles". *Angewandte Chemie* 130 (2018), 7284–7288. DOI: 10.1002/ange.201803949 (cit. on p. 110).

[345] X. Lu et al. "Global Aromaticity in Macrocyclic Cyclopenta-Fused Tetraphenanthrenylene Tetraradicaloid and Its Charged Species". *Angewandte Chemie - International Edition* 57 (2018), 13052–13056. DOI: 10.1002/anie.201807185 (cit. on p. 110).

[346] C. Liu et al. "Global Aromaticity in Macrocyclic Polyradicaloids: Hückel's Rule or Baird's Rule?" *Accounts of Chemical Research* 52 (2019), 2309–2321. DOI: 10.1021/acs.accounts.9b00257 (cit. on p. 110).

[347] C. Liu et al. "Macrocyclic Polyradicaloids with Unusual Super-ring Structure and Global Aromaticity". *Chem* 4 (2018), 1586–1595. DOI: 10.1016/j.chempr.2018.03.020 (cit. on pp. 110, 111, 121).

[348] N. Bar-Gill et al. "Solid-state electronic spin coherence time approaching one second". *Nature Communications* 4 (2013), 1743–1746 (cit. on pp. 122, 125).

[349] M. Veldhorst et al. "An addressable quantum dot qubit with fault-tolerant control-fidelity". *Nature Nanotechnology* 9 (2014), 981–985. DOI: 10.1038/nnano.2014.216 (cit. on p. 122).

[350] S. Giménez-Santamarina et al. "Exploiting clock transitions for the chemical design of resilient molecular spin qubits". *Chemical Science* (2020). DOI: 10.1039/d0sc01187h (cit. on p. 122).

[351] L. Viola and S. Lloyd. "Dynamical suppression of nonlocal decoherence in two-state quantum systems". *Physical Review A* 58 (1998) (cit. on p. 122).

[352] H. Y. Carr and P. E. M. "" *Physical Review* 94 (1954), 630 (cit. on p. 124).

[353] S. Meiboom and D. Gill. "Modified spin-echo method for measuring nuclear relaxation times". *Review of Scientific Instruments* 29 (1958), 688–691 (cit. on p. 124).

[354] A. M. Souza, G. A. Ávarez, and D. Suter. "Robust dynamical decoupling for quantum computing and quantum memory". *Physical Review Letters* 106 (2011), 1–4 (cit. on pp. 124, 125, 129, 132).

[355] A. A. Maudsley. "Modified Carr-Purcell-Meiboom-Gill sequence for NMR fourier imaging applications". *Journal of Magnetic Resonance (1969)* 69 (1986), 488–491 (cit. on p. 124).

[356] T. Gullion, D. B. Baker, and M. S. Conradi. "New, compensated Carr-Purcell sequences". *Journal of Magnetic Resonance (1969)* 89 (1990), 479–484 (cit. on p. 124).

[357] G. S. Uhrig. "Keeping a quantum bit alive by optimized π-pulse sequences". *Physical Review Letters* 98 (2007), 7–10 (cit. on p. 124).

[358] K. Khodjasteh and D. A. Lidar. "Fault-tolerant quantum dynamical decoupling". *Physical Review Letters* 95 (2005), 1–4. DOI: 10.1103/PhysRevLett.95.180501 (cit. on p. 124).

[359] N. Timoney et al. "Quantum gates and memory using microwave-dressed states". *Nature* 476 (2011), 185–188. DOI: 10.1038/nature10319 (cit. on p. 124).

[360] G. T. Genov et al. "Mixed dynamical decoupling". *Quantum Science and Technology* 4 (2019), 1–14. DOI: 10.1088/2058-9565/ab2afd (cit. on p. 124).

[361] G. de Lange et al. "Universal Dynamical Decoupling of a Single Solid-State Spin from a Spin Bath". *Science* 330 (2010), 60–64 (cit. on pp. 125, 135, 136).

[362] N. Bar-Gill et al. "Suppression of spin-bath dynamics for improved coherence of multi-spin-qubit systems". *Nature Communications* 3 (2012), 856–858 (cit. on pp. 125, 136, 137).

[363] M. J. Biercuk et al. "Optimized dynamical decoupling in a model quantum memory". *Nature* 458 (2009), 996–1000 (cit. on p. 125).

[364] H. Bluhm et al. "Dephasing time of GaAs electron-spin qubits coupled to a nuclear bath exceeding 200μs". *Nature Physics* 7 (2011), 109–113. DOI: 10.1038/nphys1856 (cit. on p. 125).

[365] L. Cywiński et al. "How to enhance dephasing time in superconducting qubits". *Physical Review B - Condensed Matter and Materials Physics* 77 (2008), 1–11. DOI: 10.1103/PhysRevB.77.174509 (cit. on pp. 125, 126).

[366] G. S. Uhrig. "Exact results on dynamical decoupling by π pulses in quantum information processes". *New Journal of Physics* 10 (2008), 083024. DOI: 10.1088/1367-2630/13/5/059504 (cit. on pp. 125, 126).

[367] W. Yang, W. L. Ma, and R. B. Liu. "Quantum many-body theory for electron spin decoherence in nanoscale nuclear spin baths". *Reports on Progress in Physics* 80 (2017). DOI: 10.1088/0034-4885/80/1/016001 (cit. on p. 126).

[368] W. M. Witzel, K. Young, and S. Das Sarma. "Converting a real quantum spin bath to an effective classical noise acting on a central spin". *Physical Review B - Condensed Matter and Materials Physics* 90 (2014), 1–6. DOI: 10.1103/PhysRevB.90.115431 (cit. on p. 126).

[369] P. Szańkowski et al. "Environmental noise spectroscopy with qubits subjected to dynamical decoupling". *Journal of Physics Condensed Matter* 29 (2017). DOI: 10.1088/1361-648X/aa7648 (cit. on p. 126).

[370] E. Dementyev et al. "Anomalies in the NMR of silicon: Unexpected spin echoes in a dilute dipolar solid". *Physical Review B - Condensed Matter and Materials Physics* 68 (2003), 1–4 (cit. on p. 127).

[371] D. Li et al. "Generating unexpected spin echoes in dipolar solids with π pulses". *Physical Review Letters* 98 (2007), 2–5 (cit. on p. 127).

[372] V. V. Kurshev and A. M. Raitsimring. "Carr-Purcell train in the conditions of partial excitation of magnetic resonance spectrum". *Journal of Magnetic Resonance (1969)* 88 (1990), 126–129. DOI: 10.1016/0022-2364(90)90113-N (cit. on p. 128).

[373] J. Du et al. "Preserving electron spin coherence in solids by optimal dynamical decoupling". *Nature* 461 (2009), 1265–1268 (cit. on pp. 128, 136).

[374] G. Mitrikas, E. K. Efthimiadou, and G. Kordas. "Extending the electron spin coherence time of atomic hydrogen by dynamical decoupling". *Physical Chemistry Chemical Physics* 16 (2014), 2378–2383 (cit. on pp. 128, 130).

[375] C. A. Ryan, J. S. Hodges, and D. G. Cory. "Robust decoupling techniques to extend quantum coherence in diamond". *Physical Review Letters* 105 (2010), 1–4 (cit. on p. 129).

[376] P. P. Borbat, E. R. Georgieva, and J. H. Freed. "Improved sensitivity for long-distance measurements in biomolecules: Five-pulse double electron-electron resonance". *Journal of Physical Chemistry Letters* 4 (2013), 170–175. DOI: 10.1021/jz301788n (cit. on p. 135).

[377] J. Medford et al. "Scaling of dynamical decoupling for spin qubits". *Physical Review Letters* 108 (2012), 1–5. DOI: 10.1103/PhysRevLett.108.086802 (cit. on p. 136).

[378] E. R. Canarie, S. M. Jahn, and S. Stoll. "Quantitative Structure-Based Prediction of Electron Spin Decoherence in Organic Radicals". *The Journal of Physical Chemistry Letters* 13 (2020), 3396–3400. DOI: 10.1021/acs.jpclett.0c00768 (cit. on p. 140).

[379] D. Van Der Spoel et al. "GROMACS: fast, flexible, and free". *Journal of computational chemistry* 26 (2005), 1701–1718 (cit. on p. 140).

[380] A. Candini et al. "Graphene spintronic devices with molecular nanomagnets". *Nano letters* 11 (2011), 2634–2639 (cit. on p. 141).

[381] C. Bonizzoni et al. "Coherent coupling between Vanadyl Phthalocyanine spin ensemble and microwave photons: Towards integration of molecular spin qubits into quantum circuits". *Scientific Reports* 7 (2017), 1–8. DOI: 10.1038/s41598-017-13271-w (cit. on p. 141).

[382] P. Haikka et al. "Proposal for detecting a single electron spin in a microwave resonator". *Physical Review A* 95 (2017), 022306 (cit. on p. 141).

[383] A. Bienfait et al. "Reaching the quantum limit of sensitivity in electron spin resonance". *Nature Nanotechnology* 11 (2016), 253–257. DOI: 10.1038/nnano.2015.282 (cit. on p. 141).

[384] E. T. Chernick et al. "Electron donor-bridge-acceptor molecules with bridging nitronyl nitroxide radicals: Influence of a third spin on charge- and spin-transfer dynamics". *Journal of the American Chemical Society* 128 (2006), 4356–4364. DOI: 10.1021/ja0576435 (cit. on pp. 143, 144).

[385] E. T. Chernick et al. "Controlling electron transfer dynamics in donor-bridge-acceptor molecules by increasing unpaired spin density on the bridge". *Journal of Physical Chemistry B* 111 (2007), 6728–6737. DOI: 10.1021/jp068741v (cit. on pp. 143, 144).

[386] M. R. Wasielewski. "Photoinduced Electron Transfer in Supramolecular Systems for Artificial Photosynthesis". *Chemical Reviews* 92 (1992), 435–461. DOI: 10.1021/cr00011a005 (cit. on p. 143).

[387] A. van der Est. "Transient EPR: Using spin polarization in sequential radical pairs to study electron transfer in photosynthesis". *Photosynthesis Research* 102 (2009), 335–347. DOI: 10.1007/s11120-009-9411-9 (cit. on p. 143).

[388] F. Kraffert et al. "Charge separation in PCPDTBT:PCBM blends from an EPR perspective". *Journal of Physical Chemistry C* 118 (2014), 28482–28493. DOI: 10.1021/jp509650v (cit. on p. 143).

[389] M. A. Lebedeva et al. "Stabilising the lowest energy charge-separated state in a {metal chromophore – fullerene} assembly: a tuneable panchromatic absorbing donor–acceptor triad". *Chem. Sci.* 7 (2016), 5908–5921. DOI: 10.1039/C5SC04271B (cit. on p. 144).